Predictive Analysis of Fracture and Fatigue in Polymer Gear Teeth: A New Theory for Preventing Failure

By

Sutartip Wittayapiyanon

A thesis submitted to the University of Birmingham for the degree of
DOCTOR OF PHILOSOPHY

Department of Mechanical Engineering
School of Engineering
University of Birmingham
2023

Abstract

This research focuses on solving wear-related challenges in involute gear-tooth polymer materials, enhancing Buckingham's and Merritt's equations, particularly in the context of elevated frictional temperatures resulting from kinematic contact behaviour. The Mason Institute of Tribology laboratory study employs the MARK II testing machine to underscore the significant consequences of erosion and wear, leading to weight reduction and wear size increase, ultimately culminating in tooth cracking. Detailed observations of the tooth surface reveal kinematic gear contact behaviour attributed to factors such as involute gear geometry failure, changing of vibration, frictional temperature issues, tooth deflection, and bending stress, particularly under extended machine cycles and heavy work loading.

The study applies four distinct coefficient theories - Buckingham, Merritt, Benedict & Kelley, and Drozdov & Gavrikov - to determine frictional coefficients through theoretical analysis and experimental testing, establishing a correlation between these coefficients and resulting gear power losses. The research focuses on polymer gears constructed from various Polyether Ether Ketone (PEEK) grades, adhering to industrial standards. Simulated designs consider temperature variations, mechanical load conditions, and changes in polymer material stiffness, examining critical factors such as load-sharing ratio, tooth bending stress, and frictional temperature between gear pairs. The structural and thermal-dynamic geometries are analyzed using Finite Element Analysis (FEA) to predict parameters including contact pressure interface, stress distribution, and tooth bending deformation behaviour. Additionally, the study explores the impact of fluctuations in frictional coefficients on actual gear power losses, emphasizing the predictive capability of power loss in polymer gears. The research rigorously compares theoretical frictional coefficient and power loss results with experimental data to validate theoretical models.

Crack propagation analysis reveals alterations in approach lengths and recess along the un-normal contact path, leading to increased wear on tooth flanks and the onset of initial cracks. The research emphasizes the importance of Linear Elastic Fracture Mechanics (LEFM) analysis, focusing on Stress Intensity Factors (SIFs) critical for evaluating fatigue crack growth, influenced by factors including coefficient of friction, strain responses, tooth wear, and stress-induced bending deformation.

In conclusion, this comprehensive thesis contributes significantly to solving wear-related issues in involute gear-tooth PEEK gears, providing valuable insights into optimizing gear design and improving the efficiency of polymer gear systems.

Acknowledgements

First and foremost, I express my deepest gratitude to my supervisor, Professor Karl Dearn, for their invaluable guidance, unwavering support, and patience throughout my PhD journey. Their extensive knowledge and rich experience have been a constant source of encouragement in my academic pursuits and daily life. I am also indebted to Dr. Amir Hajiyavand for his invaluable assistance, advice, and steadfast support, as well as to Dr. Martin Herreros Arellano for his guidance on various aspects of the research, and Professor Athanasios Tsolakis for his role as co-supervisor.

I sincerely appreciate my friends and colleagues, including Dr Iestyn Stead, Dr James Firth, Dr David Eckold, and Dr Zainab Mohammed Shukur, for their invaluable assistance, advice, and unwavering encouragement.

Furthermore, I am expressing my sincere gratitude to the Royal Thai Government Scholarships for their financial support, which has made this research endeavor possible.

Contents

List of Figures

List of Tables

Chapter 1

Introduction

1.1 Research Background and Motivation

Polymers and composite materials are increasingly utilised in the automotive and mechanical industries as viable alternatives to traditional metal gears. These engineering plastics fulfil several uses in the increasingly demanding requirements of the automotive sector. They offer adaptability and are crucial in driving necessary industrial innovations. One of the key advantages of plastic gear technology is its lightweight nature and compliance and contributes to reduced fuel consumption. This has been documented in Walton's (1998) [1] and Kono’s (2003) [2] studies.

At the University of Birmingham, various polymer composites have been developed specifically for automotive applications. The Mechanical Innovation and Tribology (MIT) laboratory is currently exploring the failure mechanisms of gear geometries when polymer materials are subjected to automotive and industrial operating environments. Investigations utilise a range of experimental equipment, but predominantly the MARK II (MK II) closed loop test machines, whilst designing gears that adhere to BS/ISO 6336, BS 6168, and VDI

2736 standards. The studies conducted by Kono and Dearn are particularly noteworthy; they evaluated spur gear models made of Polyether Ether Ketone (PEEK) using the MK II machines, as illustrated in Figure 1.1. These studies focused on enhancing these gears' thermal friction and wear resistance (Kono, 2003 [3]; Dearn, 2009 [4]).

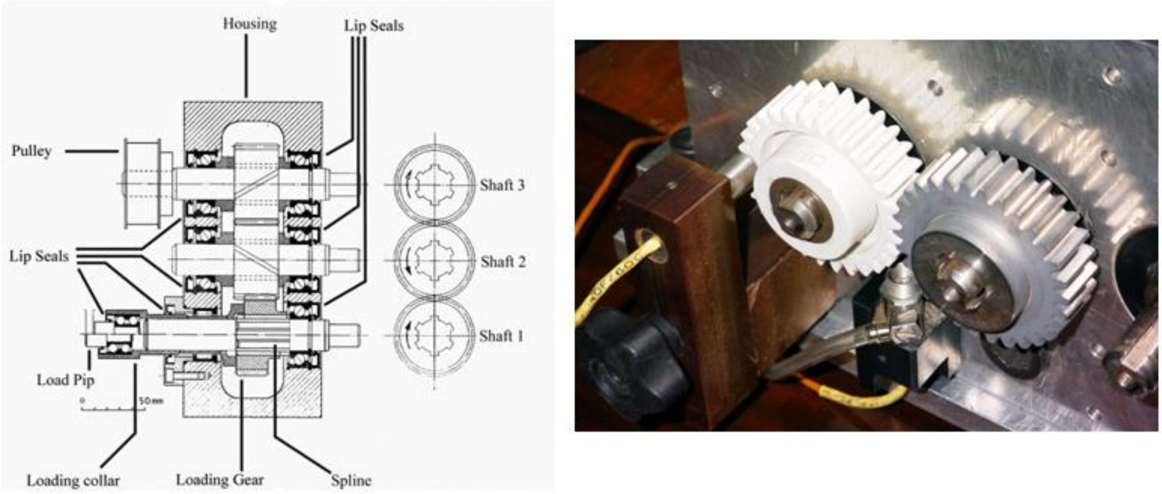

Figure 1.1 *The MK II Closed-Loop Gear Test Machine MK II machine*
(after, Kono, 2003 [3]; Dearn, 2009 [4])

Polymers offer several advantages over metal gears, including reduced weight, lower cost, enhanced corrosion resistance, and quieter operation. They also exhibit superior vibration-damping qualities, which can be beneficial in specific applications. A notable feature of polymer gears is that they may not require lubrication, making them ideal for situations where lubrication is challenging or undesirable. However, when selecting a polymer for involute gears, careful consideration must be given to material selection, gear design, and manufacturing method. Polymers with robust mechanical properties, characterised by high strength, stiffness, and wear resistance, are typically preferred. Common polymer materials for gears include acetal (POM), nylon (PA), and PEEK.

VICTREX^{TM} specialises in designing and developing PEEK gear polymers that adhere to industrial standard gear shapes. PEEK is widely recognised as one of the top-performing engineering thermoplastics, suitable for various operating conditions and applications across automotive, aerospace, energy, electronics, engineering production processes, and medical industries. Its mechanical properties include high-temperature performance, strength, stiffness, fatigue, and wear resistance. For example, PEEK 450G has a melting temperature range of 342.78 - 387.2 degrees Celsius, while its low coefficient of friction varies between 0.15 and 0.28. The friction coefficients of PEEK 450FC30 were measured using the thrust washer technique at a test speed of 1 m/s (Victrex, 2018 [5]).

Most research on plastic composite materials concentrates on their utilisation, functional features, failure characteristics, and limitations. One drawback of plastic materials is their varying severity depending on the application, such as lower heat loss and thermal expansion, environmental resistance, reduced stiffness and hardness, significant creep deformation, and often flammability.

Plastic gear materials are typically assessed in six areas concerning polymer composite materials: transmission errors, meshing behaviour, tooth wear, involute gear geometries, increased frictional heat, and cracking. For instance:

- transmission errors and increased contact stresses are significant causes of gear failure, often occurring at the gear teeth's root. High tensile and local stresses develop due to the teeth's shape [6]. The impacts of gear tooth shape and root can be seen in the "Tooth-Root Bending Stress (TSBS)" and "Tooth-Surface Contact Stress (TSCS)" parameters” [7], [8], [9], [10], [11], [12], [13], [14]. The expected failure damage of a pair of gears, as TSBS and TSCS indicate, demonstrates the gear materials' strength and vulnerability. Figure 1.2 illustrates these TSBS and TSCS parameters.

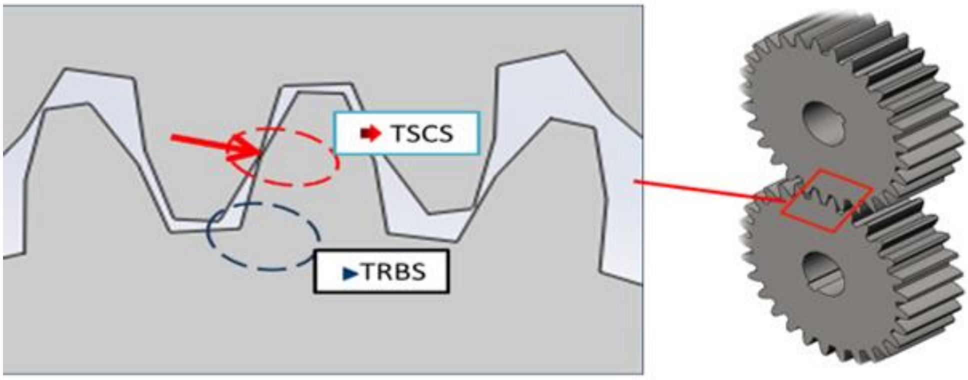

__Figure 1.2__ The Location of Tooth-Root Bending Stress (TSBS) and Tooth-Surface Contact Stress (TSCS) parameters (Lias et al., 2018 [7])

- Gear polymer tooth wear is influenced by several factors, including erosion, size changes due to fractures, deformation of debris in the microstructure, and weight loss. These characteristics are affected by load conditions, thermal damage, vibration, and mesh misalignment, which can lead to issues in involute gear geometry and gear meshing behaviour [15] [16].
- A study conducted 2004 by Senthilvelan and Gnanamoorthy on nylon 66 involute structural tooth failures revealed various types of damage to gear mechanisms as a result of experimental testing. Their findings included wear, surface cracking, tooth deformation, and improved heat resistance upon enhancing the teeth [17].

Consequently, this research aims to develop a new theory for predicting gear fracture and fatigue prior to failure. In this study, five grades of PEEK are used in MK II spur gear models to assess the acceleration vibration in the power transmission system, which in turn affects thermal friction and wear.

1.2 Research Aims and Objectives

Much existing research has focused on developing new diagnostic procedures and identifying or monitoring cracks using current methodologies. This research aims to conduct an in-depth investigation into the kinematic behaviour of polymer gears. This will lead to a new theoretical analysis for predicting changes in gear contact-line deformation, involute tooth failure, crack propagation paths, fracture modes, wear behaviour, and frictional thermal characteristics before failure occurs. This research is divided into four key areas: developing an updated equation, experimental analysis, and 3D software simulation. A schematic summary of the work is provided in Figure 1.3.

Figure 1.3 explores these aspects by analysing shifting geometries on involute teeth and the meshing error associated with increasing weight loss on tooth sides. The experimental testing and analytical modelling focus on investigating the gear wear behaviours of Poly-Ether-Ether-Ketone (PEEK) in various grades: 450G, 450FC30, 450GL30, 450CA30, and 650G.

The study employs five grades of PEEK (PEEK 450G, PEEK 450GL, PEEK 450FL, PEEK 450CA, and PEEK 650G) in experimental and analytical designs for spur gear models using the MK II machine. The objective is to evaluate the acceleration vibration of the power transmission system and its influence on thermal friction and wear. This is achieved by determining the torque at 10.8 Nm and a speed of 1,000 rpm under minimal vibration testing on the master gearbox and arm loading. The work is evaluated using closed-circuit testing with and without oil lubrication.

The overarching goal of this study is to understand the response of different grades and types of gear materials to kinematic behaviour, tooth deformation, crack propagation, and breakage, as observed in real-time gear teeth testing. To achieve this, the research objectives are divided into four distinct components:

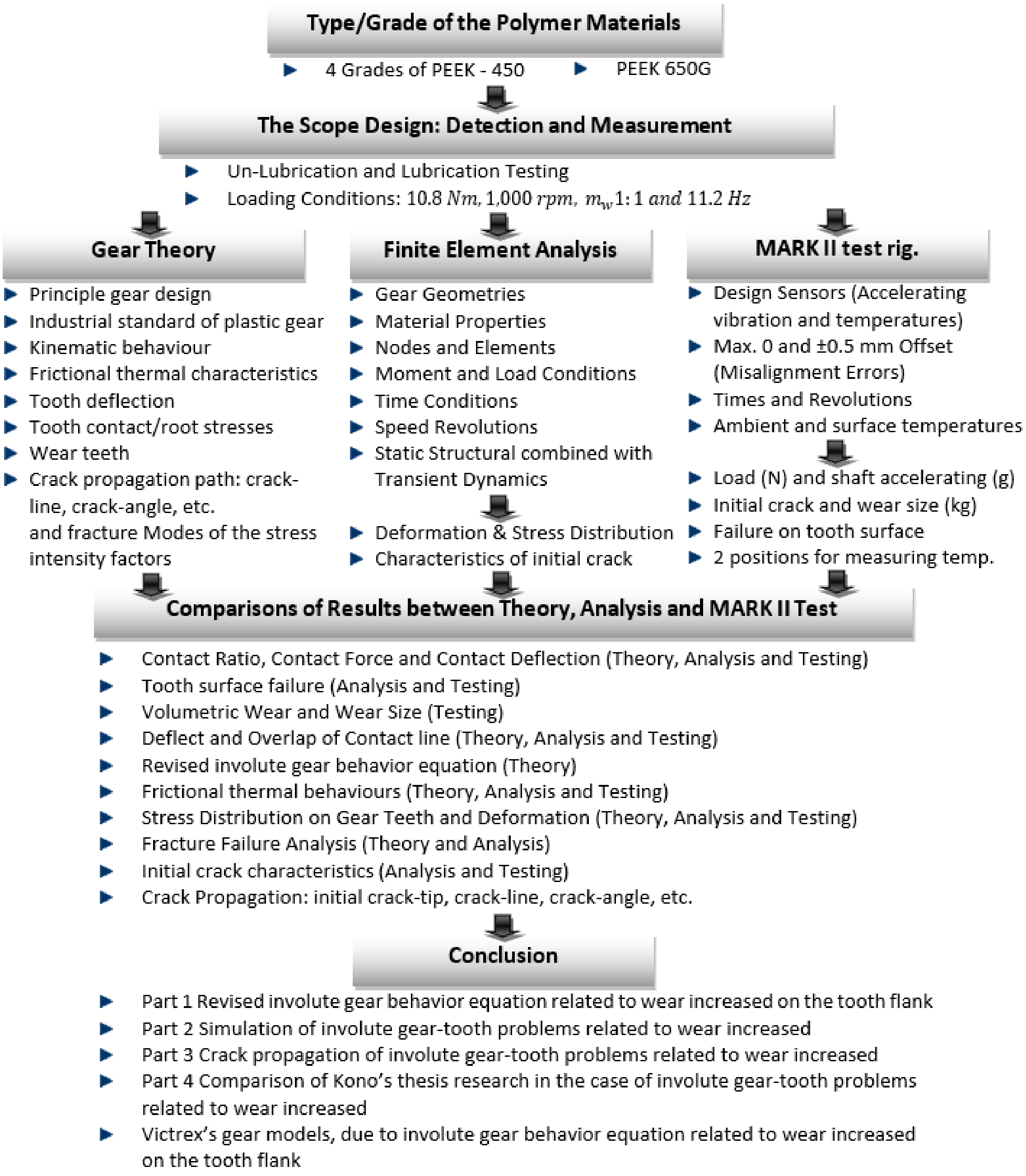

Type/Grade of the Polymer Materials

- 4 Grades of PEEK - 450
- PEEK 650G

The Scope Design: Detection and Measurement

- Un-Lubrication and Lubrication Testing
- Loading Conditions: $10.8\ Nm, 1{,}000\ rpm,\ m_w 1:1\ and\ 11.2\ Hz$

Gear Theory

- Principle gear design
- Industrial standard of plastic gear
- Kinematic behaviour
- Frictional thermal characteristics
- Tooth deflection
- Tooth contact/root stresses
- Wear teeth
- Crack propagation path: crack-line, crack-angle, etc. and fracture Modes of the stress intensity factors

Finite Element Analysis

- Gear Geometries
- Material Properties
- Nodes and Elements
- Moment and Load Conditions
- Time Conditions
- Speed Revolutions
- Static Structural combined with Transient Dynamics
- Deformation & Stress Distribution
- Characteristics of initial crack

MARK II test rig.

- Design Sensors (Accelerating vibration and temperatures)
- Max. 0 and ±0.5 mm Offset (Misalignment Errors)
- Times and Revolutions
- Ambient and surface temperatures
- Load (N) and shaft accelerating (g)
- Initial crack and wear size (kg)
- Failure on tooth surface
- 2 positions for measuring temp.

Comparisons of Results between Theory, Analysis and MARK II Test

- Contact Ratio, Contact Force and Contact Deflection (Theory, Analysis and Testing)
- Tooth surface failure (Analysis and Testing)
- Volumetric Wear and Wear Size (Testing)
- Deflect and Overlap of Contact line (Theory, Analysis and Testing)
- Revised involute gear behavior equation (Theory)
- Frictional thermal behaviours (Theory, Analysis and Testing)
- Stress Distribution on Gear Teeth and Deformation (Theory, Analysis and Testing)
- Fracture Failure Analysis (Theory and Analysis)
- Initial crack characteristics (Analysis and Testing)
- Crack Propagation: initial crack-tip, crack-line, crack-angle, etc.

Conclusion

- Part 1 Revised involute gear behavior equation related to wear increased on the tooth flank
- Part 2 Simulation of involute gear-tooth problems related to wear increased
- Part 3 Crack propagation of involute gear-tooth problems related to wear increased
- Part 4 Comparison of Kono's thesis research in the case of involute gear-tooth problems related to wear increased
- Victrex's gear models, due to involute gear behavior equation related to wear increased on the tooth flank

Figure 1.3 A Schematic Overview of the Thesis and Research

1. The first component involves conducting experiments using the MK II test equipment, focusing on real-time machine operation. These tests are conducted in a closed loop, with oil and non-lubricated conditions.
2. Similar to the first component, the second component utilises the MK II test equipment while the machine operates. This phase also tests the gear materials in a closed loop with and without oil lubrication, providing insights into their performance under different lubrication conditions.
3. The third component adapts to changes in the involute gear design by employing simulation with 3D Finite Element Analysis Dynamic Simulation (FEA-DS) software. This simulation incorporates Transient Thermal and Dynamic Structural analysis, comparing steel and polymer gears using ANSYS simulation, mainly focusing on load sharing ratio, tooth bending stress, and frictional temperature between gear pairs. Additionally, this phase involves stress distribution and deformation analysis to understand involute tooth failure and the stages of fractures in crack propagation life, starting from minor fractures and progressing to significant cracks at the TSCS and TSBS [18].
4. Finally, the research culminates by correlating the outcomes of the three previously mentioned components with existing research, including Kono's thesis and other relevant papers on industrial and automotive industry standards. This comparison mainly focuses on the impact of applied pressure and gear geometry in real-time testing, both with and without lubrication. The comprehensive analysis undertaken in this thesis explores various aspects of kinematic behaviour and static and dynamic analysis tests for linear and nonlinear problem scenarios.

Overall, this thesis aims to thoroughly examine multiple facets of gear behaviour, particularly in real-time testing, to understand better the dynamics, wear patterns, and failure mechanisms of different gear materials.

Chapter 2

Comprehensive Review of Literature in Polymer Gear Research: Bridging Theory and Practice

This literature review primarily evaluates the wear characteristics of gear polymers, which are influenced by various factors, including debris generation, the emergence of cracks affecting geometry, distortion of microstructure, and weight loss via material loss. These elements collectively impact the wear properties of polymer gear. Both theoretical and analytical approaches have been applied to study gear polymers. The research in this thesis has been designed to include four grades of polymer materials, specifically Polyether Ether Ketone (PEEK) variants: 450G, 450GL30, 450FC30, 450CA30, and 650G. Influential factors such as load conditions, frictional heat, vibration, and mesh misalignment significantly affect these characteristics, potentially leading to instability in involute gear geometry and gear meshing behaviour [15], [16].

Furthermore, the literature divides spur gear design into six categories: industrial standards, gear kinematic behaviour, failure mechanisms, flash temperature, frictional thermal effects, viscoelastic hysteretic behaviour, progressive contact, and fatigue fracture. This segmentation facilitates a detailed investigation into the mechanisms of material deterioration on the tooth flanks of polymer gears and the processes leading to their fracture and failure.

2.1 PEEK Gear Geometries

Polymers are prevalently used in the manufacturing of gear wheels, with Dennig and Vodermayer noting that PA and POM materials constitute over 85% of the total usage. These materials have performed superior to other plastic gears, particularly in power transmission applications. PEEK gears, in particular, have shown a greater load-carrying capacity at higher ambient temperatures than POM, along with enhanced resistance to friction and wear [19]. Polymer gears offer several advantages, including reduced weight, lower costs, improved corrosion resistance, and quieter operation than metal counterparts. They also possess better vibration-damping properties, which can be advantageous in specific applications. Polymer gears may not require lubrication, making them suitable for environments where lubrication is challenging or undesirable.

When designing gears, it is advisable to consult gear design handbooks and adhere to industry standards, such as the British Standard (BS), American Gear Manufacturers Association (AGMA), or American National Standard (ANSI). Collaboration with experienced gear designers or engineers specialising in polymer gears is crucial to ensure the design meets the necessary performance and reliability criteria. While the ANSI/AGMA standards primarily focus on metal gears, no specific plastic spur gears are required. The design of PEEK gear geometries typically follows standard involute gear profiles akin to those used for metal gears.

It is essential to consider the material characteristics of PEEK gears, including their coefficient of thermal expansion, temperature limitations, and the potential for creep or deformation under load. Modifying the gear shape to enhance the performance and longevity of PEEK gears in specific applications is also recommended.

2.1.1 Design and Specification Standards for Polymer Gears

2.1.1.1 BS 6336 Specification

BS 6336 is a comprehensive multi-part document divided into six sections. It covers various gear design aspects, including tooth shape, material properties, lubrication conditions, and operational parameters. This standard details methods for calculating gear load capacity, contact, and bending stresses. It considers tooth profile modifications, gear accuracy, and dynamic factors to accommodate realistic operating conditions [20].

2.1.1.2 BS 6168 Specification for the Dimensional Principal Tooth Profile Factors

BS 6168 standard specifies dimensional accuracy for spur gear plastic mouldings on metal hubs. It bases spur gear specifications on the principal dimensions of the tooth profile, including module, spur gear errors, and tolerance factors. These factors encompass adjacent tooth pitch, typical individual base pitch error, cumulative tooth pitch, radial tooth-to-tooth composite, and centre distance. The metal hub's rim proportions in moulded plastic gears play a significant role in supporting the gear teeth under operational conditions [21], as illustrated in Figure 2.1.1.

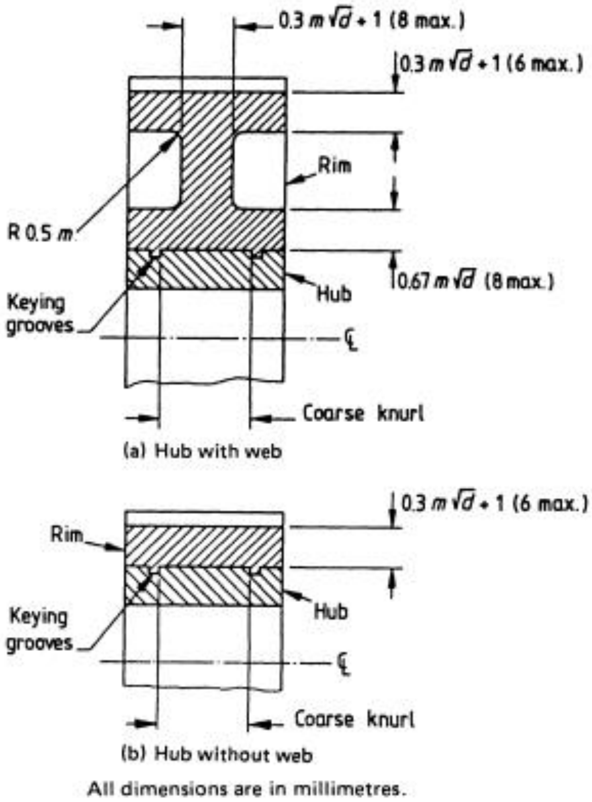

Figure 2. 1 *Metal Hub with Plastic Spur Gear Moulding Arrangements (BS 6168, 1987 [21])*

2.1.1.3 ANSI/AGMA 1010-F14 Specification for the Wear and Failure

The ANSI/AGMA 1010-F14 standard discusses the visual inspection criteria and quality standards for gear teeth. It provides insights into the physical appearance of spur gear teeth, applicable to both metal and plastic spur gears [22].

2.1.2 MIT Research Laboratory

Researchers at The University of Birmingham have extensively researched various gear polymer geometries. This research primarily focuses on the failure of spur gear designs when applied to polymeric materials in automotive environments, adhering to industry test standards. Chapter 2 delves into gear geometries for five grades of PEEK materials. These are aligned with the British or International Organization for Standardization (BS/ISO) standards for spur gears. Detailed information on these gear polymers' parameters, dimensions, and sizes can be found in Table 2.1 [3].

Table 2. 1 *Gear Polymer Geometry Parameters*

*Gear Parameters**	*Units*	*Symbols*	*Pinion/Driver*	*Gear/Driven*
Number of gear teeth	*N/A*	Z_p, Z_g	*30*	*30*
Module	*mm*	m	*2*	
Pressure Angle	*Deg.*	$\emptyset_t$	*20*	
Pitch Diameter	*mm*	d_p, d_g	*60*	*60*
Tip Diameter	*mm*	d_{tp}, d_{tg}	*64*	
Addendum	*mm*	a	*2*	
Dedendum	*mm*	d	*2.50*	
Width Face	*mm*	b	*17.40* [10] [11]	
Centre Distance	*mm*	C	*60.10* [10] [11]	

* Gear parameters and geometries used in research at the University of Birmingham

2.1.3 VICTREX™

VICTREX™ specialises in designing and developing PEEK gear polymers, adhering to industrial standard gear geometries. Recognised as one of the top-performing engineering thermoplastics, it finds application in various demanding fields such as automotive, aerospace, energy, electronics, engineering production processes, and medical industries. The mechanical engineering properties of PEEK are notable for their excellence in high-temperature performance, strength, stiffness, fatigue resistance, and wear resistance. For example, PEEK 450G has a melting temperature range of 342.78 - 387.2 degrees Celsius. In contrast, PEEK 450FC30 features coefficients of friction evaluated using the thrust washer technique at a test speed of 1 m/s, demonstrating a low coefficient of friction that ranges between 0.15 and 0.28 [23] [24].

2.2 MARK II Test Rig.

The MIT laboratory employs the MARK II test rig to evaluate the performance of polymer gears within power transmission systems. This machine was initially developed as part of White's PhD research in 1998 and is notable for its utilisation in plastic gear testing rigs. The MARK II features a unique three-shaft configuration in its master gearbox. A vital aspect of this rig is its loading mechanism, which applies force using a static weight. This design enables MARK II to gather comprehensive experimental data, particularly in accelerated vibration, friction efficiency, wear progression, and temperature fluctuation.

The master gearbox of the MARK II has been instrumental in obtaining valuable insights into the behaviour of polymer gears under various test conditions. Figure 2.2 illustrates an example of the MARK II test equipment, as further developed in the studies by Kono and Dearn [3], [4].

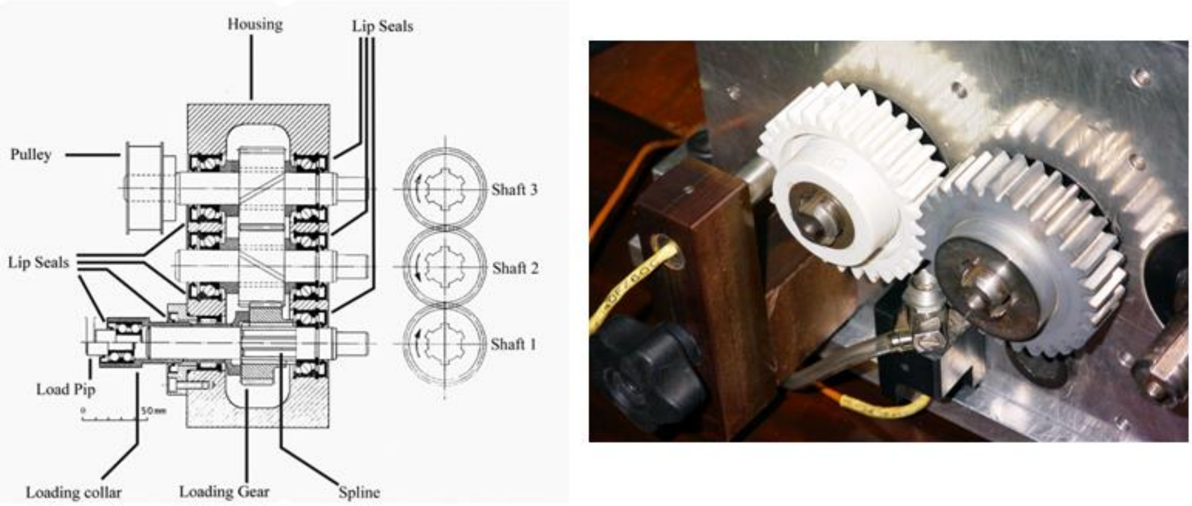

Figure 2. 2 *MARK II Machine Opened-Loop Gear Test Rig (after, [3] [4])*

2.3 Reviews of the Literature on the Failure Mechanisms of Plastic Gear

2.3.1 Transmission Errors

Transmission errors in gear systems, particularly those made of plastic or polymer-based materials, can arise from several factors related to the properties of the gear materials. Critical contributors to transmission errors in these gears include:

- **Elastic deformation** in polymer gears, particularly under loading, changes the tooth profile and can lead to potential transmission errors. This phenomenon is significant in polymer gears, where tooth deflection often has a more pronounced impact on transmission error than manufacturing precision differences. Meuleman et al. and Tharmakulasingham et al. emphasise this point, noting the importance of considering gear stiffness, especially when high transmission accuracy is required [25] [26].

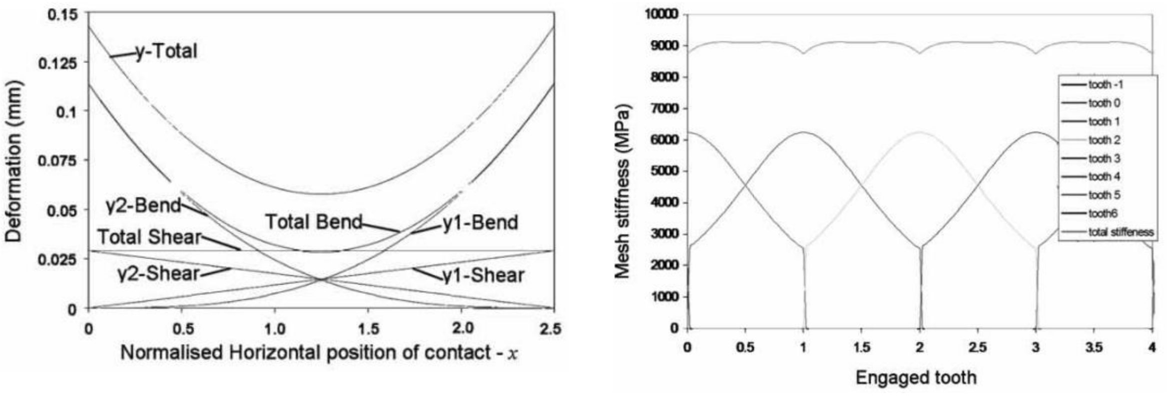

(a) Tooth deflection of POM/POM

(b) Mesh stiffness resulting from subsequent tooth pairs at a contact ratio of 1, module 2 mm, 30 teeth and 20 ° of pressure angle

Figure 2. 3 *Tooth Deflection and Gear Mesh Stiffness (POM/POM, Module 2 mm, 30 Teeth and 20 ° of Pressure Angle) (after, [25])*

Meuleman et al. specifically addressed the effect of tooth deflection in POM/POM material gears caused by shear and bending forces. They observed that shear deflection changes linearly with the distance from its support, and these deflections remain constant, as illustrated in Figure 2.3(a). In contrast, tooth bending deflection varies parabolically. It is at its minimum when the contact point is equidistant between the two extremes, corresponding to the pitch point of a pair of meshing teeth. Consequently, the total deflection sum changes parabolically with distance, reaching a minimum approximately when x ≈ 1, as shown in Figure 2.3(b).

- Transmission errors were quantified based on the overall stiffness of the mesh during multiple meshing cycles. The error was smallest when two pairs of teeth were in simultaneous contact. However, a sudden increase in error occurred when the load transitioned to a single pair of contacts. This insight underscores the dynamic nature of transmission errors in polymer gears and the critical role of elastic deformation in their performance.

Figure 2.3 elucidates the relationship between tooth deflection and gear mesh stiffness in gear mechanics. Finite Element Analysis (FEA) predicts tooth deflections based on transmission errors at varying loads, as depicted in Figure 2.4.

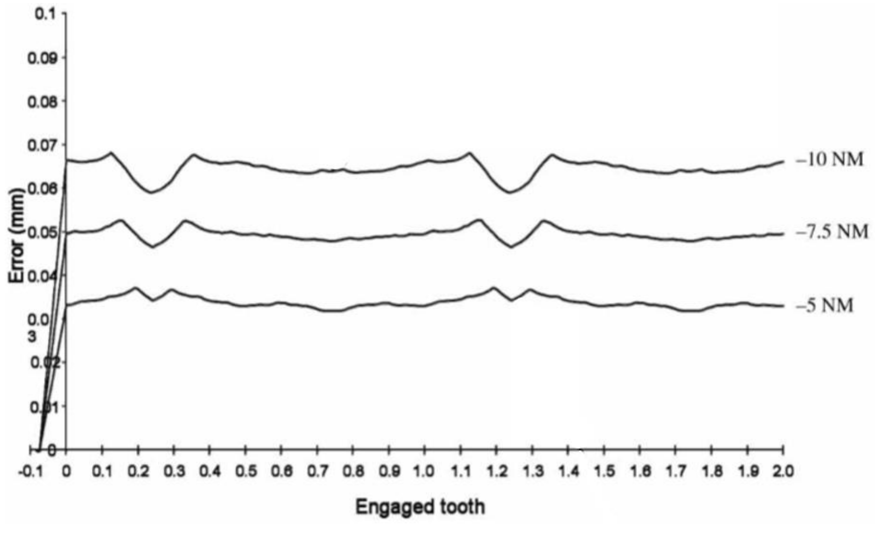

Figure 2. 4 *The Results of Tooth Deflection, as Determined by FEA, Focusing on Transmission Error Across Different Loads and Tooth Modifications (after, [25])*

Several factors significantly influence gear system performance, including:

- Hysteresis: This term describes the energy loss during cyclic loading and unloading. Such energy reduction can lead to additional transmission errors, thereby impacting the efficiency and performance of the gear system [27].
- Wear: The surface quality of polymer gears plays a crucial role, especially under high load and engagement conditions. This factor can significantly influence the incidence of transmission errors.
- Temperature Sensitivity: Fluctuations in temperature can cause dimensional changes in gear components, affecting their meshing and potentially leading to transmission errors. Hoehn and Michaelis noted that higher temperatures result in lower viscosities, leading to thinner lubrication coatings in the gear mesh. This condition adversely affects failure performance [28]. Their research aimed to determine the pitting load-carrying capacity under elevated thermal conditions. In 1988, Knauer introduced the SN-curves for pitting corrosion induced by ISO VG100 mineral oil at various oil injection temperatures, as shown in Figure 2.5. Their findings revealed that increased oil temperatures led to a marked decrease in the endurance limit for pitting. This was attributed to the heating effect on the specific carburised material of the test gears and reduced relative oil film thicknesses. Such conditions could lead to more frequent metal-to-metal contacts and increased surface shear stress [29] [30].

Figure 2.5 presents the SN curves for pitting corrosion caused by ISO VG100 mineral oil at different oil injection temperatures. These curves are crucial for understanding the impact of temperature on the endurance limit for pitting in gear materials. The concept of gear transmission error has been identified in several studies as the deviation in rotational movement observed between a pair of spur gears. This deviation can arise from various factors, including manufacturing tolerances, misalignments, effects on transmitted torque, vibration, and pitch deviation [31] [32]. Recognising and addressing gear transmission errors is crucial in constructing and operating gear systems. Minimising these errors is essential for ensuring a smooth and efficient power transfer within the gear mechanism.

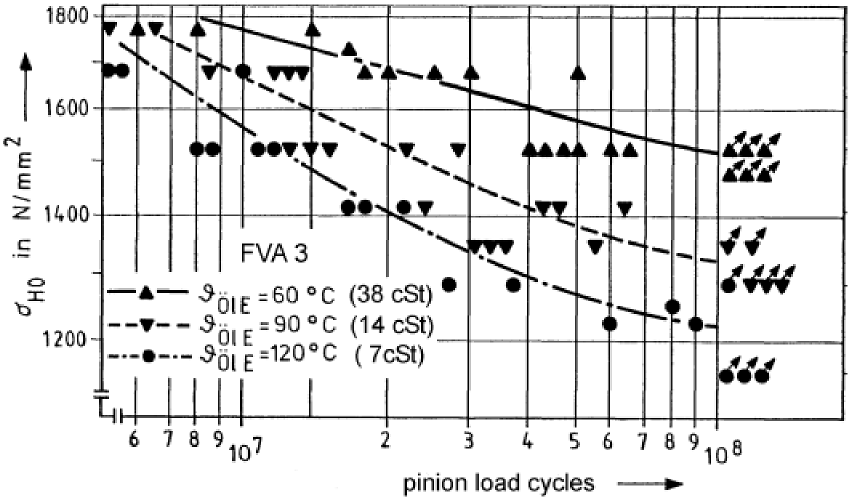

Figure 2. 5 *SN-Curves for Pitting Corrosion Caused by ISO VG100 Mineral Fuel at Various Oil Injection Temperatures (after, [30])*

2.3.2 Installation Errors

Installation errors in gear systems, including those in machine installation, assembly, and tooth modification, are identified as primary contributors to misalignment within the plane of motion. This study emphasises gear tooth modifications resulting from ill-advised or inappropriate actions and machine installation issues, frequently implicated in gear failures. These problems can often be rectified by exercising caution in the initial positioning and preparation of the installation site. The measurement and analysis of misaligned shafts are categorised into three types: parallel misalignment of shafts, angular misalignment parallel to the shafts, and angular misalignment perpendicular to the shafts on the horizontal plane [8], [11].

The study further explores how errors in machine installation influence responses to transmission issues, gear shifting, and shaft misalignment. Misalignments in gears and faults in axial deformation along the z-axis on the horizontal plane are particularly noted for affecting shaft shifting [9], [10]. The research focuses on axial misalignment error, as illustrated in Figure 2.6, which depicts pinion and gear axial misalignment errors.

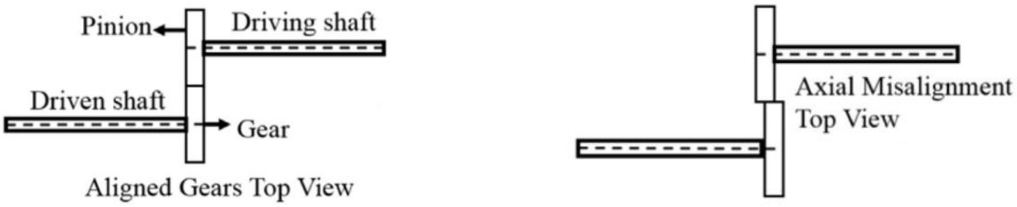

Figure 2. 6 *Pinion and Gear Axial Misalignment Errors (after, [9])*

Over time, machine operation can lead to misalignment or shifts in the gear plane of action, resulting in partial loading. Such shifts or misalignments in the gear teeth are often caused by machine installation errors, leading to changes in the shaft or gear plane [10] [33]. Wear on PEEK material gear teeth, as observed in Kono et al.'s experiment, is an example of such an effect when the machine operates at 150°C [34] [3]. Figure 2.7 shows approximate gear models that account for the impacts of shifts on the gear plane of action caused by machine installation and assembly problems. [3].

Geometric faults in gearing, such as involute alignment variations, gear tooth failures, pitch errors, run-overtime, and bearing position inaccuracy in the casing, are also referenced as sources of misalignment errors [13]. Notably, Lias (2018) investigated the shifted geometry of gears using quasi-static Finite Element Analysis (FEA) to predict and analyse tooth surface contact and tooth root deflection under axial misalignment conditions using SAE/ANSI 1045 materials. Their findings indicated that stress distributions increased by 5% and 15%, respectively [7]. These results are detailed in TABLE 2.2.

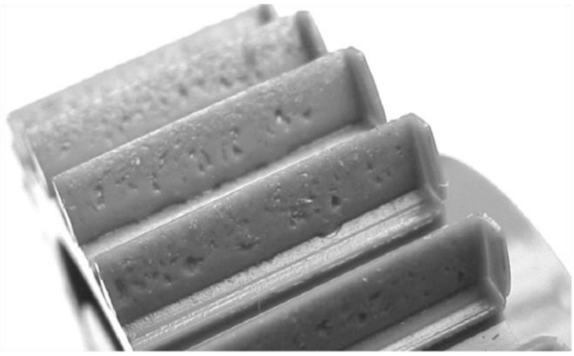

***Figure 2.** 7 An Example of Misalignment During Experimentation Showing a Shift on the Gear Plane (after, [4])*

***Table 2.** 2 The Data from M.R. Lias's (2018) Research on the Axial Misalignment of TSCS and TSBS*

	Max. TSCS		Max. TRBS	
	Axial Misalignment Conditions -z direction		Axial Misalignment Conditions -z direction	
	0.1 mm	0.5 mm	0.1 mm	0.5 mm
AMEP-I	75MPa	145Mpa	54.03MPa	54.45MPa
AMEG-I	68MPa	138Mpa	53.91MPa	54.32MPa

*** *Investigation of Axial Misalignment Effects to the Gear Tooth Strength Properties Using***

The complexity of the load distribution problem in the plane's gears-shifted geometry was "a new approach to determining load factors" [35]. Atanasovska et al. (2007) used FEA to study the load distribution on simulation gears, utilising a 526.41 kNm mater gearbox with high torque transmission and simulating misalignments of 0.1 to 0.5 mm using JUS-C4520 material. Their investigation revealed that stress distributions at the tooth surface contact and tooth root increased by about 15% [36].

2.3.3 Thermal Failure

The study conducted by Dearn et al. utilised MKII rig tests to evaluate these effects [34]. The tests were carried out over 2.75×10^{6} cycles, considering both coated and uncoated conditions of reinforced and unreinforced polymers. For the uncoated spur gears, the study identified the specific temperatures and wear rates at which there was a noticeable increase in the weight loss percentage due to pitch line fracture.

The research found that the initial fracture of the PA66 pitch line occurred after 1,500 mesh cycles at an operating temperature of 63°C, resulting in a weight loss of approximately 0.24% of the total gear mass. In contrast, by the end of the test cycle, the PEEK-450G gear type exhibited only a 0.04% loss of total gear mass, operating at a temperature of 36.5°C. This result indicates the superior material stiffness and strength of PEEK-450G compared to PA66/Nylon.

The melting point temperature of plastics is generally lower than that of metals [37]. This factor becomes critical as the gear operates and the tooth temperature gradually rises, leading to decreased mechanical strength until tooth failure or a reduction in load transmission occurs [19]. In their study, Dennig et al. tested PEEK gears under a load of 60 N/mm for 10 million cycles in an unlubricated state. Their results showed various stages of gear failure, as depicted in Figure 2.8(a). The strength behaviour was further analysed, with the typical strength curves overlapping at 75°C and 100°C, as seen in Figure 2.9. These curves illustrate that the damping properties of a material at high temperatures can be enhanced, thus allowing for the acceptance of larger loads. It was revealed that the tolerated tooth root stresses could be significantly higher than previously assumed, with a tooth root stress of 190 MPa capable of sustaining 129 N/mm.

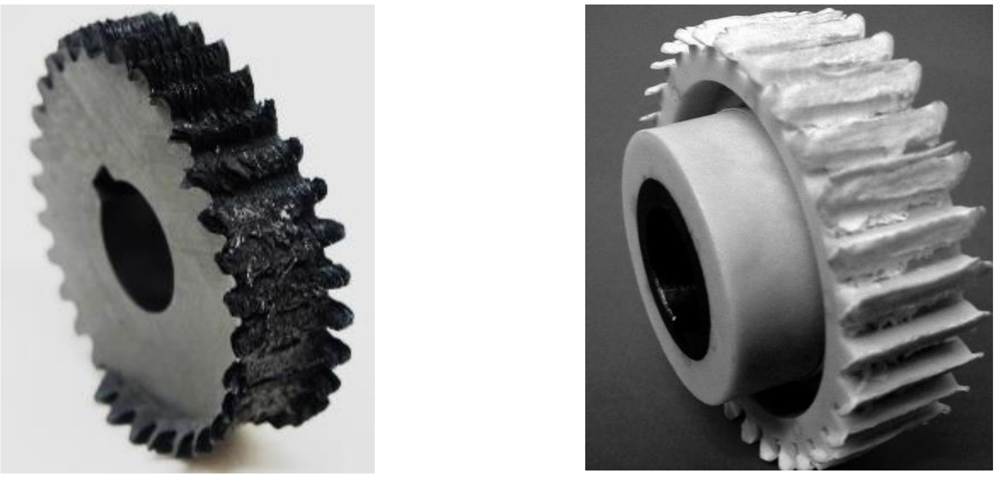

(a) PEEK [19]   (b) PA66/Nylon gear [38]

Figure 2. 8 *Thermally Overloaded Polymers Gears (after, [19] and [38])*

In Figure 2.8(b) Cropper delves into the thermal failure of plastic gears. It describes two fundamental phenomena: firstly, the large and permanent deflection of the teeth when the operating temperature reaches the melting point of the plastic, and secondly, the rapid wear and subsequent failure of the teeth when the polymer's melting point is exceeded by its operating temperature [38], [39].

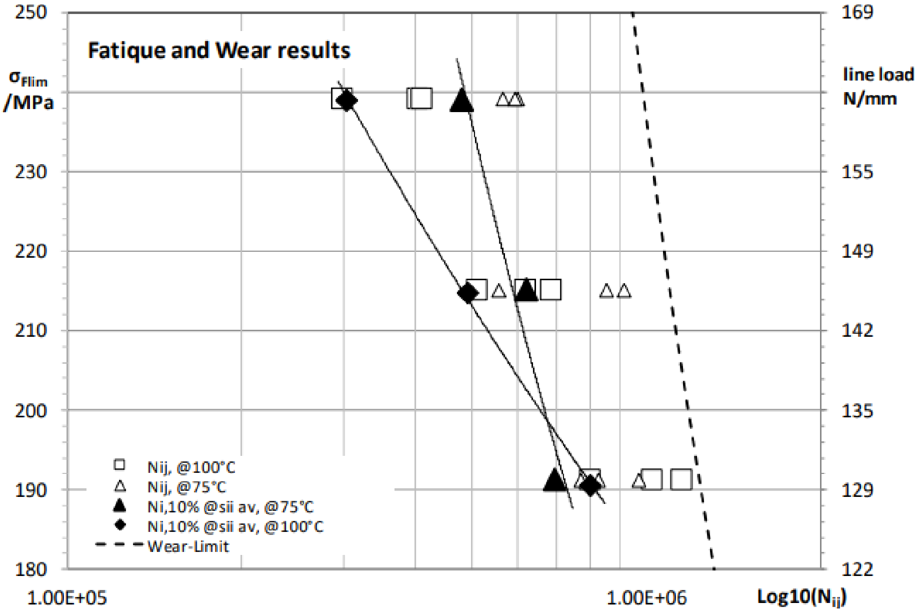

Figure 2. 9 *The Typical Strength Curves Overlap at 75 °C and 100 °C [after, [19]]*

Figure 2.9 shows the overlapping typical strength curves at temperatures of 75°C and 100°C, as documented in the study by Dennig, Monn, and Vodermayer (2019) [19].

2.3.4 Tooth Deflection

The kinematics of polymer gears during engagement can be significantly influenced by their tendency to exhibit more deflection than metal gears. In their study, Singh, Siddhartha, and Singh (2019) highlighted this aspect [40]. Various factors contribute to tooth deflection in polymer gears:

1. **Material selection:** The choice of material plays a critical role in tooth deflection. Materials with lower stiffness and elasticity modulus tend to increase tooth deflection. High-performance engineering polymers, such as PEEK (polyether ether ketone) and PAI (polyamide-imide), are renowned for their superior mechanical properties, including increased stiffness and modulus, which mitigate this issue [41].

2. **Gear tooth failure:** Considerable research has focused on improving gear tooth geometry, thickness, and profile to distribute the load more evenly and reduce tooth deflection. Considerations such as tooth involute, pressure angle, and tooth root thickness are vital. Herzog et al. (2022) investigated the effects of elastic deformation on polyamide-66 (PA66) gear teeth. They conducted load tests to examine the wear and deformation behaviour of PA66 gear meshing with steel gears. [42]. The study assessed the most significant average distance of tooth flanks of untested and tested contours in instances of wear, as shown in Figure 2.10 (a). Their findings indicated that coordinate-measured wear and plastic deformation were more significant than externally measured counterparts, suggesting that the coordinate-measuring approach slightly overestimates actual wear and deformation. Figure 2.10(b) illustrates the slope of the fit of 1.05266±0.04553.

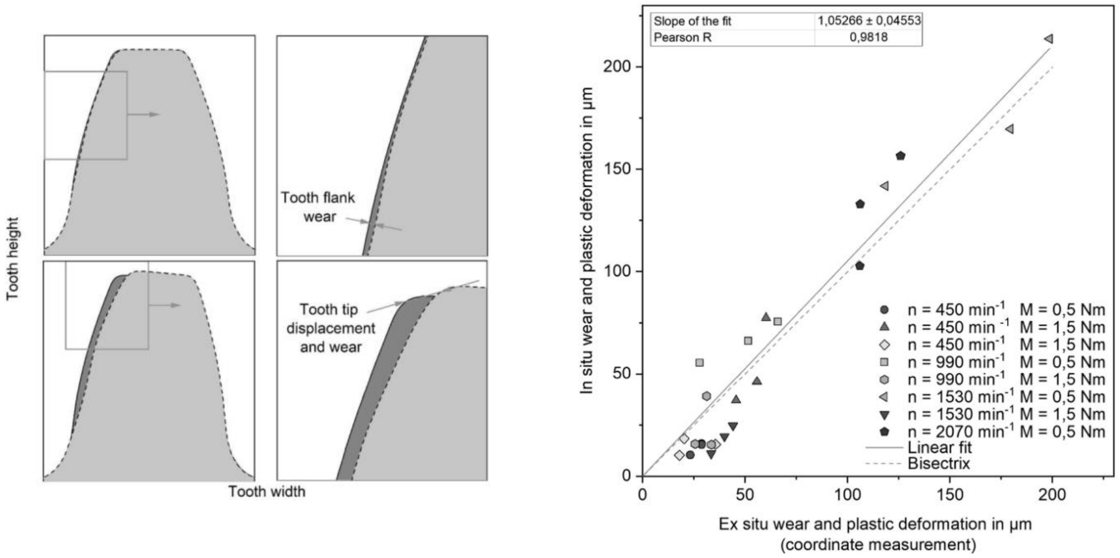

(a) Wear and Deformation Determined Using Coordinate-Measured Tooth Profiles.

(b) Measured Tooth Wear and Deformation

Figure 2. 10 *Polymer Gear Tooth Deformation and Wear (after, [42])*

3. **Un-lubrication:** Lubrication facilitates gear meshing, reducing abrasion and heat generation [43]. Adequate lubrication between gear teeth is essential to minimise friction and wear, reducing tooth deflection and prolonging gear life.

4. **Reinforcement:** Enhancing polymer gears with fillers or fibres can improve their mechanical properties and decrease deflection. For example, incorporating glass fibres into the polymer material can increase its rigidity. Cathelin et al. (2014) discussed this impact on Polyamide (PA6), particularly in high torque transmission applications. Adding fibres significantly boosts performance [44].

Tooth deflection is primarily caused by the stress and strain behaviours of a pair of gear teeth in contact. The behaviour of viscoelastic materials and the modulus of elasticity of these materials contribute to tooth displacement in both static and dynamic scenarios [45]. In 1995, N Tsukamoto illustrated this with nylon and polyacetal gears, showing the involute curve of tooth deflection under applied stress. Polyacetal gears demonstrated more deflection than nylon gears, though nylon possesses superior viscosity qualities compared to polyacetal [46], as depicted in Figure 2.11.

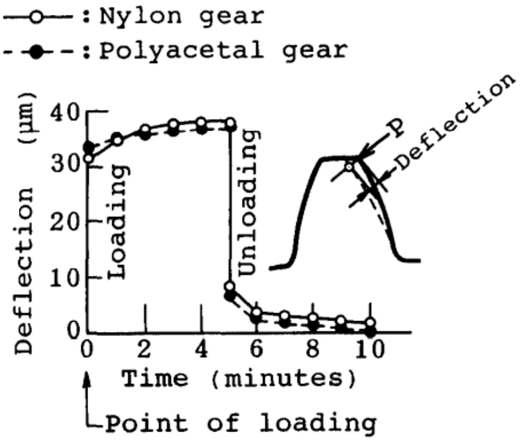

Figure 2. 11 *Nylon and Polyacetal Tooth Involute Deflection (after, [46])*

Lastly, another factor influencing tooth deflection is the sliding friction force under quasi-static conditions, which impacts the principle of transmission error (TE) in spur gears [47].

2.4 Reviews of the Literature on the Gear Kinematic Behaviour

Gear Kinematic Behaviour includes the impact of various factors on the kinematic behaviour of gears, particularly those made from polymer materials. These factors include the elastic and viscoelastic properties of the materials, their tendencies to creep, characteristics related to friction and wear, lubrication needs, temperature sensitivity, and susceptibility to contact failure.

2.4.1 Industrial Standard

BS 6336-2 specification for the calculation of surface durability

[48] BS 6336-2, provides guidelines for calculating the surface durability of gears (BS 6336-2 2008). ISO 6336-2 complements this by offering fundamental formulas for determining the surface load capacity of involute teeth. These formulas include an equation for allowed contact stress verified through practical experience, represented as involute damage curves. These curves characterise contact stress levels and life parameters restricted to typical gear materials and heat treatments, as detailed in ISO 6336-5 (BS 6336-5 2003). Factors such as life gear test results, lubricant viscosity, surface roughness, pitch-line velocity, work hardening, and tooth dimension size are considered in determining permissible contact stress [49], viz:. The permissible contact stress is determined as follows;

$$\sigma_P = \frac{\sigma_{y\ lim}\ Z_{LF}}{S_y}\ Z_L\ Z_v\ Z_R\ Z_w\ Z_x$$

The life gear test, the effect of lubricant viscosity, surface roughness, pitch-line velocity, work hardening, and tooth dimension size are all considerations.

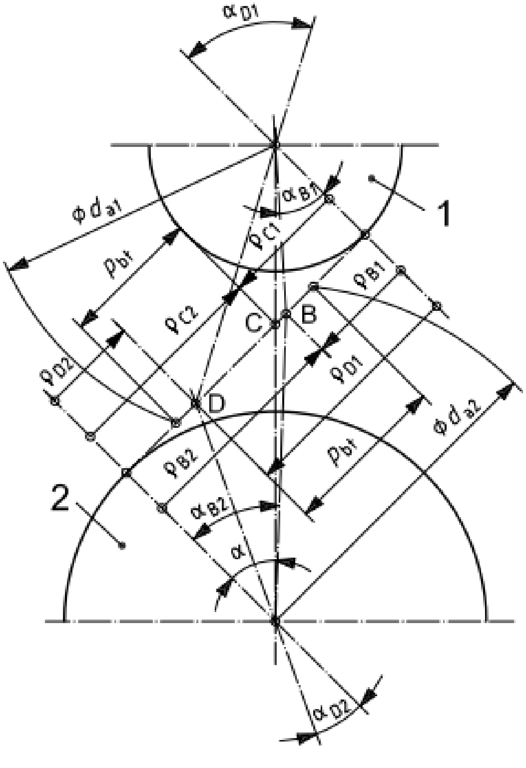

Figure 2. 12 *The Curvature of a Pair of Tooth Contacts at the Pitch Position [49]*

Figure 2.12 in the standard illustrates the principle of contact stress and related effect factors at the tooth area's pitch point, which are always considered in durability surface calculation. This calculation determines the load capacity, computed separately for pinion and wheel gears.

According to standards like BS 6168 and BS 6336, the shape of spur gears is influenced by load capacity and transmission faults. These standards account for gears that become thermally transient or vary due to flexibility and other factors impacting overall transmission efficiency. BS 6336 standards assess effects on tooth pitting and root fractures [21] [20].

BS 6336-3 specification for calculation tooth bending strength for involute spur gears

BS 6336-3 provides guidelines on calculating tooth bending strength for involute spur gears. It outlines the fundamental formulas for estimating tooth bending stress and refers to the load capacity or permitted bending stress described in ISO 6336-1 [50].

BS 6336-6 specification for calculation gear capacity

[51] Lastly, BS 6336-6 outlines the calculation of gear capacity (BS 6336-6 2006). It specifies load factors necessary for estimating gear capacity, considering various loading conditions such as continuous, intermittent, and shock loads. These factors include the magnitude of the load, the operation period, and the type of gear. The standard also sets parameters for gear stress analysis, including tooth bending stress, contact stress, and surface durability. It provides methods for calculating gear tooth stresses and assessing their impact on gear capacity, incorporating the mechanical properties of gear materials such as hardness, tensile strength, and fatigue strength. Additionally, it covers load distribution parameters like

gear alignment and backlash, explaining how these factors should be considered when determining gear strength and durability.

2.4.2 Gear Kinematic Behaviour Reviews

In the study of the kinematic behaviour of polymer gears, several key aspects are considered:

1. **Material selection:** The choice of polymer material is crucial as it directly affects the kinematic behaviour of gears. Research has explored various polymers, including polyamide (PA), polyoxymethylene (POM), polyphenylene sulfide (PPS), and PEEK, each with unique properties and performance characteristics.
2. **Frictional and wear effects:** Polymer gears often exhibit lower friction coefficients than metal gears, reducing frictional losses and increasing efficiency. However, polymers typically have lower wear resistance, especially under high-load and high-speed conditions. Research has focused on enhancing the wear resistance of polymer gears through methods like filler inclusion, surface treatments, and the development of self-lubricating polymer composites.
3. **Vibration and noise:** In applications where noise reduction is essential, the vibrational behaviour of polymer gears is a significant focus. Studies, such as the one by Kumar et al. in 2021, analyse the vibration signals of polymer gears (like Nylatron) under different experimental conditions to improve noise performance and reduce vibrations. Figure 2.13 shows the vibration signals of polymer gears in the time domain, with amplitude and sample number on the Y and X axes, respectively. The polymer gear vibration signals in time domain. The amplitude (m/s2) on the Y axis and the number of samples on the X axis. Values of rising amplitude may encounter more significant errors from [52].

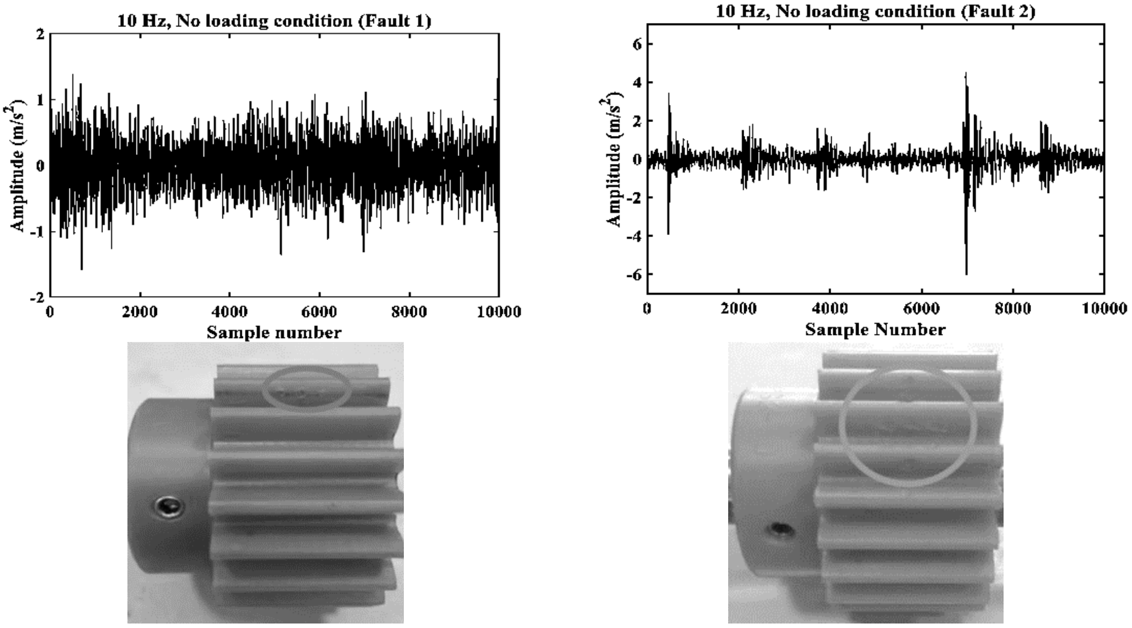

(a) 1st tooth fault

(b) 2nd tooth fault

Figure 2. 13 *Polymer Gear Vibration Signals in Time Domain (after, [52])*

4. **Temperature effects:** The thermal behaviour of polymer gears, including thermal expansion, creep, and the impact of temperature on gear performance, has been extensively studied. Understanding these effects is crucial for predicting gear behaviour under different thermal conditions.

5. **Modeling and simulation:** Using finite element analysis (FEA) and computational fluid dynamics (CFD) simulations is prevalent in studying polymer gears' stress distribution, deformation, and contact behaviour. These techniques help optimise gear design and predict kinematic performance under various operational conditions. For example, Karimpour et al. in 2010 investigated the kinematic behaviour of polymer gears in load sharing related to bending and contact stresses using FEA in non-lubricated tests, highlighting the influence of these factors on gear failure. For instance; In 2010, Karimpour et al. investigated the kinematic behaviour of gear polymer in load sharing linked to bending and contact stresses on the contact route using FEA in non-lubrication testing. They discovered higher friction on TCB load sharing, temperature, and stress distribution in various operating situations. As a

result, there is a chance that the tooth gear was destroyed due to contact stress before bending force. Bending stress had a more significant impact on failure during BS/ISO 6336 [53] testing than contact stress [54].

6. **Fatigue life:** Life can be assessed and predicted through lifespan tests. The melting of polymer gears, often due to high gear temperatures, is critical in determining fatigue life [55]. Studies like those by Itagaki et al. in 2014 use the average value of gear bulk temperature during operation as an indicator to assess fatigue life. The average bulk temperature represents the fatigue work exerted on the gears during operation, as shown in Figure 2.14. The average bulk temperature represents the fatigue work done to the test gears during operation [56] [57].

These aspects collectively contribute to a comprehensive understanding of the kinematic behaviour of polymer gears, essential for their design and application in various mechanical systems.

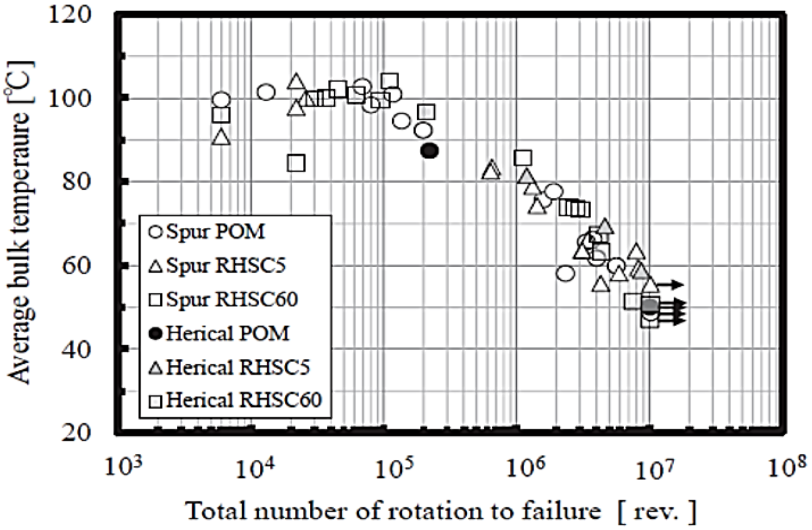

Figure 2. 14 *Fatigue Life and Bulk Temperature (after, [56])*

2.5 Reviews of the Literature on the Frictional Thermal

The flank teeth' bulk temperature, flash temperature, or melting point as the temperature rises during transmission can significantly affect gear performance. The coefficient of friction in gear meshing is influenced by the maximum flash temperature, which is theoretically predicted [58] [59]. Additionally, as illustrated in the equation, the coefficient of friction is determined by the theoretically predicted maximum flash temperature;

$$T_{f,max} = T_b + \frac{1.11\, \mu\, F_t\, \sqrt{\delta_{Ti}}\, \left|V_{rp} - V_{rg}\right|}{L_i k_i \sqrt{\omega}\, \left|\sqrt{V_{rp}} + \sqrt{V_{rg}}\right|}$$

This critical relationship reflects the interaction between mechanical stresses and temperature changes. Most research on polymer gears has concentrated on understanding how temperature affects gear performance. For instance, K. Dearn et al. (2013) investigated the temperature and wear rates of spur gear polymers PA66 and PEEK-450G under unlubricated conditions. Their findings indicated that PEEK-450G, with its higher stiffness and strength than PA66, showed only a 0.04 per cent weight loss and an operating temperature of 36.5°C at the end of the test cycle [34].

A. Pogacnik and J. Tavcar (2015) evaluated plastic gears made of POM, PA6, and PA6+GF under various loads and speeds. They focused on measuring heat-resistant grades or bulk temperature and contact stress at the root teeth during operation, following VDI 2736 guidelines [55]. Furthermore, they calculated the heat-resistant grades or bulk temperature and contact stress at root teeth during operation according to VDI 2736. Their S-N Wöhler curve revealed a temperature rise due to overload, highlighting the significance of thermal properties for polymer gears [60].

The flash temperature on the tooth flank is affected by mechanical stress-induced temperature increases and changes in the polymer material's stiffness [38], [10], [61]. Factors such as the coefficient of friction, strain behaviours, tooth wear, and bending deformation of stress influence the temperature increase. Furthermore, the coefficient of friction is crucial in the equation used to calculate the theoretical maximum flash temperature rise ($T_{f,max}$). In their structural-dynamic analysis simulations of polymer gears, Doll et al. (2015) examined viscoelastic effects, utilising a reasonable modulus of elasticity [62]. Victex's corporation provided data on the modulus of elasticity of wheel PEEKs, as shown in Figure 2.8.

2.5.1 Industrial Standard

2.5.1.1 BS/ISO 6168 Specification for a Non-Metallic Spur Gear

This section focuses on the operating temperature of non-metallic gears, as outlined in BS 6168. This standard provides equations that consider the meshing of a non-metallic gear with a steel gear, considering variations in the coefficient of friction. The factors influencing these calculations are:

$$T_f = T_b + \frac{136\, P_T\, \mu\, (1+u)}{N_g + 5}\left[\frac{1.71 \times 10^4 K_a}{b N_p (\nu m)^{K_m}} + \frac{7.33 K_b}{A}\right] + 5.0$$

where K_a is a dimensionless experimental factor of meshing materials caused by non-lubrication or oil lubrication

K_b is a drive-type correction coefficient

K_m is the constant of gear material

These variables collectively determine the operating temperature of non-metallic gears in various scenarios. Table 2.3 in BS 6168 provides a reference for the coefficient of friction, illustrating how these factors are applied and their impact on the gear's performance under different lubrication and material conditions. This approach allows for a more precise understanding and predicting gear behaviour under various operational circumstances.

Table 2. 3 *BS 6168 Referenced the Coefficient of Friction*

Gear meshing	*Non-lubrication*	*Oil lubrication*
PA 66 vs Steel	*0.25*	*0.05*
PBT vs Steel	*0.25*	*No information*
PET vs Steel	*0.22*	*0.06*
POM vs Steel	*0.21*	*No information*

2.5.2 Flash Temperature and Thermal Characteristics Prediction Reviews

Flash temperature is typically estimated by considering the heat generated through exothermic reactions and the material's thermal properties, such as thermal conductivity and specific heat capacity. The calculation involves assessing the energy input into the bulk system and the heat dissipation rates [58] [20]. B. Cerne et al. and X. Tian et al. made significant contributions to improving the flash temperature equation for a pair of gear polymers, particularly in an analytical context. B. Cerne et al. focused on generating the heat flux necessary for Finite Element Analysis. According to the flash temperature equation, important factors include the coefficient of friction and gear efficiency [63].

D.M. Nuruzzaman et al. conducted research on the changes in the coefficient of friction and wear rates with varying sliding speeds, specifically for Nylon and PTFE [63]. They found that the coefficient of friction increased and varied in tandem with the wear rate and the length of the sliding velocity. In 2013, M.A. Chowdhury demonstrated that the coefficient of friction depends on the increase in average load and rises with increasing sliding speed and differences in polymer materials [64].

Therefore, the determination of flash temperature is influenced by the rise in temperature caused by mechanical stresses and variations in the stiffness of the polymer material [38] [10] [61]. This temperature rise is affected by various factors, including the coefficient of friction, strain behaviour, tooth wear, and bending deformation of stress.

Additionally, the coefficient of friction is crucial in computing the theoretical maximum flash temperature rise ($T_{f,max}$).

2.5.3 Frictional Effects Reviews

Wear mechanisms observed in polymer gears are affected by operating conditions, particularly thermal conditions and there are many instances of thermal-influence in polymer gear wear behaviour. Key aspects covered in this section include the tribological performance of polymers and their composites, which are affected by the polymer molecular structure, transmission errors, load, sliding speed, temperature, and environmental factors. Pioneering studies by El-Tayeb and Mostafa, El-Tayeb and Gadelrab, Bahadur and Zheng, Bahadur and Polineni, Watanabe, and Bahadur and Tabor have contributed significantly to understanding these dynamics [65] [66] [67] [68] [69] [70]. The research encompasses strategies such as optimising gear tooth profiles, surface treatments, and coating techniques to mitigate friction and wear.

In 1989, Bahadur and Zheng focused on the tribological behaviour of polyester composites, particularly their resistance to wear and frictional forces. They examined wear mechanisms like abrasive and adhesive wear, assessing the composite's capabilities to withstand frictional forces [67]. Figure 2.15 illustrates the variation in the coefficient of friction at different sliding speeds with varying proportions of fibreglass in polyester. The figure reveals that as the fibre content increases from 10% to 50% by weight, the steady-state coefficient of friction rises from 0.35 to 0.67. The lowest friction coefficient was observed at 10% fibre content, indicating a decrease in friction as the percentage of fibre decreases.

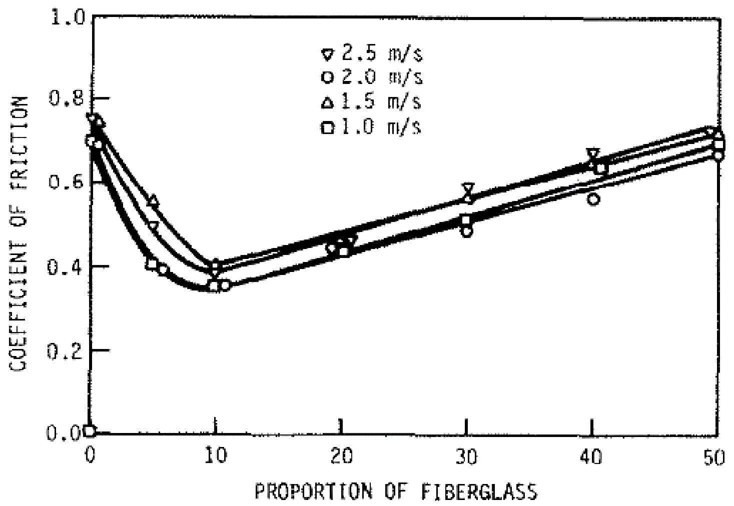

***Figure 2. 15** The Variation in Coefficient of Friction for Different Sliding Speeds with Fibre-Glass Proportion (By Weight) in Polyester [after, [67]]*

[61] [71] The coefficient of friction, as outlined by Merritt (1954) and Buckingham (1949), denotes the ratio of the frictional force to the normal force between two surfaces in contact. In gears, two types of friction coefficients are generally considered:

1. Dynamic Friction Coefficient: This represents the friction between moving gear teeth, impacting power transmission efficiency and contributing to losses and wear in gear systems
2. Kinetic Friction Coefficient: This coefficient is key during the engagement and disengagement of gears, representing the resistance to sliding between the gear teeth. It influences the smoothness of gear operation and can affect the system's performance and durability.

[72] This coefficient is key during the engagement and disengagement of gears, representing the resistance to sliding between the gear teeth. It influences the smoothness of gear operation and can affect the system's performance and durability.

***Table 2. 4** The Friction Power Loss Resulting from Meshing Gears with Different Coefficient of Friction Formulae*

References	*Velocity at 1200 rpm*	
	Frictional of power loss	*Coefficient of friction*
Drozdov and Gavrikov	*194.9*	*0.0441*
Benedict and Kelley	*183.2*	*0.0388*
Schlenk (Without Lubri.)	*207.9*	*0.0427*
Schlenk (With Lubri.)	*145.6*	*0.0299*
Xu at al.	*341.0*	*0.0654*

Figure 2.16 demonstrates that Xu Hai's coefficient of friction equation yields significantly larger results than observed, especially when operating conditions exceed the author's recommended surface roughness bounds of 0.4 μm [73].

Park (2018) [47], found that the friction force varies in the double-mesh region and reverses at the pitch point. This observation was based on calculations using Benedict & Karlly's and Xu's equations, with Xu's surface roughness set at 0.4 μm. As depicted in Figure 2.17, Benedict, Karlly's, and Xu's friction coefficients significantly decrease at the pitch point, approximating a value of 0.1 at 300 rpm. Although Benedict and Karlly's coefficient of friction increases at the pitch point, Xu's unexpectedly decreases. However, both coefficients align at points away from the pitch point. The tooth load, friction force, and transmission errors are considered using the friction coefficient at 3 rpm to capture the quasi-static effect.

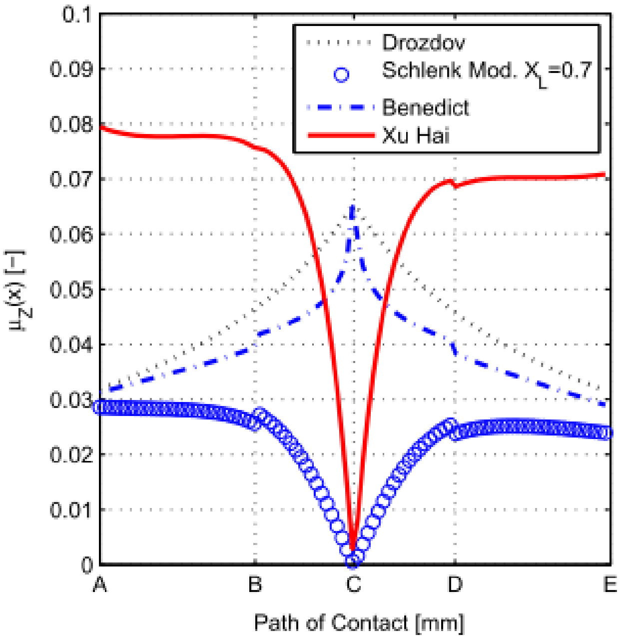

Figure 2. 16 *Coefficient of Friction Along the Line of Contact for a Spur Gear (after, [47])*

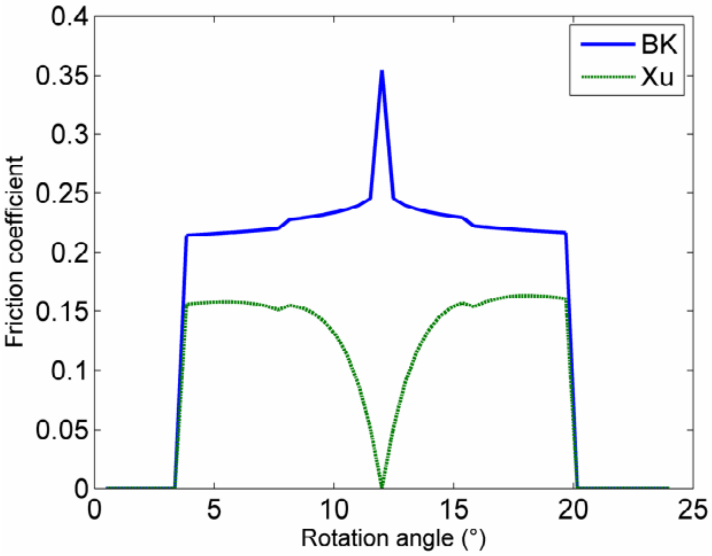

Figure 2. 17 *Unmodified Gears' Sliding Friction Coefficient (after, [47])*

Table 2.5 consolidates five equations of the coefficient of friction along the path contact for this chapter, presenting the frictional power loss resulting from meshing gears with different coefficient of friction formulae.

Table 2. 5 *Equation's coefficient of friction for spur gear applied*

	Formulae	Functional Details
[71]	$\mu_B(t) = (1-\eta)\cdot\left[\frac{2\cdot(\vartheta_{S_a}+\vartheta_{S_a})}{({\vartheta_{S_a}}^2+{\vartheta_{S_r}}^2)\left(1+\frac{1}{m}\right)}\right]$ $\mu_{BS}(t) = 0.030\,(l_{oil})^{-0.05}\cdot\left(\frac{(R_{a,p}+R_{a,w})}{2}\right)^{0.25}\left(\frac{W_t}{v_t\sin\varphi\,\rho_{relc}}\right)$	The fluctuation of the coefficient of friction's sliding speed based on the involute gear teeth geometry concept influenced.
[61]	$\mu_M(t) = (1-\eta)\cdot\frac{1}{\sec\varphi}\cdot\left[\left(\frac{d_p d_g}{d_p+d_g}\right)\left(\frac{l_p+l_w}{{l_p}^2+{l_w}^2}\right)\right]$	The fluctuation of the coefficient of friction's sliding speed based on the involute gear teeth geometry concept influenced.
[73]	$\mu_{B\&K}(x) = 0.0127\ \log\left[f_N(x)\frac{2.97\times10^4}{\chi\ v_s(x)\ v_r(x)^2}\right]$	The fluctuation of the coefficient of friction's rolling speed based on the dynamic viscosity and load influenced.
[74]	$\mu_{D\&G}(x) = \left[\,0.8\sqrt{\nu}\ v_s(x)+v_r(x)\phi+13.4\right]^{-1}$	The fluctuation of the coefficient of friction's sliding speed effective.
[75]	$\mu = \frac{C_0 V_s^{0.23}}{P_{H,max}}$	The fluctuation of the coefficient of friction's sliding speed effective for plastic gears.
[76]	$\mu_{MS}(x) = \mu_S(Schlenk)\tanh\left(\frac{\varepsilon_\alpha}{\varepsilon_\alpha-1}\ \lvert SRR(x)\rvert\right)$	The fluctuation of the coefficient of friction's sliding-to-rolling reaches 20% of gear meshing.
[77]	$\mu_H(x) = e^{f_{Xu}}\lvert SRR(x)\rvert\ p_h^{b2}\ U_S^{b3}\ \eta_x^{b6}\ R_X^{b8}$	The fluctuation of the coefficient of friction's depending on the significant parameters based on numerical results from an EHL model

2.6 Reviews of the Literature on the Viscoelastic Hysteretic Behaviour

Viscoelastic hysteretic deformation of gears is primarily induced by stress and strain behaviours, which increase wear [78]. This deformation is attributed to the rise in temperature caused by mechanical stresses and variations in the stiffness of polymer materials [38] [79] [61]. Dearn and Kukureka (2009) described this phenomenon as viscoelastic hysteretic deformation in their study in Chapter 14 of the Book of Polymer Tribology [39]. They emphasised that the temperature rise during gear meshing transmission can result in changes in the bulk temperature, flash temperature, or even the melting point of the temperature on the flank teeth. Which the temperature rise caused by mechanical stresses and variations in the stiffness of the polymer material affects the viscoelastic hysteretic behaviour [38] [79]. The temperature rise that happens during gear meshing transmission might cause the bulk temperature, flash temperature [58] [59], or melting point of the temperature on the flank teeth.

Doll et al. (2015) further investigated this effect, focusing on the viscoelastic influence on structural-dynamic analysis simulations of polymer gears. They considered the modulus of elasticity suitable for representing bending deformation due to stress and strain behaviours [62].

[62] Figure 2.18 illustrates the boundary conditions applied to the simulated polymer specimen, which included a convection heat transfer coefficient of 1 [W/m^{2}K], an ambient temperature of 23 Celsius, a torque of 10 Nm, and an angular velocity of 1000 rpm. These conditions helped define applied loads' magnitude, direction, duration, constraints, or fixed regions for simulating clamping or attachment points.

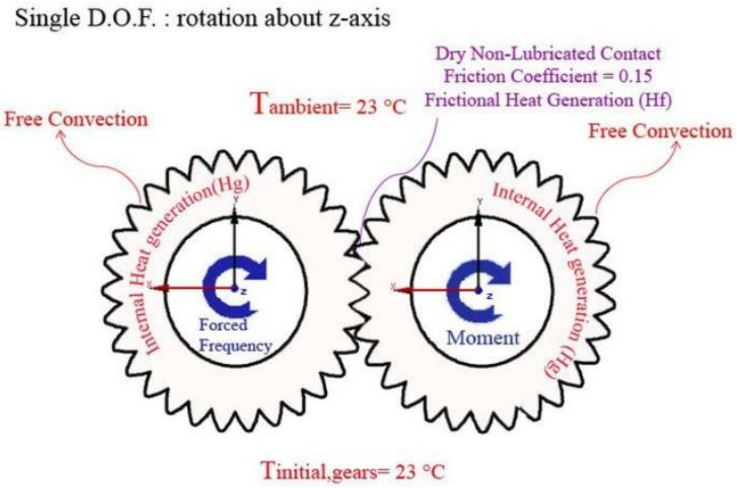

Figure 2. 18 *The Boundary Conditions for Structural-Dynamic Analysis Smulations for a Suitable Modulus of Elasticity in Polymer Gears due to Bending Deformation (after, [62])*

The analysis determined the maximum strain energy density (U) The analysis determined the maximum strain energy density (E_{loss}) was calculated. This process is considered hysteresis caused by heat loss and generation due to one-gear revolution and sliding friction. Figure 2.19 presents the strain energy for one gear revolution, showcasing how Doll analysed and interpreted the strain energy density to gain insights into the material's behaviour. The strain energy density distribution provides valuable information on stress concentration, fatigue-prone regions, or failure-prone areas. However, the intensity and length of the strain vary depending on the element's size and position within the mesh.

$$E_{loss} = H\,U_{max}$$

where H is the hysteresis caused by heat loss and heat generated due to one gear revolution and the sliding friction. For instance, the strain energy behaviour

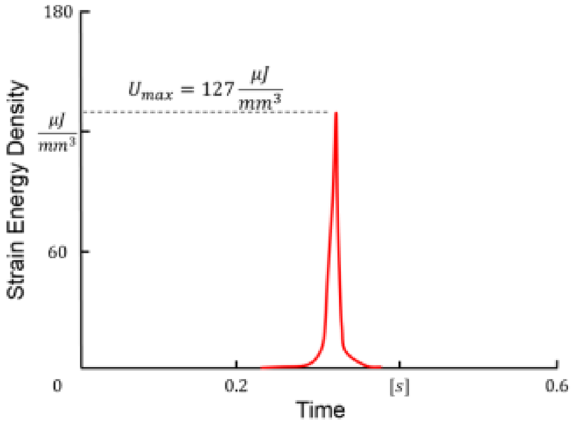

Figure 2. 19 *Strain Energy for One Gear Revolution (After, [62])*

The strain energy density in Figure 2.19, Doll analyzed and interpreted to gain insights into the material's behaviour. The hysteresis in the percentage heat loss varies exclusively as a function of each element's temperature. High-strain energy density regions indicate significant deformation and energy storage areas, while low values represent regions with less deformation.

Therefore, the strain energy density distribution can provide information on stress concentration, fatigue-prone regions, or areas prone to failure. However, the intensity and length of that strain vary depending on the element's size and position within the mesh.

Cerne and Duhovnik (2018) used analytical Finite Element Analysis to significantly improve the flash temperature on the Polyoxymethylene (POM) pairs gear model, focusing on the thermo-mechanical response of a steel-POM spur gear pair. They considered steady-state situations, constant contact area, and the heat flux created by the simulation [79]. As a result, the growth rate of strain rate and flash temperature was linked to the viscoelastic hysteretic behaviour, which depends on dynamic mechanical analysis and simulation, as shown in Figure 2.20.

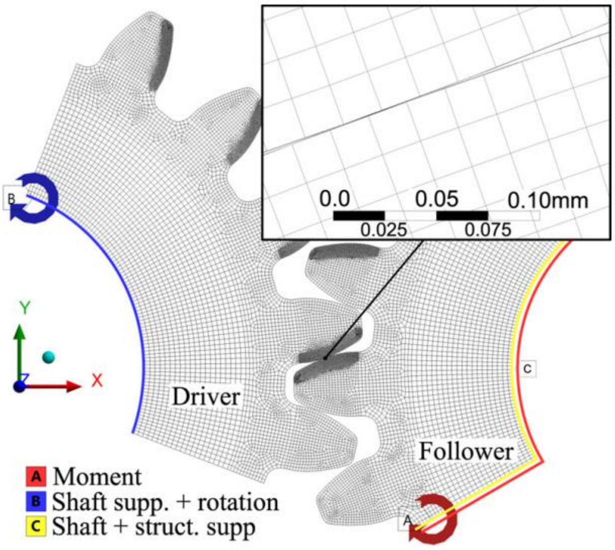

Figure 2. 20 *Gear Meshing Conditions Settings in an Example Dynamic Mechanical Analysis and Simulation (after, [79])*

Figure 2.21 illustrates the transient FEM model at the middle tooth profile, indicating the temperature-dependent viscoelastic and linear elastic models (POM and Steel). The simulation results highlight the critical role of POM's temperature and strain rate-dependent viscoelastic properties in determining the thermo-mechanical response of a steel-POM spur gear pair. These findings emphasise the importance of considering these material behaviours in gear system design to optimise performance and ensure reliable operation under varying flash temperatures and loading conditions.

Considering the temperature and strain rate-dependent viscoelastic properties of Polyoxymethylene (POM) in the thermo-mechanical response of steel-POM spur gear pairs is essential. The simulation results emphasise that these material behaviours are crucial for optimising gear system performance and ensuring reliable operation under varying conditions, such as flash temperatures and loadings.

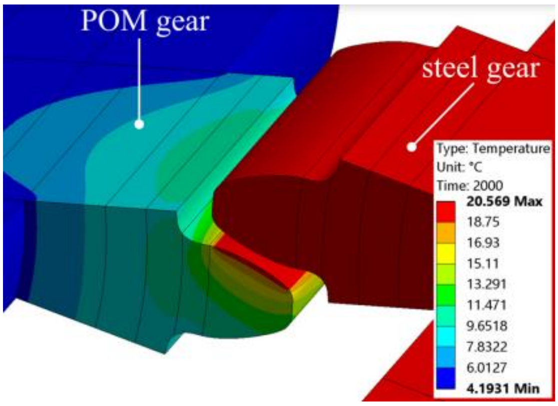

(a) Simulation of Temperature Gradient at 2000 Second

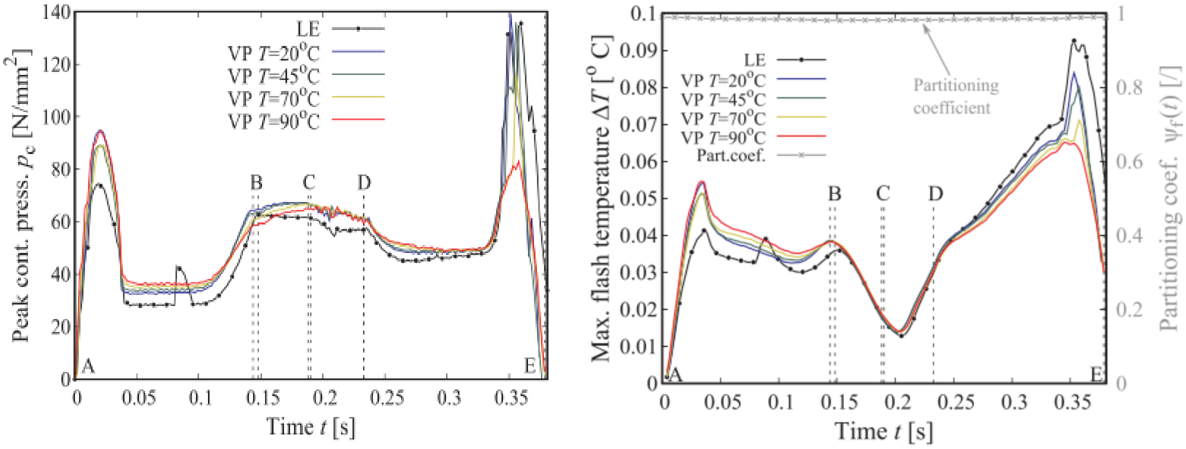

(b) Pressure Contact *(c) Flash Temperature*

Figure 2. 21 *The Transient FEM model at the Middle Tooth Profile Indicates the Temperature-Dependent Viscoelastic and Linear Elastic Models (POM & Steel) (after, [79])*

Figure 2.21 (a) presents data from a simulation at 2000 seconds, explicitly examining the temperature increase gradient from the initial temperature recorded at 0 seconds during load tests. Figures 2.21 (b) and 2.21 (c) analyse the transient Finite Element Method (FEM) model at the middle tooth profile, showing the temperature-dependent viscoelastic and linear elastic models under pressure contact conditions. The research investigated variations in flash temperature distribution at the points of most significant divergence, identifying differences of up to 27%. It was noted that in scenarios of higher material temperatures, the total frictional heat generated during a meshing cycle is not significantly influenced by the viscoelastic properties of the material, with variations in heat generation of up to 6%.

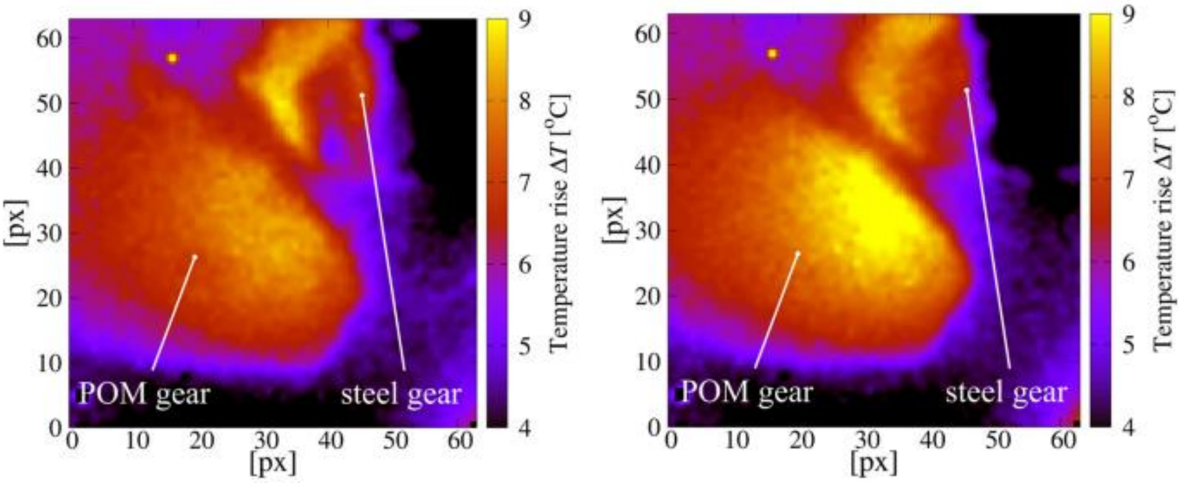

(a) Minimum Temperature Gradient *(b) Maximum Temperature Gradient*

Figure 2. 22 *Infrared Temperature Data Between a Gear of Tooth Pairs (POM & Steel) (after, [79])*

Figure 2.22 offers infrared temperature data between gear tooth pairs made of POM and Steel. This figure, specifically parts (a) and (b), compares the temperature gradient between tooth pairs with the lowest and highest temperature increase values, measured during a single running cycle at 3400 seconds. Following the experiment by Cerne and Dubrovnik, substantial temperature gradient divergences were observed in POM-PA66 gear pairs, showing an increase of 25%. These discrepancies were less pronounced in steel-POM (and steel-PA66) combinations, though they were still noticeable along the tooth flank.

[80] The 2021 study by Zorko utilised a thermal camera with 3x3 pixel resolution to measure temperature changes in polymer gears on a progressively curved contact path. As depicted in Figure 2.23, the findings provided significant insights into the gear's thermo-mechanical behaviour at the root gears, including temperature distribution and heat generation. This study aimed to improve gear design and performance by understanding the effects of thermal stresses during operation.

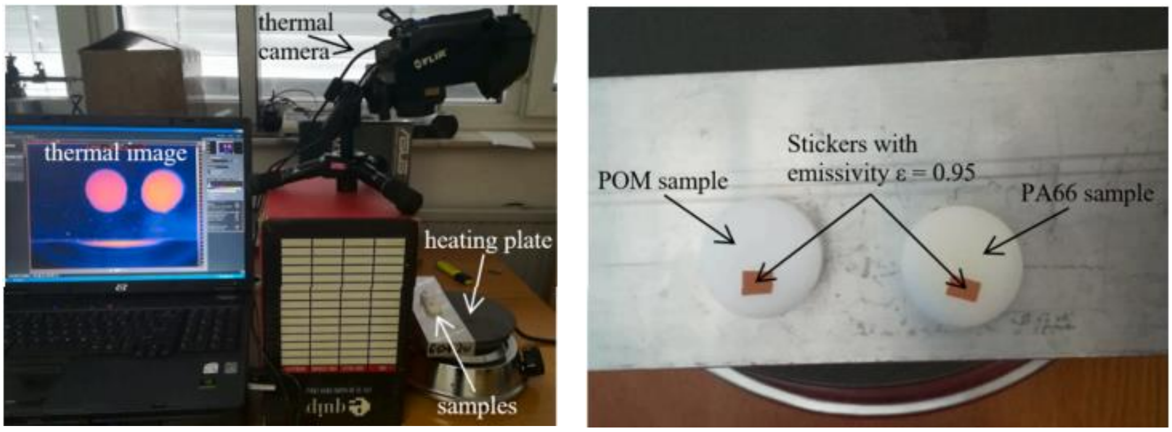

(a) Computer and thermal camera setting

(b) Sample heat plate

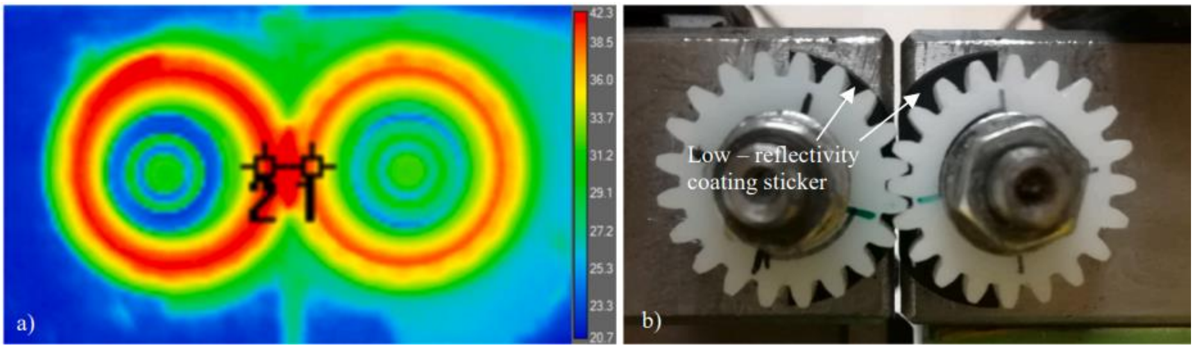

(c) Thermal camera 3x3 pixel

(d) POM and PA66 setting

Figure 2. 23 *An Experimental Set-Up to Measure the Thermal Behaviour of a Polymer Gear Set (after, [80])*

Zorko's results showed an average variation of 12% between observed and calculated temperatures, with a standard deviation of 7%. The temperatures measured were consistently lower than those predicted by the root temperature equation based on the VDI 2736 standard. This equation calculates tooth loss in degrees (H_v) and power transmitting over a pair of gear calculated (P), providing valuable data for understanding and predicting gear behaviour under different thermal conditions.

$$T_{root} \approx T_{amp} + P\mu H_v \left[\frac{k_{root}}{b\,z}(v_t m_n)^{0.75} + \frac{R_{\lambda,G}}{A_G}\right] ED^{0.64}$$

2.7 Reviews of the Literature on the Progressive Contact Effects

The effects of progressive contact on gear operation are critical and governed by industrial standards and practical implications.

2.7.1 Industrial Standard

The standard focuses on the peculiarities of progressive contact in atypical contact path conditions. This condition, characterised by continuous movement towards the tip of gear teeth, is a notable feature of polymer gear teeth and aligns with BS/ISO 6336 requirements [53]. The development of the progressive contact line's angle is a direct consequence of this type of contact.

2.7.2 Progressive Contact Effect Reviews

In automotive research, gear teeth often do not engage as typically as expected in the standard spur gear models. This results in an abnormal contact path directed towards the contact tip of the gear teeth. The typical normal of the contact path and point, as described by Merritt (1954), undergoes expansion due to the movement towards outward and inward contact points across the profiles of the driving and driven teeth. This continuous movement of spur gears leads to the formation of a progressive contact line and an angle of progressive contact [61].

Karimpour, Dearn, and Walton (2010) shed light on the impact of such progressive contact. They demonstrate how the direction of the path contact line changes due to the points of outward and inward contact associated with sliding and rolling velocities. This results in a separate line of progressive contact and a distinct contact path angle, referred to as the angle of progressive contact. Their research highlights the significance of the relationship between the contact path and the progressive contact in forming these angles [54].

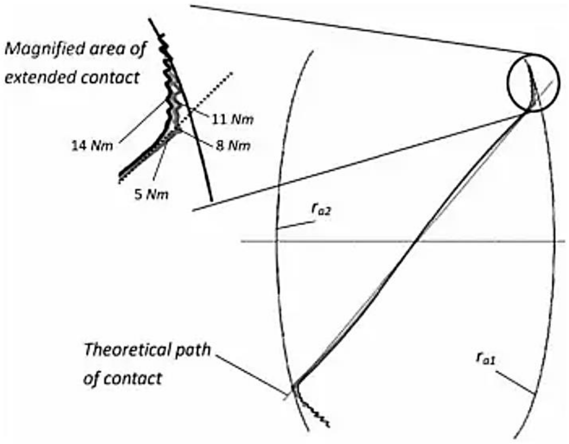

Figure 2. 24 *Simulated Extension to the Line of Contact (after, [54])*

Developing a progressive contact line increases the common normal of contact path and contact points indefinitely. The movement to the point of outward and inward contacts across the driving and driven teeth profile, respectively, was described and related to sliding and rolling velocities. [61]. The contact angle contains a distinct line of increasing contact and contact path. The contact angle contains a separate line of increasing contact and contact path. Therefore, the occurrence of the angles is referred to as the angle of progressive contact. The relationship between the contact path and the progressive contact establishes these angles.

Karimpour's research in 2009 simulated contact stress and applied a load of 7 Nm to gear polymer. They discovered increasing contact lines near both teeth' first and ended tips [54], shown in Figure 2.4. the common normal of contact path to the contact point C_3 (above the tooth flank) continually extends outward through the C_4 of motion, a combination of sliding and rolling velocities. It will result in an increased contact angle, γ.

Merritt's 1954 textbook presents an equation for calculating the sliding velocity generated by increased angular velocity along the contact path that continuously drives a pair of gears. This sliding velocity, denoted as V_s, is vital in understanding gear dynamics (V_s) [61] provided in the equation.

$$V_s = S_i(t)\left[\omega_p + \omega_g\right]$$

Additionally, Errichello's work further elucidates this concept, showcasing the rolling velocity at the moment of impact as depicted in Figure 2.25 [81] [82] [83]:

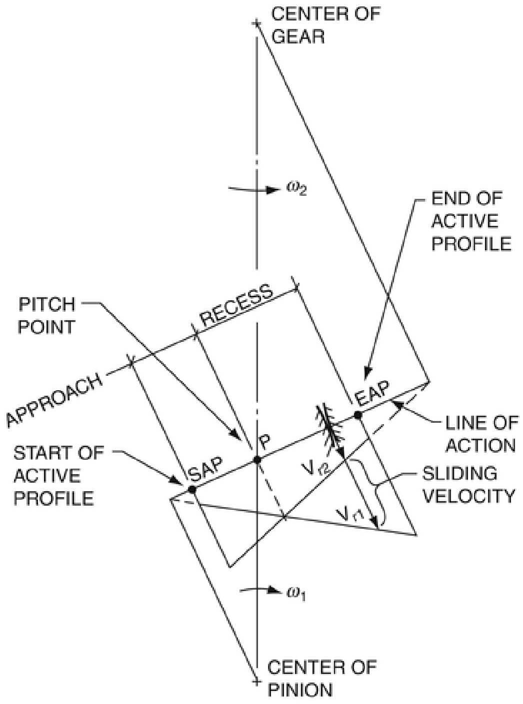

Figure 2. 25 *Rolling and Sliding Velocities at Contact Point (after, [81])*

Figure 2.25 illustrates the rolling and sliding velocities at the contact point between gears. The principal formula to calculate the rolling velocity, V_r, at any point on the cylindrical surface, is also applicable at the point of contact. This formula determines V_r by multiplying the angular velocity with the radius of the rolling body.

$$V_r = \ \omega \cdot r$$

Moreover, Merritt's equation highlights the rolling velocity along the line of contact path during progressive engagement.

$$V_{rp} = V \cos \emptyset [\tan \gamma + \tan(\emptyset + \alpha)]$$

$$V_{rg} = V \cos \emptyset [\tan \gamma + \tan(\emptyset - \delta)]$$

Min et al.'s research further contributes to this understanding by stating that the line of action dictates the instantaneous point of contact between the gear teeth throughout their rotational engagement and disengagement [84].

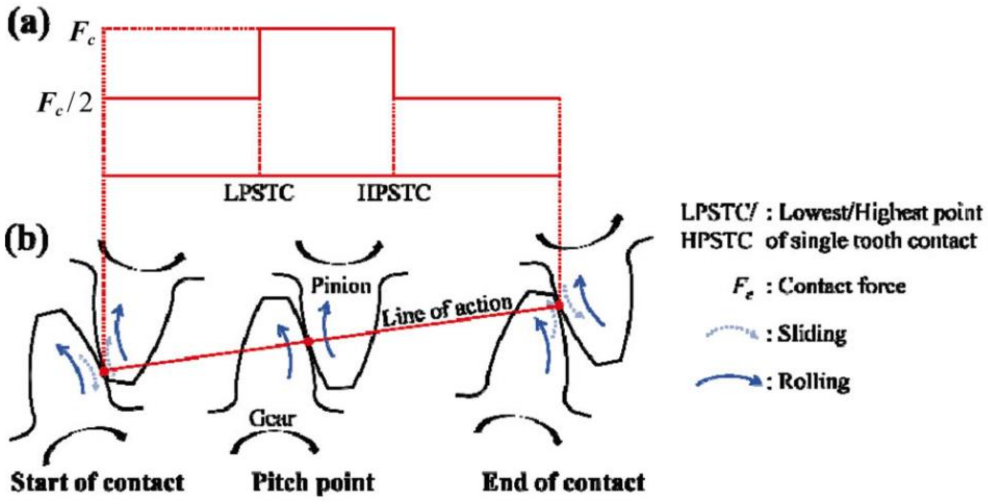

Figure 2. 26 *Involute Spur Gear Contact Behaviour (after, [85])*

Figure 2.26 from the work of Witold et al. (2014) offers a comprehensive view of the contact behaviour of a coated polymer involute spur gear. This figure details the line of action and the distribution of contact stress across the gear tooth, from the lowest point at the tooth base to the highest at the pitch point. Correct coating selection and lubrication are essential to enhance gear efficiency and longevity, ensuring smooth and reliable operation across various applications [85].

In conclusion, Figure 2.26 (a) and (b) provides a comprehensive understanding of the contact behaviour of a coated polymer involute spur gear. It highlights the line of action and the distribution of contact stress, with the lowest point at the base of the gear tooth and the highest point at the pitch point. Proper coating selection and lubrication are essential to enhance gear efficiency and longevity, ensuring smooth and reliable operation in various applications.

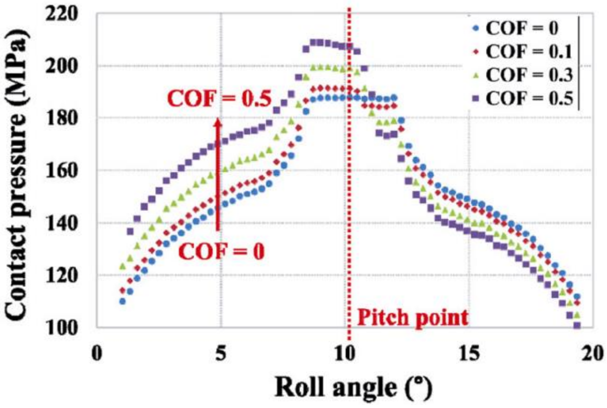

***Figure 2. 27** The Highest Contact Pressure Values for a Pair of Uncoated Gear Teeth in Each Contact Position Concerning COFs (after, [80])*

Figure 2.27 provides insight into the impact of friction on contact stress in a pair of uncoated gear teeth. It illustrates the highest contact pressure values at different contact positions for varying Coefficients of Friction (COFs). The graph underscores how changes in

COFs significantly affect contact stress, with higher COFs increasing contact pressure and vice versa.

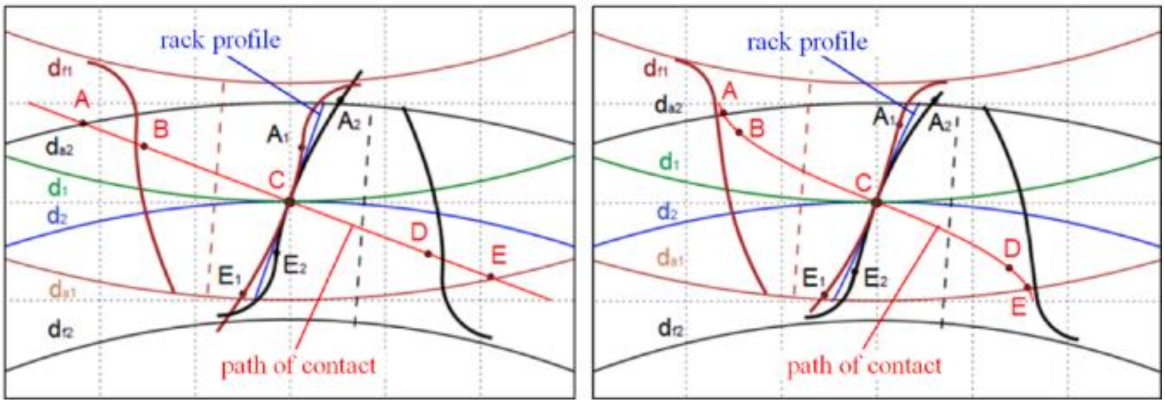

(a) Involute Gears with a Straight-Line Path of Contact

(b) S-Gears with a Progressive Curved Path of Contact

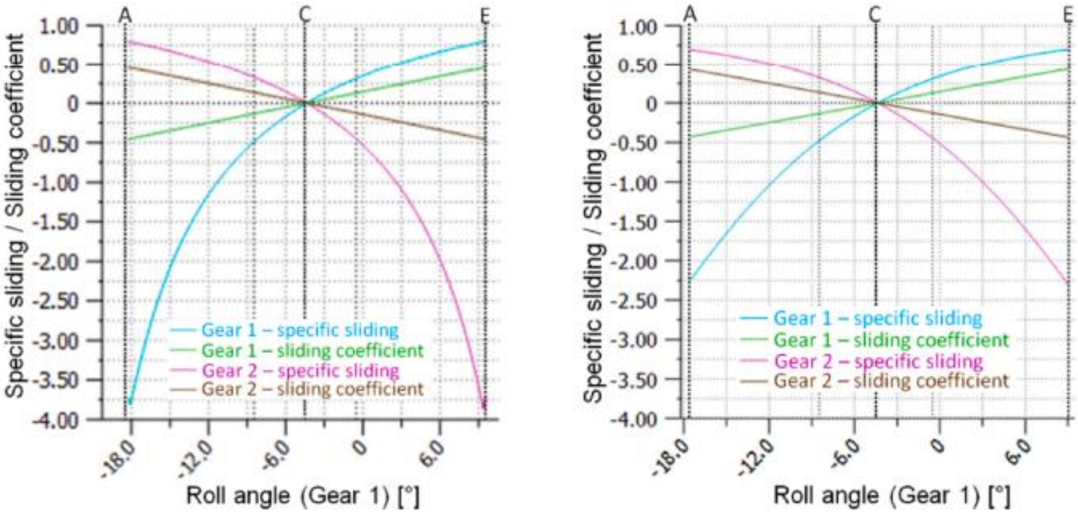

(c) Specific Sliding and Sliding Coefficient Calculation for an Involute Gear

(d) Specific Sliding and Sliding Coefficient Calculation for a S-Gears

Figure 2. 28 *The Comparisons Between the Involute Gears with a Straight-Line Path of Contact and S-Gears with a Progressive Curved Path of Contact, Based on Specific Sliding and Sliding Coefficient (after, [80])*

[80] In the context of PA66 and POM gears, Zorko's 2021 study underscores the significant differences in geometry and contact path between gear types - traditional involute gears with a straight-line contact path and S-gears with a progressive curved contact path. As

shown in Figure 2.28 (a) and (b), these geometric variations are essential in optimising gear design for various applications, considering factors like load distribution, stress concentrations, and wear during gear meshing.

Figure 2.28 (c) and (d) presents a comparative analysis of specific sliding and sliding coefficients between involute gears and S-gears. The findings indicate that S-gears demonstrate more efficient meshing behaviour with shorter sliding distances and higher sliding coefficients than involute gears. This comparative study of the sliding characteristics of different gear geometries is crucial for optimising gear design and achieving smooth, reliable, and efficient gear meshing in various applications [80].

2.8 Reviews of the Literature on the Crack Propagation and Fatigue Fracture

Crack propagation and fatigue fracture in polymer materials are critical areas in understanding the durability and longevity of these materials in practical applications. This section examines the state of crack propagation, explicitly detailing the crack tip's initial size, the crack's angle, its length in Cartesian coordinates, and the radial coordinate of the crack line. These aspects are crucial to the theory of Modes of fracture and the stress intensity factor. The critical stress intensity factor, particularly in Fracture Mode I, is a significant focus here. Fracture Mode I involves in-plane tensile opening, a primary failure mode in many polymer materials. Figure 2.29 in the literature illustrates this mode, showcasing the crack opening at the pitch and root of a toothed gear. A force vector or tensile opening triggers this mode [11] [86] [45] [87] [88] [7] [61] [21] [89] [90] [91] [92] [93] [94] [95], which is caused by a force vector or tensile-opening [96].

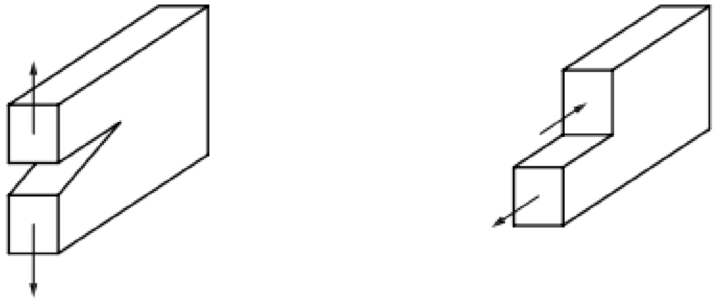

(a) Mode I-Tension Opening *(b) Mode II-in Plane Shear*

Figure 2. 29 *Illustration of Fracture Modes*

The literature review references multiple sources to understand this topic comprehensively. These include works by Prabhakaran, Balaji, and Joel (2014), Kinloch and Young (1983), Huh et al. (2006), Schreurs (2012), Chen and Shao (2011), Lias et al. (2018), Merritt (1954), and several standards and publications like BS 6168 (1987), AGMA 908 (1989), AGMA 2001-B88 (2001), and others. These references offer a wide-ranging perspective on crack propagation and fatigue fracture, highlighting the importance of understanding these phenomena in the context of polymer gear durability and performance.

The review also highlights the work of Lee et al. (2006), which addresses the force vector or tensile-opening aspect of crack propagation. By compiling these diverse sources, the literature review thoroughly explores the mechanisms and implications of crack propagation and fatigue fracture in polymer materials. This is an essential consideration for engineers and researchers working with these materials.

2.8.1 Industrial Standard

2.8.1.1 BS 2782 Standard for Plastic/Polymer Materials Testing

This standard addresses the effect of changing the notch-tip radius on the impact strength testing results. According to BS 2782-306A (2006), variations in the notch-tip radius can significantly alter the outcomes of notch-beam tests for various polymer materials [97].

For Nylon material (PA66), an impact strength effect at about 1.95 mm of a notch-tip radius is recommended to be 40 kJ/m^2 (PA66). [11]. Additionally, the Izod and Charpy impact tests are utilised to measure Nylon's tensile impact resistance, providing valuable insights into fracture mechanics by examining the energy absorbed during shock loading or dynamic impact [98], [99].

Mixed mode fracture behaviour in polymer composites is evaluated using three-point bend tests in a non-symmetrical arrangement following ASTM D5045 standard procedures [100] [101].

2.8.1.2 BS 7910 Specification for Crack Behaviour

[102] BS 7910 Specification for crack behaviour (2015) encompasses a range of methodologies for structural integrity testing, including fracture mechanics, fault assessment processes, and flaw characterisation. This standard is instrumental in determining stress intensity factors, critical fault sizes, and crack propagation rates. It plays a crucial role in assessing the integrity of structures with faults, like cracks. Different fracture modes, such as Mode I and II, are defined under this standard to characterise crack propagation and failure behaviour in polymer materials.

Mode I fracture or Opening Mode, is characterised by the crack surfaces being pushed apart perpendicularly to the crack plane, propagating in the direction of the applied tensile stress. This mode is associated with a tensile stress state.

Mode II fracture, or Sliding Mode, involves the crack surfaces sliding parallel to the crack plane, indicative of a shear stress state. In this mode, the fracture propagates along the direction of the shear stress. Figure 2.29 illustrates these fracture modes, visually representing how Mode I and Mode II fractures occur in polymer materials. Understanding these modes is essential for analysing the behaviour of materials under different stress conditions and developing more resilient polymer products.

2.8.2 Crack Propagation and Fatigue Fracture Reviews

The study of crack propagation and fatigue fracture, mainly focusing on predictive techniques for fatigue cracks in mixed modes, describes the behaviour of fatigue crack propagation under various static force situations, including biaxial loading, tensile opening, and shear opening in the plane of fractures, is explored. Research has concentrated on the propagation of cracks in gear teeth, examining the fracture behaviour of polymer materials in both Modes I (tensile-opening) and Mode II (shear-opening) fracture modes [103], [104].

In the context of gear polymer models, Mode I fracture is crucial. It is suggested that this mode, which involves locating the crack tip at the point of material failure, is the primary mode of concern. The growth criteria of a crack are determined at the crack tip, depending on the stress state. With prolonged load application, the continuous action can lead to a mixed mode (Mode I and Mode II) of fatigue crack growth, eventually leading to severe breakage.

- Mode I fracture, in the concept of the initial crack in this research concerning gear polymer models, is suggested that only Mode I, which locating the crack-tip at material failure. The crack growth criteria can be found at the crack tip and depend on the stress state.

After receiving the load at a long period of time, continuous action leads to Mixed Modes (Mode I and Mode II) of fatigue cracking growth until severe breakage.

- Experimental and theoretical analyses have been utilised to predict the formation of fatigue cracks in the fracture of Mixed Modes [103] [104] [45] [88]. G.C. Sih's 1974 work predicted fatigue-crack growth under Mixed Modes of fracture, combining theoretical and experimental investigation [105].

Zappalorta et al. (2013) explored Mixed-mode fractures by altering crack directions and angles [101].

In 2015, Ma et al. investigated the dynamic behaviour of a perforated gear system, mainly focusing on the impact of crack propagation paths [106]), shown in Figure 2.30. Using ANSYS software, a finite element model was established to calculate varying on-time mesh stiffness for a perforated gear with cracks in both the tooth and root (rim). The study revealed three distinct periods related to gear body slots during one rotation of the perforated gear, noting that rim cracks significantly impact vibration responses more than tooth cracks.

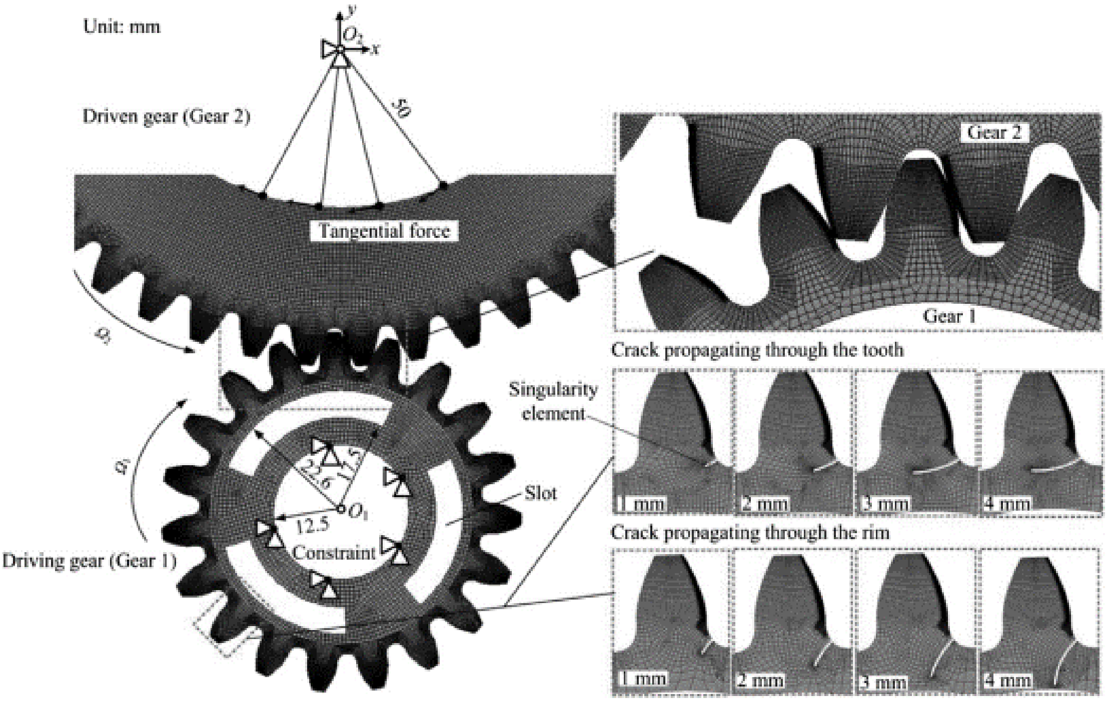

Figure 2. 30 *Tooth Gear-Meshing (after, [106])*

[80] In 2021, Zorko studied the mechanical behaviour of polymer gears with a progressive curved path of contact, focusing on driven S-gears made from PA66 and POM materials. The study revealed initial cracks on PA66 and POM-driven S-gears subjected to maximum principal stress and high-cycle tooth bending fatigue. The investigation highlighted

that crack initiation is crucial for predicting gear life and preventing catastrophic failures, and further crack propagation analysis can help optimise gear design and material selection and experimental testing at 0.6 Nm and 1400 rpm.

It was found that the tooth failed after 48.12 million cycles, as shown in Figure 2.30. The crack initiation was crucial for predicting gear life and preventing catastrophic failures. Further crack propagation analysis will aid in optimizing gear design and material selection to enhance fatigue resistance and thermo-mechanical performance.

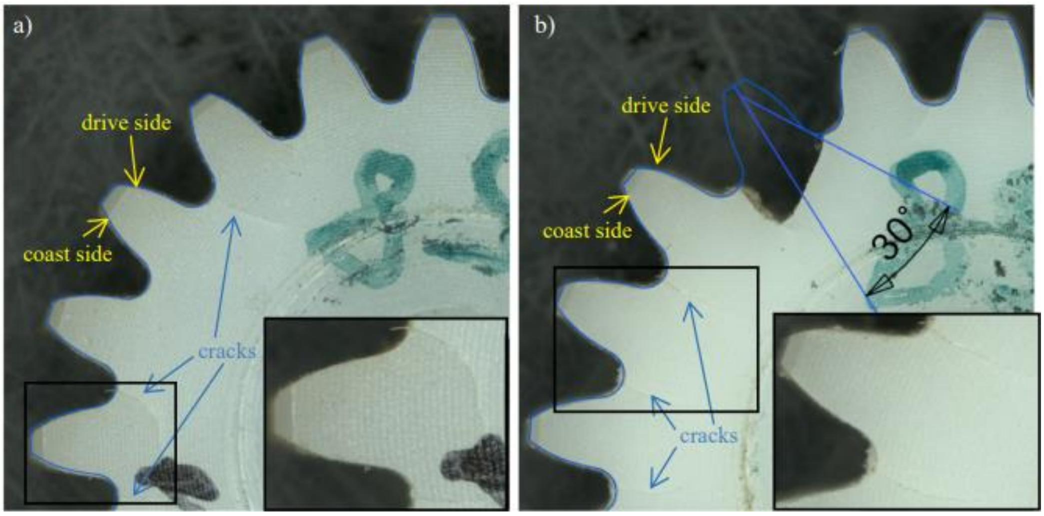

(a) Driven PA66 *(b) Driven POM*

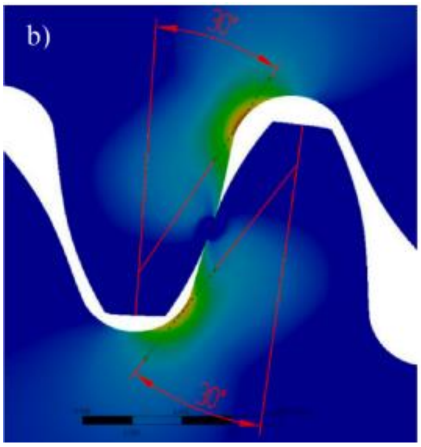

(c) Principal Bending Stress from Simulation

Figure 2. 31 *Mechanical Behaviour of Polymer Gears with a Progressive Curved Path of Contact, Specifically Driven S-Gears (after, [80])*

Figure 2.31 showcases the mechanical behaviour of polymer gears with a progressive curved contact path, specifically driven S-gears. The crack initiation point, corresponding to the 30 tangent points, is identified, with the maximum bending stress indicated in red areas. This visualisation aids in understanding the second fracture propagation course, where the crack's starting point does not correspond to the 30 degrees of tangent. On the drive and driven gears, multiple cracks were observed to start approximately amid the root rounding.

2.10 Closing and Outline of Thesis

Chapter 2 of this thesis presents a comprehensive framework of the theoretical literature relevant to the research. It provides an overview and central concepts that will be implemented in the subsequent investigation. The research is structured to explore and design five critical sections: "Failure modes, flash temperature, frictional thermal effects, viscoelastic hysteretic behaviour, and fatigue fracture," each representing kinematic behaviour in polymer gear systems.

A significant aspect of this research is to examine changes in the form of polymer gear tooth flanks and the process of material deterioration leading to fracture. These investigations will be conducted using the MK II test rig located in the MIT laboratory. The study focuses on various Polyether Ether Ketone (PEEK) composites, including PEEK-450G, 450GL, 450FC, 450CA, and 650G. These materials represent a range of polymer composites that will be scrutinised for their performance and characteristics.

The research is designed to perform experimental and model analysis according to BS/ISO 6336 and VictrexTM industry standards for gear geometry. The methodology includes determining the torque at 9.38 Nm and a rotational speed of 1,000 rpm. Additionally, the master gearbox and armloads will undergo a limited vibration test to assess their performance under specific conditions.

Figure 2.32 in the thesis encapsulates the theoretical literature and serves as a visual summary of the studies. This figure is instrumental in illustrating the main concepts that form the foundation of the research, guiding the investigation towards a comprehensive understanding and design of polymer gear systems.

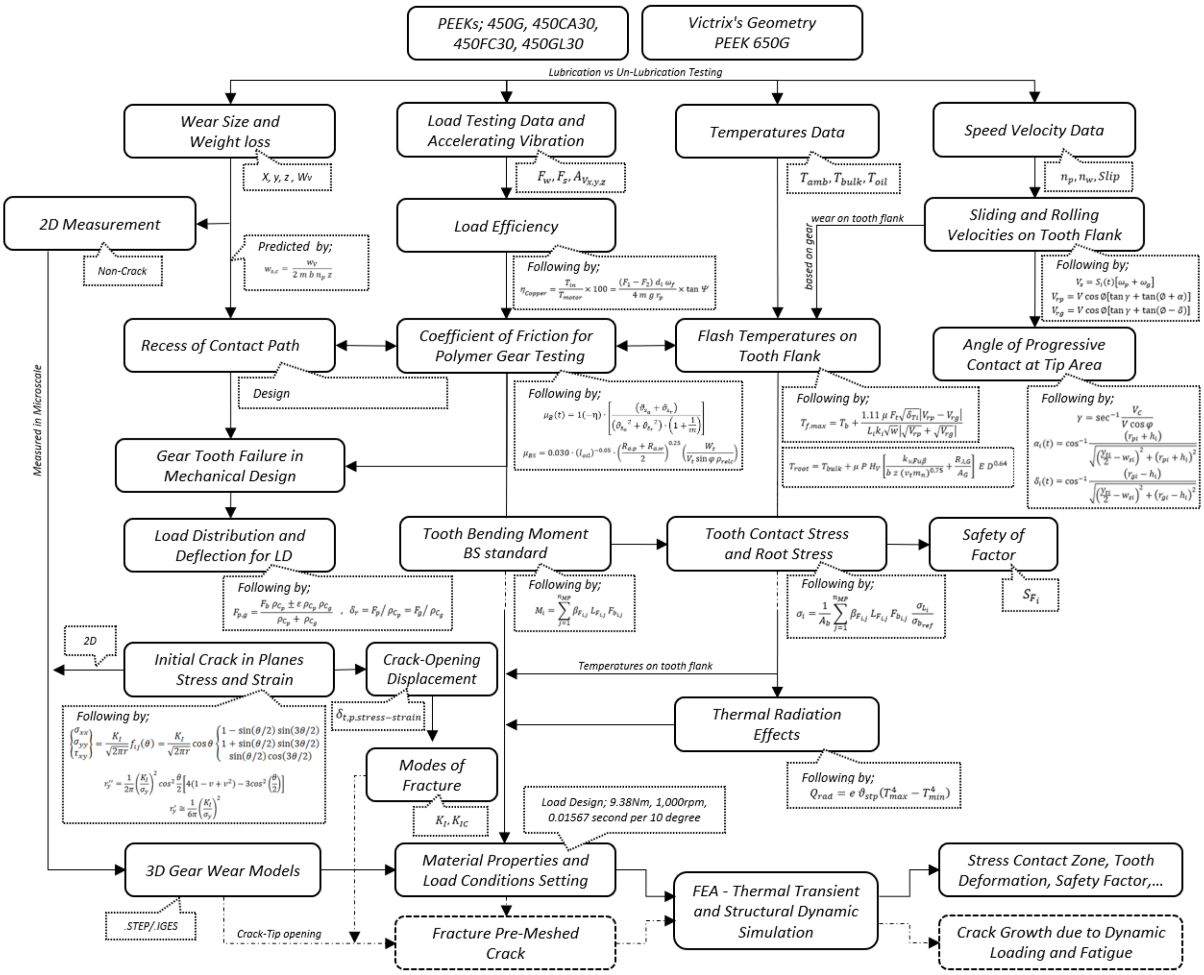

Figure 2. 32 *The Main Concepts and the Theoretical Works to be Implemented in This Research.*

Chapter 3

Theoretical Foundations of Polymer Gear Design: Meshing Behaviour and Gear Geometry

The primary theory of polymer gears encompasses the essential principles and considerations for designing and operating gears constructed from polymers (plastics). These gears are prevalently used in various applications where attributes such as lightweight, corrosion resistance, low noise production, and cost-effectiveness are paramount. This research delves into the behaviour of gear meshing, explicitly focusing on the extension of gear tooth contact. It examines how contact deformations, including contact ratio, pitch point, contact lines, pressure angle, centre distance, and others, vary in response to stress distribution and deformation analysis.

3.1 Spur Gear Geometry

Polymers are becoming a viable alternative to metal gears, with investigations into several polymer composite materials for potential application in various applications of increasing torque transmission, including the automotive industry. A large body of research has been developed at the University of Birmingham, predominately based on the Birmingham Standard geometry that adheres to the BS/ISO 6336 gear standard [54], [107]. Gear geometry, which encompasses the specific form, size, and factors defining the physical properties of a gear, is illustrated in Figure 3.1. It includes several gear features, such as the involute tooth profile, pitch, and backlash.

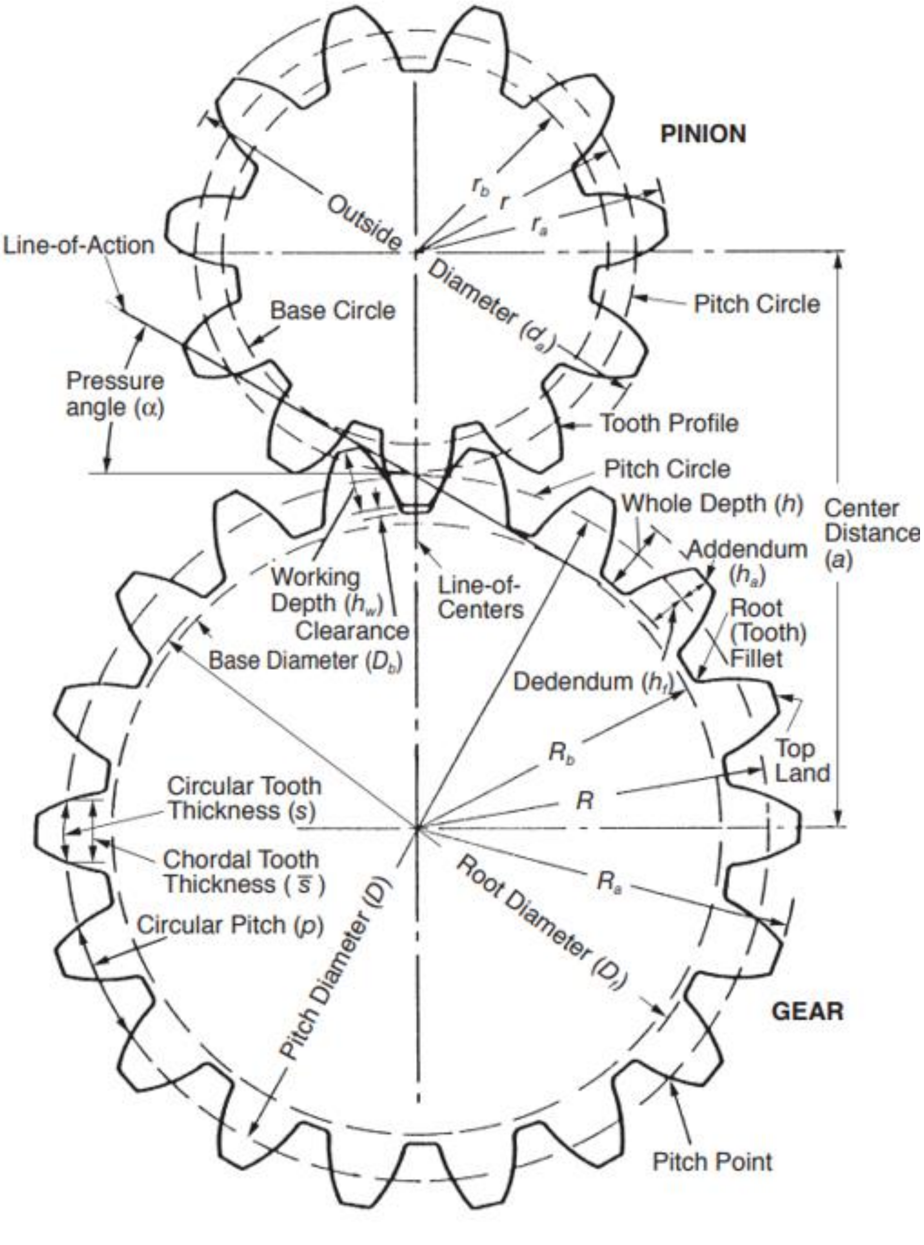

Figure 3. 1 *Principal Gear Geometry (adapted from, [108])*

- **Pitch point:** The pitch represents the distance between corresponding points on adjacent teeth, often referred to as circular or diametral pitch. It is a crucial parameter in defining the involute tooth profile, gear size, and spacing.
- **Backlash:** Backlash denotes the clearance or play between meshing gear teeth. It significantly impacts the precision and accuracy of gear operation, including factors like vibration and noise.
- **Involute tooth profile:** The gear teeth's physical shape, determined by the tooth profile, is vital for efficient meshing and smooth operation. The involute tooth profile affects load distribution, contact stress, power transmission errors, short-term durability, and backlash.

3.1.1 Involutes Tooth Profile

An involute tooth gear is widely employed in gear systems due to its advantageous properties, such as maintaining a constant angular velocity ratio and ensuring smooth operation. A specific mathematical curve defines the involute profile and is extensively utilised in various gear applications [71] [61] [109].

a. Standard of Involute Tooth Profile

Standard gear meshing involves movement along the involute and curvature surfaces, following a straight line, and traversing the contact path in a cycloid tooth gear [71]. This contact path is evident in the line of approach and recess relative to the base pitch on regular gear teeth. Theoretical perspectives on gear meshing highlight the initial point and end of gear engagement, emphasising the significance of the involute profile in ensuring efficient and smooth gear operation. Tooth contacts adhere to the contact path's line of action and are influenced by the degree of the pressure angle, as detailed by Merritt (1954), Colbourne (1987), and Long, Lord, Gethin, and Roylance (2003). [61] [110] [111]. Figure 3.2 provides a summarised depiction of the state of the contact line.

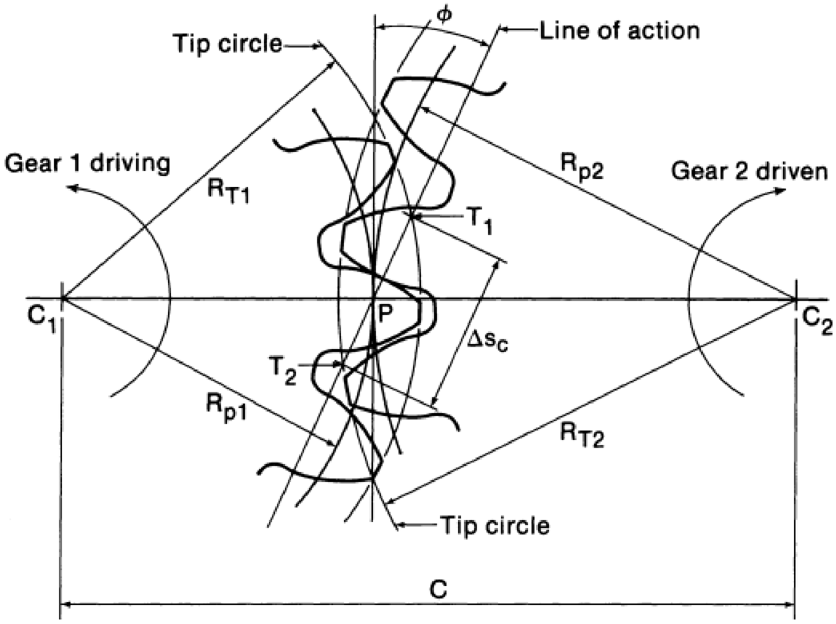

Figure 3. 2 *Illustrates of the State of the Contact Path Line (adapted from Colbourne (adapted from [110])*

The research by Merritt and Buckingham has identified the point of contact as being determined by the sliding and rolling velocities. Typically, at the pressure angle, the initial point of contact is found at the wheel tip (driven gear) of the tooth on the driving teeth ($a_1, b_1 = c_1$), continuing through the pitch point and ending at the pinion tip (drive pinion) of the driven gear teeth ($a_5, b_5 = c_5$), as cited by Merritt (1954) and Buckingham (1949). [61], [71].

[108] QTC Gears (2022) presents a taut string analogy to demonstrate the development and interaction of mating teeth. Envision a string unwinding from one base circle and winding onto another, as illustrated in Figure 3.3 (a). This action causes a single point on the string to trace an involute simultaneously on each base circle's rotating plane. These involutes are conjugate, sharing a normal and tangent. By winding a second taut string in the opposite direction around the base circles, as seen in Figure 3.3 (b), involutes with opposite curves are

formed, facilitating motion reversal. Proper spacing of these pairs results in an involute gear tooth, depicted in Figure 3.3 (c).

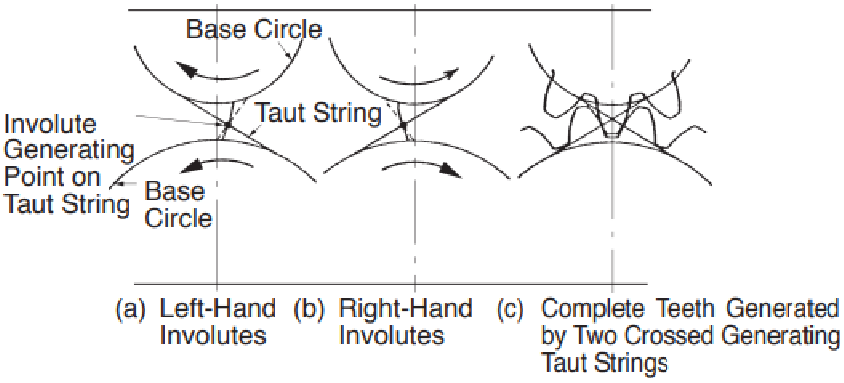

Figure 3. 3 *Illustrates the Generation and Interaction of Gear Teeth (adapted from, [108])*

3.1.2 Transverse Contact Ratio

The average load-sharing ratio for conventional spur gears in surface contact teeth, known as the transverse contact ratio or CR, is crucial when two gears mesh and rotate. The contact deformation of standard spur gears with the transverse contact ratio is calculated using a formula based on the Hertzian equation [61] and the pressure angle to the action-angle ratio [21] in the transverse plane.

$$CR = \frac{\sqrt{r_{k_1}^2 - r_{g_1}^2} + \sqrt{r_{k_2}^2 - r_{g_2}^2} - c\sin\theta_b}{\pi m \cos\emptyset_t}$$

$$CR = \frac{\sqrt{\left(r_{pi} + a\right)^2 - r_{pi}^2\cos\emptyset_t} + \sqrt{\left(r_{gi} + a\right)^2 - r_{gi}^2\cos\emptyset_t} - c\sin\emptyset_b}{\pi m \cos\emptyset_t}$$

Key variables include:

r_{pi}, r_{gi}	Radial pitch of pinion and gear at real-time testing (mm)
$\emptyset_t$	Pressure Angle $(Deg.)$

$\emptyset_b$ Contact Base Angle $(Deg.)$

3.1.3 Approach and Recess Lengths

The specific values for approach and recess lengths are contingent on the gear module, pressure angle, number of teeth, and the gears' specific application. These values are outlined in gear design handbooks or industry standards, such as AGMA (American Gear Manufacturers Association) standards for standard gears. The principle of base pitch, as presented in Merritt's and Buckingham's handbook p_b, is illustrated in Figures 3.4 and 3.5 and by the equation [61], [71]:

$$p_o\, r_c = l_w + l_p$$

The contact trajectory, incorporating the approach and recess lines, is dictated by the fundamental pitch of conventional gear teeth. The critical dimensions of the approach (l_w) and recess (l_p) segments are defined based on BS 6168 (1987) [21].

$$l_p = r_b\, \beta_r$$

$$L_p = \sqrt{\left(r_{pi} + a\right)^2 - r_{pi}^2 \cos^2 \emptyset_t} + \sqrt{\left(r_{gi} + a\right)^2 - r_{gi}^2 \cos^2 \emptyset_t} - c \sin \emptyset_b$$

This research integrates Merritt’s and Buckingham’s equations to analyse the gear tooth contact extension's gear meshing behaviour. Figure 3.5 focuses on how contact deformations, such as approach and recess lines, contact ratio, pitch point, contact lines, pressure angle, and centre distance, influence gear operation.

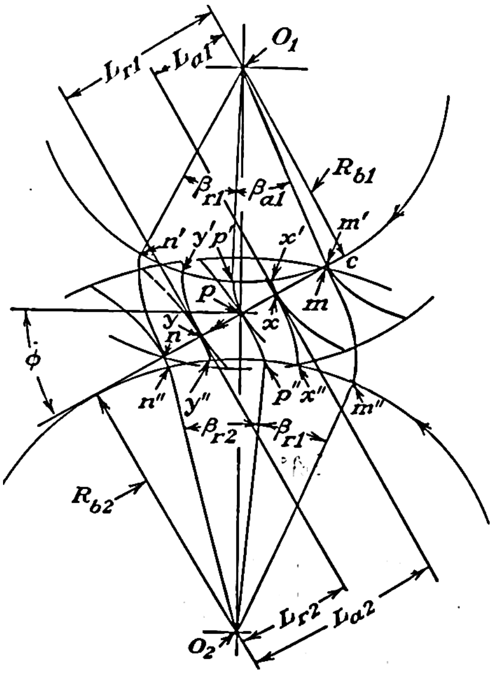

Figure 3. 4 *Approach and Recess Lines According to Buckingham's Equation (adapted from, [71])*

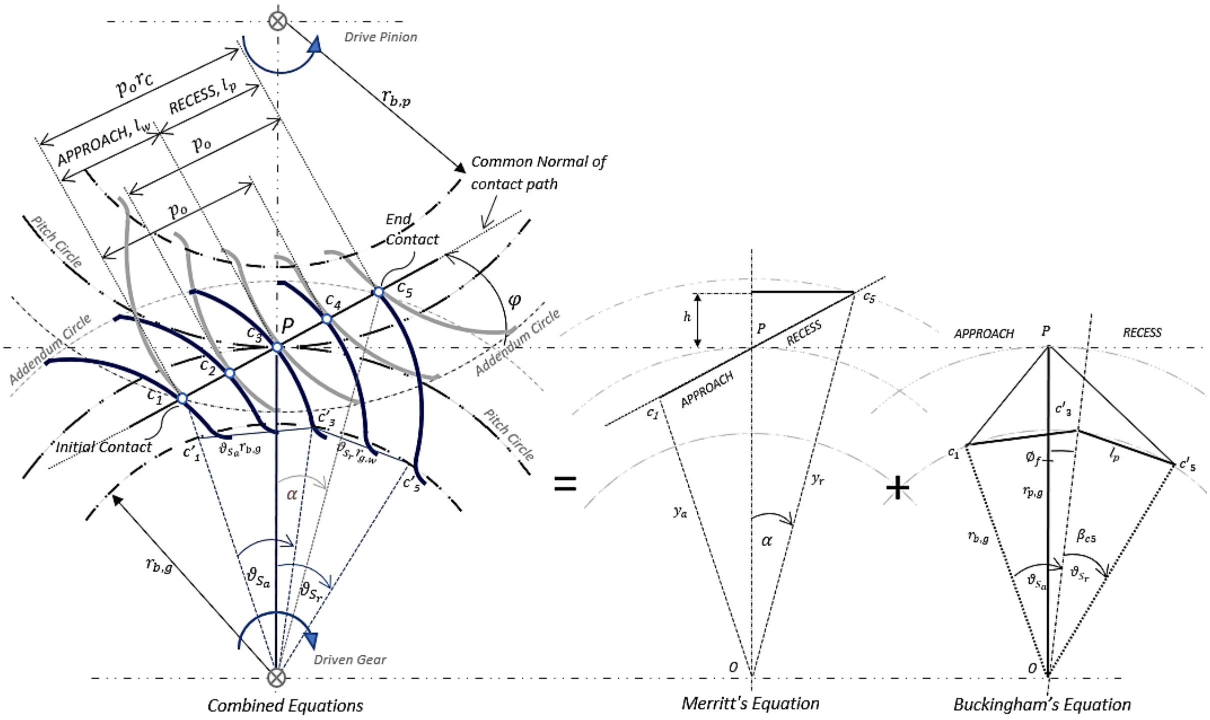

Figure 3. 5 *The Combination of Merritt's and Buckingham's Equations*

3.1.4 Ball Contact in the Involute Tooth Gear

Buckingham's handbook provides a method for measuring ball contact in involute tooth gears. The equations determine the geometry of the involute tooth gear and the fundamentals of ball contact. According to Reece, Gerpen, Reece, and Iowa (1987), the equation for a standard-size ball calculates the interface of contact point movements from the centre of a pair of gear teeth [112]. The equation for measuring ball contact size is defined as follows:

$$d_{ball,min} = \frac{1.68}{N_p} \cdot d_p$$

where	d_p	Pitch diameter in millimetres,
	N_p	Number of pinion teeth,
	d_{ball}	Diameter of ball contact calculated based on the pressure contact (φ_1 and φ_2) of the tooth arc diameter (d_{arc}).

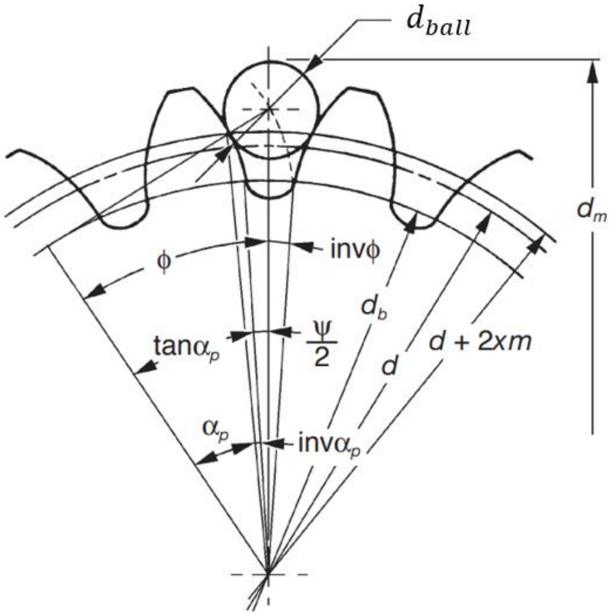

Figure 3. 6 *Illustration of Ball Contact Measurement (adapted from, [108])*

As detailed in Figure 3.6, the provided equations enable the calculation of over-ball measurements for specific tooth thickness, regardless of where the ball engages the tooth profile, as described by QTC Gears (2022) [108]. This approach offers a consistent methodology for assessing tooth dimensions.

Even Number of Teeth and Odd Number of Teeth

$$d_{ball,even} = d_m - \frac{d_p \cos \varphi}{\cos \varphi_b}$$

Involute function

$$inv\varphi_b = \frac{T_i}{d} + inv\varphi + \frac{d_{ball}}{d_p \cos \varphi} - \frac{\pi}{z}$$

Tooth thickness (T_i) from a given over-pins measurement (d_m). The equations facilitate a simplified calculation approach.

$$T_i = d_p \left(\frac{\pi}{z} + inv\varphi_c - inv\varphi + \frac{d_{ball}}{d_p \cos \varphi} \right)$$

$$\varphi_c = \cos^{-1} \left(\frac{d_p \cos \varphi}{d_m - d_{ball}} \right)$$

3.1.5 Contact Pressure Angle

The pressure angle is crucial in gear design as it impacts contact properties, load distribution, and the efficiency of the gear system. It is formed by the line perpendicular to the tooth surface and the line representing the force applied to the gear tooth. The contact pressure angle at half the tooth thickness on its exterior is denoted by φ_2, while the pressure angle of the involute teeth function is represented by φ_1. The base circle, φ_b, is calculated using Buckingham's equation for the involute function.

$$\varphi_b = inv.\varphi_1$$

$$\varphi_b = \left[\frac{\sqrt{\left(r_{ref}^2 - r_b^2\right)}}{r_b} - \tan^{-1}\frac{\sqrt{\left(r_{ref}^2 - r_b^2\right)}}{r_b}\right], \quad \tan\varphi_1 = \frac{\sqrt{\left(r_{ref}^2 - r_b^2\right)}}{r_b}$$

therefore, $inv.\varphi_1 = \tan\varphi_1 - \varphi_1$

where r_b Radius of the driving/driven gear's base circle (mm);

r_{ref} Initial and end of a pair gear contacts for radius reference (mm).

The pressure contact angle involves the interaction between the line of contact path and the base circle, with the radian angle starting at the origin of the dotted involute and extending across the ball circle, viz:

$$inv.\varphi_2 = \left[\left(\frac{T_1}{2\, r_{arc}}\right) + (\tan\varphi_1 - \varphi_1) + \left(\frac{d_{ball}}{r_b}\right) - \left(\frac{\pi}{N_{p,g}}\right)\right]$$

$$r_{ref} = r_b \cos\varphi_2$$

3.1.6 Base Pitch and Contact Path

Merritt characterises the standard base pitch as the distance between the base circle (p_c) and the consistent directionality of successive gear outlines. The base circle and the tooth flank curve are used to calculate this measurement. The primary base pitch is derived accordingly, offering a precise gear design and analysis measure [61].

$$p_b = p_c \cos\varphi_1 = \frac{\pi\, d_p}{N_p}\cos\varphi_1$$

The conjugate motion action of involute tooth flanks is parallel and originating from the base pitch measured along a straight edge's position, as Buckingham (1949) described [71]. This motion consistently manifests at every point along the involute tooth flank, as illustrated in Figures 3.1, 3.4, 3.5, and 3.7.

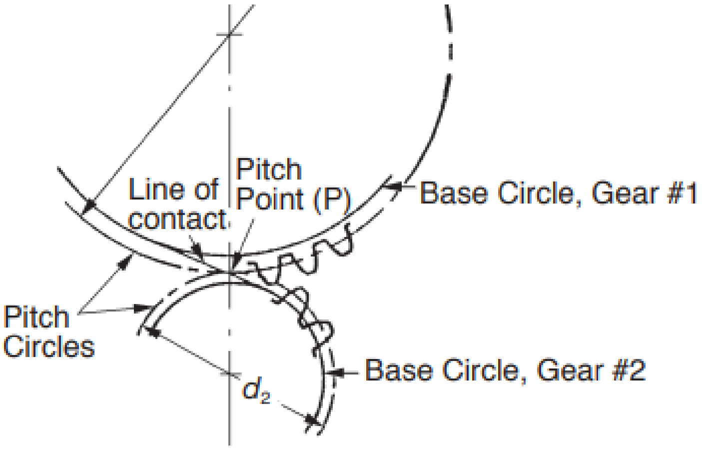

***Figure 3.** 7 Base Circle (adapted from, [108])*

3.2 Sliding and Rolling

[113] In 2021, Budinski characterised sliding and rolling as lateral slips caused by lateral deformations that occur by Hookean behaviour. The compressive stresses involved are Hertzian in nature, with the possibility of vibrational contributions. The shear stress condition in sliding and rolling is altered due to the induced lateral displacement, as depicted in Figure 3.8.

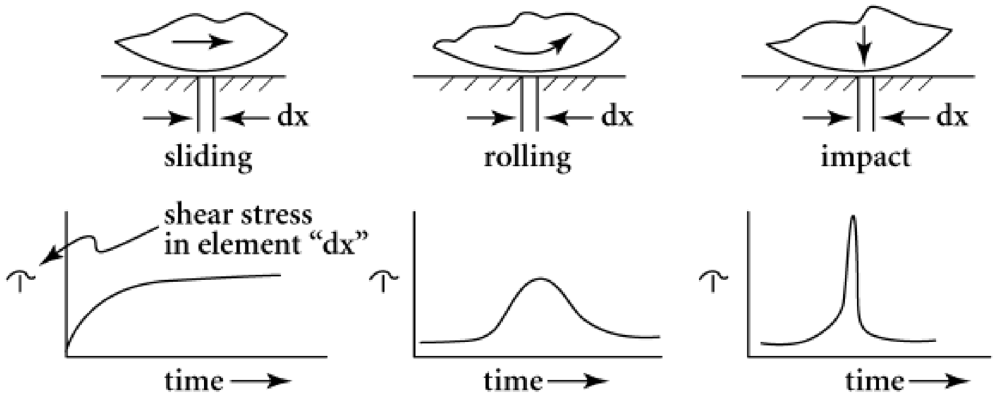

(a) Sliding *(b) Rolling* *(c) Impact*

***Figure 3. 8** Shear Stress Condition in Sliding and Rolling (adapted from, [113])*

Budinski's research in 2021 also highlights the energy loss due to sliding friction, which occurs when one tooth moves over another across a small distance dx during the time interval dt [114]:

$$dE = \mu F \, dx$$

$$dx = (Rolling|Sliding|Impact) \, dt$$

when $v = \omega \, r$

$$dx = (\omega_1 + \omega_2) \, x \, dt$$

$$dx = (\omega_1 + \omega_2) \, [r_b \tan \Psi - r_b \tan \Psi(\alpha + 0)] \, dt$$

As shown in Figure 3.2.1, the sliding wear leads to material removal from the contacting surfaces due to frictional forces, abrasive particles, or asperities. The wear rate in sliding is generally higher than in rolling due to increased contact area and frictional forces. Rolling wear, however, results in material fatigue and surface distress due to repeated loading and unloading at the contact points, even though it typically involves lower wear rates than sliding wear.

[61], [71] Merritt (1954) and Buckingham (1949) have established that the sliding velocity is determined by the increased angular velocity on the contact path driven by a pair of gears. This appears as the contact velocity and is calculated using specific equations based on the theory of sliding velocity on the tooth flank (V_s):

$$V_s = \left[\omega_p + \omega_g\right] S_i(t)$$

and the contact velocity (V_C):

$$V_C = V \cos \emptyset \sec \gamma$$

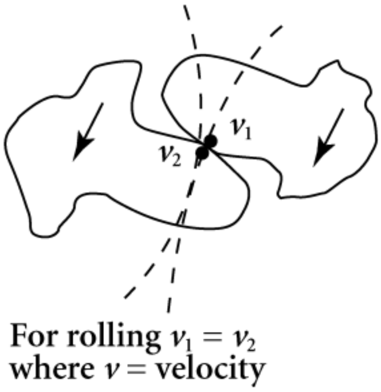

Figure 3. 9 *Rolling Gear Teeth (adapted from [113])*

The theory of involute gear meshing emphasises the importance of the shape and rolling angle. The tooth profiles, derived from the contact ratio and path contact, determine the rolling angle. The roll angle, as discussed by Beghini, Presicce, and Santus (2004), extends from the root to the tip of the gear teeth, ranging from the "start of the active profile of roll angle, RA" to the "end of the active profile of roll angle" [115]. In this study, the focus is on the driven gear, with the tipping point corresponding to the starting active profile of the roll angle and the base circle corresponding to the end active profile, as shown in Figure 3.10.

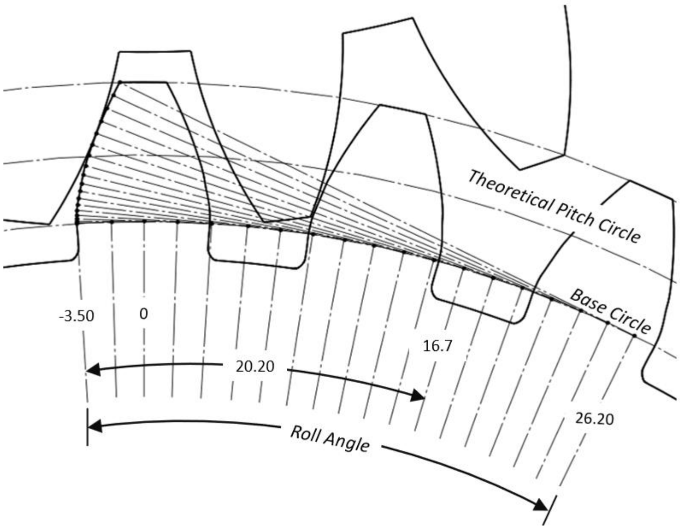

Figure 3. 10 *Rolling Angle (RA)*

3.3 Coefficient of Friction

Friction results in various forms of wear and erosion, as indicated in Figure 3.11. Notably, rolling friction is often less than sliding friction. This difference plays a significant role in gear design and material selection, influencing the longevity and efficiency of gear systems.

In his work on the modes of friction, Budinski described a coefficient of rolling friction (μ_r) in addition to the coefficient of friction for sliding. This coefficient is a combination of the rolling force F_r and the normal force on the revolute element N_r. Figure 3.11 depicts these modes of friction.

Takanashi and Shoji (1981) and Takahashi, Itakagi, Takahashi, Koide, and Kobori (2017) formulated an equation to determine the coefficient of friction μ for plastic gears [75], [116];

$$\mu = \frac{C_0 V_s^{0.23}}{P_{H,max}}$$

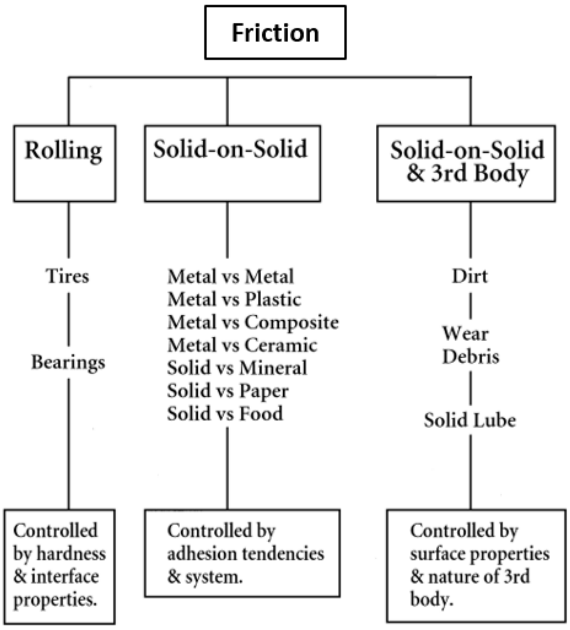

Figure 3. 11 *Modes of friction (adapted from, [113])*

This equation, derived for un-lubricated conditions, includes the plastic-plastic coefficient C_0 approximated as 3.19. Buckingham (1949) noted that the concept of the involute gear teeth geometry significantly influences the time and load condition test. When evaluating load/transmission efficiency and the gear contact ratio (m_g) in millimetres, the frictional behaviour or coefficient of friction is not constant under the teeth involute [71].

$$\mu_B(t) = \left(1 - \eta_B\right) \cdot \left[\frac{\left(\vartheta_{s_a} + \vartheta_{s_r}\right)}{\left({\vartheta_{s_a}}^2 + {\vartheta_{s_r}}^2\right) \cdot \left(1 + \frac{1}{m_g}\right)}\right]$$

Buckingham's equations consider the approach angle (ϑ_{S_a}) and recess angle (ϑ_{S_r}) incorporating the effects of oil lubrication.

$$\vartheta_{S_a} = \left\{\frac{\left[\sqrt{r_{ag}^2 - r_{bg}^2} - r_g \sin\varphi_1\right]}{r_{bp}}\right\}_B , \qquad \vartheta_{S_r} = \left\{\frac{\left[\sqrt{r_{ap}^2 - r_{bp}^2} - r_p \sin\varphi_1\right]}{r_{bg}}\right\}_B$$

This research employs Buckingham's equations to measure and derive the coefficient of friction.

$$\mu_{BS}(t) = 0.030\,(l_{oil})^{-0.05} \cdot \left(\frac{\left(R_{a,p} + R_{a,w}\right)}{2}\right)^{0.25} \left(\frac{W_t}{v_t \sin\varphi\, \rho_{relc}}\right)$$

The fluctuation of the coefficient of friction with rolling speed, influenced by dynamic viscosity and load, was represented by an equation from Benedict and Kelley (1961) [73]:

$$\mu_{B\&K}(x) = 0.0127\ \log\left[f_N(x)\frac{2.97 \times 10^4}{\eta\ v_s(x)\ v_r(x)^2}\right]$$

Drozdov and Gavrikov (1968) contributed to understanding the sliding speed's effect on the coefficient of friction [74]:

$$\mu_{D\&G}(x) = \left[\, 0.8\sqrt{\nu}\ v_s(x) + v_r(x)\phi + 13.4\right]^{-1}$$

Diez-Ibarbia et al. modified the Schlenk (1994) equation, considering that the coefficient of friction remains essentially constant above 20% of the slide-to-roll ratio (SRR). This modification is particularly relevant when the meshing process approaches the one-to-two tooth transition in a spur gear, with a calibrate factor X_L of 1 without lubrication.

$$\mu_{MS}(x) = \mu_S(Schlenk)\tanh\left(\frac{\varepsilon_\alpha}{\varepsilon_\alpha - 1}\ |SRR(x)|\right)$$

The coefficient of friction, as derived from numerical results using an EHL model confirmed by actual traction curves [77], was adjusted using a unique function based on significant parameters, including Xu's parameters $b2, b3, b6$ and $b8$.

$$\mu_H(x) = e^{f_{Xu}}|SRR(x)|\ p_h^{b2}\ U_S^{b3}\ \eta_x^{b6}\ R_X^{b8}$$

The coefficient of friction in unlubricated contacts is influenced by surface roughness, materials of the contacting surfaces, applied load, sliding speed, and relative velocity. Unlubricated contacts are more prone to wear and heat generation due to increased friction, leading to material deformation, adhesion, and surface damage, thereby reducing performance. The relevant equations can be applied according to the methodologies of Buckingham, Merritt, Diez-Ibarbia et al., and Takanashi & Shoji.

3.4 Load Efficiency

Load efficiency considers various factors affecting gear performance under different loads, such as material properties of the gear teeth, lubrication, gear tooth profile, and operating conditions (e.g., rotational speed, temperature, and applied load). These factors collectively influence the gear system's efficiency, durability, and operational reliability.

Torque, a fundamental aspect of gear mechanics, is critical in determining efficiency, typically expressed as a percentage. This efficiency represents the ratio of helpful output power (power delivered to the output shaft) to the input power (power supplied to the input shaft). For example, suppose a gear system has an efficiency of 90%. In that case, this indicates that 90% of the input power is effectively transmitted to the output, with the remaining 10% being lost as heat or other forms of energy loss.

[38] Copper (2003), in his thesis "Efficiency and Friction of Plastic Cylindrical Gears," delved into the efficiency and friction characteristics of plastic cylinder gears, incorporating MK II test rig experiments. The study referenced the load efficiency equation employed by various researchers:

$$\eta_{Copper} = \frac{T_{in}}{T_{motor}} \times 100 = \frac{(F_1 - F_2)\, d_l \omega_f}{4\, m\, g\, r_p} \times \tan \Psi$$

[117] Anderson & Loewenthal (1979) presented power-loss statistics, predicted by their own, Shipley's, Buckingham's, Merritt's, and Chiu's equations, in Figure 3.11. This figure demonstrates gearset efficiency against torque at constant speed values. These efficiency losses are further detailed in Table 3.1, referencing the sliding and rolling losses equations.

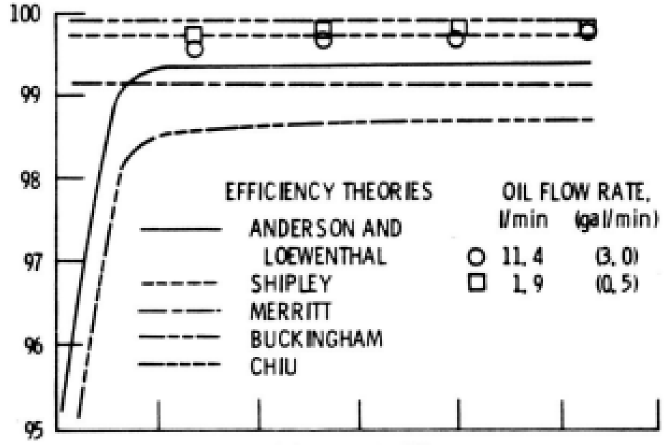

(a) Pinion speed, 250 rpm.

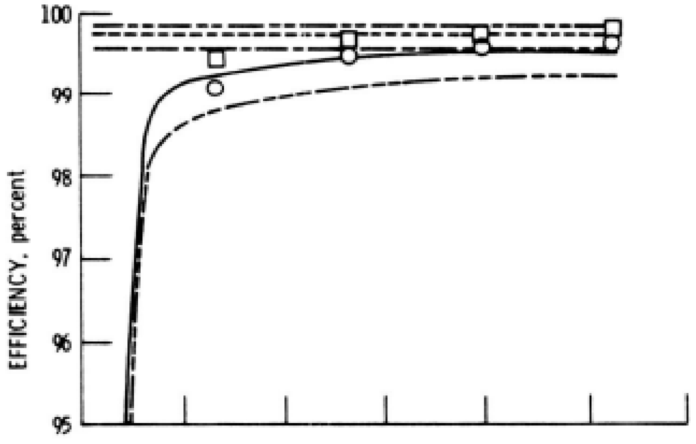

(b) Pinion speed, 1000 rpm.

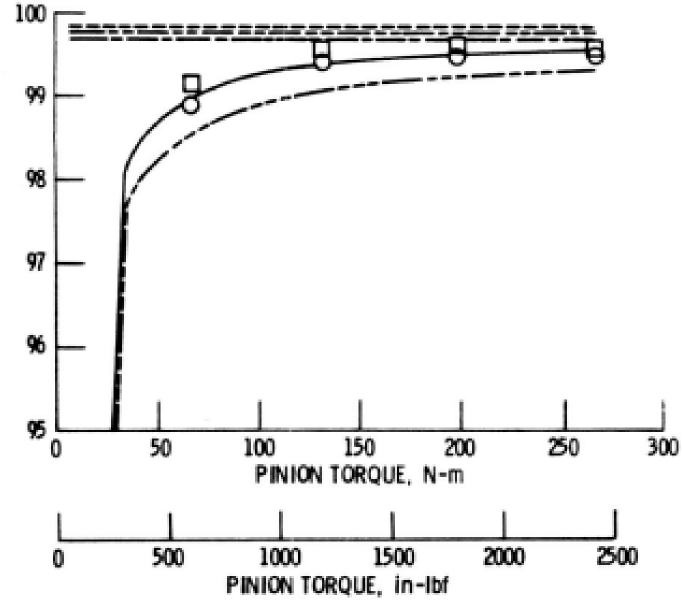

(c) Pinion speed, 2000 rpm.

Figure 3. 12 *Predictions for Gearset Efficiency Compared to Fletcher and Bamborough's Data (adapted from, [117])*

Table 3. 1 *Percent Efficiency Losses References the Sliding and Rolling Losses Wquations*

	Formulae	Functional Details
[71]	$\eta_B = 1 - \mu_B(t) \cdot \left[\frac{\left({\vartheta_{s_a}}^2 + {\vartheta_{s_r}}^2\right) \cdot \left(1 + \frac{1}{m_g}\right)}{\left(\vartheta_{s_a} + \vartheta_{s_r}\right)}\right]$	During the approach and recess
[118]	$\eta_C = \left[1.54 \times 10^{-5}(\sigma + 0.55) W_P {v_p}^{1/2}\, \rho-^{1/2}\mu-^{1/8} I_1\right] - \left[(1.43 \times 10^{-3}) \sin^2\theta v_p E'\rho F I_2 \left(\frac{\mu v_p}{E'\rho}\right)^{0.71}\right]$	A method of calculating the average loss along the line of contact by numerically integrating the instantaneous values of sliding and rolling loss.
[61]	$\eta_M = 1 - \ \mu_M(t) \cdot \frac{\sec\varphi}{\left[\left(\frac{d_p d_g}{d_p + d_g}\right)\left(\frac{l_p + l_w}{{l_p}^2 + {l_w}^2}\right)\right]}$	At a location that is situated in relation to the pitch point, base pitch along the path of contact, diametral pitch, contact ratio, and tooth loading, power loss is assessed.
[117]	$\eta_{A\&L} = 2.82 \times 10^{-7}(1.54 \times 10^{-5}$ $\left(1 + 2.3\frac{F}{r_p}\right) n_p^{2.8} r_p^{4.6}(0.028\mu + 0.019^{0.2})$	By numerically integrating the instantaneous values of these losses throughout the path of contact, the sliding and rolling losses were computed.
[119]	$\eta_{A\&L} = \frac{50f}{\cos\theta}\left(\frac{H_S^2 + H_r^2}{H_S + H_r}\right)$ H_S and H_r are specific sliding of approach and recess, respectively.	This approach includes account for sliding loss but not rolling loss.

3.5 Tooth Gear Deformation

Gear bending deformation, a result of stress and strain behaviours, leads to increased wear, termed the viscoelastic hysteretic effect [39]. Temperature increases influence this deformation due to mechanical loads and changes in the stiffness of polymer materials.

In gear deformation analysis, the action tangent plane and the coordinates (x, y, z) are calculated using vector methods, which relate to varying meshing over time [120], as illustrated in Figure 3.5.1.

$$x_i(t) = \ r_b\left[(\emptyset_{b_i}(t) + \emptyset_{C_i}) \cos\emptyset_{b_i}(t) - \sin\emptyset_{C_i}\right]$$

$$y_i(t) = r_b\left[\cos \emptyset_{b_i}(t) + (\emptyset_{b_i}(t) - \emptyset_{C_i}) \cos \emptyset_{b_i}(t) - \cos \emptyset_{C_i}\right]$$

The approximate coordinate, $z_i(t) \approx 0 - 0.5\ mm$ to the shifted of gear.

Jabbour et al. (2021) described teeth deformation under load impact in plastic gears. They established teeth *i1* and *i2* along the contact path line on teeth *k1* and *k2*, illustrating the strain on the driving gear caused by the rotation of an angle *Du* due to the deformation of teeth *i1* and *i2* [121].

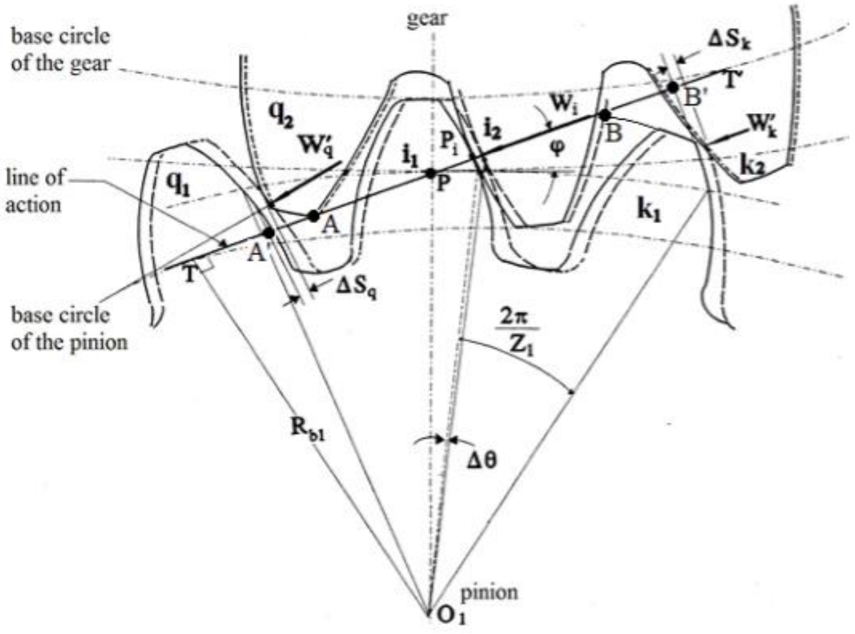

Figure 3. 13 *Bending Deformation of Tooth Wear (adapted from, [121])*

Figure 3.13, the coordinate distance *x* reflects the effects of tooth bending deformation in millimetres. The loading angle, $\emptyset_{bi}$ is based on the standard theory of AGMA 908-B89 and is determined by:

$$\emptyset_{bi} = \tan\left[\left(\frac{r_b}{r_o}\right)^2 - 1\right]^{-0.5} - \left[inv\ \emptyset_n + \frac{t_i}{2}\right]$$

$$inv\ \emptyset_{ci} = inv\ \emptyset_{ti} + \frac{t_i}{2}$$

$$t_i\ = \frac{\pi}{2} + 2(x - \Delta t_n)$$

the pressure angle $\emptyset_{ci}$ at the root of the gear teeth (*degrees*) and the normal circular tooth thickness t_i with references at the pitch point (*mm*).

3.6 Hysteresis Effect

[62] Doll, Verdesca, Bastos, Osswald, & Kleiss (2015) explored the hysteresis effect, which occurs when the deformation or stress response lags behind the applied load or strain. Hysteresis can lead to energy losses, heat generation, and time-dependent behaviour during gear operation in polymer gears. By incorporating hysteresis effects into simulations, engineers better represent the gear's performance, including potential fatigue or wear characteristics. The hysteresis energy values can be quantified based on these analyses, providing insights into polymer gears' material and design choices.

$$H = \frac{Energy_{Loss}}{Total\ Energy}$$

For each element each cycle, the highest value of the strain energy density is obtained to compute the energy loss. This formula is based on the maximum strain energy density per revolution-element, denoted as ϵ_{max}.

$$Energy_{Loss} = H\ \epsilon_{max}$$

3.6.1 Heat Generation

[79] [62] Cerne, Duhovnik, & Tavcar (2019), and Doll, Verdesca, Bastos, Osswald, & Kleiss (2015) have discussed that in polymer gears, the viscoelastic behaviour and hysteresis effects result in energy dissipation in the form of heat. This heat generation occurs due to internal friction and molecular movements within the polymer material as it deforms during gear meshing and operation. Accurately assessing this heat generation is crucial for understanding the gear's thermal behaviour and potential impact on performance.

A significant source of heat generation is the sliding friction at the sides of the gear teeth. Cerne et al. have represented the heat generated by sliding friction using a formula involving pressure distribution *P*.

$$H_f = \mu \, P \, v_s$$

Doll et al. provide insights into the heat generated during a meshing cycle. Their equation factors in the pressure $P_C(t)$ and contact area $A_C(t)$ during the meshing process.

$$H_f(t) = \mu \int_o^t v_s \, \pi \, P_C(t) A_C(t) dt$$

where $P_C(t)$ and $A_C(t)$ are the pressure and area of contact, respectively.

This research uses a quasi-viscoelastic simulation methodology for polymer PEEK gears, employing ANSYS to incorporate the viscoelastic properties of the material into the simulation. This approach helps understand how the gear responds to different loading conditions over time, particularly for predicting heat generation due to hysteresis effects and other viscoelastic behaviours.

3.6.2 Viscoelastic Hysteretic Behavior

Temperature increases influence the viscoelastic hysteresis behaviour due to mechanical loads and changes in the stiffness of the polymer material. This is covered in the works of Copper (2003) [38], Curà, Mura, & Gravina (2013) [10], and Merritt (1954), and involves bending deformation from stress and strain behaviours. Analysing the viscoelastic effect on structural-dynamic simulation provides a reasonable modulus of elasticity.

Doll, Verdesca, Bastos, Osswald, & Kleiss (2015) analysed polymer gears for the viscoelastic effect on structural-dynamic simulations, aiming to derive a reasonable modulus of elasticity [62]. The strain and temperature increase rate in viscoelastic hysteresis requires dynamic mechanical analysis and simulation. The temperature on the tooth flank surface is calculated from the maximum flash temperature rise ($T_{f,max}$),

$$T_{f,max} = T_b + \frac{1.11\, \mu\, F_t \sqrt{\delta_{Ti}} \left|V_{rp} - V_{rg}\right|}{L_i k_i \sqrt{\omega} \left|\sqrt{V_{rp}} + \sqrt{V_{rg}}\right|}$$

$$\sqrt{\delta_{Ti}} = \frac{k_i}{b_i}$$

$$b_i = \sqrt{k_i\, \rho_i\, C_{pi}},$$

Using a factor of 1.11 for the semi-elliptic contact pressure distribution and considering the contact width ω based on Hertz theory. Peclet numbers and Blok's equations (Blok, 1963) are also used in this context [58],

$$L_i = \frac{V_i\, \omega}{4\, \delta_{Ti}} = \frac{V_i\, b}{2\, \delta_{Ti}}$$

The mean flash temperature for polymer gear pairs T_{fm} is considered for determining the meshing teeth temperature in bulk temperature for lubrication tests [116]

$$T_b = 0.41T_{fm}$$

3.7 Crack Propagation

The various equations presented are crucial for theoretical calculations in six key areas: meshing behaviour of contact extension, tooth wear and thermal characteristics prediction, viscoelastic hysteretic behaviour, un-normal contact path and progressive contact, dynamic frictional effects & coefficient of friction, and fatigue fracture – initial and crack growth. Understanding these aspects is vital for predicting and mitigating issues like crack propagation in polymer gears, ensuring their reliability and longevity in practical applications.

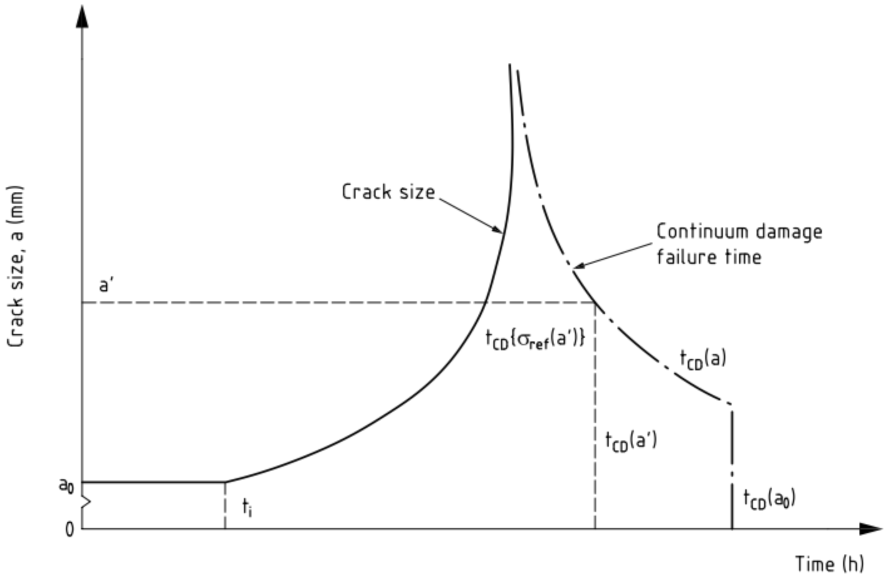

Figure 3. 14 *Schematic Illustrating Crack Behavior Under Constant Load at High Temperature (adapted from, [102])*

The equations mentioned throughout the chapter are integral to various steps in gear design, culminating in a comprehensive research process from start to finish. The standard references included are ISO/BS 6336 1-20, ISO/BS 6168, VDI 2736, DIN 3990-3, AGMA 2001-B88, AGMA 908, and AGMA 2101. BS 7910 (2015) [102] explores the cracking behaviour in components subjected to constant loading but increasing temperatures. This behaviour is schematically depicted in Figure 3.14, showing the crack's progression under these conditions.

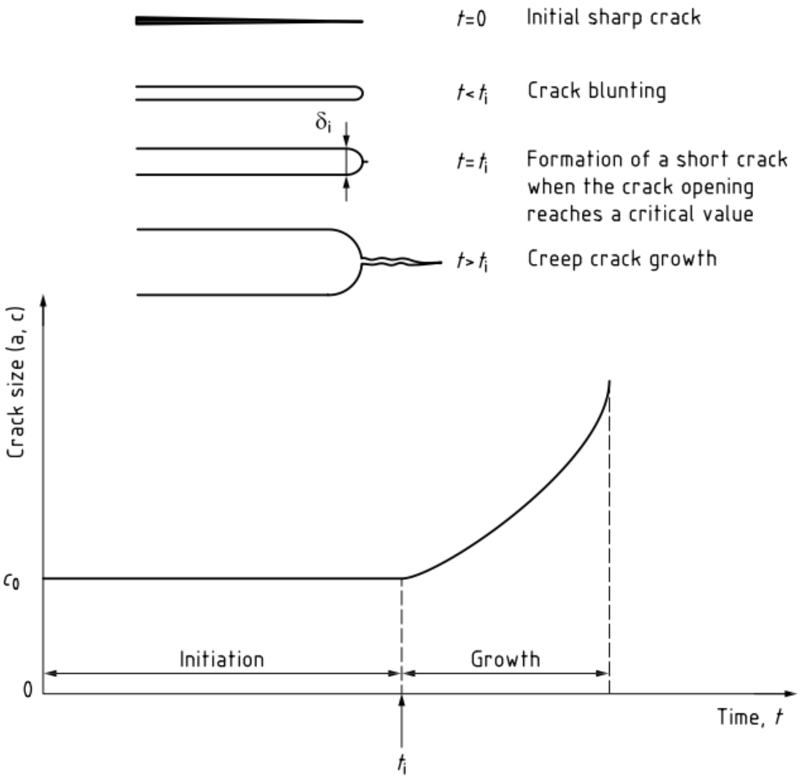

Figure 3. 15 *Illustrates Crack Growth and Failure Circumstances Schematically (adapted from, [102])*

The initial phase of crack growth can account for a significant portion of the gear's lifespan, Figure 3.15. A crack extension of up to 1 mm is commonly recommended for predicting initiation duration. Failure can occur prematurely due to plastic collapse or brittle fracture if the crack length reaches an unacceptable limit for the given load.

[122] In 2022, Yang et al. introduced the concept of a spatial crack in gear teeth, which propagates in depth, width, and height, Figure 3.16. This model more closely represents real-world scenarios compared to the oversimplified uniform and non-uniform crack models.

A spatial crack forms a three-dimensional surface, requiring a comprehensive model that considers depth, angle, length, and height for calculating varying times of mesh stiffness.

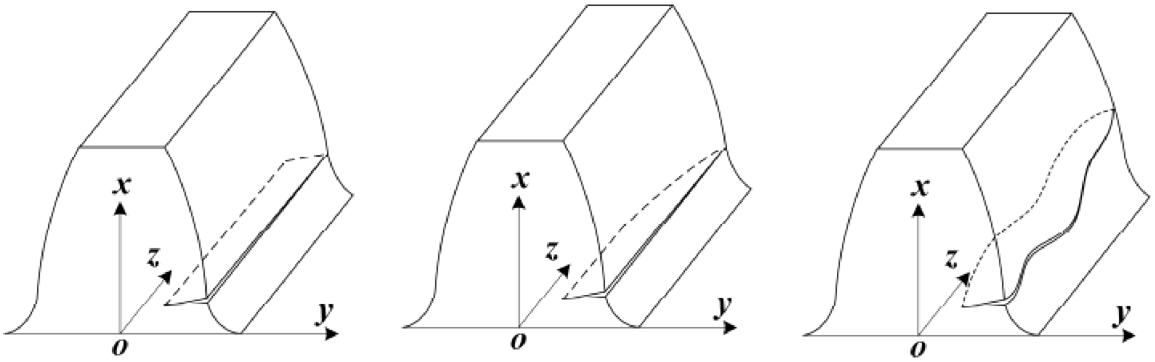

(a) Uniform-Crack *(b) Non-Uniform Crack* *(c) Spatial-Crack*

Figure 3. 16 *Tooth Crack Types (adapted from, [122])*

3.8 Stress Distribution at Initial Crack-Tip

Kinloch A. J. and Young R. J. (1983) reported on the fracture behaviour of polymers. Internal friction and thermal viscosity behaviour occur when molecular chains alter their conformations, allowing polymer segments to slide past one another. This thermal viscosity is highly temperature-dependent and is explained by considering the flow rate viscosity of polymer materials [86].

The stress amplitude versus logarithm cycles-to-failure (S-N) curves represents the cyclic life, which increases with decreasing stress amplitude. In the intermediate stress range, there is an approximately linear relationship between stress amplitude and the logarithm of the cycles-to-failure, an example of which is shown in Figure 3.17.

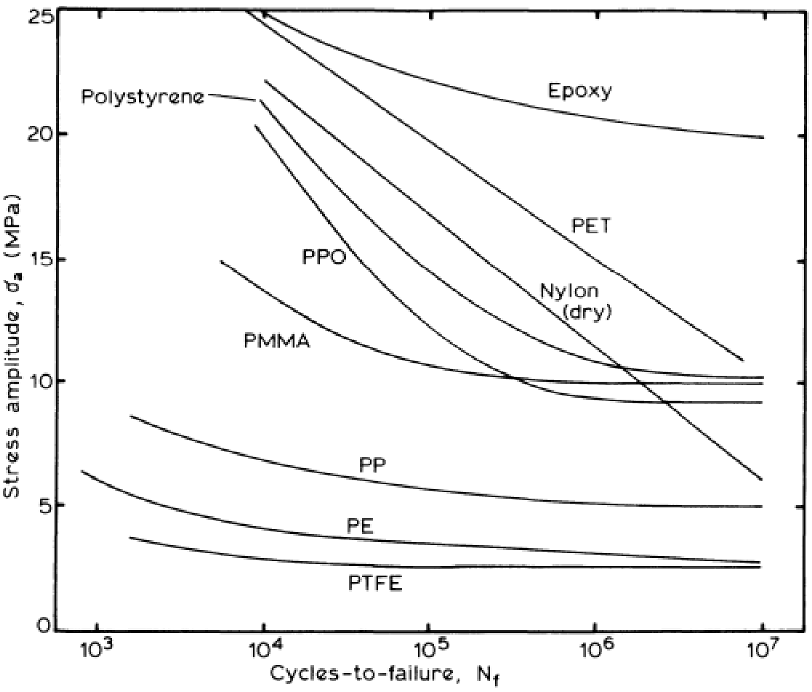

Figure 3. 17 *Tested Polymeric Materials' Stress Amplitude vs. Log Cycles to Failure (S-N) Curves (adapted from Riddell)*

3.8.1 Yield Von-Mises Criterion

[123] Sun & Jin (2012) discussed the yield Von-Mises criterion, which posits that material yielding occurs due to distortional deformation. In the context of linear elastic materials, the strain energy density (∈) is a crucial parameter. The energy stored in the material due to deformation is utilised to assess the onset of yielding. This criterion helps understand when and how materials under stress might begin to yield, providing crucial insights for designing durable and reliable gears.

The yield Von-Mises criterion determines yielding or failure by the strain energy density (∈)which varies based on the material and deformation conditions. This is calculated using Hook’s law, considering the following parameters:

$$\in = \frac{1}{12\exists}[(\sigma_1 - \sigma_2)^2 + (\sigma_2 - \sigma_3)^2 + (\sigma_1 - \sigma_3)^2] + \frac{1}{18K}(\sigma_1 + \sigma_2 + \sigma_3)^2$$

- K represents the bulk modulus, a material property that characterises resistance to volume change or dilatational deformation. The second term associated with K in the expression indicates the strain energy due to changes in volume within the material.

($\in_{cr}$) the distortional energy can be found using the shear modulus ∃ *(GPa)*.

$$\in_d = \frac{1}{12\exists}[(\sigma_1 - \sigma_2)^2 + (\sigma_2 - \sigma_3)^2 + (\sigma_1 - \sigma_3)^2] = \frac{1}{12\exists}\,(2\sigma_Y^2)$$

$$\in_{cr} = \frac{1}{6\exists}\sigma_Y^2$$

An arbitrary Cartesian coordinate system (x, y, z) determines the plastic zone along the crack line (x-axis) in an elastic-perfectly plastic solid with a Mode I crack.

$$\frac{1}{2}\left[\left(\sigma_{xx} - \sigma_{yy}\right)^2 + \left(\sigma_{yy} - \sigma_{zz}\right)^2 + (\sigma_{zz} - \sigma_{xx})^2 + 6\left(\sigma_{xy}^2 + \sigma_{yz}^2 + \sigma_{zx}^2\right)\right] = \sigma_Y^2$$

Initial stress calculations along the x-axis, based on the elastic K-field, help identify regions where plastic deformation occurs and provide insights into the extent of this deformation around the crack.

$$\sigma_{xx} = \frac{K_I}{\sqrt{2\pi x}} = \sigma_1, \qquad \sigma_{yy} = \frac{K_I}{\sqrt{2\pi x}} = \sigma_2$$

$$\sigma_{zz} = \sigma_3 = \begin{cases} 0\,, & plane\ stress \\ 2\,v\dfrac{K_I}{\sqrt{2\pi x}}\,, & plane\ strain \end{cases}$$

Tada, Paris, and Irwin (2000) provide comprehensive solutions for stress in (K_I) is crucial for understanding crack behaviour and its potential to propagate or cause failure in structures. In Irwin's plastic zone model, the stress distribution within the plastic zone alone cannot counterbalance the external load. Therefore, the material in the plastic zone yields, leading to stress redistribution outside the plastic zone to achieve equilibrium and maintain structural stability. This redistribution helps in effective load transfer and distribution within the material, as illustrated in Figure 3.18, [124].

$$\sigma_{yy} = \sigma_Y^* = \begin{cases} \sigma_Y\,, & plane\ stress \\ \dfrac{1}{1-2\nu}\sigma_Y\,, & plane\ strain \end{cases}$$

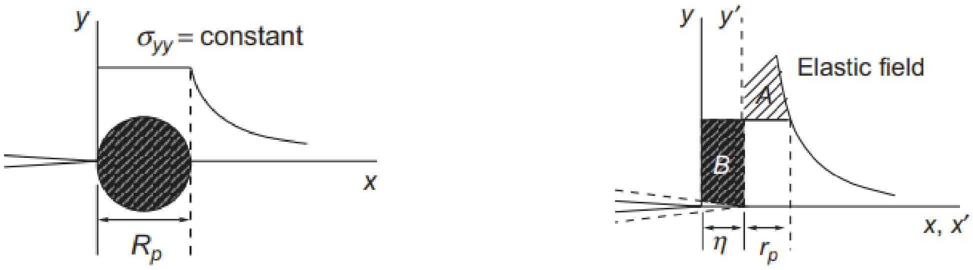

(a) Crack-Tip of Plastic Zone *(b) Fictitious Crack Tip*

Figure 3. 18 *Irwin's Plastic Zone Model (adapted from, [125])*

$$\int_0^{r_p} \sigma_{yy} dx - \sigma_Y^* r_e = r_e^* \sigma_Y^*$$

$$\frac{K_I}{\sqrt{2\pi x}}\sqrt{r_e} - r_e = r_e^* \sigma_Y^*$$

Thus, the plastic zone ball-size is followed by:

$$R_e = r_e + r_e^* = \frac{1}{\pi}\left(\frac{K_I}{\sigma_Y^*}\right)^2$$

For Irwin's model, planes of stress and stain are given by

$$r_e = \frac{K_I^2}{6\pi\sigma_Y^2}, \qquad r_e = \begin{cases} \dfrac{K_I^2}{2\pi\sigma_Y^2}, & plane\ stress \\ (1-2\,\nu)^2\dfrac{K_I^2}{2\pi\sigma_Y^2}, & plane\ stress \end{cases}$$

3.8.2 Mechanics of Linear-Elastic Fracture

Under linear-elastic fracture mechanics (LEFM), an initial yield crack for a small scale is described by Irwin's equation. The stress intensity factor is adjusted to account for plastic deformation near the crack tip by adding half the size of the plastic zone to the crack length. This adjusted factor helps describe fracture behaviour in materials that have experienced plastic deformation.

$$K_I = \sigma\sqrt{\pi(a + r_e)} = \sigma\sqrt{\pi\left(a + \frac{K_I^2}{2\pi\sigma_Y^2}\right)}$$

In a semi-infinite plate, the expression for the stress intensity factor in LEFM is used.

$$K_I = 1.1215\sigma\sqrt{\pi\left(a + \frac{K_I^2}{2\pi\sigma_Y^2}\right)} = \frac{1.1215\sigma\,\sqrt{\pi a}}{\sqrt{1 - 0.6289\,(\sigma/\sigma_Y^*)^2}}$$

When the applied stress (σ) compared to the yield strength-based reference stress (σ_Y^*) is significantly smaller ($\sigma/\sigma_Y^* < 1$), the adjusted stress intensity factor converges to the value predicted by LEFM.

3.8.3 Hydrostatic Stress-Hook's Law

Plasticity theories assume hydrostatic stress (uniform stress in all directions) does not induce plastic deformation, and volumetric deformation is purely elastic. This assumption has been validated through experiments with metals, particularly under mild deformation conditions. Consequently, volumetric and distortional deformations are treated as separate phenomena in plasticity.

In linear elastic materials, the relationship between volumetric strain e_k and hydrostatic stress σ_k, can be established using certain equations.

$$\sigma_k = 3Ke_k$$

and

$$\sigma'_{ij} = 2$$

These equations help understand how materials respond to stress regarding volume change and deformation characteristics.

In the context of Hooke's law, the values of i, j, and k represent the Cartesian coordinates 1, 2, and 3 (or x, y, and z). According to this law, the increments in elastic strain in a linear elastic material are directly related to increments in stress. The relationship is described by specific equations that correlate changes in strain with corresponding changes in stress.

$$de^e_{ij} = \frac{1}{2\exists}\left[d\sigma_{ij} - \frac{\nu}{1+\nu}\,\delta_{k,ij}\,d\sigma_{kk}\right]$$

The increments in elastic strain as follows

$$de^p_{ij} = \frac{3}{2}\,\sigma'_{ij}\,\frac{\frac{\sqrt{2}}{3}\left[\left(de^p_{xx} - de^p_{yy}\right)^2 + \left(de^p_{yy} - de^p_{zz}\right)^2 + \left(de^p_{zz} - de^p_{xx}\right)^2 + 6\left(de^p_{xy} + de^p_{yz} + de^p_{zx}\right)\right]^{1/2}}{\sqrt{\frac{3}{2}\sigma'_{ij}\sigma'_{ij}}}$$

The constitutive of elastic-plastic is:

$$de_{ij} = de^e_{ij} + de^p_{ij}$$

3.8.4 Paris's Law

The Paris law is a fundamental equation in material science, specifically used for describing the rate of fatigue crack propagation in materials. It establishes a relationship between the crack growth rate (da/dN) and the stress intensity factor (SIF) range ΔK, along with material constants C and m. This empirical law is vital for estimating the crack growth rate over time under cyclic loading conditions.

$$da/dN = C(\Delta K)^m$$

An increment in crack length [125] is calculated based on the fatigue life cycles, following the Paris law framework.

$$\int_o^{\Delta a} \frac{da}{C(\Delta K)^m} = \int_o^{\Delta N} dN = \Delta N$$

3.9 Vibration Responses

[126] Ma et al. (2015) conducted a study exploring the impact of different gear crack propagation paths on the vibration responses of a perforated gear system. Their analysis focused on the system's vibration behaviours when operating at a constant speed, examining how different crack propagation paths within the gear influence vibration patterns. This research provides valuable insights into the dynamic behaviour of gear systems under various crack scenarios. One common approach in mechanical fault detection is using statistical features like the Root-Mean Square (RMS) value. The RMS value is a mathematical method to quantify the overall magnitude of vibration, calculated as the square root of the mean of the squared values of vibration data points [127]:

$$RMS = \sqrt{\frac{1}{N}\sum_{n=1}^{N}(x(n) - \bar{x})}\ , \quad \bar{x} = \sqrt{\frac{1}{N}\sum_{n=1}^{N}\big(x(n)\big)}$$

To assess the vibration levels in a cracked gear system, the relative change of the cracked signal indicator (denoted as "r") is used, comparing "crack" and "health" states (cracked and healthy gears, respectively).

$$r_{RMS} = \frac{RMS_{crack} - RMS_{health}}{RMS_{health}} \times 100\%$$

Additionally, the percentage change in amplitude (Amp) within the frequency spectrum is employed as an indicator to evaluate the vibration level.

$$r_{Amp} = \frac{Amp_{crack} - Amp_{health}}{Amp_{health}} \times 100\%$$

3.10 Equation Summarizes

The research presented here studies the behaviour of gear tooth contact extensions within gear meshing. It scrutinises how various contact deformations, such as contact ratio, pitch point, contact lines, pressure angle, centre distance, and others, change in response to stress distribution and deformation analysis. The summarised results for the abbreviated equations, encapsulating the essence of this research, are presented in Figure 3.19.

This summary in Figure 3.18 provides a concise overview of the essential findings and mathematical formulations from the literature, offering a comprehensive basis of this research contained in this thesis.

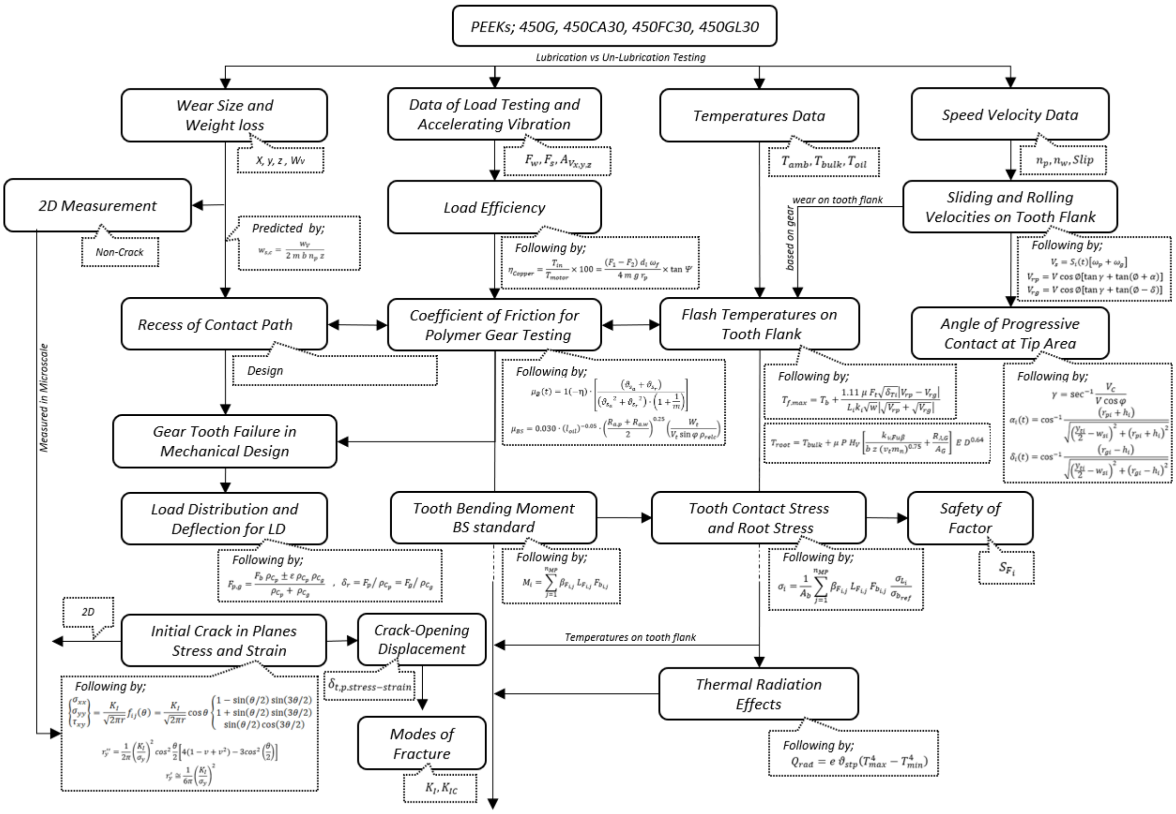

Figure 3.18: Summary of the Equations

3.11 Chapter Summary

Chapter 3 analysed gear theory, focusing on polymer gears and examining their design and operational aspects. It explored gear meshing behaviour, looking at contact deformations, pitch point contact, pressure angle, and centre distance. The chapter provided insights into spur gear geometry and discussed the application of polymer gears in torque transmission. Theoretical perspectives were integrated with practical applications, highlighting the importance of gear geometry, involute tooth profile, pitch, and backlash in gear operation and performance.

Chapter 4

Experimental Insights into Gear Meshing Dynamics: Load Tests and Wear Analysis in PEEK Steel Gear Meshes

This chapter focuses on experimental data related to load tests, thermal performance, and vibrations. The study investigates gear meshing involving different materials. A STEEL Grade 8 pinion, acting as the driver, engages with various PEEK materials for the wheel (450G, 450CA30, 450FC30, and 450GL30), all featuring a 20-degree pressure angle. Victrex's PEEK 650G with a 30-degree pressure angle is also examined. The tests, spanning 24 hours or 1.44 million cycles, assessed increased wear by measuring weight loss and tooth flank wear size. Data collection included surface temperature, acceleration vibration, load tests, and tooth wear.

4.1 Materials and Methods

4.1.1 Material Grades and Mechanical Properties

PEEKs, advanced engineering polymers known for exceptional properties, emerged in the 1980s and have become popular in industries requiring superior strength, durability, and thermal stability. PEEK, specifically from Victrex Company, conforms to the BS/ISO 6336 industrial standard for gear geometry design. Its mechanical properties enable adequate endurance of high thermal temperatures [128]. This study focuses on gear meshing with different materials: a STEEL Grade 8 pinion as the driver and various PEEK materials for the wheel (450G, 450CA30, 450FC30, and 450GL30) with a 20-degree pressure angle. Victrex's PEEK 650G, with a 30-degree pressure angle, is also included. Additionally, Victrex's PEEK 650G with a pressure angle of 30 degrees is considered.

Table 4. 1 *Physical, Thermal, and Mechanical Properties*

Physical, Thermal & Mechanical Properties	*Temperature Ref.*	*Unit*	*450G*	*450CA30*	*450FL30*	*450GL30*	*Standard Ref.*
Density		$kg\ m^{-3}$	1300.00	1400.00	1450.00	1510.00	ISO-1183
Coefficient of Thermal Expansion	Avg. below, 143 ℃	$\mu\ K^{-1}$	55.00	40.00	45.00	45.00	ISO-11359
	Avg. above, 143°C		140.00	100.00	115.00	110.00	ISO-11357
Viscosity		cP	350000	550000	675000	550000	
Poisson's Ratio (23°C)		N/A	0.3779				
Thermal Conductivity		$W/cm\ °C$	0.0029	0.0095	0.0085	0.003	ISO-22007-4
Isotropic Elasticity							
Tensile Modulus		GPa	4.00	28.00	13.00	11.50	ISO-527
Flexural Modulus		GPa	3.80	24.00	11.50	11.00	ISO-178
Tensile Yield Strength	275 ℃	MPa		50.00	35.00	35.00	ISO-527
	175 ℃			85.00	55.00	60.00	
	125°C			160.00	95.00	115.00	
	23°C		98.00	265.00	150.00	185.00	
Alternating Flexural Strength	275 ℃	MPa		65.00	45.00	50.00	
	175 ℃		19.00	130.00	80.00	80.00	ISO-178
	125°C		85.00	275.00	160.00	190.20	
	75°C		86.20				
	23°C		165.00	380.00	230.00	275.00	
Alternating Compressive Strength	200°C	MPa		70.00	45.00	55.00	
	120°C	MPa	70.00	200.00	110.00	160.00	ISO-604
	23°C		125.00	300.00	170.00	250.00	ISO-604
Izod Impact	Notched, 23°C	kJ/m^2	8.00	50/10.50	35/7.00	65/12.00	ISO-180
Charpy Impact	Notched, 23°C	J/cm^2	0.70	4.50/0.70	350/0.50	5.50/0.80	ISO-179

The investigation aims to replicate Kono's research [2], examining torque load (10.80 Nm) and speed (1,000 rpm) in unlubricated tests with four PEEK grades against a STEEL pinion gear. Victrex's PEEK 650G is similarly tested in a gear pair. Tables 4.1 and 4.2 and Figure 4.1 present a detailed overview of the four PEEK wheel grades, covering aspects like density, thermal properties, material strength, and initial isotropic elasticity.

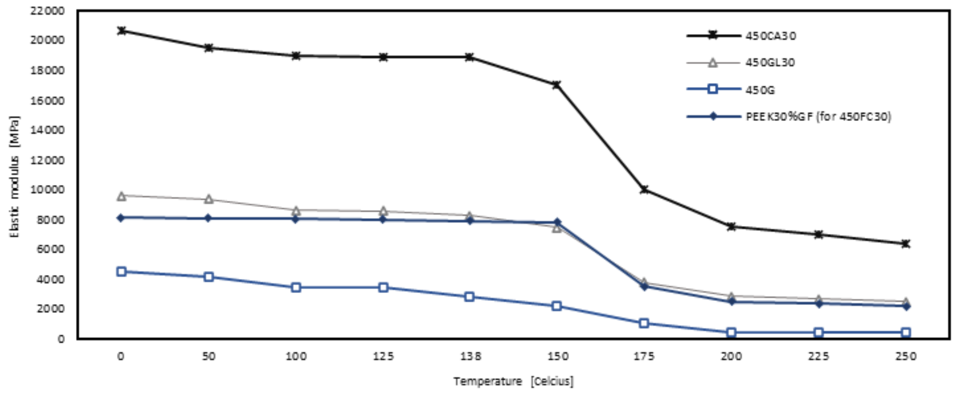

Figure 4. 1 *Flexural/Elastic Modulus vs Temperature for Four Grades of PEEKs, Referred to VICTREX® PEEK Materials and Plastic Technology (adapted from [129])*

Table 4. 2 *Mechanical Properties of PEEK 650G*

Physical, Thermal & Mechanical Properties	*Temperature Ref.*	*PEEK 650G*	*Unit*	*Standard Ref.*
Density		*1300.00*	$kg\ m^{-3}$	ISO-1183
Isotropic Secant Coefficient of Thermal Expansion	Avg. below, 143 ℃	*45.00*	$\mu\ K^{-1}$	ISO-11359
	Avg. above, 143℃	*125.00*		ISO-11357
Thermal Conductivity		*0.0029*	$W/cm\ °C$	ISO-22007-4
Isotropic Elasticity				
Tensile Modulus		*3.90*	GPa	ISO-527
Flexural Modulus		*3.60*	GPa	ISO-178
Tensile Yield Strength			MPa	ISO-527
Alternating Flexural Strength	175 ℃	*9.00*	MPa	ISO-178
	125℃	*16.00*	MPa	ISO-178
	75℃	*85.00*	MPa	ISO-178
	23℃	*155.00*	MPa	ISO-178
Alternating Compressive Strength	120℃	*65.00*	MPa	ISO-604
	23℃	*120.00*	MPa	ISO-604
Izod Impact	Notched, 23℃	*9.50*	kJ/m^2	ISO-180
Charpy Impact	Notched, 23℃	*1.00*	J/cm^2	ISO-179

Victrex's PEEK displays remarkable mechanical attributes such as high strength, stiffness, thermal stability, low friction coefficient, excellent wear resistance, chemical resilience, dimensional stability, electrical insulation properties, and lightweight nature. For detailed mechanical properties of PEEK 650G, refer to Table 4.2.

4.1.2 MARK II Test Rig.

The gear testing experiment utilises the MARK II master gearbox, consisting of an electric DC motor, an inverter motor controller, a load arm, and a loading mechanism, as shown in Figure 4.2. The MARK II gearbox contains two identical STEEL helical gears, each with 52 teeth, a 20-degree pressure angle, a 30-degree helix angle, and a 60 mm pitch diameter. To drive and load the master gearbox, 2.2 kW permanent magnet DC motors are used. The experimental analysis process, detailed in Figures 4.2 and 4.3, outlines the methodology for polymer gear testing.

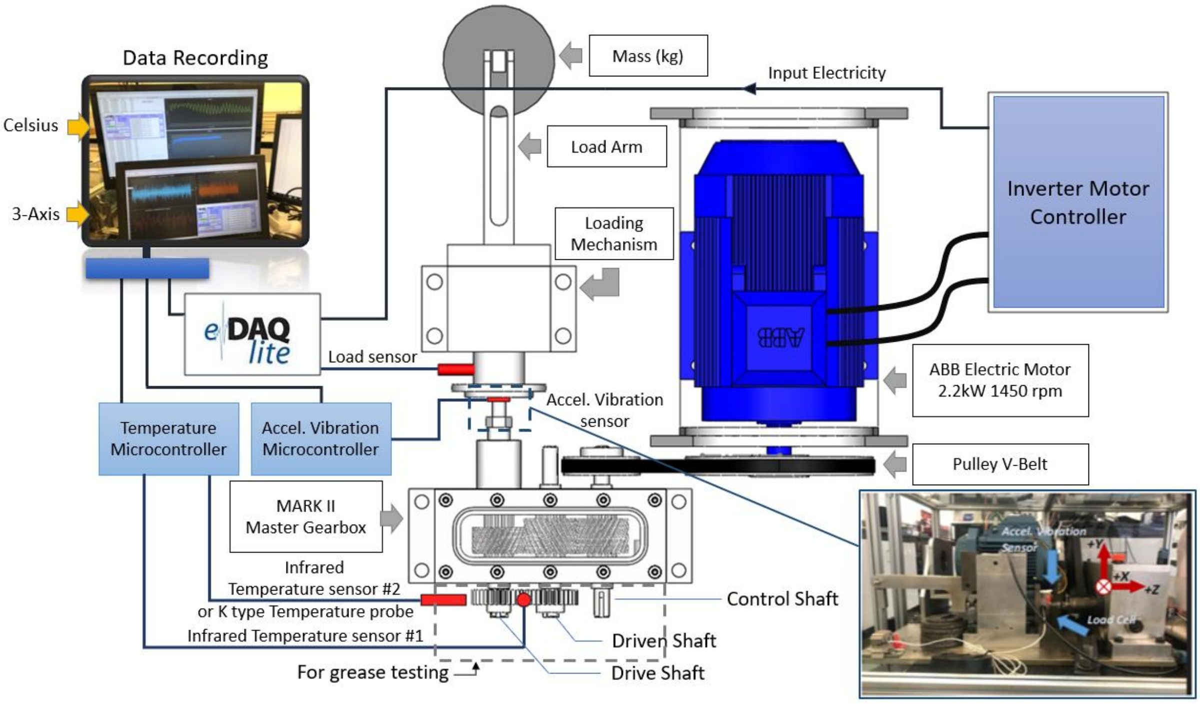

***Figure 4. 2** Schematic Diagram of MARK II Test Rig.*

The MARK II test rig's schematic diagram illustrates sensors used under dry conditions for data collection, including:

- An accelerometer measuring acceleration in three dimensions (x, y, z), where each significant bit represents ±1g (1g = 9.81 m/s²), mounted on a wheel shaft to monitor real-time vibration changes during tooth meshing under load.
- Infrared temperature sensors measure the initial and surface temperatures of tooth flanks in Celsius.
- A SoMat e-DAQ lite system monitoring the real-time resistive load on gear transmission in Newton units, complemented by a temperature probe (K-type) tracking grease temperature increase. Figures 4.3 and 4.4 show the positions of temperature and vibration sensors. The experiment calculates average initial and bulk temperatures on the tooth flank's width.

The temperature and vibration sensors' positions are shown, in Figures 4.3 and 4.4. The experiment calculates the average initial and bulk temperatures on the width-tooth flank.

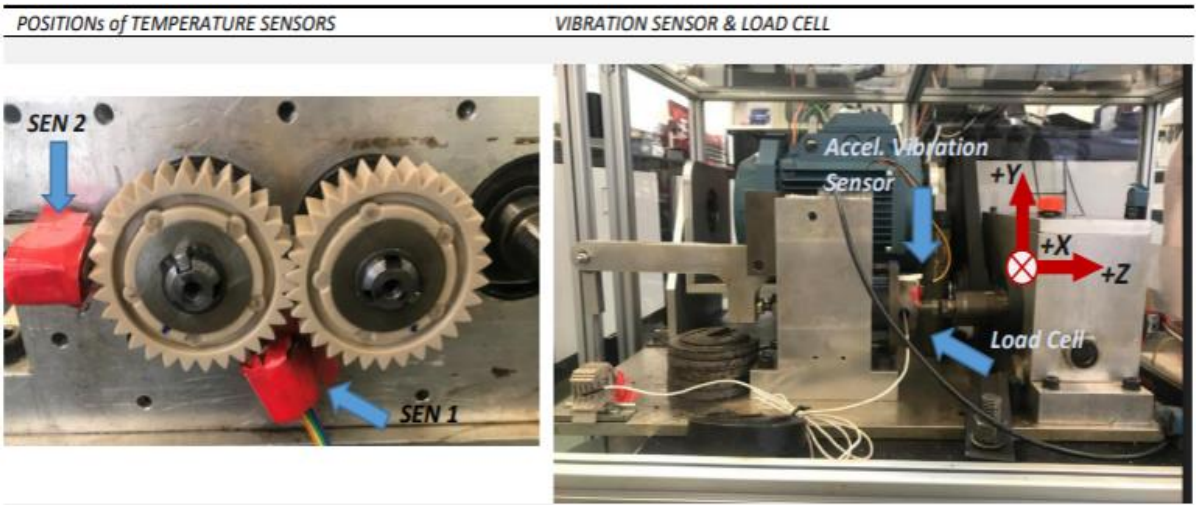

Figure 4. 3 *Temperature and Vibration Sensors' Positions on the MARK II Test Rig.*

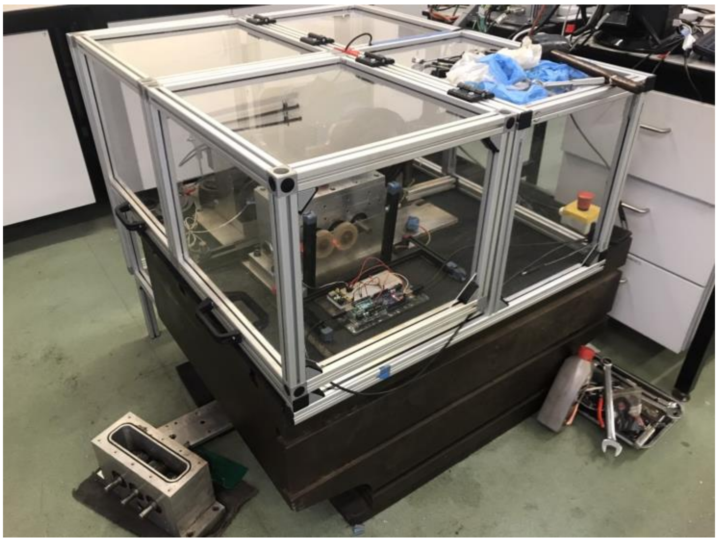

__Figure 4. 4__ Safety Enclosure of the MARK II Test Rig.

4.1.3 Gear Geometries

__Table 4. 3__ Gear Geometries and Specification of Test for PEEKs and STEEL G.8

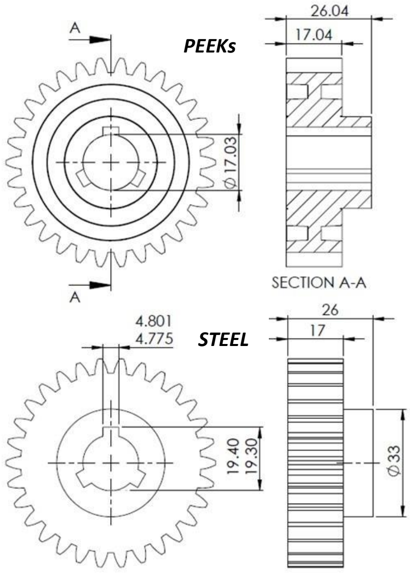

GEAR TESTING		***PEEKs (BS-PA20)*** **450G | 450CA30 | 450FC30 | 450GL30**	***STEEL*** G.8
MODULE	m	*2 mm*	
PRESSURE ANGLE	$\emptyset_1$	*20 Deg.*	
GEAR RATIO	m_w	*1:1*	
TOOTH NUMBER	N_p	*30*	
PITCH DIAMETER	d_g	*60 mm (±0.20)*	
Dia. of ADDENDUM	d_a	*64.00|63.60|64.00|64.00*	*63.95*
SHAFT DIAMETER	d_S	*17.03 (+0.02) mm*	*17.03 (+0.02) mm*
TOOTH THICKNESS Ref. on CIRCULAR	t_{ref}	*3.1016 mm*	*3.0616 mm*
TOOTH ROOTH CRITICAL	t_{cr}	*1.4321 mm*	*1.3895 mm*
Dia. of BALL CONTACT	d_{ball}	*59.8937 – 59.8084 mm*	
BASE DIAMETER	d_b	*~56.3816 mm (Test Measured)*	
TOOTH ROOT DIAMETER	d_r	*54.8901 mm*	*54.7802 mm*
Dia. of INVOLUTE TOOTH LIMIT AT ROOT	d_{INV}	*56.8293 mm*	*56.6900 mm*
Dia. of TOOTH ARC	d_{arc}	*58.4802 mm*	-
CENTRE DISTANCE for MARKII Rig. SETTING	C	*60.10 – 60.27 mm*	

**GEAR GEOMETRY REFERENCES Based design on ISO/BS 6336 and DIN 867*

The gear geometries involve a 20-degree pressure angle for PEEK450 versus STEEL Grade 8 and a 30-degree angle for PEEK460G. The number of teeth and gear ratio is tailored to specific gear applications, aiming for the desired speed reduction or increase. The gear teeth profile, designed with these pressure angles in mind, strives for optimal gear meshing and minimal friction. Tables 4.3 and 4.4 detail these gear specifications. Furthermore, Figures 4.5, 4.6, and 4.7 illustrate the meshing display for each gear pair.

***Table 4. 4** Gear Geometries and Specification of Test for Victrex's PEEK*

DRAWING for SHAFT DIA. & KEY	*Description*		
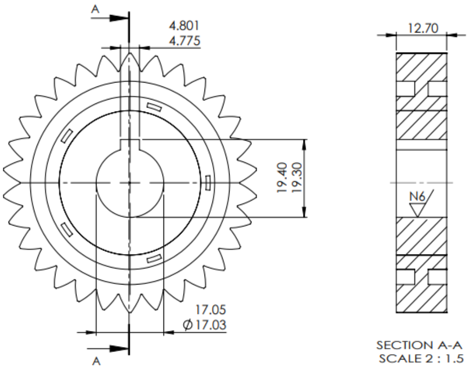	*GEAR TEST No.*		*2 and 3*
	GEAR WEIGHT	*pinion*	*93.7388 gram*
		wheel	*93.3302 gram*
	LOAD TEST	*Weight (Force)*	*4.6kg (180N)*
	SPEED	n_p	*~1000 rpm (11.3Hz)*
	SHAFT DIAMETER	d_S	*17.03 (+0.02) mm*
	OUTSIDE Dia. of HUB	d_H	*35.50 mm*
	GEAR RATIO	m_w	*1:1*
	TOOTH NUMBER	N_p	*30:30*
	No. of TOOTH	*3 vs 2 (pinion vs wheel)*	
	DATE of TEST:	*29-04-2021(start)*	
	END of TEST:	*18-05-2021*	
	MATERIALS:	*PEEK 650G vs PEEK 650G*	

PEEKs - 450G vs Steel G.8

PEEKs - 450FC30 vs Steel G.8

PEEKs - 450CA30 vs Steel G.8

PEEKs - 450GL30 vs Steel G.8

***Figure 4. 5** Meshing Display of 450G, 450CA30, 450FC30, and 450GL30 vs STEEL Grade 8*

Figure 4. 6 *Meshing Display of Victrex gears*

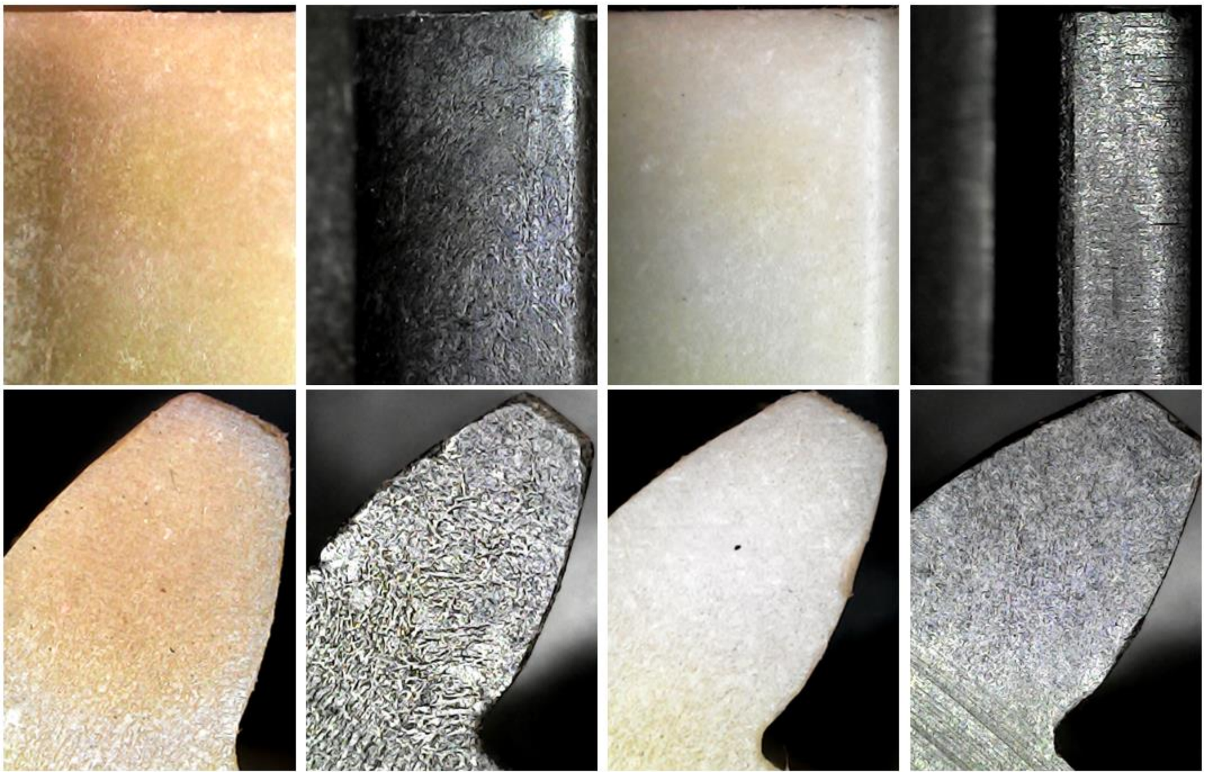

PEEK 450G PEEK 450FC PEEK 450GL PEEK 450CA

Figure 4. 7 *Gear Tooth Design for 450G, 450FC30, 450GL30, and 450CA30*

4.1.4 Numerical Model Set-Up and Test Methodologies

Table 4. 5 *Load Conditions Setting of MITs, 2021-2022*

Parameters	***Units***	***Values***
Weight Apply	*lb*	*10.10 (4.58 kg)*
Torque for Shaft Driving	*Nm*	*9.38*$^{(*)}$ *(~180 N)*
Frequency Drive	*Hz*	*11.30*
Speed Velocity (Output)	*rpm*	*998 (on Teeth)*
One Cycle (Time per Revolution)	*sec*	*0.05998*
Bending Moment Arm at Tooth Tip for Load Application, y_{bm}	*mm*	*3.76**
Nominal Load of Contact Line, F_n	*N*	*332.73**
Tangential Load in Plane of Action, F_t	*N*	*296.68**
Working Pressure Angle at Tooth Tip, φ_t	*Deg*	*26.92**

**Referenced by Kono's experiment* [3].

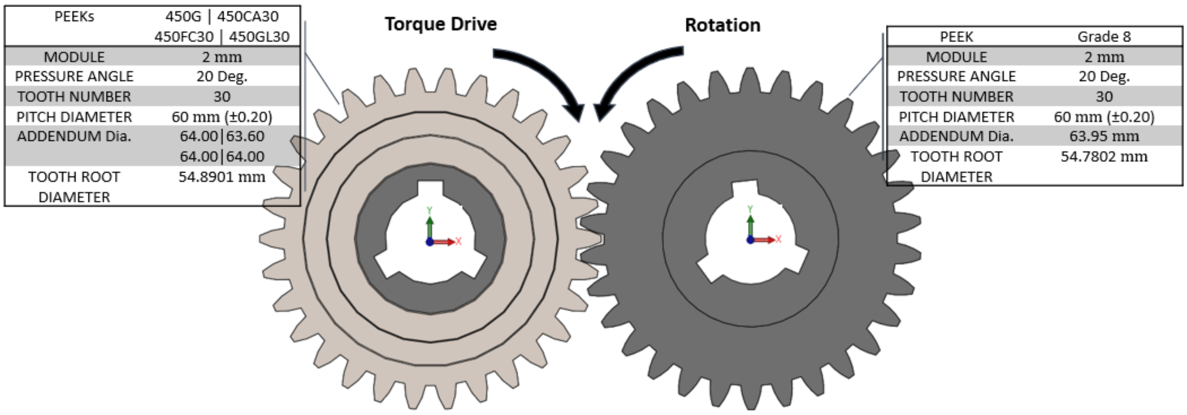

PEEKs	450G | 450CA30 450FC30 | 450GL30
MODULE	2 mm
PRESSURE ANGLE	20 Deg.
TOOTH NUMBER	30
PITCH DIAMETER	60 mm (±0.20)
ADDENDUM Dia.	64.00|63.60 64.00|64.00
TOOTH ROOT DIAMETER	54.8901 mm

PEEK	Grade 8
MODULE	2 mm
PRESSURE ANGLE	20 Deg.
TOOTH NUMBER	30
PITCH DIAMETER	60 mm (±0.20)
ADDENDUM Dia.	63.95 mm
TOOTH ROOT DIAMETER	54.7802 mm

Figure 4. 8 *Numerical Model Setup for PEEK and STEEL Grade 8*

This section outlines the numerical model setup for PEEK and STEEL Grade 8 gears, as depicted in Table 4.5 and Figure 4.8. It includes gear rotation direction and dimension specifications. The study applies a 9.38 Nm load under dry and wet conditions at a speed of 1,000 rpm for calculation and simulation analysis post-experimental design and workflow completion over failure cycles. Figure 4.9 presents a schematic diagram of the test methodologies conducted every 24 hours or 1.44 million cycles, examining enhanced wear characteristics. These tests evaluated tooth flank wear by measuring weight loss and wear size. Data on teeth wear, including weight loss and tooth flank wear size, were collected.

Finite Element Analysis (FEA) simulations were conducted explicitly for Dynamic Structural analysis with Transient effects. The analytical approach involved theoretical analysis of tooth wear behaviour, accounting for geometric alterations in involute gear teeth and meshing discrepancies. Predictions were made for contact pressure interface, stress distribution expansion, equivalent elastic strain, and tooth bending deformation behaviours.

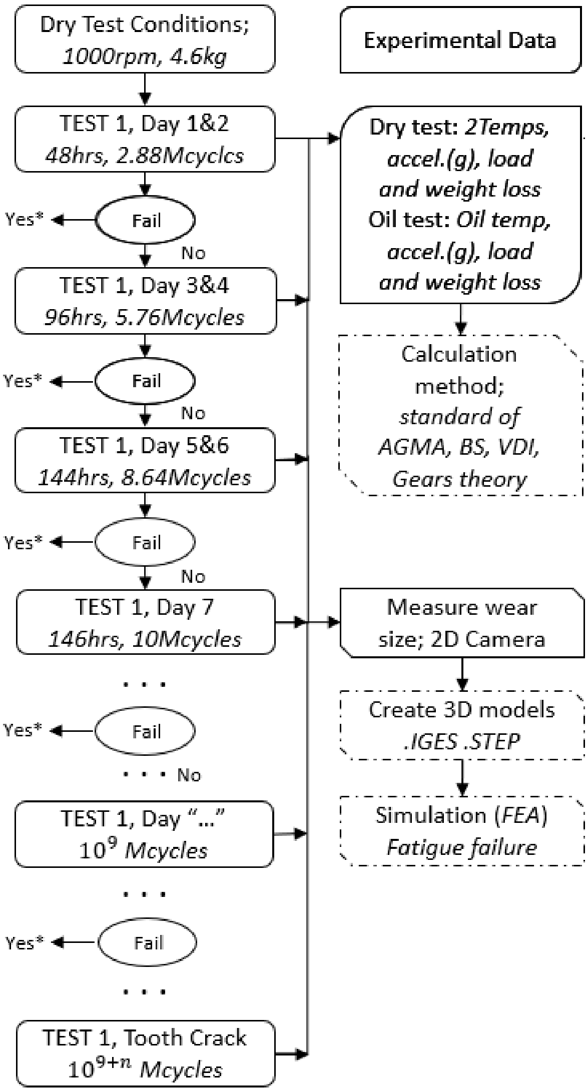

Figure 4. 9 *Schematic Diagram of the Test Methodologies*

4.2 Experimental Data

The research involved 24-hour or 1.44 million cycle tests, evaluating increased wear through weight loss and tooth flank wear size. Data collection encompassed surface temperature, acceleration vibration, load tests, and teeth wear.

4.2.1 Surface Temperature Data

Experimental data from real-time tests tracked temperature changes for four grades of PEEK wheel materials over 10 million cycles. During the test, heat loss through convection and radiation affected the temperature of the surrounding tooth area. Figures 4.10 and 4.11 present temperature data collected throughout the test, ranging from the initial temperature at engine start (16.98 - 28.04 Celsius) to the bulk temperature (T_b) maintained up to 10 million cycles (167 hours). Data collection occurred during an overnight test lasting 20 - 24 hours (equivalent to 72,000 - 86,400 seconds). Over this period, temperatures gradually increased over the first 3-5 hours, stabilised to a steady state, and eventually plateaued, reflecting the gear teeth surface temperature. Results consistently demonstrated that grade 450G exhibited higher temperatures than 450FL30, 450CA30, and 450GL30, respectively.

Transmission efficiency and friction coefficients were compared to theoretical predictions and initial performance over 10 million cycles. Load tests and comparisons of the four PEEK wheel grades enabled the calculation of gear transmission efficiency percentages. Notably, grade 450CA30 exhibited a lower coefficient of friction, approximately 0.2461, while maintaining efficient power transmission. Conversely, the most significant friction coefficient increase and transmission efficiency reduction were observed in the heavily worn teeth of 450GL30. Similar increases in friction coefficients were also noted for 450G and 450FC30.

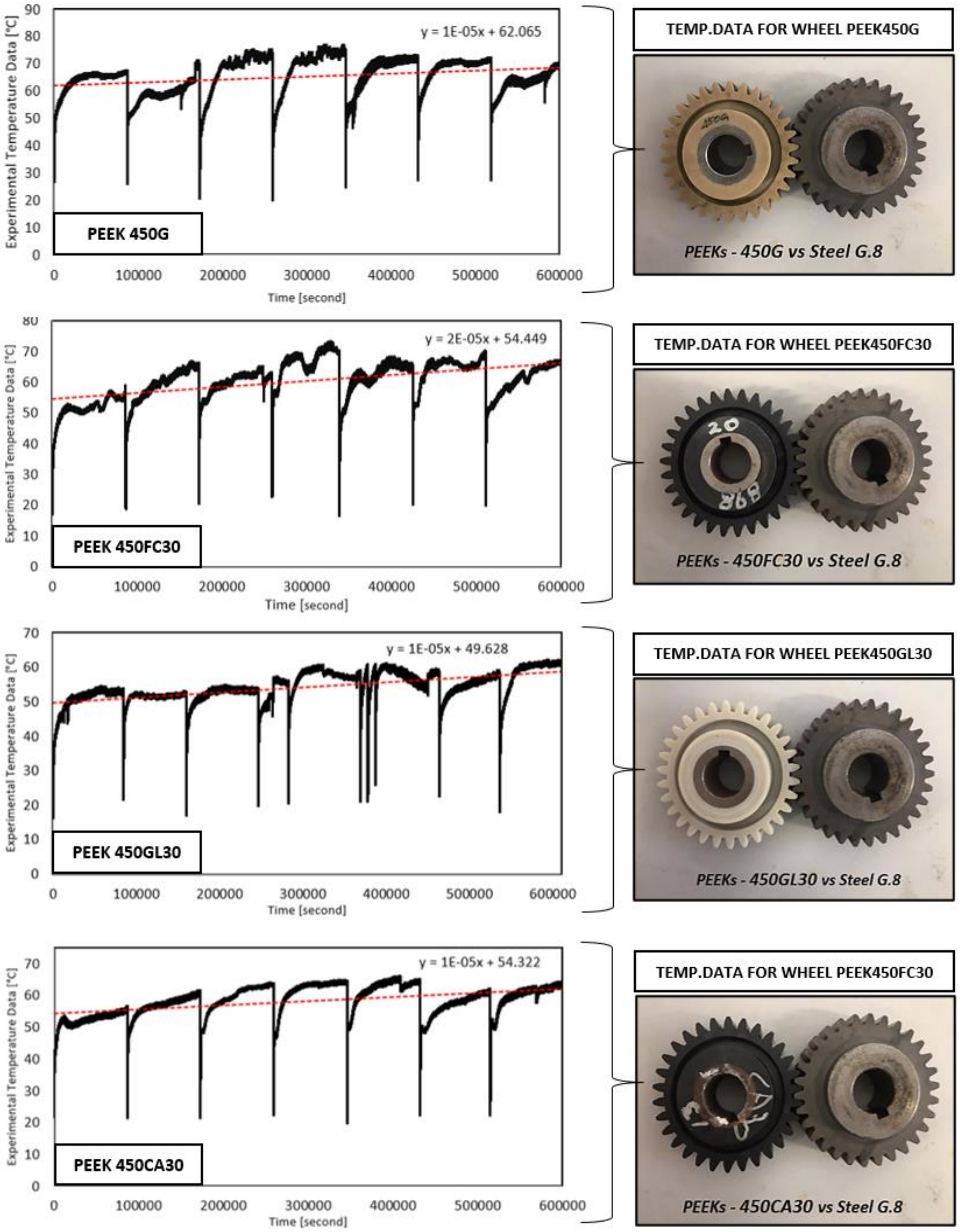

Figure 4. 10 *Time (Seconds) Averaged Temperature Measurements on Wheel Teeth Flanks*

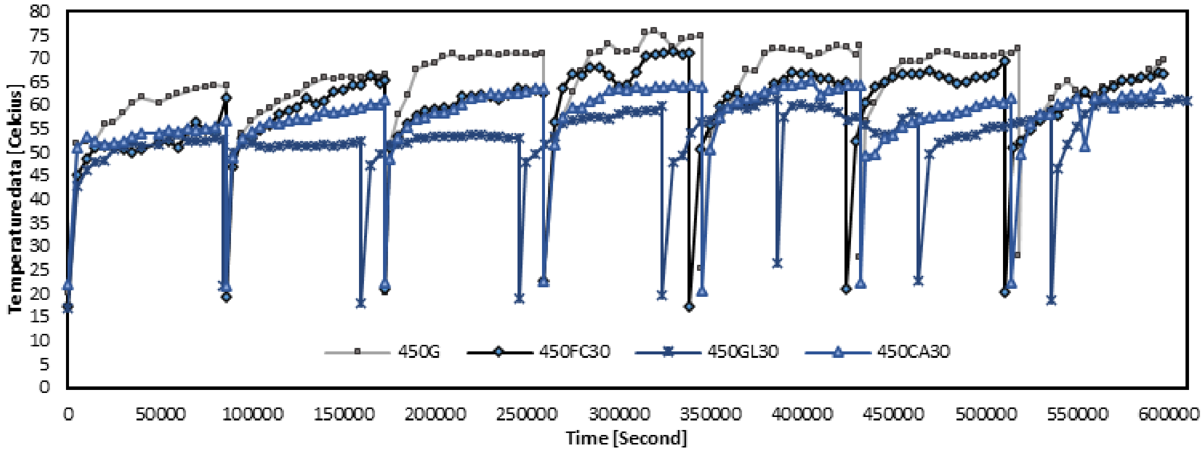

Figure 4. 11 *Bulk Temperature on Width-Tooth Flank, Due to 10.8 Nm of Torque and 1,000 rpm*

4.2.2 Wear Losses

a. Wear Geometries of Wheel Polymer at 10 Million Cycles

The wear geometries of the polymer wheel at 10 million cycles were thoroughly analysed using two-dimensional and three-dimensional involute curve sketches. The 3D geometries were modelled by approximating the involute curve, considering factors such as volume loss, weight loss, and the density of the PEEK material. Wash measurements were conducted using a Pylon micro-camera (PylonC) with high precision (ranging from 0.01 mm – 0.1 μmm) to enhance tooth impression techniques. This data was instrumental in generating two-dimensional and exporting three-dimensional involute curve representations of the worn teeth.

Figure 4.12 illustrates changes in tooth shape detected using a Pylon C camera. This camera was employed to identify surface defects on the teeth of the PEEK wheel, as shown in Figure 4.13. Key positions such as "Tip-Circle, Highest-Point of Single-Point Contact (HPSTC), Lowest-Point of Single-Point Contact (LPSTC), and Base Circle" are highlighted.

The collected tooth wear data facilitated the creation of three-dimensional representations of the worn teeth. Measurements of wear distance in two dimensions were undertaken using 2D and 3D programming designs. Consequently, predictions of volume and weight losses are presented in Figure 4.14, based on the methodology referenced by Kono (2003) [2]. Figure 4.15 provides an example of load sharing along the tooth flank when e < 2, showing that the bending moment due to an un-shared load at HPSTC is 1.42 times greater than that of a shared load at the tip.

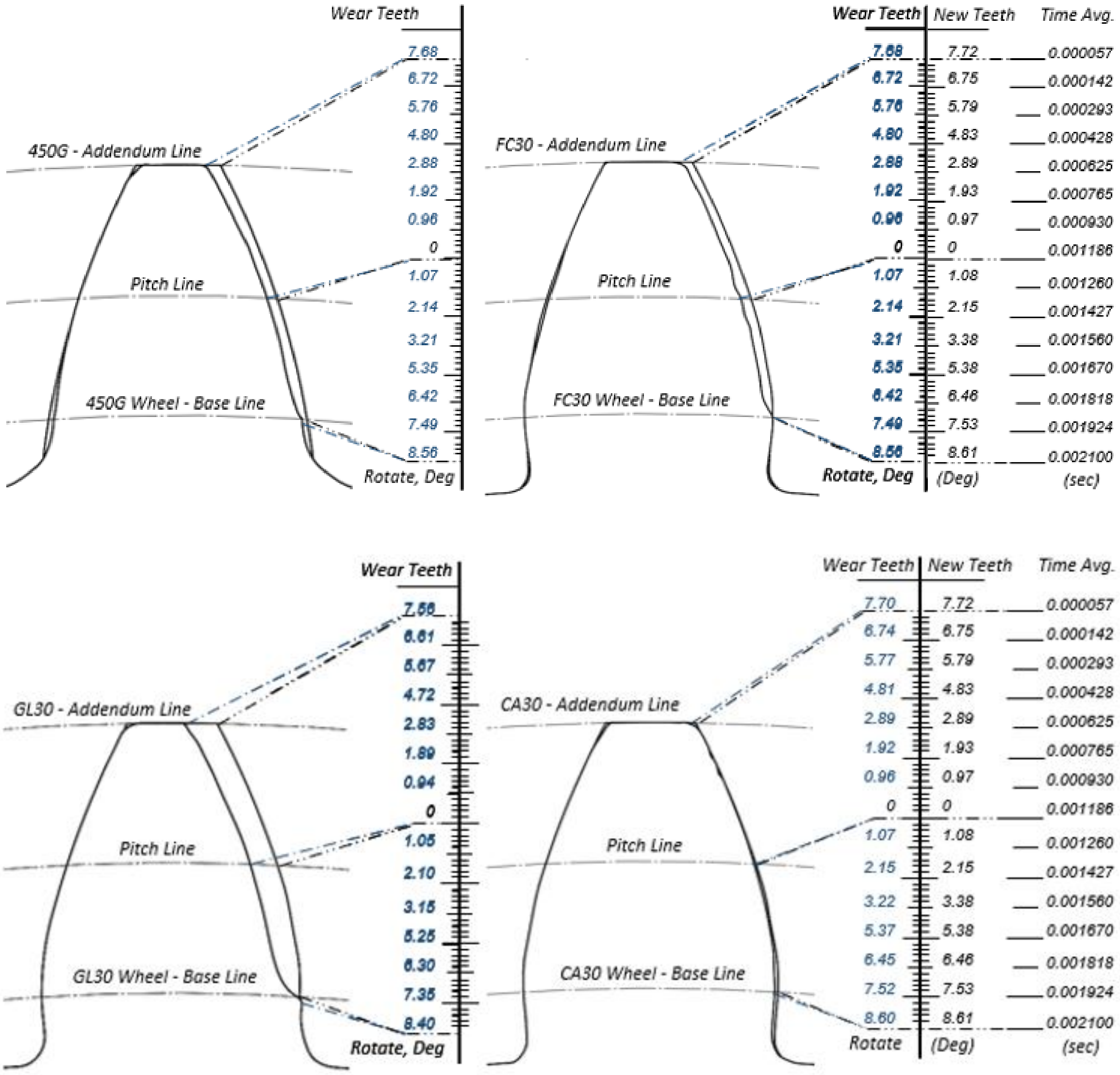

Figure 4. 12 *Line-Sketch of a 2D Involute Curve on Wear*

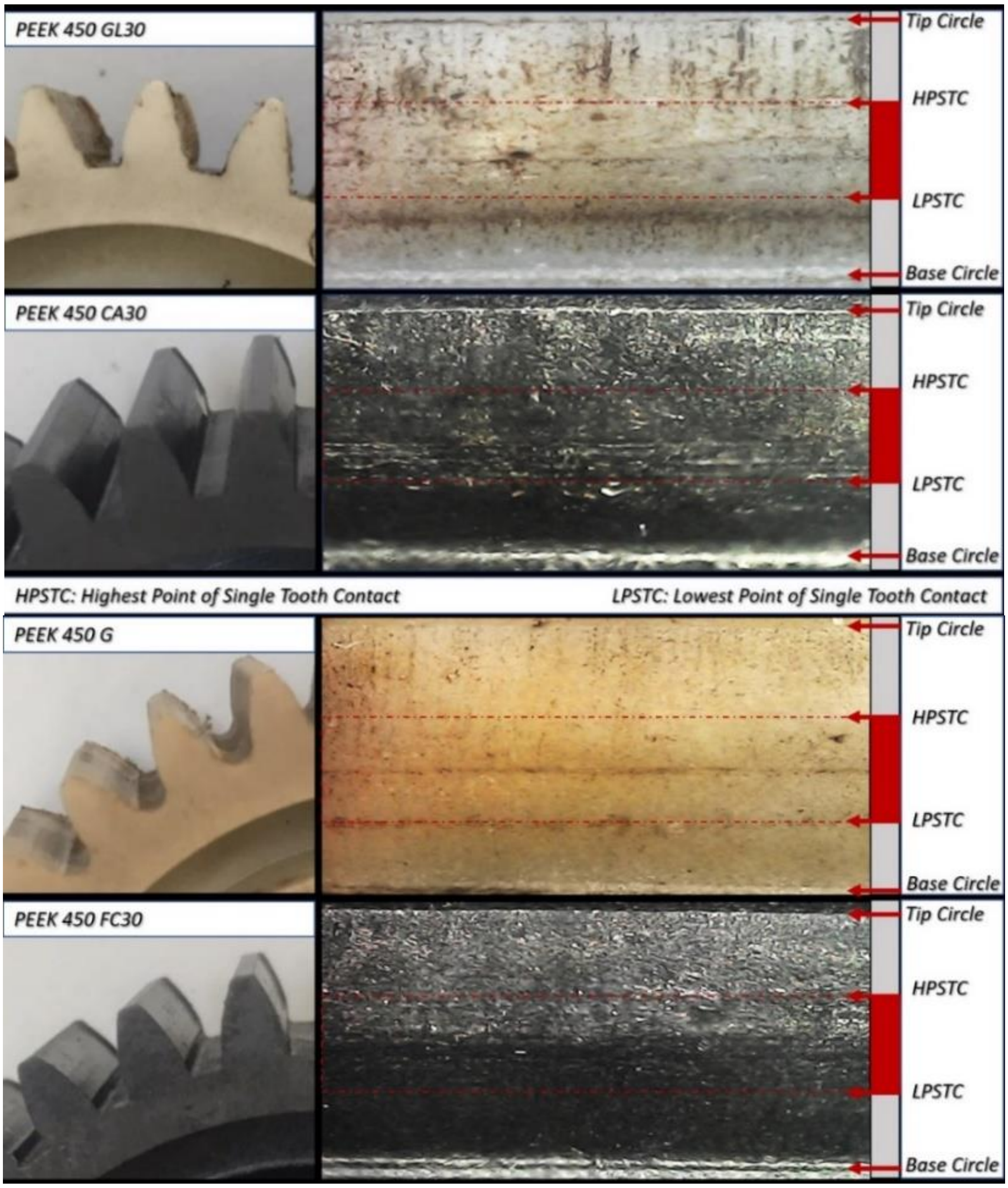

Figure 4. 13 *Tooth Surface Failure Using Micro-Camera, at 10 Million Cycles*

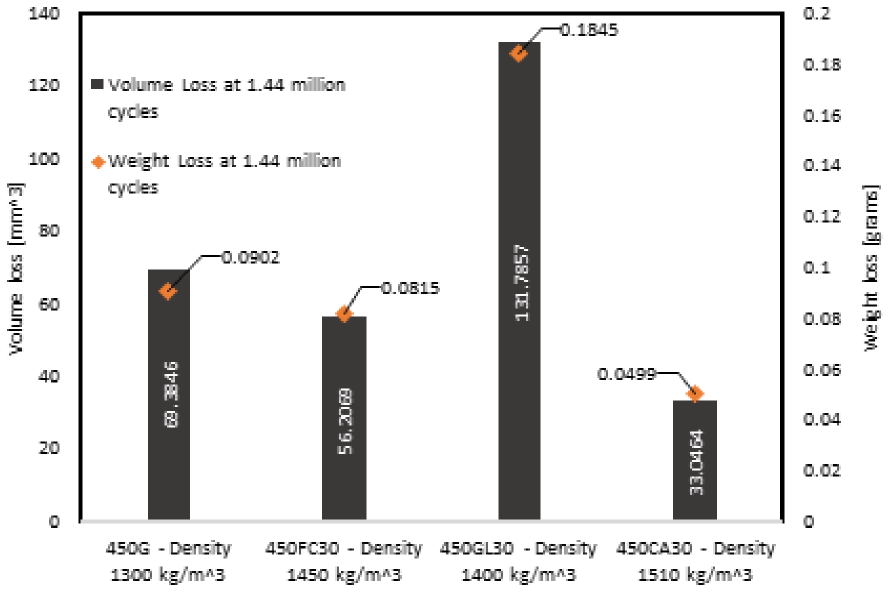

(a) At 1.44 million Cycles

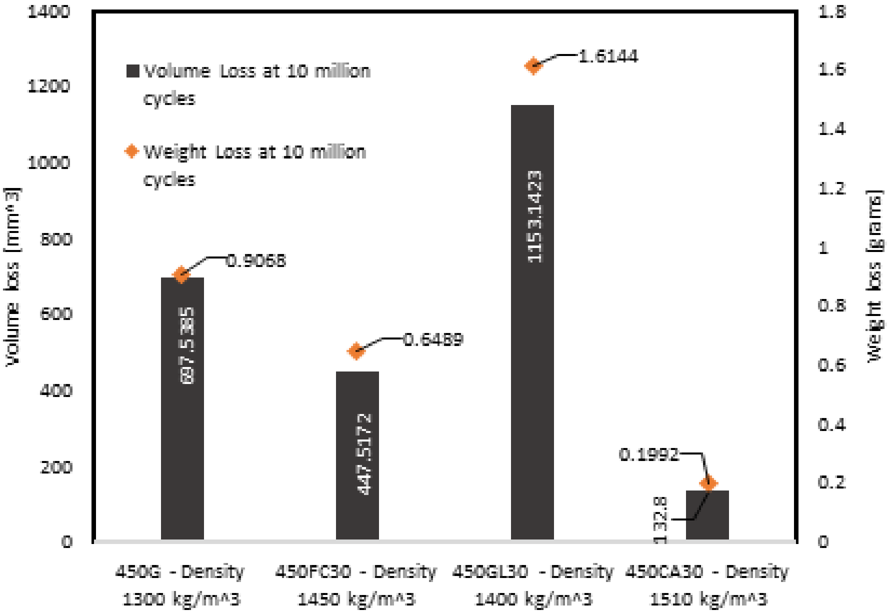

(b) At 10 million Cycles

Figure 4. 14 *Volume Losses Due to Velocity Movement, at 1.44 and 10 Million Cycles for BS-20PA – PEEKs (450G, 450CA30, 450FC30, and 450GL30) vs STEEL Testing*

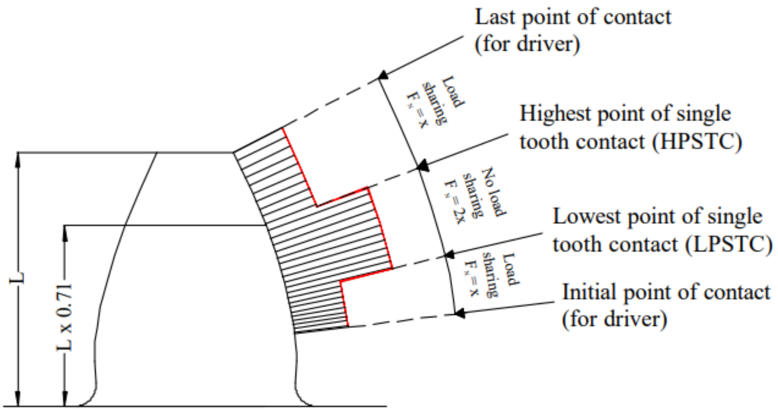

Figure 4. 15 *Load Sharing Along the Tooth Contact Surface*

Experimental data in Figure 4.14 quantifies volume and weight loss failures, divided into two categories: weight loss in grams and volume loss in mm^3. The order of increasing gear volume loss, from highest to lowest, is PEEK 450GL30 > 450G > 450FC30 > 450CA30. 450CA30 demonstrated the lowest volume loss and exhibited higher strength and density than the other PEEK grades.

4.2.3 Accelerating Vibration Data

An accelerometer was employed to detect the accelerating vibration due to Earth's gravity, as depicted in Figure 4.16. The accelerometer's digital output represented a significant bit per ±g, with 1g equivalent to $9.81 m/s^2$. Measurements were conducted on three axes: ±x, ±y, and ±z. Positioned on a wheel shaft, the accelerometer monitored vibration changes during real-time tooth meshing under load conditions. Data collection occurred at 1-second intervals throughout the test duration of 10 million cycles. The results from this vibration testing are illustrated in Figure 4.16.

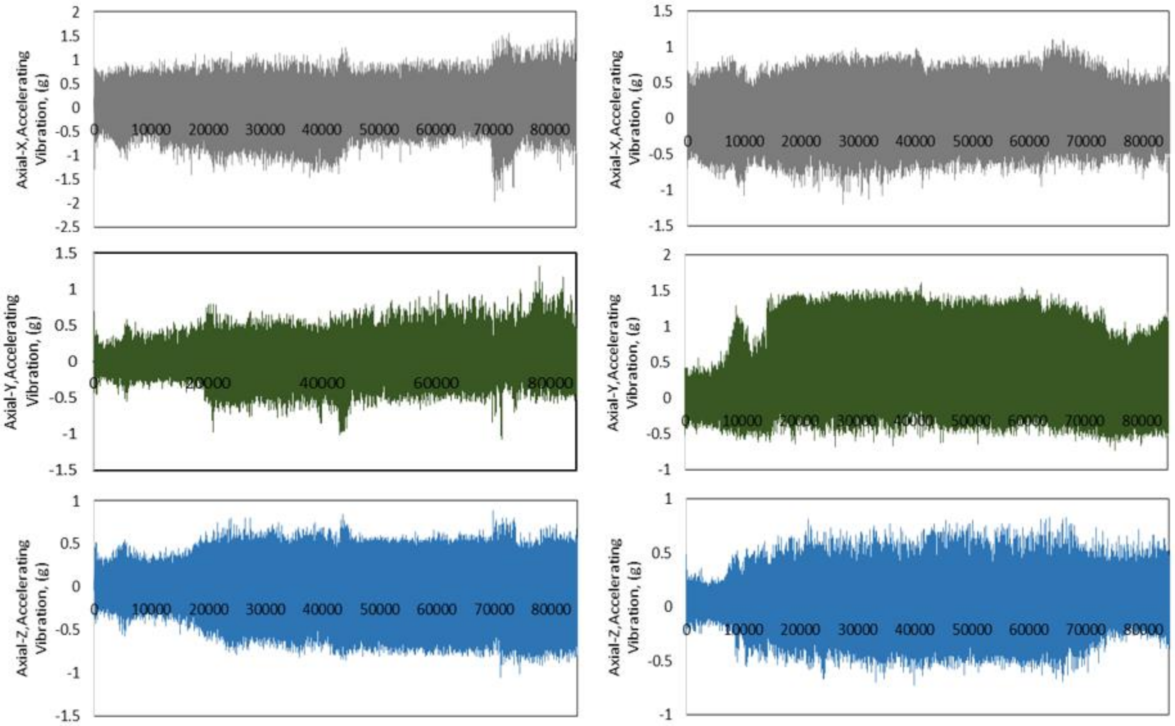

(a) 450G, accelerating vibration (g)

(b) 450FC30, accelerating vibration (g)

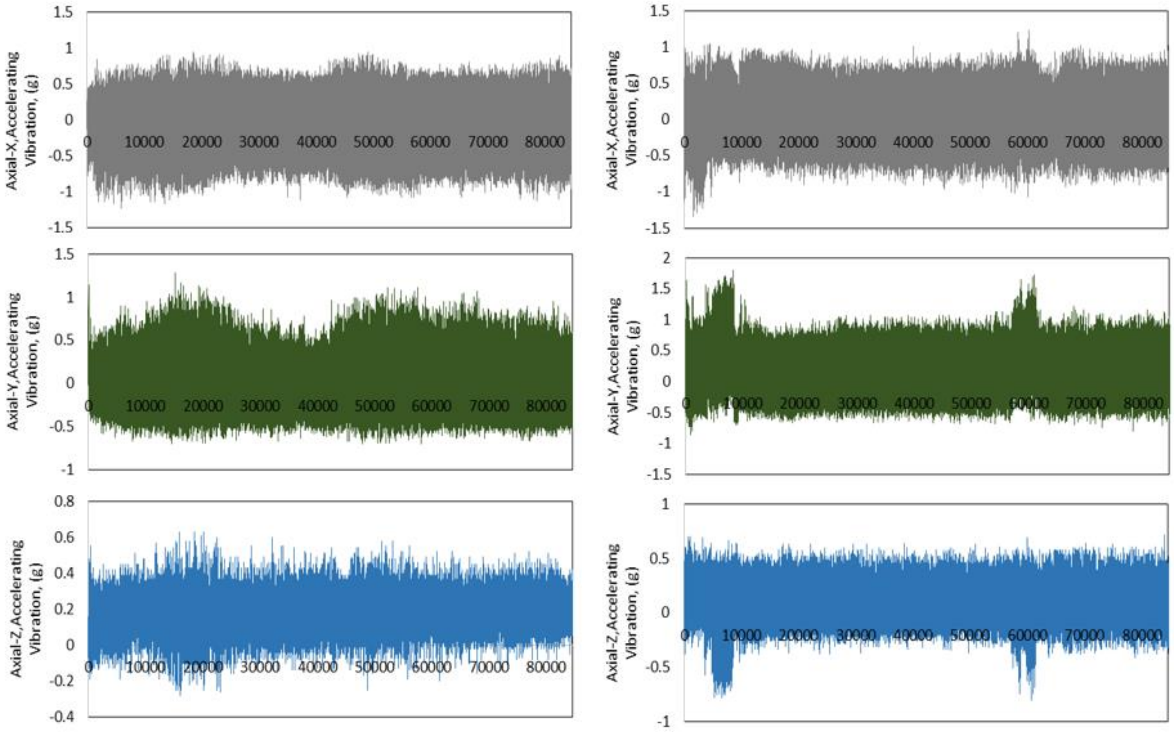

(c) 450GL30, accelerating vibration (g)

(d) 450CA30, accelerating vibration (g)

Figure 4. 16 *Collected Accelerating Vibration Data on the Shaft Based on Time (Seconds))*

Vibration changes during engagement involve damaged gear teeth, variable meshing stiffness, and transmission errors. In Figure 4.16, frequency data was collected every second at 8.56 and 10 million cycles (equivalent to 1.44 million cycles over 24 hours).

In the axial-x direction, all four-wheel PEEKs initially exhibited ±1g of vibration. However, for 450G, the vibration increased to ±1.5g, starting at 7.3 million cycles. The axial-y direction showed significant variations, with the highest and lowest concentrations observed in 450GL30 (ranging from -1.5g to 0.6g). Meanwhile, 450G, 450FC30, and 450CA30 experienced an increase to about ±0.70g. Under shaft load in the axial-z direction, 450G and 450GL30 demonstrated a higher average significance in forward and backward movements, around ±0.60g. The lowest frequency of accelerating vibration was observed in 450CA30 and 450FC30. Consequently, 450GL30 was found to experience tooth failure faster than other grades, considering the data from 3-axis accelerating vibration measurements alongside weight and volume losses.

4.2.4 Reaction force and load efficiency of un-lubrication testing

Load efficiency, as investigated in Copper's thesis [38], examines plastic cylinder gears' efficiency and friction characteristics. Experiments were conducted on the MK II test rig, employing the following load efficiency equation:

$$\eta_{Copper} = \frac{T_{in}}{T_{motor}} \times 100 = \frac{(F_1 - F_2)\, d_l \omega_f}{4\, m\, g\, r_p} \times \tan \Psi$$

Critical parameters for load calculations include weight testing, torque, and revolutions. For instance, a weight of 4.6 kg is considered in these calculations. These parameters are crucial in analysing the performance and efficiency of plastic cylinder gears in research conducted by Copper and Kono. Table 4.6 provides the required information for determining load efficiency values, and Figure 4.17 presents the relationship between load and force reaction of the rig applied in the horizontal axial.

Table 4. 6 *Required Information for Determining Load Efficiency Values*

Efficiency Description					
Pulley Ratio	*3*	*N/A*			
Speed of gear output	*329*	*rpm*	*11.3 Hz*	r_p (m)	*0.03*
Average of arm loading	*180*	*N*	*Approx.*	$\tan(30°)$	*0.5774*
Weight/Mass applied	*4.6*	*kg*	*180.5040*	*N (4mg)*	
Load Efficiency	$(T_{in}/T_{motor}) \times 100\%$				
Torque load of plastic gear motor	$T_{in} = (F_1 - F_1)d$	*Nm*	$v_p(m/s)$	*Angular, Hz*	
Angular velocity	$w = v_p/r_p$	*rad/sec*	*3.1416*	*104.72*	
Reaction force of rig. applied in Horizontal Axial, F_2	*180.5040*	*N*			
$F_1 = F_2/4$	*45.126*	*N*	*Power of motor*	*2.2*	*kW*
Displacement btw loads call and axis of rotation of cradle	*630*	*mm*			

F_2	***Torque applied***	***% of Efficiency***
175	*8.568255326*	*91.35318366*
176	*8.634228926*	*92.05658222*
177	*8.700202526*	*92.75998077*
178	*8.766176126*	*93.46337932*
179	*8.832149726*	*94.16677788*
180	*8.898123326*	*94.87017643*
181	*8.964096926*	*95.57357498*
182	*9.030070526*	*96.27697353*
183	*9.096044126*	*96.98037209*
184	*9.162017726*	*97.68377064*
185	*9.227991326*	*98.38716919*
186	*9.293964926*	*99.09056775*
187	*9.359938526*	*99.7939663*
188	*9.425912126*	*≈100*

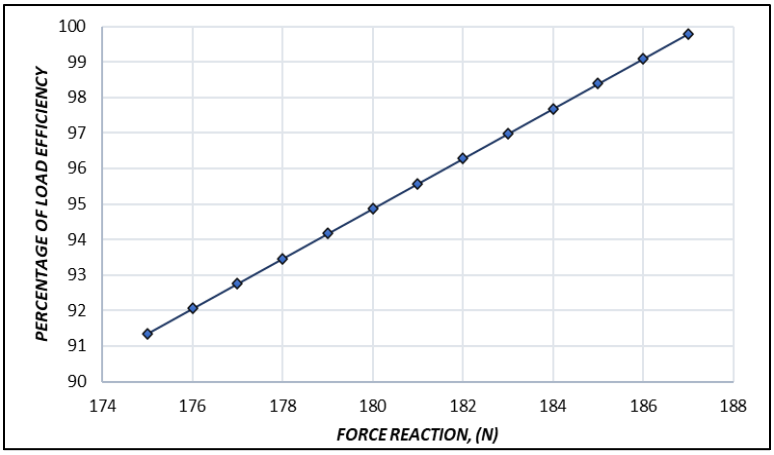

Figure 4. 17 *Relationship Between Load and Force Reaction of Rig Applied in Horizontal Axial*

The reaction force indicates the worn PEEK gear's response to mechanical loads and interactions during operation, recorded using e-DAQ. It provides insights into how the gear's condition impacts the forces it generates and encounters. Figure 4.18 shows the maximum force and torque reactions collected from the experiment.

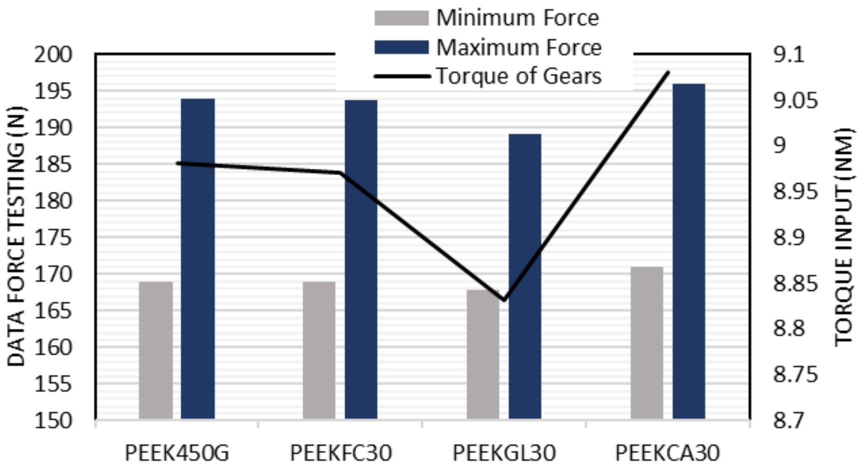

Figure 4. 18 *Force and Torque Reaction from Experimental Testing*

Factors like damaged gear teeth, variable meshing stiffness, temperature increase, load, and transmission errors accelerate vibration changes during gear engagement. Figure 4.19 highlights critical findings in the axial-y direction, where frequency data was collected near the end of the 10 million cycles (equivalent to 858,092 and 875,312 seconds). Notably, 450GL30 showed the highest and lowest significant concentrations, ranging from -1.5g to 0.6g. In contrast, 450G, 450FC30, and 450CA30 experienced an increase to approximately ±0.70g

(a) PEEK 450G

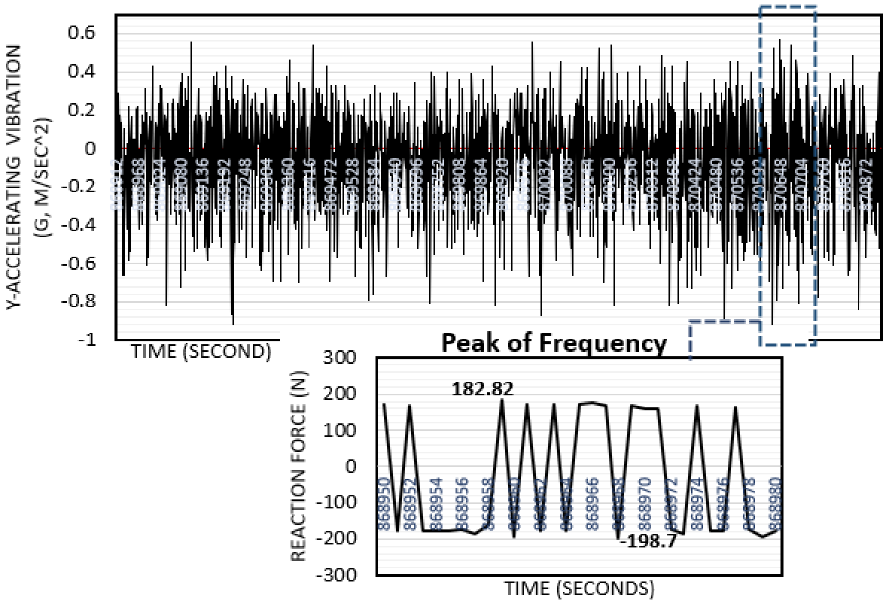

(b) PEEK 450FC30

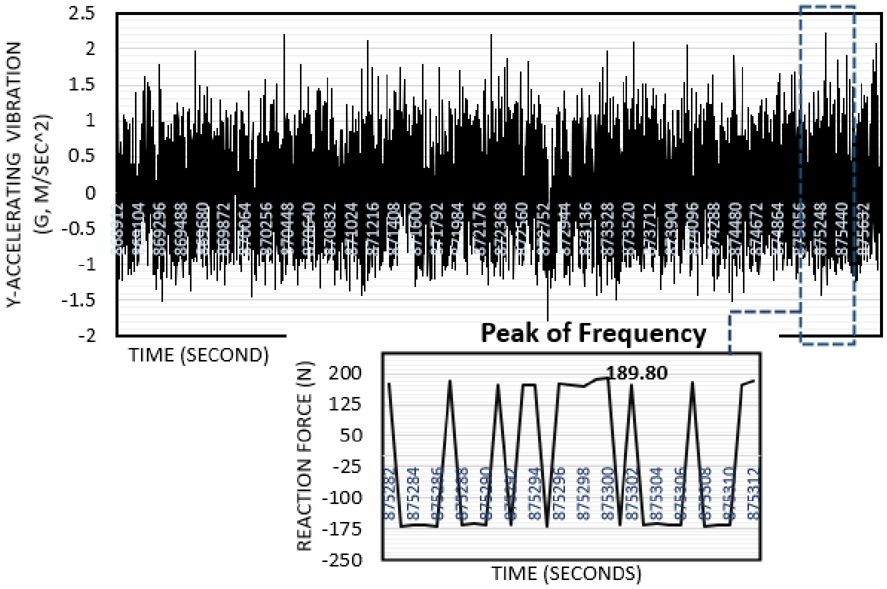

Figure 4. 19 *Peak Frequency of Accelerating Vibrations and Peak Reaction Forces, Based on Time (Second)*

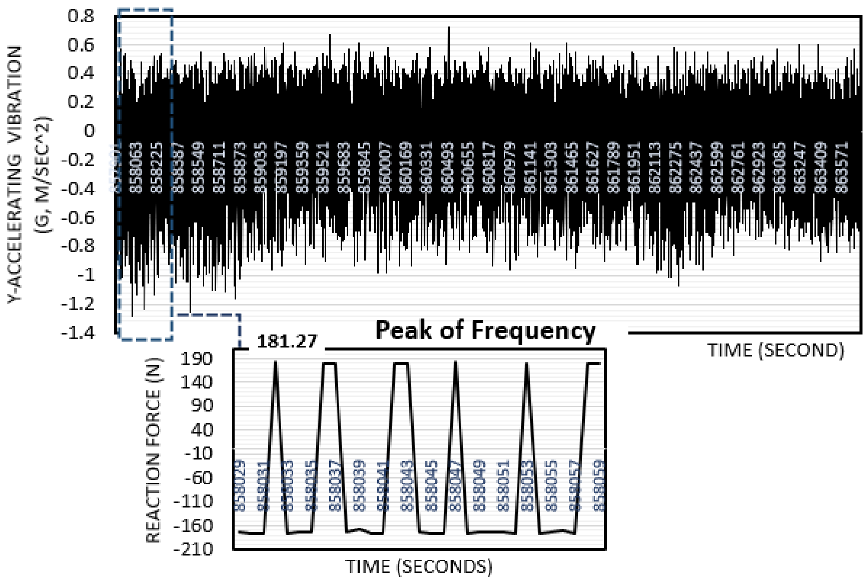

(c) PEEK 450GL30

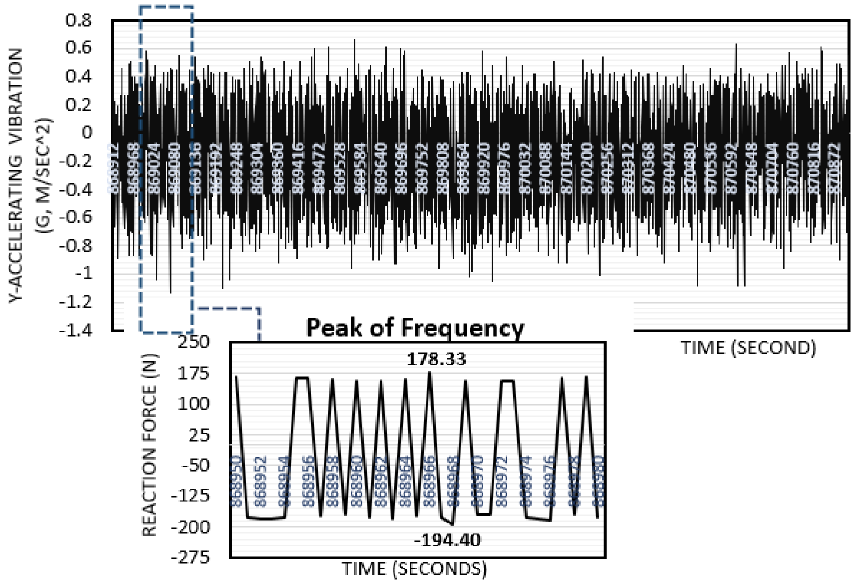

(d) PEEK 450CA30

Figure 4.19 (Cont.) *Peak Frequency of Accelerating Vibrations and Peak Reaction Forces, Based on Time (Second)*

4.3 Tooth Crack

4.3.1 Peak Frequency of Vibration and Temperature data

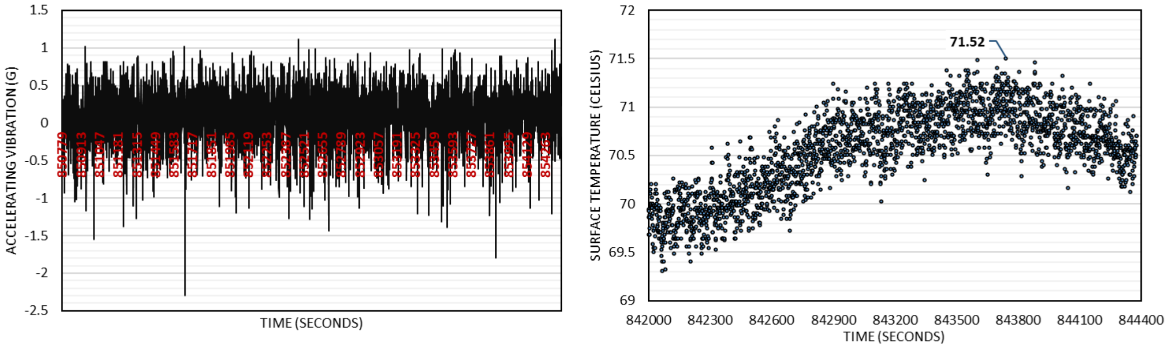

(a) PEEK 450G

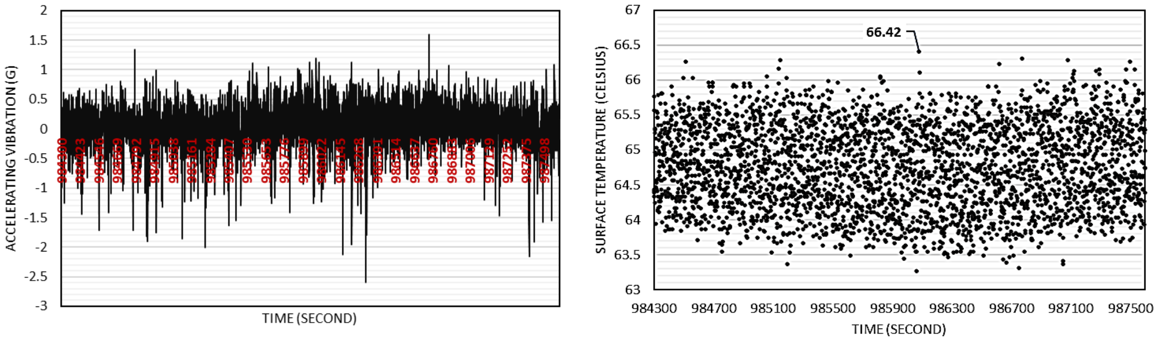

(b) PEEK 450FC30

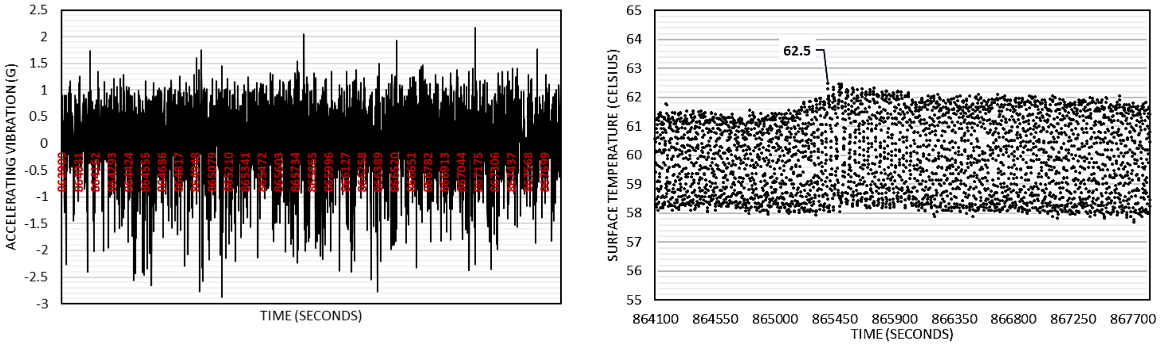

(c) PEEK 450GL30

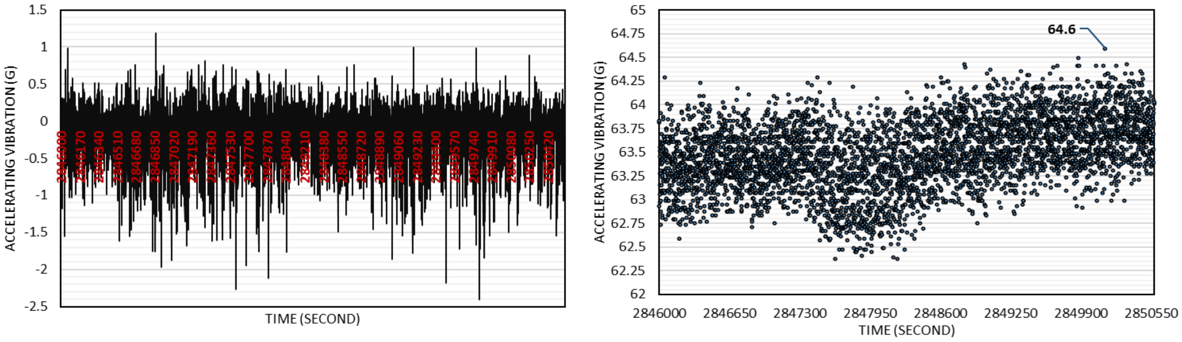

(d) PEEK 450CA30

(a) Accelerating Vibration, g (m/s^2)   (b) Surface Temperature (°C)

Figure 4. 20 *Peak Frequency of Accelerating Vibration and Temperature Data*

This study segment collects data on accelerating vibration and temperature for four PEEK 450 materials. The results are compiled in Figure 4.20. This data includes peak temperatures observed on the width-tooth flank during real-time testing before the cycle's end.

Peak vibration frequency, the findings indicate a substantial change in the vibration behaviour of the system, likely linked to the emergence of a tooth crack. The data collected from the 3-axis accelerating vibration measurements and weight and volume loss data revealed additional insights, as presented in Figure 4.20 (b).

The graph in Figure 4.20 (a) displays the temperature measurements taken on the width-tooth flank. These measurements were recorded every second until the completion of the initial testing, which also encompassed peak vibration frequency. This collected temperature data was subsequently used for comparative analysis of temperature increases. All data has been collected in Appendix A, where the compiled temperature measurements and additional data are available for a more detailed and comprehensive analysis of temperature variations over time. In terms of peak vibration frequency, the findings indicate a significant change in the vibration behaviour of the system, likely indicative of the emergence of a tooth crack. The data gathered from the 3-axis accelerating vibration measurements, alongside weight and volume loss data, provided additional insights into this phenomenon, as depicted in Figure 4.20 (b).

Additionally, Figure 4.21 was utilised to detect worn teeth from the initial running phase until the end of the cycle.

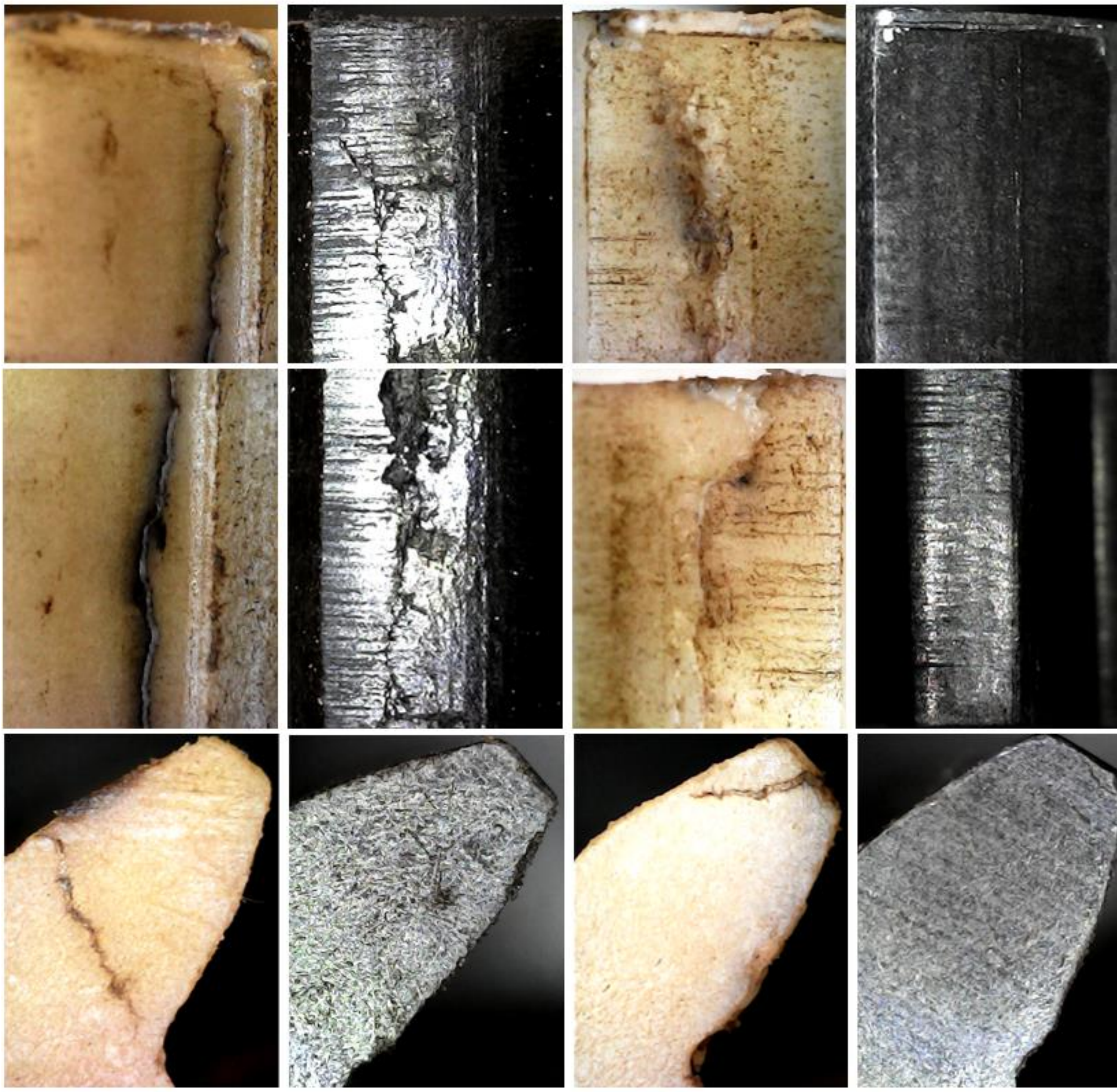

(a) PEEK 450G
14.17 million cycles
(Crack)

(b) PEEK 450FC30
17.52 million cycles
(Crack)

(c) PEEK 450GL0
11.40 million cycles
(Crack)

(d) PEEK 450CA30
50.10 million cycles
(Crack)

Figure 4. 21 *Micro Camera Detected Worn Teeth at Initial Running Until End of Running*

4.3.2 Detection of Tooth Crack

Figure 9.10 is crucial in detecting internal cracks or defects visible on the gear's surface. These images offer a detailed view of the gear's internal structure at the micrometre level, providing essential insights into the wear and damage sustained by the gear teeth throughout the experiment. This level of detail is instrumental in understanding the progression and impact of tooth cracks on gear performance and durability.

4.4 Chapter Summary

This chapter presented the experimental techniques and some preliminary data for the analysis of gear meshing, particularly involving steel and various PEEK grades. Key aspects of the included load tests, thermal performance, vibrations, and gear tooth wear. The experiments involved examining their interaction under different conditions over a 24-hour period or 1.44 million cycles. Some of the testing was aimed at replicating previous research examining torque load and speed in unlubricated tests.

Data collection included parameters such as surface temperature, acceleration, vibration, load tests, and tooth wear. The chapter also presents detailed mechanical properties of PEEK materials, their endurance under high temperatures, and their conformity to industrial standards.

Chapter 5

Advancing Polymer Gear Tooth Wear Analysis: A Revised Equation for PEEK Gears

Gear tooth failures can lead to an increase in frictional temperature behaviours. Under test load conditions, there is a significant magnification of erosion and wear on the surfaces of gear teeth. This phenomenon is particularly evident in the altered kinematics and geometry of polymer gear teeth involutes. A revised equation is proposed to address these changes in involute tooth geometries. This equation is grounded in the meshing kinematic behaviour, encompassing aspects such as ball contact, the contact path line (including approach and recess sections), base pitch, and contact angles. These are all formulated concerning the established frictional temperature. Additionally, the investigation delves into tooth wear characteristics, focusing on aspects like weight and distance. Frictional behaviours on the tooth flank are analysed, drawing on Buckingham's and Merritt’s equations.

5.1 Research background

The amplification of gear tooth surface erosion and wear under test load conditions is a notable concern. Gear tooth failures have a direct impact on frictional temperature behaviours. Notably, there is evidence of reduced weight loss on tooth contact surfaces, particularly for polymer materials. Consequently, this research studies the kinematics of geometry change in involutes. It aims to predict the behaviour of PEEK spur gears, with the revised equation being adapted to address changes in tooth wear size specific to polymer materials. This is based on the approach and recess equation per Merritt's and Buckingham's methodologies.

5.2 Revised Equations

5.2.1 Meshing behaviour for contact extension

The kinematic behaviour of spur gears is crucial, referring to the motion and interaction of teeth in a pair of such gears. These are typically cylindrical gears with straight teeth mounted on parallel shafts.

5.2.1.1 Involute Tooth Geometries

According to Buckingham's and Merritt's equations, an involute gear tooth is characterised by parallel involute curves and curvature surfaces. It exhibits a linear contact path in cycloid teeth and maintains a standard base pitch.

This research primarily aims to measure the diameter of the ball contact. The spatial arrangement of two involutes on gear teeth is pivotal in determining the measure over balls, under the arc tooth thickness, and the pressure angle. However, unlike standard gear contact, polymer gear teeth used in automotive research do not engage in a common normal state. This study, therefore, scrutinises the changes in the involute wear of the teeth relative to the standard gear's involute geometry, as illustrated in Figure 5.1. The design is divided into three sections: ball contact, base pitch, and contact path.

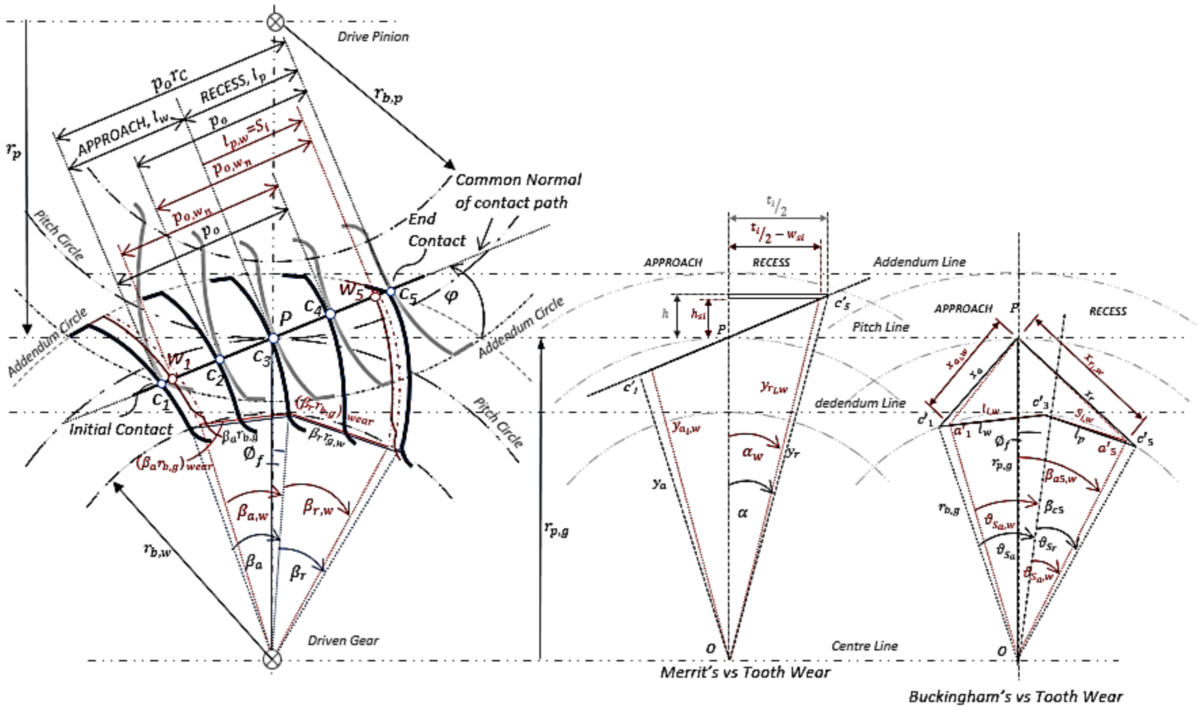

Figure 5. 1 *Involute Tooth Wear, Relative to the Gear Standard of Involute Geometry*

An equation for the kinematic behaviour of gears has been developed and refined, focusing on the changes in involute tooth geometries influenced by ball contact. Solving this equation can predict gear wear for both tooth and ball contact geometries in polymer materials. The diameter of the ball contact circle varies along the thickness of the gear tooth and can be accurately measured at this circle. Figures 5.1 and 5.2 illustrate tests conducted on a 450GL30 gear over 10 million cycles. The results show a more significant reduction in tooth thickness compared to standard gears. Consequently, this study has formulated a new equation for calculating the diameter of the ball contact.

$$d_{ball,w} = d_{ball} + w_{s,T_i}$$

where	$d_{ball,w}$	is a new ball size contact from wear size increased (mm)
	w_{s,T_i}	is the wear on the polymer teeth (mm)
	T_i	is number of teeth

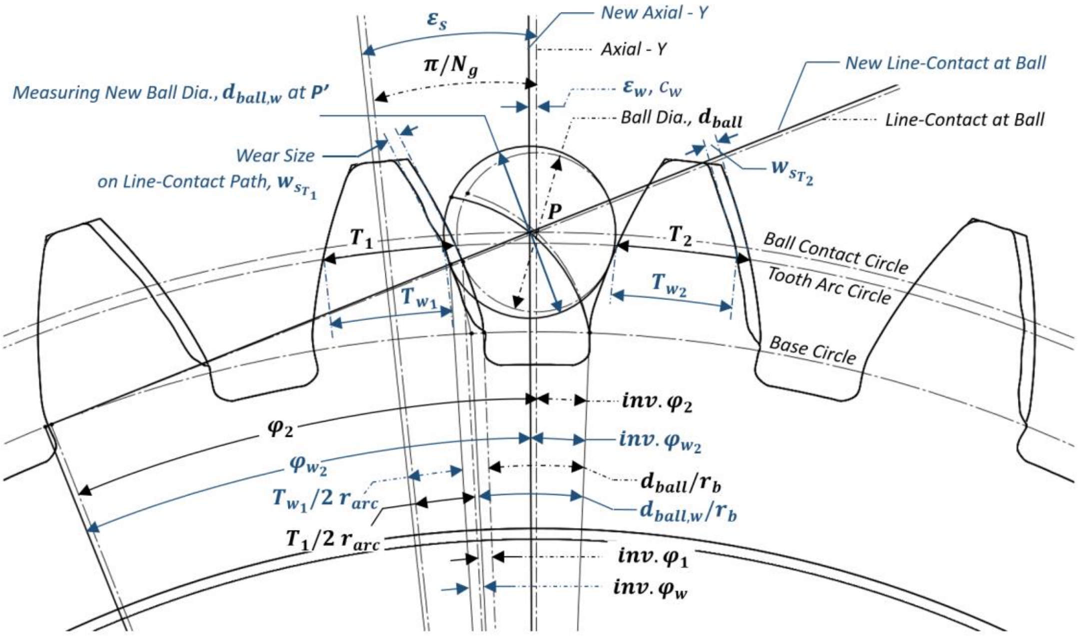

Figure 5. 2 *Involute Tooth Gear Geometry and Ball Contact (Unworn and Worn Teeth)*

The standard circular pitch as depicted in Figure 5.3, is determined through the following computation:

$$p_c = \pi\, \frac{{}^{\pi}d_p}{N_p}$$

$$p_c = d_{ball} + T_i$$

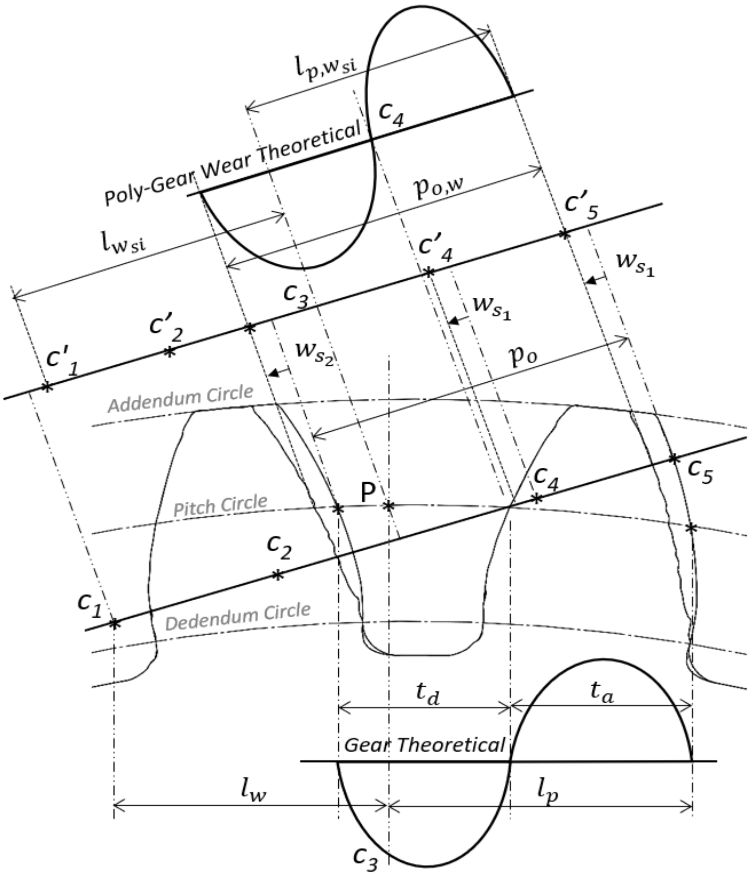

Figure 5. 3 *Changing in Circular Pitch*

when w_{s,T_i} and w_{s,T_i} are not equal zero, thus $p_c = p_{c,w}$;

$$p_{c,w} = d_{ball,w} + T_{w_i}$$

In the event of base pitch failure and wear on the involute teeth, the value of p_b differs from $p_{b,w}$. Hence, the distance, l_f between the centre of the worn teeth and the point of ball contact is calculated as follows:

$$l_{f,w} = \left[\frac{1}{2}\left(T_i + w_{s,T_i}\right)_{in} + \left(\frac{d_{ball}}{2} + w_{s,T_i}\right)_{out} \right]$$

$$l_{f,w} = \frac{T_{w_i}}{2} + d_{ball,w}$$

The angle deviation from the Y-Axis to the new axis at the point of ball impact is given by ε_s;

$$\varepsilon_s = \frac{\pi}{N_w} + \varepsilon_w = \sin^{-1}\left[\frac{l_f \cos\varphi_1}{r_b}\right]$$

$$\varepsilon_s = \sin^{-1}\left[\frac{\left(T_{w_i} + r_{ball,w}\right) \cos\varphi_1}{r_b}\right]$$

The worn teeth corresponded to the axial shift, denoted as (c_w) in millimetres;

$$c_w = \frac{w_{s,T_i}}{2} = \frac{r_{ref} \sin\varepsilon_s}{\cos\varphi_1}$$

The summary results for these simplified equations focus on developing a new theory for estimating gear tooth fatigue and fracture before failure occurs. A novel theory design for this research is the distance of tooth wear size for changing contact paths: recess and approach.

5.2.1.2 Base Pitch and Contact Path Analysed

The unvarying and uniform standard base pitch corresponds to the parallel involutes gap between the base circle p_c and the congruous directionality of successive gear outlines. This metric is gauged along the base circle and tooth flank curve [61]. Consequently, the principle of base pitch is given by;

$$p_b = p_c \cos\varphi_1 = \frac{\pi\, d_p}{N_p} \cos\varphi_1$$

The conjugate motion action of involute tooth flanks is parallel, originating from the base pitch measured along the position of the straight edge [71]. Therefore, as illustrated in Figure 5.1, it is manifested at every point along the involute tooth flank.

The path of contact, comprising the approach and recess lines, is contingent upon the fundamental pitch of the conventional gear teeth. Consequently, the critical dimensions of the principle of approach (l_w) and recess (l_p) segments are:

$$l_p = \sqrt{\left(\frac{1}{2}d_p + a\right)^2 - \left(\frac{1}{2}d_p \cos\varphi_1\right)^2} - \frac{1}{2}d_p \sin\varphi_1$$

By Buckingham's equations, which consider the approach angle (ϑ_{S_a}) and recess angle (ϑ_{S_r}), the following applies:

$$\vartheta_{S_a} = \left\{\frac{\left[\sqrt{r_{ag}^2 - r_{bg}^2} - r_g \sin\varphi_1\right]}{r_{bp}}\right\}_B, \qquad \vartheta_{S_r} = \left\{\frac{\left[\sqrt{r_{ap}^2 - r_{bp}^2} - r_p \sin\varphi_1\right]}{r_{bg}}\right\}_B$$

Conventional gear theory suggests using steel as superior to polymer materials because they are more susceptible to wear and tear than their metallic counterparts. Specifically, gear polymer failures are more prone to erosion and wear on the tooth flank due to load conditions. Consequently, this section has developed an equation for gear wear of polymer material in cases of involute tooth failure. In addition, it has revised some related theories regarding changes to involute tooth geometries, considering factors such as the contact path (sections of approach and recess lines), base pitch, ball of contact, contact angles, and others. The principle of base pitch, p_b is defined as follows;

where $p_c = p_{c,w}$ and $p_b\, r_c = l_w + l_p$

$$p_b = p_{b,n\,MCycles}$$

$$p_{b,w} = p_{b,n\,MCycles} = \left[\, l_{f,w} + \left(\frac{T_i}{2} + r_{ball,w}\right)\right] \cos\varphi_1$$

and

$$\left(l_w + l_p\right)_o \neq \left(l_w + l_p\right)_{o,n\,MCycles}$$

Compute

$$\left(l_w + l_p\right)_{n\ MCycles}\ (t)$$

From the given formulas, we compute the collection of contact points as:

$$\left(l_w + l_p\right)_{n\ MCycles}\ (t) = \int_{c_i c_{i+1}}^{c_{4i} c_{4i+1}} \left(l_w + l_p\right)(t, x)\, dx$$

$$l_w + l_p = p_b\, r_{c,w} + [(c_1 c_2) + (c_4 c_5)]$$

The standard for the contact ratio, calculated as the average number of gear teeth, is established through:

$$r_c = \frac{\sqrt{r_{ap}^2 - r_{bp}^2} + \sqrt{r_{ag}^2 - r_{bg}^2}}{p_b} - C \sin \varphi_1$$

The contact ratio over time, the wear teeth and the gear ratio are also critical considerations.

$$\left(r_{c,g}\right)_w = r_c + (c_4 c_5)$$

For Gear ratio, $m_g \leq 2$, the following applies:

$$w_{s,MCycles} = (c_1 c_2) + (c_4 c_5)$$

$$\sum w_{s,MCycles} = (w_g + w_p)_{c_3} + (w_g + w_p)_{c_5}$$

In testing, a pair of gears meshing together often employs different materials for the steel pinion and polymer wheel. Consequently, the wear size of the pinion is denoted as $w_p = 0$. An estimation of the lengths of approach and recess equations for worn teeth is then derived:

$$w_{s,MCycles} = w_{g,c_3} + w_{g,c_5} = w_{s_{T_1}} + w_{s_{T_2}}$$

at c_5, $w_{g,c_5} = w_{s_{T_5}} + c_p$

This leads us to the following conclusions:

$$w_{s,MCycles} = w_{s_{T_1}} + \left(w_{s_{T_2}} + r_{tip}\right)$$

Contact stress and surface temperature significantly influence tooth wear behaviour in polymer gears. The individual wear rate of PEEK is determined by analysing enhanced wear characteristics, including weight and wear size on the tooth flank. Kim (2006) defined the wear volume (w_V) by calculating the estimated wear loss against the density, considering the individual wear rate and the characteristics of each cycle [130]:

$$w_{s,c} = \frac{w_V}{2\, m\, b\, n_T\, z}$$

Therefore, the equations for estimating the lengths of approach and recess for worn teeth are:

$$l_{w_{si}} + l_{p,w_{si}} = (p_b\, r_c)_{cycles}$$

$$l_{p,w_{si}} = r_b\ \vartheta_{s_r,w} = \left[\left(\frac{r_a - r_p}{\sin\varphi_1}\right) + \left(\frac{w_{s,MCycles}}{\tan\varphi_1}\right)\right]$$

and the recess angle ($\vartheta_{s_r,w}$);

$$\vartheta_{s_r,w} = \sin^{-1}\left[\left(\frac{l_{p,w_{si}}\cos\varphi_1}{r_{ec}}\right) + inv.\varphi_2\right]$$

5.2.2 Tooth deformation

The viscoelastic hysteretic deformation of teeth, generated by stress and strain behaviours that increase wear, is a significant consideration [39]. This deformation is influenced by the rise in temperature caused by mechanical stresses and the variability in the stiffness of polymer materials.

Figures 5.4 and 5.5 illustrate the bending deformation of tooth wear failure and the action tangent plane, with the coordinates of x, y, and z representing the tooth gear's deformation. Wan et al. (2015) described this estimation based on vector methods related to variable meshing over time [120]. The coordinates of x, y, and z of the tooth gear's deformation are determined by:

$$x_i(t) = r_b\left[(\emptyset_{b_i}(t) + \emptyset_{C_i})\cos\emptyset_{b_i}(t) - \sin\emptyset_{C_i}\right]$$

$$y_i(t) = r_b\left[\cos\emptyset_{b_i}(t) + (\emptyset_{b_i}(t) - \emptyset_{C_i})\cos\emptyset_{b_i}(t) - \cos\emptyset_{C_i}\right]$$

Approximate coordinate, $z_i(t) \approx 0 - 0.5\ mm$ shiftes of gear.

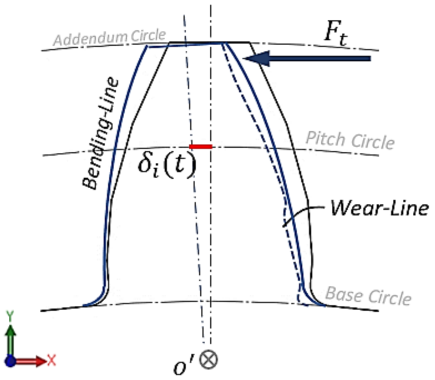

***Figure 5. 4** Bending Deformation of Tooth Wear Failure*

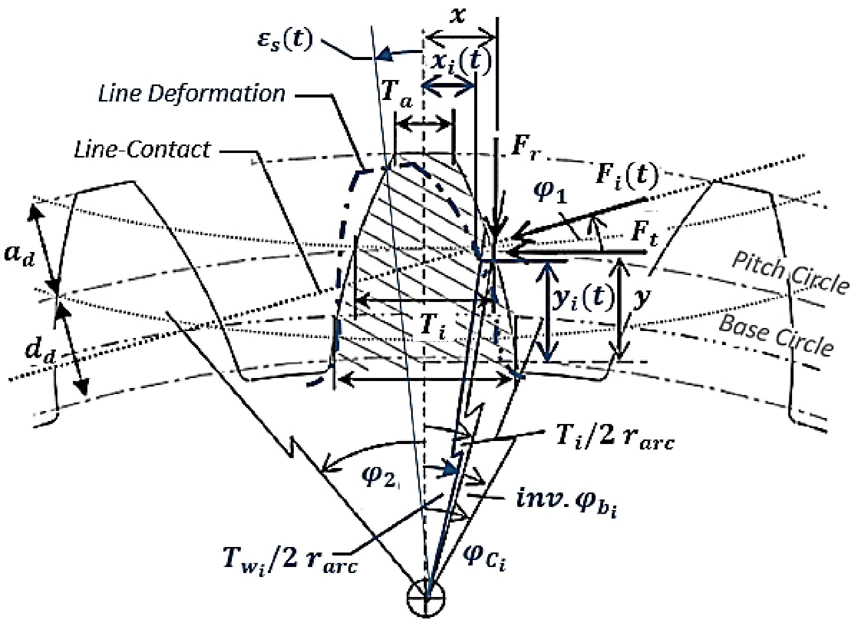

Figure 5. 5 *2D of Tooth Gear Tangent-Plane of the Action and the Force Reaction*

The x-coordinate distance from the impacts of tooth bending deformation is $x_i - \delta_t - w_{si}$ where w_{si} is wear size in mm. The loading angle, $\emptyset_{bi}$, is calculated using the AGMA 908-B89 standard theory and is determined by:

$$\emptyset_{bi} = \tan\left[\left(\frac{r_b}{r_o}\right)^2 - 1\right]^{-0.5} - \left[inv\ \emptyset_n + \frac{t_i}{2}\right]$$

$$inv\ \emptyset_{ci} = inv\ \emptyset_{ti} + \frac{t_i}{2}$$

$$t_i = \frac{\pi}{2} + 2(x - \Delta t_n)$$

when $\emptyset_{ci}$ represents a pressure angle at root of gear teeth (*Degrees*)

t_i represents the standard circular tooth thickness with references at the pitch point in millimetres (mm).

5.2.3 Coefficient of Friction Revised

The principle of involute wheel geometry changes over time and under load condition tests, resulting in variable frictional behaviour or friction coefficients, μ. This design derives two theories from Buckingham and Merritt. Thus, the coefficient of friction along the contact path and the angles of approach and recess are derived as follows:

$$l_w + l_{p_{o,inc}} \neq l_w + l_{p_{o,nMcycles}}$$

$$l_w + l_{p_{o,inc}} > l_w + l_{p_{o,nMcycles}}$$

and $$\vartheta_{s_a} \neq \vartheta_{s_a,w} \text{ , } \vartheta_{s_r} \neq \vartheta_{s_r,w}$$

For the changing circular pitch, P_o, the following applies:

when $$P_{o,inc} \neq P_{o,nMcycles}$$

$$P_{o,inc} > P_{o,nMcycles}$$

As calculated by Buckingham's and Merritt's equations, the coefficient of friction is not constant and varies based on factors such as gear materials, lubrication, loads, and speeds. Gear behaviour is reflected in curves illustrating the average coefficient of friction against sliding speeds, which encompass approach and withdrawal sliding velocities, as shown in Figures 5.1, 5.2, and 5.3.

Involving involute gear geometry, weight increase leads to volume loss on tooth flanks and deflection effects. Additionally, heat loss temperature changes over time as the gear tooth contact moves across involute and curvature surfaces. During time and load condition testing, the principle of involute gear shape changed, resulting in non-constant frictional behaviour, as indicated by the coefficient of friction (μ). This design is based on Buckingham's and Merritt's equations [71] [61], which take into account the load/transmission efficiency and the module (m) in millimetres.

$$\mu_B(t) = (1-\eta) \cdot \left[\frac{\left(\vartheta_{s_a} + \vartheta_{s_r}\right)}{\left({\vartheta_{s_a}}^2 + {\vartheta_{s_r}}^2\right) \cdot \left(1 + \frac{1}{m_g}\right)} \right]$$

Merritt's equation followed by:

$$\mu_M(t) = (1-\eta) \cdot \frac{1}{\sec\varphi} \cdot \left[\left(\frac{d_p d_g}{d_p + d_g} \right) \left(\frac{l_p + l_w}{{l_p}^2 + {l_w}^2} \right) \right]$$

where m_g is the gear contact ratio

As a result, this study focused on the coefficient of friction and reveals that failures and transmission defects cause different friction problems in the involute gear geometries. Gear failures and transmission problems increase weight and volume loss on tooth sides and deflection effects. Furthermore, the heat loss temperature fluctuates over time as the gear tooth contact moves along the involute and curvature surfaces.

5.3 Materials and Methods

5.3.1 Establishing Mechanical Properties

In this investigation, Kono's research is replicated by subjecting various grades of PEEK to specific torque and speed conditions. Unlubricated tests were conducted using four different PEEK grades against a Steel pinion gear. Detailed information regarding these PEEK grades' mechanical properties and elastic modulus can be found in Table 4.1 and Figure 4.3.

5.3.2 Test methodologies and equipment

The experimental procedure, illustrated in Figures 4.3 and 4.8, involves schematic diagrams of the test methodologies for unlubricated testing. These tests were carried out at using the MKII test rig. The experiment spanned 10 million cycles and was conducted under dry conditions, specifying weight and speed. Data collection included measuring accelerating vibration, temperature effects, and resistive load detection using E-DAQ equipment.

5.4 Numerical Models

Table 4.3 offers comprehensive information regarding the numerical gear geometries and specifications for both PEEK and Steel gears. This table includes detailed descriptions and drawings of these gears, providing a brief overview of these materials' gear configurations and characteristics.

5.5 Results

5.5.1 Specific Wear Rate

In polymer gears, wear is primarily influenced by contact stress and surface temperature. The study mainly focused on the specific wear rate of PEEK, evaluating increased wear characteristics such as weight and wear size changes on the tooth flank. Continuous testing was conducted for up to 10 million cycles to analyse the impact of gear surface wear on overall gear performance. Figure 5.6 displays the data collection results, showing weight loss and instances of involute tooth gear failures, as indicated by wear size.

Real-time testing was employed to gather data on weight reduction. This involved comparing BS-20PA – PEEKs against Steel G.8, subjected to a torque of 9.38 Nm and a speed of 1,000 rpm using the MARKII testing setup. After 10 million cycles, 450GL30 exhibited significant weight reduction and shape change on the tooth flank (approximately 1.6144 grams): 450 G and 450FC30 experienced weight reductions of 0.9068 and 0.6489 grams, respectively. 450CA30 showed lower weight loss at 1.44 million cycles, with continual minor weight reduction and tooth surface modification (0.1992 grams) over 10 million cycles during continuous testing.

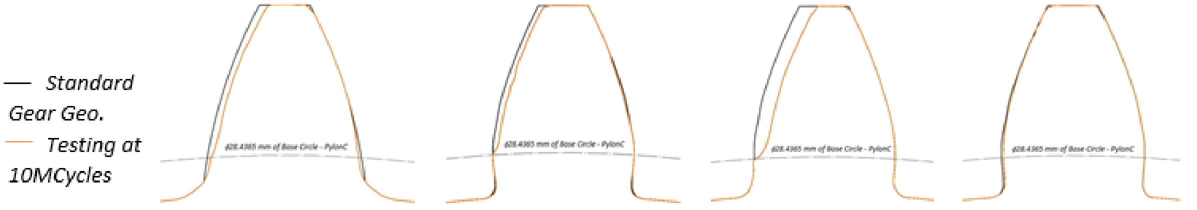

PEEKs	**450G**	**450FC30**	**450GL30**	**450CA30**
Volume/ Weight Losses	697.5385 mm^3/ 0.9068 grams	447.5172 mm^3/ 0.6489 grams	1153.1423 mm^3/ 1.6144 grams	132.8000 mm^3/ 0.1992 grams
Wear Size	- 0.1349 mm/tooth	- 0.1355 mm/tooth	- 0.3544 mm/tooth	- 0.0327 mm/tooth

Figure 5. 6 *Weight Reduction for BS-20PA – PEEKs*

5.5.2 Contact Path Calculated

Deviations from the ideal tooth profile can significantly alter the contact path and ratio. This phenomenon was particularly noticeable in non-conjugate gears across various test cases [131]. As a result, the contact ratio was deduced from the gathered test data. Figure 5.7 depicts these changes in the contact ratio due to worn teeth at 1.44 million and 10 million cycles.

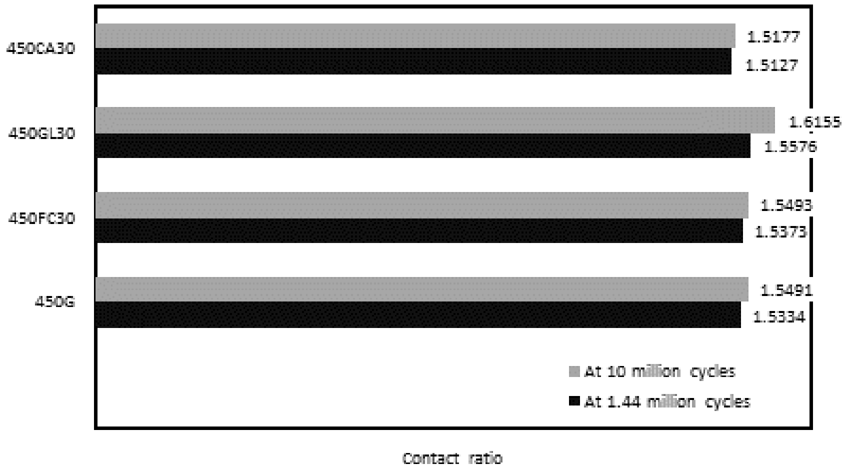

Figure 5. *7 Contact Ratio Changing Due to Worn Teeth*

5.5.3 Analysing the Geometry of Involute Tooth Gears and Ball Contact

This study segment involved analysing the tooth shape of four different PEEK grades using a Pylon camera after enduring 10 million cycles. The observed variations in tooth thickness led to an in-depth investigation into spur gear kinematics, mainly focusing on factors that affect the size of ball contact. Table 5.1 presents comprehensive calculations for the geometry of involute tooth gears and ball contact. This includes data on tooth shape and thickness changes resulting from wear throughout 10 million cycles. Additionally, Table 5.2 visually depicts the wear-induced changes in gear tooth shape and thickness.

Table 5. 1 *Calculations for Involute Tooth Gear Geometry and Ball Contact; Changes in Gear Tooth Shape and Thickness Due to Wear After 10 million Cycles*

	r_{arc} (mm)	C (mm)	$d_{ball,w}$ (mm)	r_b (mm)	$inv.\varphi_1$	T_1 (mm)	$inv.\varphi_2$	ε_s (rad)	c_w (mm)	ε_w (deg)	π/Ng (rad)	$T_1/2r_{ar}$ (rad)	d_{ball}/r_b (rad)
450G	30.135	60.27	3.5313	28.4365	0.0149	2.6731	0.5626	0.0023	0.1338	6.1338	0.2386	0.0443	0.1242
450FC30	30.135	60.27	3.5325			2.6404	0.5621	0.0024	0.1351	6.1351	0.2399	0.0438	0.1242
450GL30	30.135	60.27	3.7488			2.4525	0.5666	0.0064	0.3640	6.3640	0.4688	0.0407	0.1318
450CA30	30.135	60.27	3.4			2.7847	0.5600	0.0006	0.0329	6.0329	0.1377	0.0462	0.1196
Initial Running	30.135	60.27	3.4	28.4365	0.0149	2.8174	0.5604	0	0	0	0.1048	0.0467	0.1196

Table 5. 2 *Wear Size*

	w_{s,T_1} (mm)	w_{s,T_2} (mm)
450G	0.1349	0.1347
450FC30	0.1355	0.1356
450GL30	0.3544	0.3544
450CA30	0.0327	0.0326

5.5.4 Calculating the Approach and Recess of Contact Path Lines

The calculations highlight changes in the lengths of approach and recess along the un-normal contact path attributed to the intensified wear observed on the tooth flank after 10 million cycles. Table 5.3 elucidates how these altered involute tooth geometries significantly impact tooth flank geometry equations.

The study closely examined the changes in the contact path, precisely the approach and recess lines, on worn teeth. These alterations were quantified through analyses of ball contact and involute curve geometries. From these observations, new insights were gained into modifying involute tooth geometries. The research resulted in a practical equation for calculating wear size on the tooth flank during various approaches, recess times, and cycles, as depicted in Figure 5.8.

Table 5. 3 *Modified Involute Tooth Geometries for Unworn and Worn Teeth, Considering the Contact Path Line (as seen in Figures 5.2 and 5.3)*

	Initial Run	**At 1.44 million cycles**				**At 10 million cycles**			
		450G	**450FC30**	**450GL30**	**450CA30**	**450G**	**450FC30**	**450GL30**	**450CA30**
Wear Size per one tooth, $w_{s,10\ MCycles}$ (mm)	0	0.0837	0.0962	0.1627	0.0433	-0.1349	-0.1355	-0.3544	-0.0327
APPROACH, $l_{w_{si}}$ (mm)	-4.0236	-3.3745	-3.3629	-3.3002	-3.4371	-3.6503	-3.6496	-3.4391	-4.0382
RECESS, $l_{p,w_{si}}$ (mm)	4.8814	5.6830	5.7172	5.8999	5.4977	5.4997	5.5014	6.1029	4.9266
ANGLE of APPROACH, $\delta_{S_{a,w}}$ (Deg.)	-8.1744	-6.8557	-6.3913	-6.3913	-6.9828	-7.4160	-6.9111	-6.9265	-8.1331
ANGLE of RECESS, $\delta_{S_{r,w}}$ (Deg.)	9.9211	11.5456	11.6151	11.9864	11.1693	11.1733	11.0800	12.2915	9.9224
CONTACT PATH, (mm)	8.9050	9.0575	9.0801	9.2001	8.9348	9.1500	9.1511	9.5420	8.9647

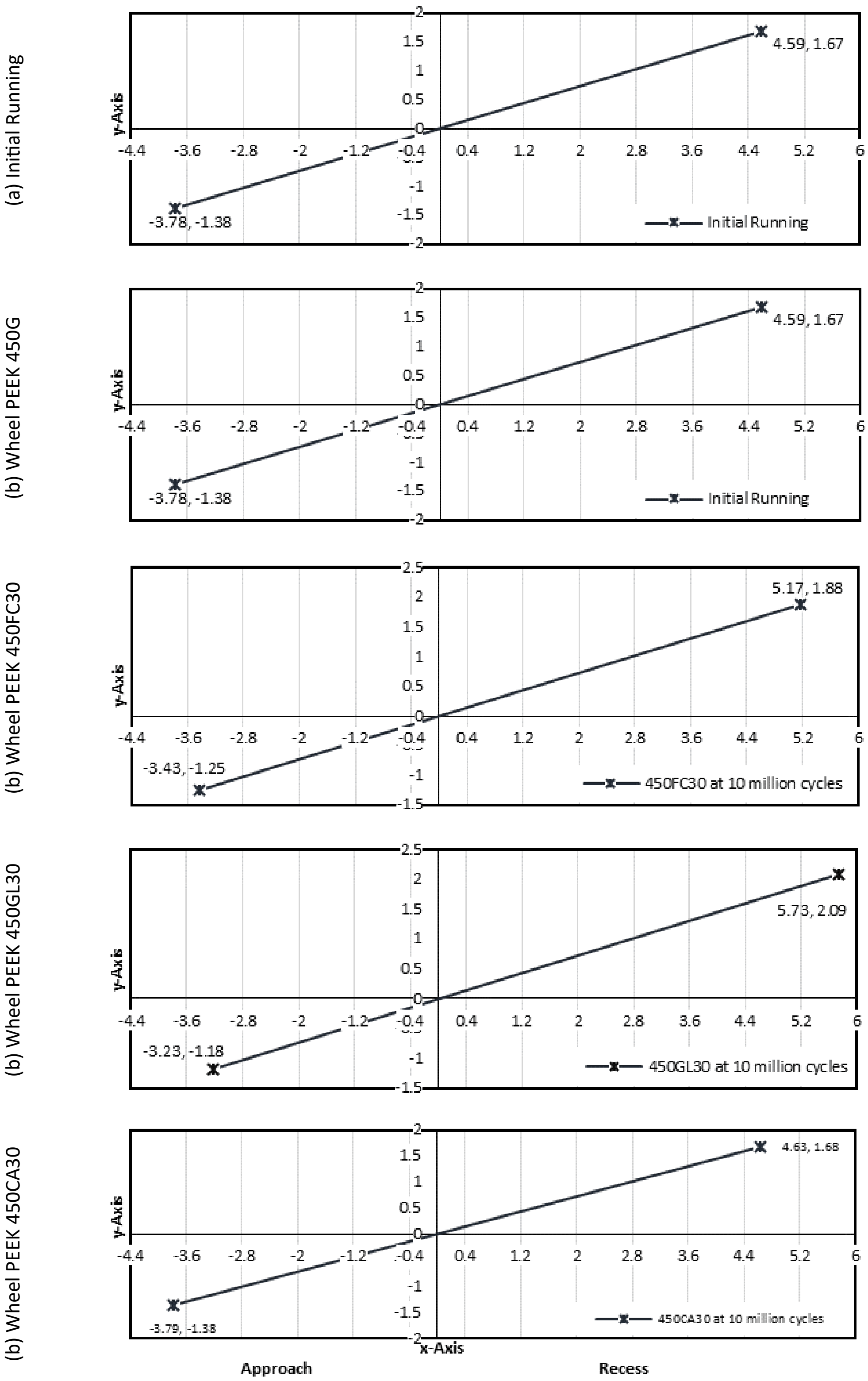

***Figure 5. 8** Illustration of Changes in Approach and Recess Lines on Worn Teeth for PEEKs - BS-PA20*

5.5.5 Frictional Heating

Flash temperature is affected by both the temperature rise due to mechanical loads and changes in the stiffness of polymer materials. Several factors, including the coefficient of friction, strain responses, tooth wear, and stress-induced bending deformation, influence these variations. The study investigated the behaviour of polymer gears, explicitly focusing on the viscoelastic effect. This was explored through structural-dynamic analysis simulations using a sensible modulus of elasticity. For detailed information on the specific modulus of elasticity related to the wheel made from PEEK material, refer to Chapter 4.

In Figure 5.9 (a) and (b), the results for the coefficient of friction are visually represented, illustrating changes in wear size on the tooth flanks. The study compares variations in transmission efficiency and the coefficient of friction against theoretical expectations and initial running conditions. Measurements were taken at the beginning of the running phase, after 1.44 million, and at 10 million cycles. Load tests assessed Gear transmission efficiency by comparing four PEEK wheels, specifically the MKII - 2022 and the 450CA30. Notably, the 450CA30 displayed a lower coefficient of friction, approximately 0.2461, while maintaining optimal power transmission performance. The most significant increase in the friction coefficient and the decline in transmission efficiency were observed in the 450GL30, which experienced the highest wear on its teeth. The 450G and 450FC30 showed similar increases in the coefficient of friction.

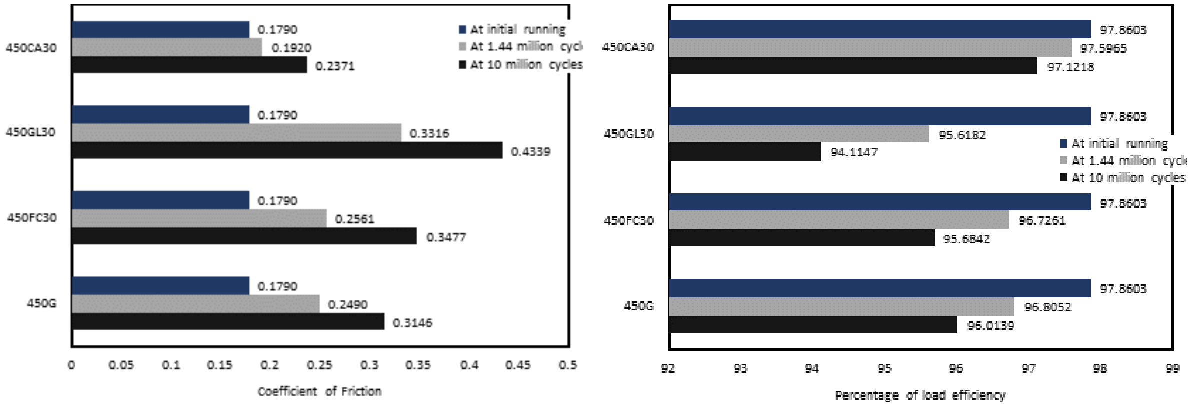

(a) Coefficient of Friction

(b) Percentage of Load Efficient

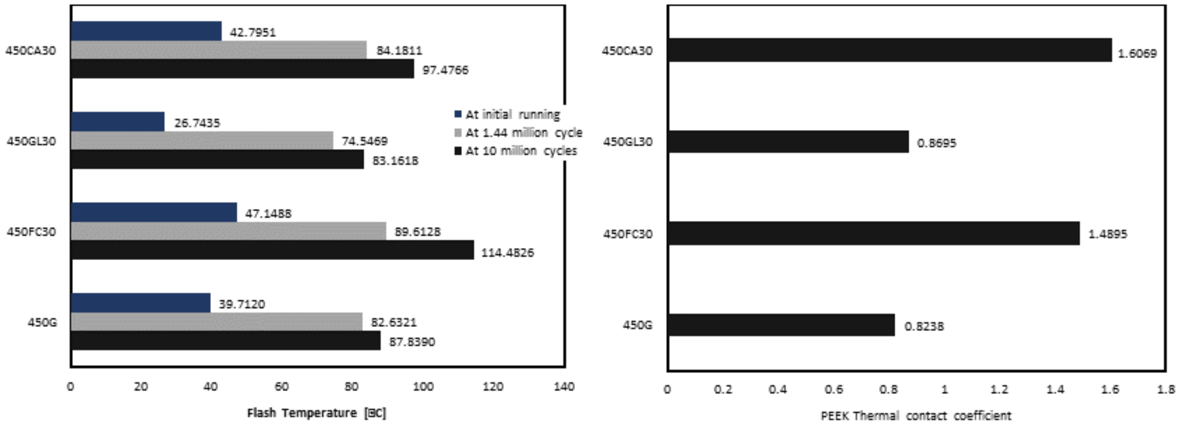

(c) Flash Temperature

(d) PEEK Thermal Contact Coefficient

***Figure 5. 9** Coefficient of Friction and Flash Temperature Due to Wear for BS-20PA - PEEKs vs Steel Testing at 1.44 and 10 million Cycles, Respectively*

Figure 5.9 (c) and (d) illustrate the correlation between variations in the thermal contact coefficient and flash temperature calculation. However, the 450CA30 and 450FC30 exhibited higher flash temperatures and thermal contact coefficients than the 450G and 450GL30. This phenomenon is primarily influenced by the material properties, specifically the materials' thermal conductivity, density, and specific heat, which significantly affect flash temperature behaviour.

5.5.6 Tooth Deformation Calculated

The calculated results indicate substantial tooth deformation along the 3-axial directions due to wear, measured after 10 million cycles. Influenced by the boundaries of material properties, Table 5.4 shows that the 450GL30 experienced the most significant deformation. In contrast, the 450FC30, 450G, and 450CA30 exhibited similar levels of deformation.

Table 5. 4 *Tooth Bending Deformation in Three-Axial Directions*

	Max. Tooth Deformation in Axial x, ($\boldsymbol{mm}$)	*Tooth Deformation in Axial y,* ($\boldsymbol{mm}$)	*Gear Shift in Axial z,* ($\boldsymbol{mm}$)
450G	*-2.2639*	*1.8092*	*-0.1800*
450FC30	*-2.2578*		
450GL30	*-2.4878*		
450CA30	*-2.2845*		

5.6 Chapter Summary

This study thoroughly explored PEEK involute wheel failures and the increased friction on gear teeth resulting from kinematic contact. The investigation into the influence of the contact path's approach and recess lines on tooth flank wear led to several key conclusions:

(a) A revised equation for changing involute tooth geometries based on ball contact was proposed, leading to developing a specific gear wear equation for polymer materials. This equation takes into consideration the wear of teeth and ball contacts. The study also analysed frictional behaviours on the tooth flank, referencing Buckingham's and Merritt’s equations.

(b) An equation was formulated to account for the changes in the approach and recess lines on the un-normal contact path. This equation was instrumental in understanding the modifications in gear tooth geometry due to wear.

(c) The study observed that the most significant increase in the friction coefficient and a decline in transmission efficiency occurred in the 450GL30 gear, which exhibited the highest wear on its teeth. Similarly, the 450G and 450FC30 gears showed notable increases in their friction coefficients.

These findings contribute to a better understanding of gear wear, particularly in PEEK materials, and offer valuable insights into the kinematics of gear teeth under various wear conditions. Developing these equations and analysing frictional behaviour provide crucial information for improving the design and durability of polymer gears.

Chapter 6

Advanced Evaluating Involute Tooth Wear in PEEK Gears: Advanced

This chapter presents a comparative analysis of four PEEK grades - 450G, 450FC30, 450GL30, and 450CA30 - in wheel applications with a 20-degree pressure angle (PA20), subjecting the gears to 10 million cycles using Structural & Transient Dynamic models. The examination reveals changes in the contact pressure stress interface and the expanded stress distribution on tooth flanks. As a result, the research summarised in this chapter highlights noticeable variations in load sharing, tooth deformation, and equivalent stress behaviours.

6.1 Research background

This chapter delves into the behaviour of polymer gears through theoretical (as continued in Chapter 5), experimental, and analytical simulation methods. Using simulations, it emphasises the effects of changing and imperfect involute tooth geometries on weight loss, wear depth, load sharing ratio, frictional values, and surface temperature between gear pairs (steel vs. polymer). The chapter concludes by analysing contact ratio, frictional temperature, and tooth bending stress between gear pairs through Transient Thermal and Dynamic Structural simulations.

The research is centred on increased wear in involute tooth problems through simulation design. A comprehensive methodology was adopted, incorporating finite element analysis to conduct dynamic structural and transient thermal simulations. The focus was on the meshing dynamics of the gear pair between Pinion Steel and Wheel, identifying critical points (PEEKs) at 10 million cycles. Experimental conditions were set with a load of 9.38 Nm, a speed of 1000 rpm, and 15 degrees of gear rotation in 0.0024995 seconds. Using three-dimensional tooth profiles, ANSYS software was utilised to simulate the gear PEEK geometries. Boundary conditions were meticulously established, covering factors such as the coefficient of friction, flash temperature, augmented formulation, and interface adjustments for contact interaction. These parameters were integrated into the dynamic structural and thermal transient analyses, yielding substantial insights into the wear behaviour of gear teeth under the specified conditions.

6.2 Methodology and Boundary Conditions

6.2.1 Methodology

Through experimental testing and analytical simulation, this chapter explores the gear wear characteristics of four PEEK grades - 450G, 450FC30, 450GL30, and 450CA30. The primary focus is evaluating the load-sharing ratio, tooth bending stress, and frictional temperature variations between gear pairs (steel vs. polymer). These evaluations use ANSYS simulation tools, particularly emphasising Transient Thermal and Dynamic Structural simulation. A schematic overview of the chapter's approach is presented, with detailed information referenced in Chapter 4. The investigation aims to understand the impact of changes in involute tooth geometries and meshing errors on increased weight loss on the tooth flanks.

6.2.2 Boundary Conditions

The experimental aspect of this research involved analysing the effects of torque and rotational speed on gear wear. The torque was set at 9.38 Nm, and the rotational speed was maintained at 1,000 rpm, as detailed in Table 4.5 and Figure 4.7. Notably, an increase in wear on the tooth flank was observed during real-time machine operation, with the wear accumulation reaching up to 10 million cycles. The significance of these factors lies in their contribution to a deeper understanding of gear wear and its implications for long-term machinery performance.

6.3 Calculating

6.3.1 Demonstrating the Impact of Revised Involute Tooth Geometries

This part of the investigation involved calculating the contact path between gear teeth, revealing variations in the approach lengths and recess along the non-normal contact path. These variations were derived based on factors like circular pitch and the contact path line using revised equations. A notable observation was increased tooth flank wear, as evidenced by measurements taken after 10 million cycles. Chapter 5 of the thesis further elaborates on the impact of these revised involute tooth geometries, confirming that changes in the equations governing tooth flank geometry significantly affect wear behaviour.

6.3.2 Calculating the Coefficient of Friction and Flash Temperature

The study also investigated the role of various factors, including the coefficient of friction, strain responses, tooth wear, and stress-induced bending deformation, in influencing gear behaviour. Special attention was given to the behaviour of polymer gears, taking into account the viscoelastic effect through structural-dynamic analysis simulations. For a comprehensive understanding of these aspects, Chapter 5 provides detailed information.

6.4 Numerical Model

Finite element analysis (FEA) utilising ANSYS software was employed to examine gear meshing and rotation, focusing on dynamic structural and transient thermal simulations. The behaviour of gear systems, specifically between pinion Steel and wheel PEEKs, was studied over 10 million cycles. The analysis accounted for a load of 9.38 Nm, a speed of 1,000 rpm, and a 15-degree rotation occurring in 0.002499 seconds. The finite element modelling provided insights into the gears' stress distribution, deformation patterns, and thermal responses.

6.4.1 Designing of 3D-Geometries

The standard involute gear profile, defined by the shape of an involute curve and the base circle diameter, ensures consistent pitch and pressure angles. Marples Gear Inc. examined how this gear profile influences power transmission and noise during gear meshing. Their analysis offers valuable insights into the operational characteristics of gear sets, enhancing the understanding of performance and noise behaviour.

Figure 6.1 depicts two-dimensional and three-dimensional involute gear profiles at 10 million cycles for BS-20PA – PEEKs. In this figure, two- and three-dimensional geometries were generated and incorporated into the simulation. The figure presents front views of a 2D line sketch depicting involute curves on worn teeth, captured by a Pylon micro-camera. 450GL30 showed the most significant wear among the PEEK grades analysed, while 450G and 450FC30 exhibited similar wear patterns. In contrast, 450CA displayed minor wear loss, indicating distinct wear behaviours across the different PEEK grades.

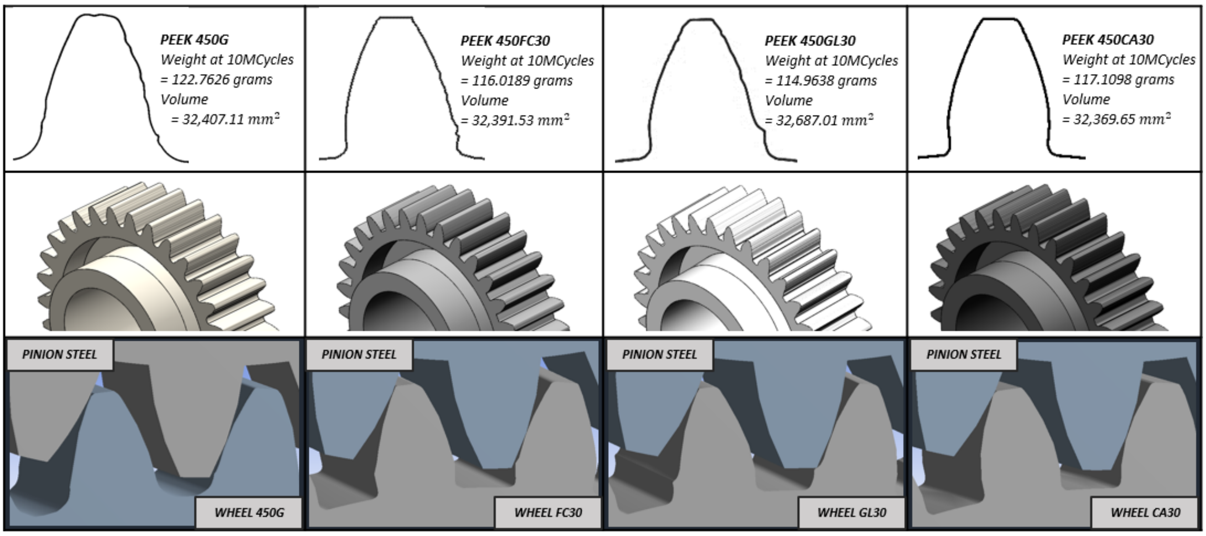

***Figure 6. 1** Two- and Three-Dimensional Involute Gear Profiles at 10 Million Cycles, for BS-20PA – PEEKs*

6.4.2 Gear Meshing

A dynamic spur gear meshing behaviour model was developed, considering contact ratio, time-varying meshing stiffness, and backlash. Considerations for elastic contact, temperature rise on the tooth flank, and lubrication were also included. Applying the involute gear meshing theory, the time-varying backlash was used to determine tooth profiles. This involved calculating the roll angle from the root to the tip of gear teeth within the "start active profile of roll angle" to "end active profile of roll angle" range [115], illustrated in Figure 3.10, rolling angle (RA).

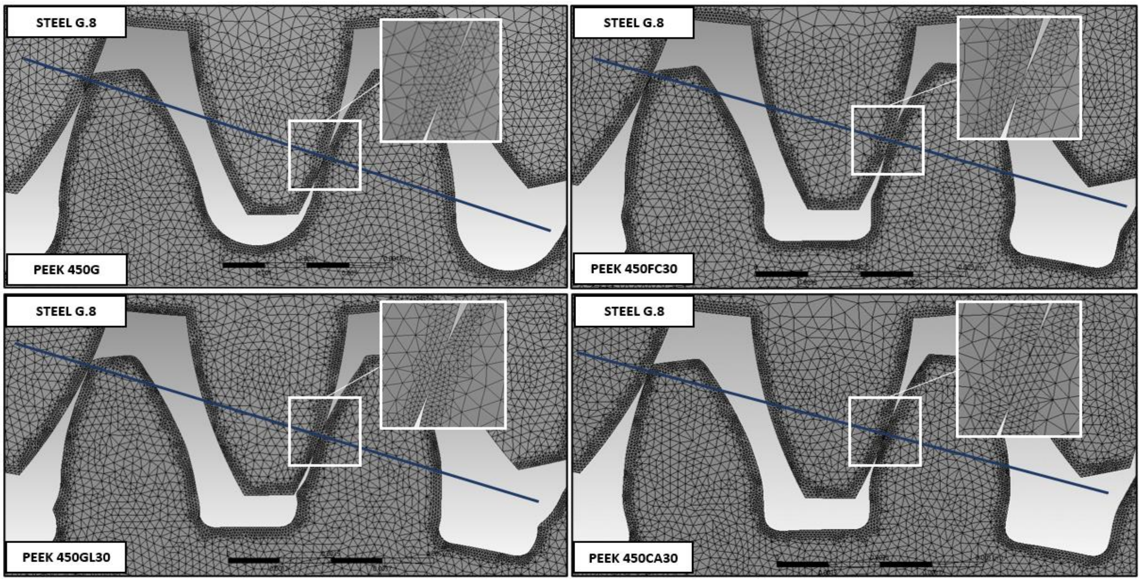

(a) At 1.44 Million Cycles

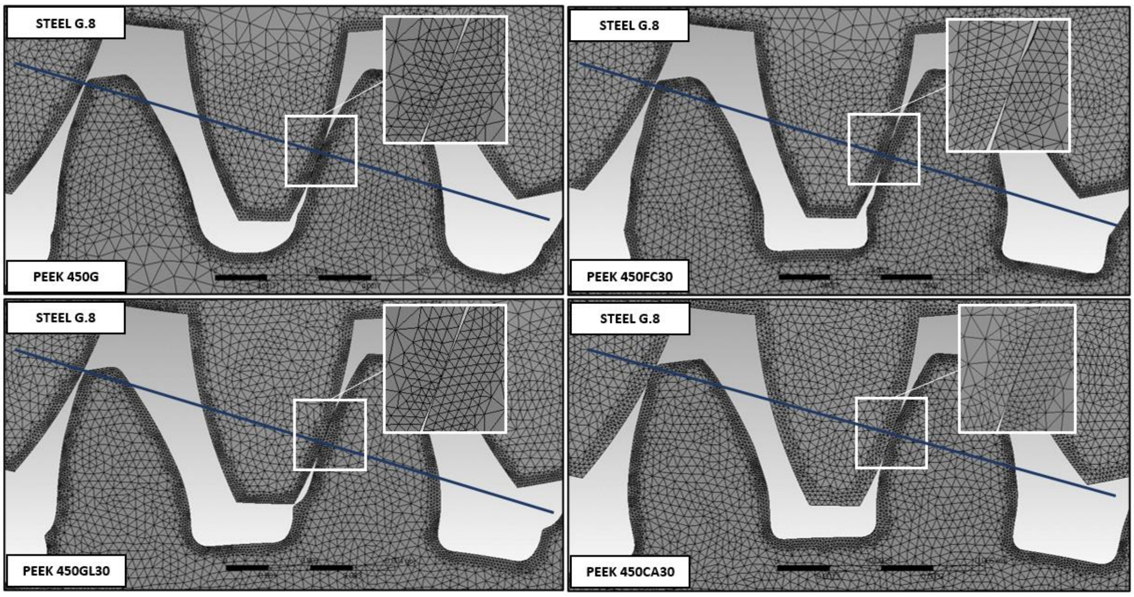

(b) At 10 Million Cycles

Figure 6. 2 *Polymer the Pair Gears Geometries of the Numerical Model and Mesh Element*

This numerical model, as shown in Figure 6.2, depicts Ansys's mesh and element qualities, focusing on the new line of contact path influenced by tooth surface failures. Distortions and deformations in polymer gear failures can impact mesh quality. Therefore, contact tetrahedrons were used, devising and applying meshing techniques to number tooth surface defects accurately. This approach is critical for enhancing mesh quality, even as polymer gears undergo deformation and distortion from tooth contact surfaces.

6.5 Simulating Results

6.5.1 Flash Temperature and Coefficient of Friction

The ANSYS simulation analysis, incorporating dynamic mechanical analysis and simulation, produced results in Figure 6.3.

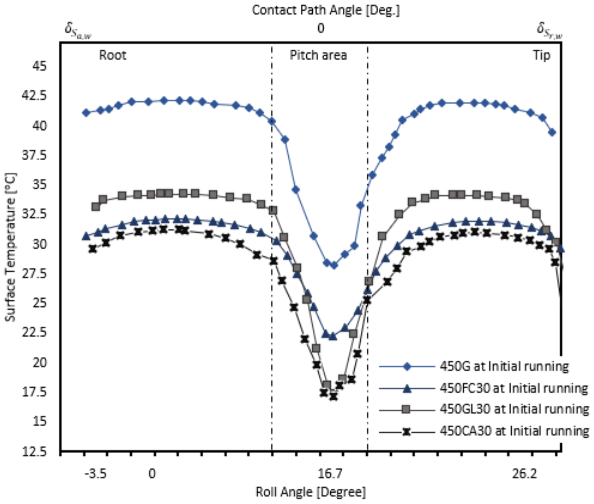

(b) At Initial Running

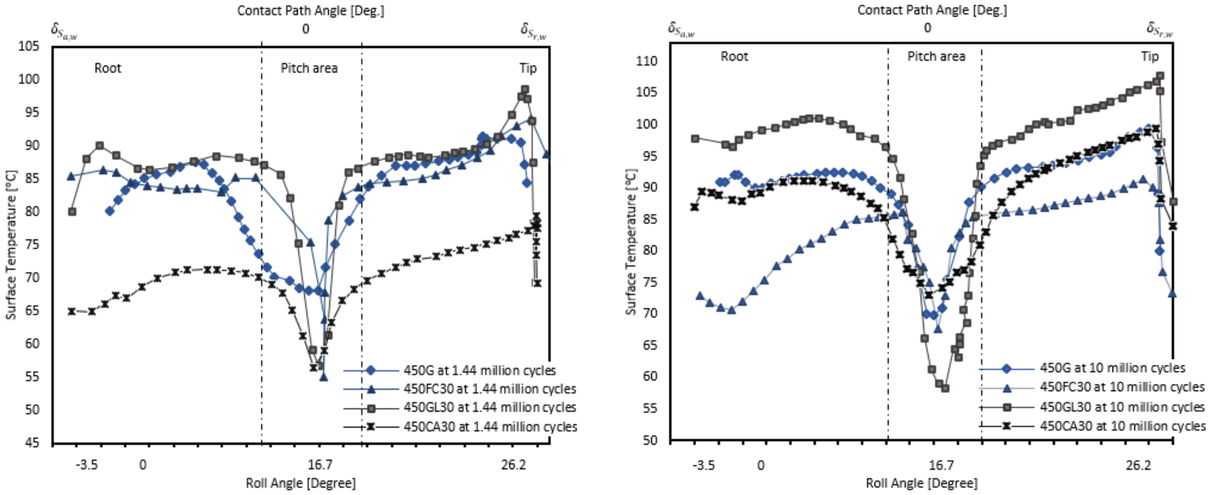

(b) At 1.44 Million Cycles

(c) At 10 Million Cycles

Figure 6. 3 *Maximum Flash Temperatures of Wheel PEEKs*

These results, obtained over 10 million cycles, showed the peak flash temperatures for different wheel PEEKs: 450G, 450FC30, 450GL30, and 450CA30. The study examined the relationship between alterations in thermal contact coefficient and flash temperature. It was observed that 450CA30 and 450FC30 experienced elevated flash temperatures and thermal contact coefficients compared to 450G and 450GL30.

Figure 6.3 illustrates the peak flash temperature distribution under diverse load contact conditions at 1.44 and 10 million cycles. The presence of worn teeth during meshing allowed for a more accurate assessment of frictional heat losses and the consequent temperature rise. Notably, the 450GL30 material exhibited a significantly higher temperature increase over extended durations and cycles, showing the fastest and most pronounced deterioration, leading to failure. The figure summarises the pattern of flash temperature increase and the material's susceptibility to damage and failure.

6.5.2 External Heat Flux Generation

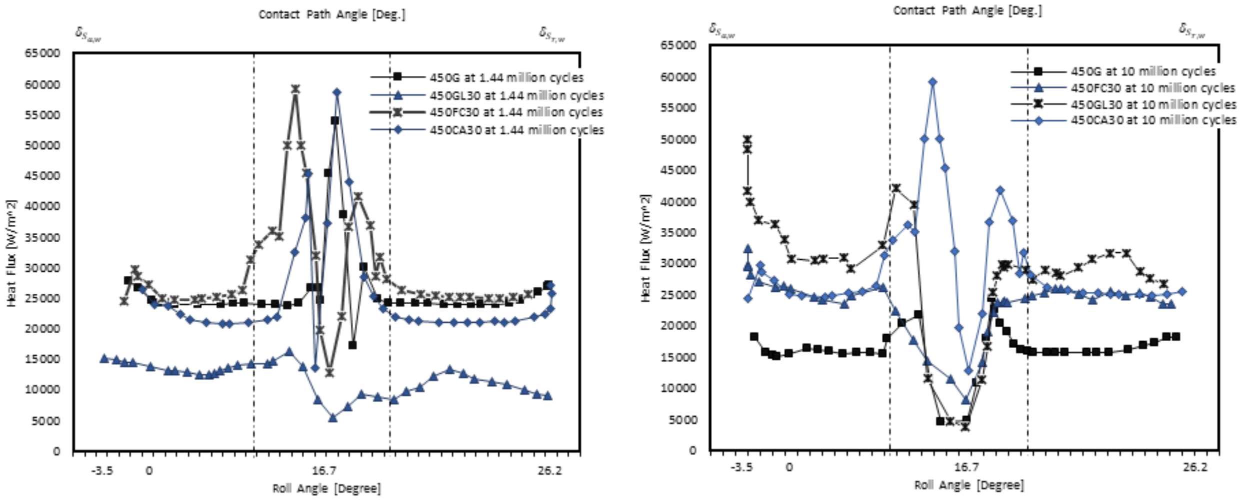

(a) At 1.44 Million Cycles *(b) At 10 Million Cycles*

Figure 6. 4 *Maximum Heat Flux*

The chapter investigates the augmentation of frictional contact on gear teeth, corresponding to kinematic contact behaviour. It analyses frictional heat flux and convective heat transfer coefficient through the Nusselt number equation. The results, shown in Figure 6.4, provide insights into the frictional involute gear approach and its comprehensive understanding of heat-related aspects in gear transmission.

6.5.3 Tooth Contact Pressure Stresses

Factors affecting gear tooth surfaces, including wear, material properties, friction, and temperature effects, are compared. It compares the contact pressure of PEEK wheels on load-sharing using the results from Figure 6.5. The analysis includes new wheels versus worn teeth (1.44 and 10 million cycles) across four PEEK grades, considering their impact on involute gear and structural integrity.

Figure 6.5 presents the calculation results using a programmable approach to study contact pressure stresses caused by worn teeth deformation. This analysis encompasses factors like load conditions, contact ratio computation, elastic modulus, friction coefficient, flash temperature, and the time taken for a 15-degree rotation in 0.0024995 seconds The Hertz equation within gear meshing simulation explores how contact pressure stress functions under varied conditions of changing involute surfaces and simulation parameters.

Factors affecting gear tooth surfaces, including wear, material properties, friction, and temperature effects, are compared. It compares the contact pressure of PEEK wheels on load-sharing using the results from Figure 6.5.

At 10 million cycles, PEEK 450G showed high-contact stress values, with the highest stress at the root or base circle. For PEEK 450FC30, the highest-pressure contact stress values were different compared to other PEEKs, notably at the tip, pitch area, and root or base circle. PEEK 450GL30 showed similar high-pressure contact stress values as PEEK 450G, while

PEEK 450CA30 displayed the lowest pressure contact stress values among the PEEKs, particularly with high effects at the tip and root teeth.

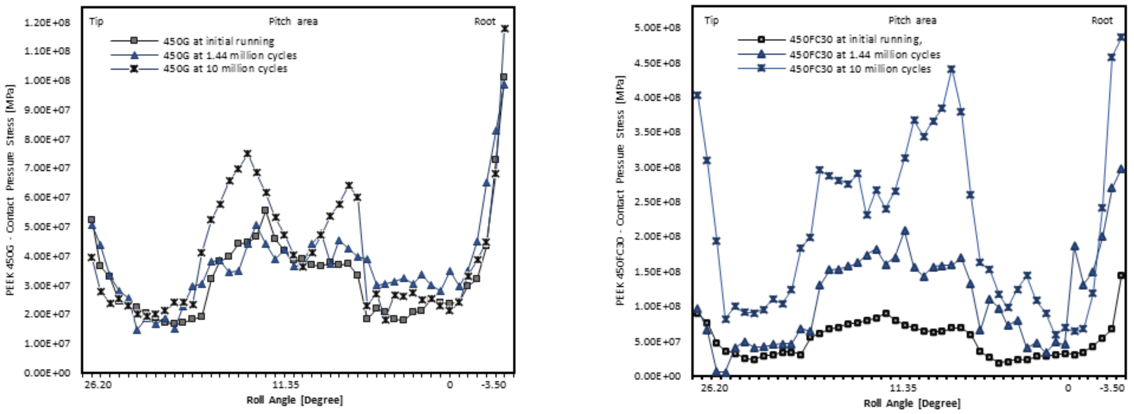

(a) Wheel PEEK 450G *(b) Wheel PEEK 450FC30*

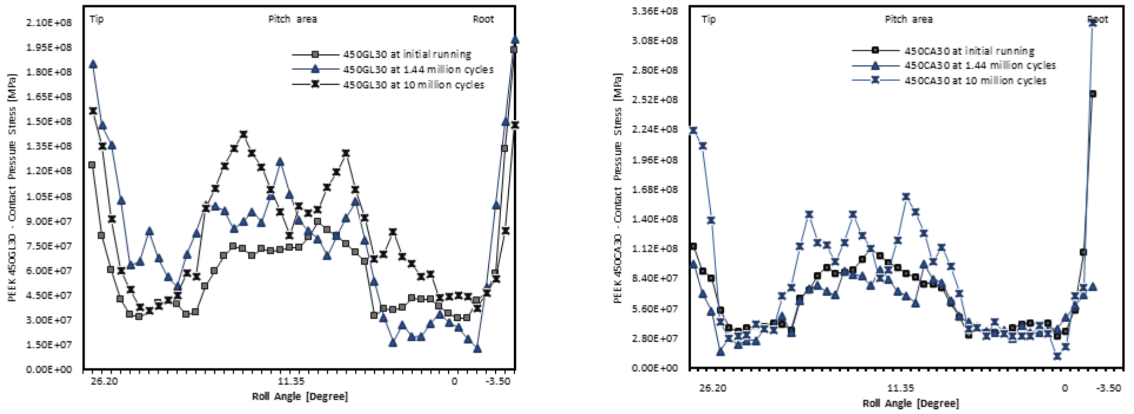

(c) Wheel PEEK 450GL30 *(d) Wheel PEEK 450CA30*

Figure 6. 5 *Maximum Contact Pressure Stresses*

6.5.4 Rotational Correlation on the Roll Angle Measures Equivalent Stress and Tooth Deformation on Tooth Contact

This study used a programmable method to calculate and analyse the equivalent stresses affecting the tooth flank in a pinion Steel versus wheel PEEK transmission system. The analysis considered the deformation changes due to wear and encompassed factors such as contact ratio, load, and material conditions, factoring in the time required for a 15-degree rotation in 0.002499 seconds. The findings on the equivalent stress distribution behaviour at 10 million cycles for the pinion Steel versus wheel PEEKs transmission system are depicted in Figures 6.6 and 6.7 and summarised in Table 6.1. These results include information on tooth deformation obtained through simulation analysis.

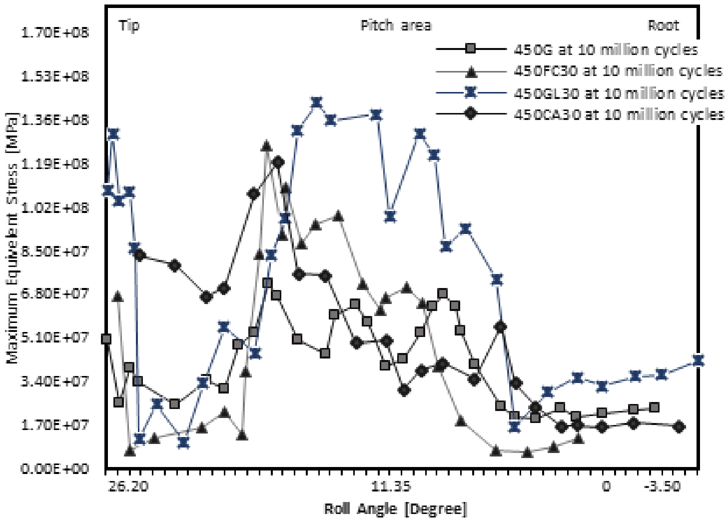

Figure 6. 6 *Presents the Comparisons of the Maximum Equivalent Stresses*

Table 6. 1 *Shows the Results of Four PEEK Polymer Gears, at the Pitch Area Meshing Teeth*

	10MCycles-450G	**10MCycles-450FC30**	**10MCycles-450GL30**	**10MCycles-450CA30**
Tensile Yield Strength at 23°C	*98 MPa*	*95 MPa*	*185 MPa*	*265 MPa*
Elastic Modulus at 23°C	*4.00-4.20 GPa*	*8.05-13.00 GPa*	*9.48-11.50 GPa*	*20.00-25.00 GPa*
PEEK Density	$1300\ kg/m^3$	$1450\ kg/m^3$	$1400\ kg/m^3$	$1510\ kg/m^3$
Weight Loss at 10MCycles	*0.9068 g*	*0.6489 g*	***1.6144 g***	*0.1992 g*
Transmission Efficiency	*96.0139%*	*95.6842%*	***94.1147%***	***97.1218%***
Coefficient of Friction at 10MCycles	*0.3146*	*0.3477*	***0.4339***	*0.2371*
Flash Temperature at 10MCycles	*87.8390℃*	*114.4826℃*	*83.1618℃*	*97.4766℃*
ANSYS-Max. Equivalent Elastic Strain	***0.0277 m/m***	*0.0018 m/m*	*0.0150 m/m*	*0.0119 m/m*
ANSYS-Max. Equivalent Stress at HPSTC	*89.97 MPa* 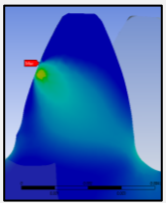	***193.74 MPa*** 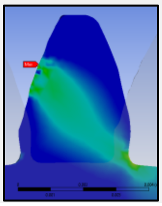	***142.66 MPa*** 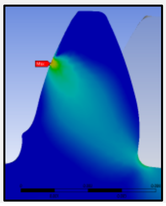	*119.26 MPa* 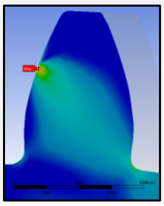
ANSYS-Max. Deformation at Pitch Area	$5.5889\times10^{-6}mm$	$3.4441\times10^{-7}mm$	$\mathbf{7.1621\times10^{-6}mm}$	$1.3289\times10^{-6}mm$

At 10 million cycles, the ANSYS simulation results in Figures 6.5, 6.6, and Table 6.1 demonstrate the behaviour of maximum equivalent stresses on contact tooth flanks, indicating more significant changes in involute tooth failures. Among the wheel PEEKs, PEEK 450G exhibited the lowest maximum comparable stress values, primarily at the HPSTC, around 89.97 MPa. The whole tooth deformation was recorded at the pitch area, measuring approximately 5.5890×10^{-6} mm.

For PEEK 450FC30, the highest maximum equivalent stress values were observed compared to other PEEKs. These peak stresses occurred at the tip and pitch area (HPSTC and LPSTC), with values of 194.61, 193.74, and 215.32 MPa, respectively. The highest values of maximum equivalent stress for PEEK 450GL30 were also at the tip and pitch area of HPSTC, reaching approximately 108.14 and 193.74 MPa, respectively.

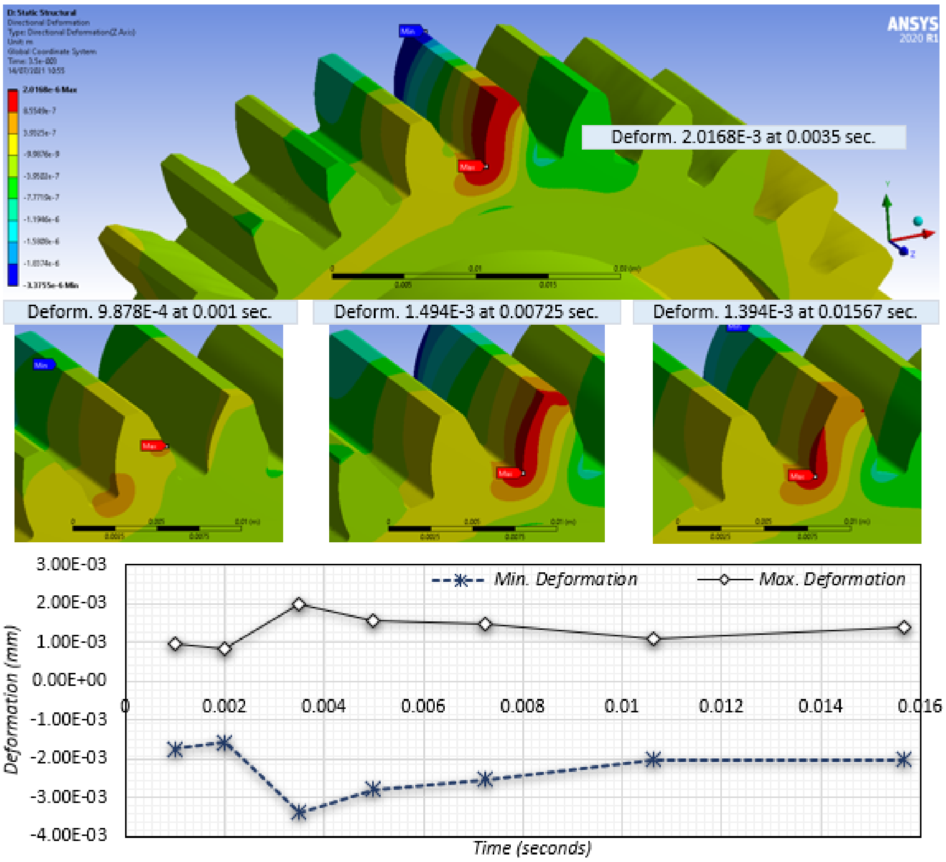

Figure 6. *7 Display the Maximum and Minimum of Deformation for PEEK 450GL30*

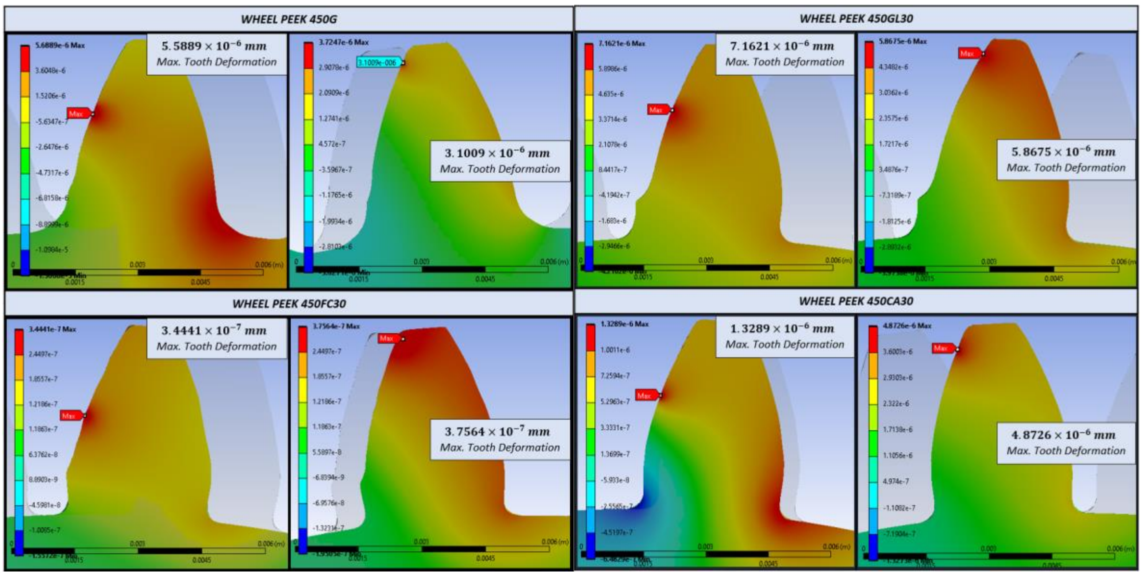

Figure 6. 8 *Shows the Maximum Deformation Informed*

According to Table 6.1, Figures 6.7 and 6.8, the results of maximum and minimum tooth deformation behaviour in the last meshing teeth indicate the following:

(a) Wheel 450G exhibited the lowest maximum equivalent stress values compared to other PEEKs, with the highest effect at HPSTC, reaching approximately 89.97 MPa. The maximum tooth deformation occurred at the pitch area, measuring about 5.5889×10^{-6} mm.

(b) Wheel 450FC30 displayed the highest maximum equivalent stress values among the PEEKs. It experienced peak stresses at the tip and pitch area (HPSTC and LPSTC), measuring 194.61, 193.74, and 215.32 MPa, respectively. The highest tooth deformation occurred at the tip, measuring about 3.7564×10^{-7} mm.

(c) Wheel 450GL30 showed higher maximum equivalent stress values at the tip and pitch area (HPSTC), measuring 108.14 and 193.74 MPa, respectively. The maximum tooth deformation was observed at the pitch area, measuring about 7.1621×10^{-6} mm.

(d) Wheel 450CA30 exhibited lower maximum equivalent stress values than 450FC30 and 450GL30. The highest stress was at the pitch area (HPSTC), measuring about 119.26 MPa. The maximum tooth deformation was observed at the tip, measuring about 4.8726×10^{-6} mm.

In conclusion, the variations in maximum equivalent stresses and tooth deformation behaviour of wheel PEEKs are influenced by involute tooth wear, material strength, elastic modulus, and significant frictional temperature effects.

6.6 Chapter Summary

The chapter's findings on wheel PEEKs (Polyetheretherketone materials) reveal variations in maximum equivalent stresses and tooth deformation behaviour. These variations are attributed to several factors:

1. Escalated Involute Tooth Wear: The degree of wear on the tooth flank of the gears, particularly evident in the involute tooth profiles, played a crucial role in determining the stress and deformation behaviours observed. The chapter highlights that increased wear, influenced by the gear's operation and meshing dynamics, significantly impacts the gear's structural integrity.

2. Material Strength and Elastic Modulus: The intrinsic properties of the PEEK materials, such as strength and elastic modulus, were critical in defining the gear's response to operational stresses. Materials with higher strength and stiffness demonstrated better resistance to deformation and wear, impacting their overall performance and durability.

3. Friction-Induced Temperature Effects: Pronounced temperature effects induced by friction at the gear teeth contact points were a significant factor. The chapter notes that higher friction levels lead to elevated temperatures, which can alter the material properties and increase wear and deformation.

4. Material Properties Influence: The specific material properties of the PEEK grades, including thermal conductivity, density, and specific heat capacity, emerged as significant influencers. These properties play a vital role in how the material responds to thermal stresses

and distributes heat, affecting the dynamics of flash temperature and the gear's thermal behaviour.

5. Frictional Coefficients and Flash Temperatures: Variations in frictional coefficients and flash temperatures significantly influenced the involute tooth geometries. The chapter demonstrates that changes in friction levels and resultant temperature variations can alter the tooth flank wear pattern and rate.

6. Impact of Approach and Recess Lines: The research also highlights the impact of the gear's approach and recess lines on tooth flank wear. These geometrical aspects of the gear teeth contribute to how the gears mesh and subsequently influence the wear patterns.

7. Comparison Among PEEK Grades: 450GL30 showed the most rapid volume loss and significant acceleration in vibration among the various PEEK grades studied. This suggests that this particular grade may be more prone to wear under certain operational conditions. In contrast, 450CA30 demonstrated lower volume loss and exhibited higher strength and density compared to other grades, indicating its potential for better durability and wear resistance performance.

In summary, the chapter provides comprehensive insights into how different factors, particularly material properties and operational conditions, affect the performance and longevity of PEEK gears in transmission systems. The observed variations in stress, deformation, and wear behaviours underscore the importance of considering these factors in gear design and material selection.

Chapter 7

Frictional Coefficients and Power Loss in PEEK Gears: Analysing Wear and Efficiencies

This chapter examines the influence of varying frictional coefficients on actual power losses in gears. It focuses on aspects that affect tooth wear and gear loading, particularly on polymer gears. The study aims to predict power loss accurately, particularly when contact is reduced due to tooth flank wear, which could lead to worn teeth failure.

This research theoretically explains the transition from sliding to rolling during gear meshing. This transition is crucial as it affects the transfer of power loss within the system, eventually manifesting as heat and other forms of dissipation. To corroborate these theoretical insights, the study includes a comparison with experimental data from Kono's tests. This comparative analysis validates the theoretical predictions, providing a comprehensive evaluation of the reliability of the frictional coefficient models used in this study.

7.1 Research Background

The study delves into factors influencing wear behaviour, focusing on the tribological performance of polymers and composites. Considered factors include the polymer's molecular structure, transmission errors, applied load, sliding speed, temperature, and environmental conditions [65] [66] [67] [68] [69] [70]. The review also covers strategies to enhance gear performance, such as optimising tooth profiles, applying surface treatments, and using coatings to reduce friction and wear effectively. In 1989, Bahadur and Zheng investigated the tribological behaviour of polyester composites, examining their wear resistance and performance under various frictional conditions. Their study also analysed wear mechanisms, such as abrasive and adhesive wear, to assess the composites' resilience to frictional forces [67]. The frictional resistance between contacting surfaces is not uniform and varies along the contact path, influencing the sliding velocity between gear teeth. Understanding this variance is crucial for predicting frictional behaviour in applications like machinery design, optimising material pairing, and ensuring systems' smooth operation involving sliding or rolling surfaces.

In 2016, Fernandes and colleagues presented findings incorporating friction coefficient data from various equations, including those developed by Drozdov and Gavrikov, Schlenk, Bennedict and Kelley, and Hai. They employed an algorithm accounting for load distribution along the contact path to calculate power loss for each equation. Interestingly, these equations predicted significantly higher power loss values than those measured. Even Schlenk's equation, used without calibration for lubricant factors, yielded results closely aligned with other equations' predictions [72] [132]. Thus, this chapter provides a visual representation of how the friction coefficient changes along the contact path of a spur gear, as illustrated in Figure 2.16 in Chapter 2.

Therefore, this chapter explores the effects of variations in the frictional coefficient on power losses in gears. It considers critical factors such as tooth wear and the impact of load on gears, with the overarching aim of establishing a clear relationship between these variables and the power losses resulting from sliding within the gear system.

7.2 Theory

This section delves into the investigation of the frictional coefficient, concentrating on various factors related to the shape and characteristics of spur gears. It also examines the conditions influencing the amount of power loss and the frictional coefficient associated with PEEK gears.

7.2.1 Involute Wear of Teeth in Unlubricated Testing

A novel equation has been developed to predict gear wear in polymer materials, with a specific focus on involute tooth failure, as outlined in Chapter 4. This equation is an advancement over Buckingham and Merritt's formulas. It integrates modifications based on various theories, considering critical elements such as the contact path (including approach and recess lines), base pitch, the ball of contact, and contact angles. This improved equation presents a more comprehensive and accurate framework for assessing gear wear in polymer materials.

7.2.2 Instantaneous Frictional Coefficient

A novel equation has been developed to predict gear wear in polymer materials, with a specific focus on involute tooth failure, as outlined in Chapter 4. This equation is an advancement over Buckingham and Merritt's formulas. It integrates modifications based on various theories, considering critical elements such as the contact path (including approach and recess lines), base pitch, the ball of contact, and contact angles. This improved equation presents a more comprehensive and accurate framework for assessing gear wear in polymer materials.

The friction coefficients derived from five different equations and their respective impacts on power loss during gear meshing are detailed in Table 7.1. The study presents five friction coefficient equations applied to spur gears in unlubricated conditions, explicitly focusing on contact along the gear path. This information offers insights into how various frictional formulas influence gear performance under non-lubricated conditions.

Table 7. 1 *Coefficient of Friction Equations Used in This Research*

Formulae	**Functional Details**
[71] Buckingham's equation $\boldsymbol{\mu_B(t) = (1 - \eta) \cdot \left[\frac{2 \cdot (\vartheta_{S_a} + \vartheta_{S_a})}{({\vartheta_{S_a}}^2 + {\vartheta_{S_r}}^2)\left(1 + \frac{1}{m}\right)} \right]}$	The fluctuation of the coefficient of friction's sliding speed based on the involute gear teeth geometry concept influenced.
[61] Merritt's equation $\boldsymbol{\mu_M(t) = (1 - \eta) \cdot \frac{1}{\sec \varphi} \cdot \left[\left(\frac{d_p d_g}{d_p + d_g} \right) \left(\frac{l_p + l_w}{{l_p}^2 + {l_w}^2} \right) \right]}$	The fluctuation of the coefficient of friction's sliding speed based on the involute gear teeth geometry concept influenced.
[73] Benedict & Kelley's equation $\boldsymbol{\mu_{B\&K}(x) = 0.0127 \log \left[F_N(x) \frac{2.97 \times 10^4}{\chi\, v_s(x)\, v_r(x)^2} \right]}$	The fluctuation of the coefficient of friction's rolling speed based on the dynamic viscosity and load influenced.
[74] Drozdov & Gavrikov's equation $\boldsymbol{\mu_{D\&G}(x) = \left[0.8 \sqrt{\nu}\, v_s(x) + v_r(x)\phi + 13.4 \right]^{-1}}$	The fluctuation of the coefficient of friction's sliding speed effective.

7.2.3 Power Losses

This segment assesses power loss in gear characteristics such as pitch point location, base pitch along the contact path, diametral pitch, contact ratio, and tooth loading. Rao's 1979 [133] study examines how gear friction coefficients and forces impact power loss within mechanical systems, focusing on gear systems. This research investigates the friction between gear components and the forces exerted on gears contributing to power dissipation or loss.

$$dP = \mu F_N(x) dx$$

$$dx = (sliding\ velocity) dt = (\omega_p + \omega_g) x dt$$

$$dx = \left(\omega_p + \omega_g\right)[r_b tan\varphi - r_b \tan\left(\alpha + \theta\right)]dt$$

The power loss, dE, is considered in terms of the immediately apparent resisting torque and angular distance for less than one wheel revolution, θ.

$$dP = T(x)d\theta$$

$$T(x) = \dot{\omega}_g I_p$$

The polar moment of inertia of the pinion or wheel for sliding velocity, denoted as $I_{p,g}$, plays a role here.

$$\dot{\omega}_p(x) = \frac{\mu\, r_b F_N(x)\left(1 + \frac{\omega_g}{\omega_p}\right)[r_b tan\varphi - r_b \tan\left(\alpha + \theta\right)]}{I_p + \left(\frac{\omega_g}{\omega_p}\right)^2 I_g}$$

The power loss differential over a meshing cycle is calculated, leading to the total power loss based on sliding velocity.

$$P_{p,g} = \frac{\mu\, r_b F_N(x)\, I_{p,g}\left(1 + \frac{\omega_g}{\omega_p}\right)}{I_p + \left(\frac{\omega_g}{\omega_p}\right)^2 I_g}\,[(\beta_a - \beta_r)\, tan\varphi - ln(\forall)]$$

$$\forall = \frac{cos^2\varphi}{cos(\varphi - \beta_a)\, cos(\varphi + \beta_r)}$$

$$P_{total} = P_p + P_g$$

Power loss in gear mechanical systems stems from friction and other resistive forces during sliding or relative motion. This loss, critical for designing and analysing mechanical systems, especially those involving moving parts or sliding contacts, directly affects system efficiency and performance. It is calculated or estimated by considering factors such as sliding velocity.

7.3 Experimental Data

7.3.1 Kono's Experimental Data (2003)

Kono's 2003 experiments focused on measuring the wear of gear teeth, revealing notable changes in the flank profile. The wear was meticulously recorded throughout the experiments. Figures 7.1 and 7.2 visually present the profile changes in a gear tooth during a specific test involving 450G, 17 Nm of torque, and a temperature of 120 ºC for lubrication testing. These observations enabled the study to quantify the wear depth at the pitch point and plot it against the number of cycles, offering valuable insights into the wear behaviour of gear teeth over time.

7.3.1.1 Involute Wear of Teeth in Unlubricated Testing

This section draws from Kono's test data to predict the wear size and weight loss for PEEK 450G. It involves translating the inspection data from Figures 7.1 and 7.2 into volume loss measurements, specifically from Kono's experiments conducted under certain operating conditions: 10 million cycles, 1000 rpm speed, and a torque of 10.88 Nm. The objective is to gauge the extent of gear damage in terms of depth and volume, providing crucial information on the wear characteristics of PEEK 450G material under these specific conditions.

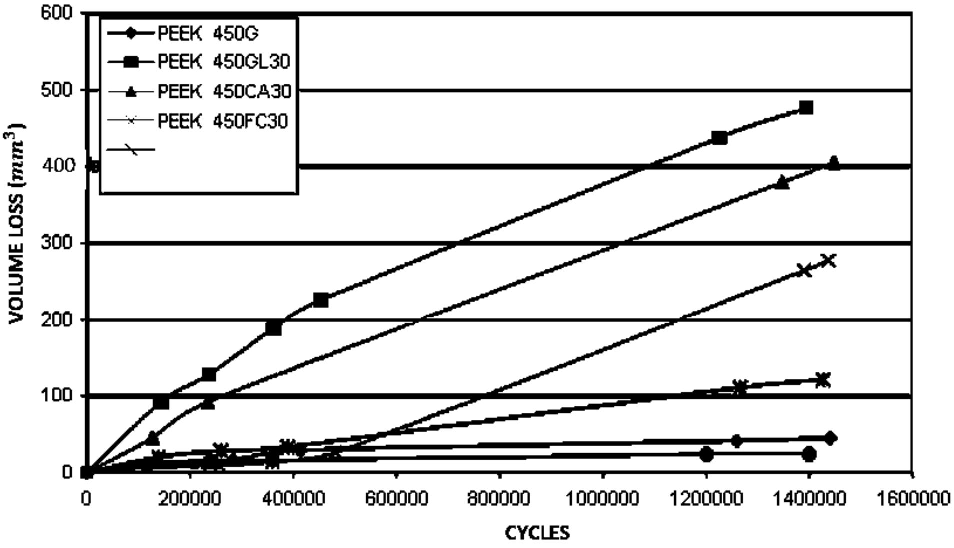

Figure 7. 1 *PEEK Volume Losses as a Function of Cycle Number (adapted from, [3])*

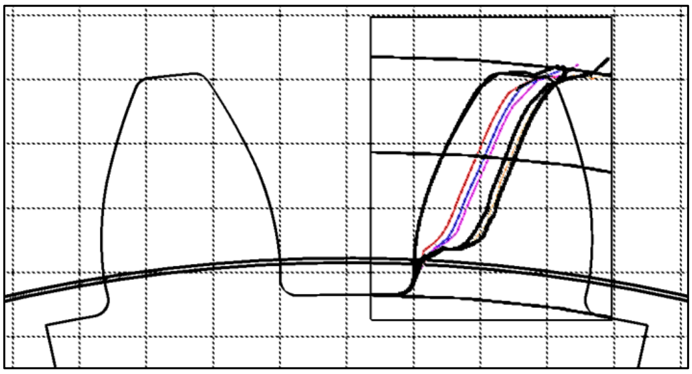

Figure 7. 2 *Depicts the Expected Result of Kono's Involute Wear Teeth Utilising Programmed Designed in 2023 (adapted from, [3])*

Two instruments were utilised for the gear wear measurement process: a Coordinate Measuring Machine (CMM) and a Talysurf, with tolerances of 0.01 micromillimeters. Kono applied programming designs for measuring wear on gear teeth, creating two-dimensional representations of the involute curves on the worn teeth, and projecting weight loss. In the results, the "typical measurement results" are depicted with black lines, whereas the desired or expected dimensions are shown in red lines and generated using AutoCAD software. Each error measurement indicates the discrepancy between the actual measurements from the CMM and Talysurf and the ideal dimensions established in AutoCAD. Figure 7.2 visually demonstrates Kono's concept of involute wear teeth, depicting how it would appear when transformed into programmed designs in 2023.

In Figure 7.1 and 7.2, Kono's worn teeth profiles have been transformed into 2D programming designs, showcasing the evolution of his work. Four different PEEK grades were tested for wear, exhibiting varying degrees of volume loss. The results indicate that 450GL30 showed the highest wear at 380 mm^3, followed by 450CA30 at 295 mm^3, 450FC30 at 160 mm^3, and 450G with the most minor wear loss at 35 mm^3. Figure 7.3 visually represents the concept of wear in Kono's teeth, as introduced in 2003, emphasising that the 2D geometries in the figure were generated or updated in 2023. This information is crucial in understanding the wear characteristics of different PEEK materials and the progression of wear observed in Kono's research.

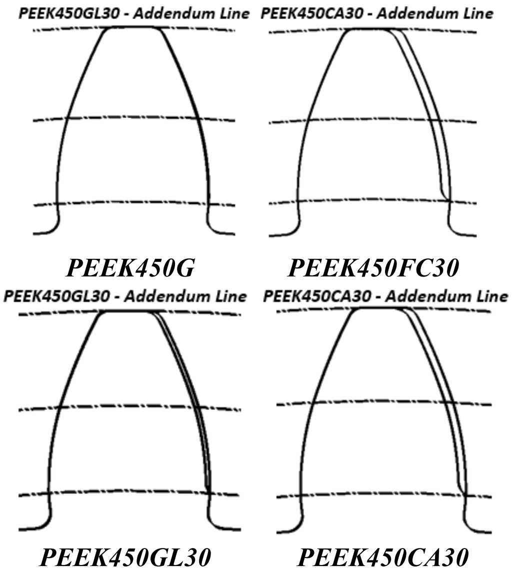

PEEK450G ***PEEK450FC30***

PEEK450GL30 ***PEEK450CA30***

Kono 2003's Volume losses
(450G) -35.00 mm^3
(450FC30) -160.00 mm^3

Kono 2003's Wear distance
(450G) -0.0197mm/tooth
(450FC30) -0.081 mm/tooth

Kono 2003's Volume losses
(450GL30) -380.00 mm^3
(450CA30) -295.00 mm^3
Kono 2003's Wear distance
(450GL30) -0.192 mm/tooth
(450CA30) -0.151 mm/tooth

Figure 7. 3 *The Involute Wear Teeth were Reported by Kono in 2003, Whereas the 2D Geometries were Created in 2023 (adapted from, [3])*

7.3.1.2 Unlubricated Testing for Reaction Force and Load Efficiency

A loading mechanism was employed in the experiments to generate an axial force reaction. Utilising an arm with a mechanical advantage of 4, this mechanism meant that the force applied to the piston was four times greater than the weight on the hanger. This setup demonstrated a linear relationship between the weights and axial thrust. Imperial weights were used to apply torque to the master gearbox. Table 7.2 presents the force reactions on gear teeth corresponding to different levels of applied torque, offering essential data for the experiments.

Table 7. 2 Torque and Force Reactions (after, [3])

Motor Torque, $\boldsymbol{T_m}$ $(\boldsymbol{Nm})$	*Axial Force,* $\boldsymbol{F_a}$ $(\boldsymbol{N})$
8.11	*159.12*
10.88	*209.35*

[3] Load efficiency, particularly in dry running conditions, is important. Inefficient gear trains can convert a considerable portion of mechanical power into heat due to friction, compromising stiffness and strength. The coefficient of friction, especially in conformal contact, may not remain constant and can be influenced by factors like gear torques and speeds. Figure 7.4 illustrates the experimental results, displaying the relationship between Kono's load efficiency percentages and axial force. This provides valuable insights into the efficiency of the gear system under various load conditions

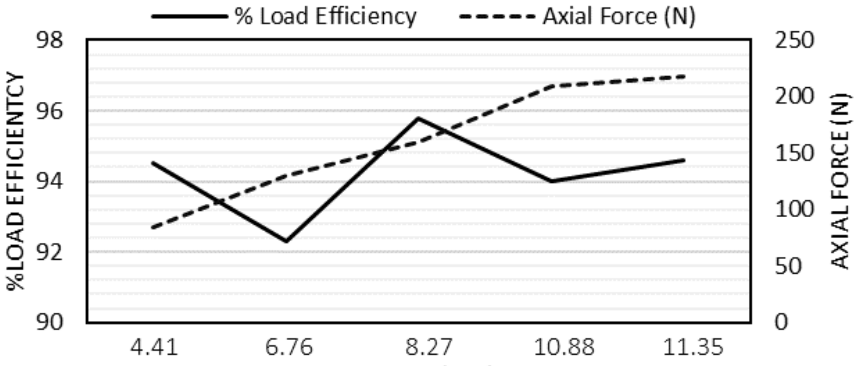

***Figure 7. 4** The Relationship Between Kono's Load Efficiency Percentages and Axial Force*

The gear system's efficiency depended on the transmitted torque, with a noticeable impact observed when the torque exceeded a certain threshold. It's important to note that this analysis did not consider bearing losses. As depicted in Figure 7.4, the minimum efficiency curves were observed at a torque of 4.11 Nm and a speed of 1000 rpm. Across a wide range of axial force and speed, the gear pair's efficiency remained consistently around 94.5%, highlighting the system's performance under different torque and speed conditions.

7.3.1.3 Surface Temperature Data of Unlubricated Testing

Kono measured the surface temperature of the PEEK 450G driving gear after contact with the driven gear. This surface temperature was plotted against the speed of the gears. Generally, there was a slight increase in temperature with speed in all results, except for the highest loads of 8.27 and 10.88 Nm at a speed of 1000 rpm. Figure 7.5 shows that the gear temperature exhibited a linear increase to approximately 103 ºC and 137 ºC under these specific load and speed conditions. These findings offer insights into the temperature behaviour of the gear system under various operational conditions.

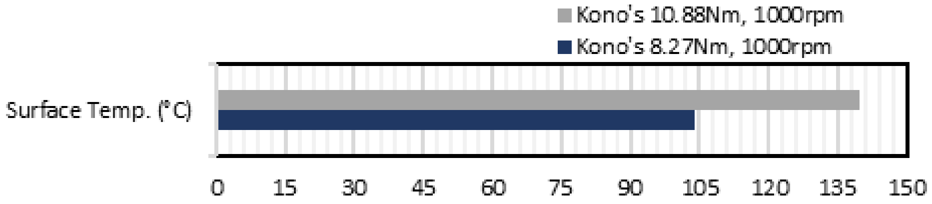

***Figure 7. 5** Surface Temperature Kono's Data*

7.3.2 Experimental in Unlubrication testing, 2023

In Chapter 4, PEEK gears were tested under specific conditions involving applying a torque load of 9.38 Nm and a speed of 1,000 rpm. Unlubricated tests were conducted with four distinct PEEK grades (450G, 450GL30, 450CA30, and 450FL30) in contact with a steel pinion gear. This chapter aimed to evaluate three key aspects: understanding the change in involute wear of the gear teeth, determining the reaction forces generated, and assessing the power transmission efficiency under these torque and speed conditions. These investigations offer vital insights into the performance and wear behaviour of PEEK gears under the specified testing scenario.

7.3.2.1 Involute wear teeth of un-lubrication testing

Programming designs were used to create two-dimensional representations of involute curves on worn gear teeth and to predict weight loss. Among the tested PEEK grades, 450GL30 showed the highest wear, while 450G and 450FC30 exhibited similar wear characteristics. In contrast, 450CA experienced the most minor wear loss. Combining the Pylon C camera with programming designs enabled the creation of detailed two-dimensional representations of involute curves on the worn teeth, facilitating weight loss estimations, as explained in Chapter 4 and illustrated in Figure 7.6.

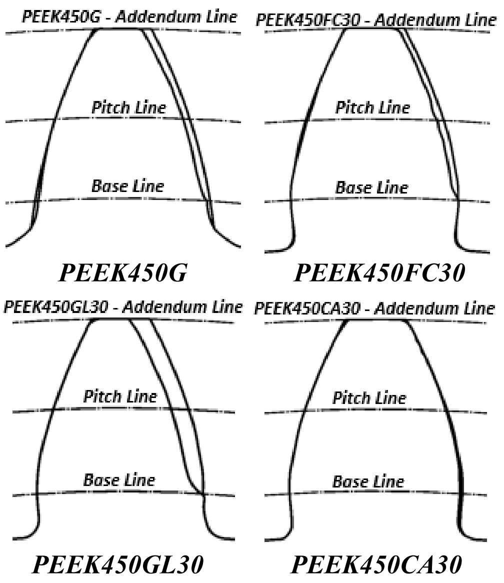

PEEK450G ***PEEK450FC30***

PEEK450GL30 ***PEEK450CA30***

2023's Volume losses

(450G) -697.5385 mm^3

(450FC30) -447.5172 mm^3

2023's Wear distance

(450G) -0.1349mm/tooth

(450FC30) -0.1355 mm/tooth

2023's Volume losses

(450GL30) -1153.1423 mm^3

(450CA30) -132.8000 mm^3

2023's Wear distance

(450GL30) -0.3544 mm/tooth

(450CA30) -0.0327 mm/tooth

Figure 7. 6 *Involute Curves on Worn Teeth and Weight Loss Predictions*

7.3.2.2 Reaction force and load efficiency of un-lubrication testing

The reaction force recorded the response of the worn PEEK gear to mechanical loads and interactions during operation, captured by the e-DAQ recording. The data includes the maximum force and torque reactions, detailed in Chapter 4. Figure 4.18 presents results related to the acceleration of vibrations and reaction forces for the four different PEEK materials—analysis of the vibration data allowed for its conversion into real-time force reactions. Notably, the highest force reactions, as shown in Figure 4.18 (a), (b), and (d) for PEEK materials 450G, 450CA30, and 450FC30, were 198.70 N, 194.10 N, and 189.80 N, respectively. In comparison, the calculated reaction force applied by the rig in the horizontal axial direction was 180.504 N. The force reactions in Figure 4.18 demonstrate that vibrations can significantly impact shafts, leading to fluctuating forces and influencing gear contact surface wear. In contrast, the material 450GL30 in Figure 4.18 (c) experienced less vibration and a maximum applied force of 181.27 N.

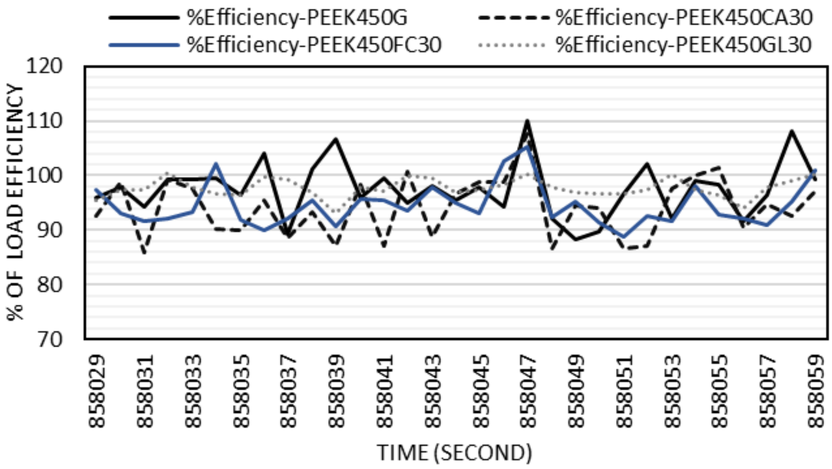

***Figure 7.** 7 Transmission Efficiency Against PEEK Material Performance Projections Before the End of 10 Million Cycles*

These force reactions shed light on the effects of vibration on shafts, leading to changes in force and affecting gear contact surface wear. Figure 7.7 displays the experimental results, indicating the average transmission efficiency percentages during the initial running phase.

All four PEEK materials showed an average transmission efficiency of around 97.86%. However, before reaching 10 million cycles, the average transmission efficiency varied for each PEEK type:

- PEEK450G: 95.75%
- PEEK450GL30: 94.17%
- PEEK450FC30: 95.64%
- PEEK450CA30: 96.81%

These results suggest a gradual decline in transmission efficiency as the gear systems undergo extended testing. Each PEEK material demonstrated slightly different performance characteristics throughout this process.

7.3.2.3 Involute of Involute Tooth Geometries

The calculations regarding the contact paths account for variations in the length of the approach and recess sections along the non-normal contact path. These variations are influenced by factors such as circular pitch and redefined equations of the contact path line, as observed in Kono's tests. Notably, these variations in the contact path contribute to increased wear on the tooth flank. This is evidenced by measurements taken over 10 million cycles, as discussed in Chapter 4.

7.4 Results of Frictional Coefficient

The calculation of friction coefficients in this study employs four different methods attributed to Buckingham, Merritt, Benedict & Kelley, and Drozdov & Gavrikov. Each technique utilises specific coefficients or parameters to describe the relationship between the friction coefficient and power loss.

Drozdov and Gavrikov's equation addresses damage occurring in scenarios where two bodies in contact experience both rolling and sliding motion. It factors in the kinematic viscosity of air at the surface temperature of interest, determined as the highest temperature detected using infrared temperature measurement techniques. This equation considers the nature of contact between surfaces and the properties of air at the observed temperature, providing valuable insights into damage assessment.

7.4.1 Kono's Frictional Coefficient Predictions

This section focuses on predictions of the frictional coefficient based on the wear of gear teeth. While Kono conducted tests and gathered volume loss data in 2003, the current study involves designing and calculating the length of the contact path, considering sliding and rolling velocities. Figure 7.8 illustrates predictions for Kono's frictional coefficient based on skating and rolling velocities in a system redefined in the current work. The study utilises PEEK materials 450G, 450FC30, 450GL30, and 450CA30, focusing on the system after 10 million cycles, specifically under the conditions of worn gear teeth.

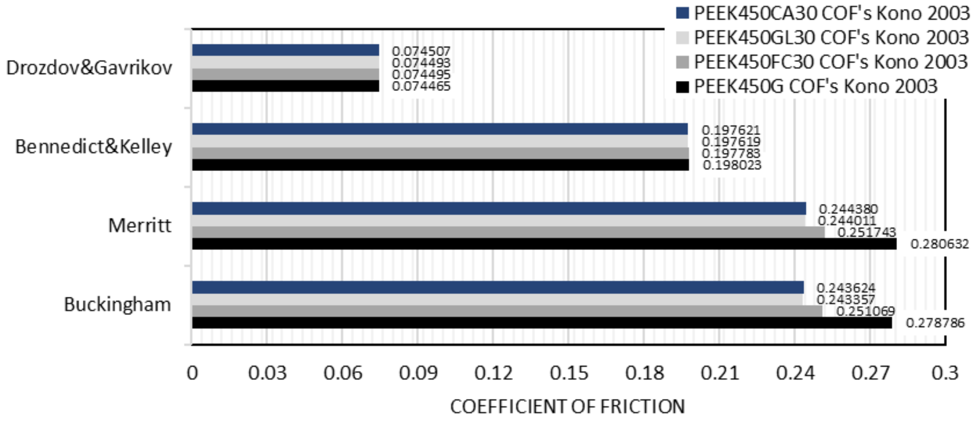

Figure 7. 8 *Kono's Frictional Coefficient Predictions*

The calculations shown in Figure 7.8 reveal that the friction value, according to the Drozdov and Kelly equation, is the lowest among the compared theories. In contrast to the other three theories, the Drozdov and Kelly equation predicts friction values below 0.1, while the other three theories yield more than 0.1. Notably, Merritt's equation [134] demonstrates the most significant increase in friction values among these equations.

An average temperature estimation is provided for PEEK materials 450FC30, 450GL30, and 450CA30, which were not explicitly specified in Kono's experiments. The analysis suggests that the coefficient of friction for these materials falls within a temperature range of 110 to 130 degrees Celsius. This temperature range serves as a reference point for assessing the behaviour of these PEEK materials in the study.

7.4.2 Frictional Coefficient Predictions

As outlined in Chapter 4, predictions for the coefficient of friction data from each equation are presented along the contact path. These predictions are made in the context of the rig applying a reaction force of 180.504 N in the horizontal axial direction. The equations were utilised to calculate force reactions along this path, resulting in predictions of power loss for the meshing gears based on time and accelerating vibration data. These predictions are displayed as real-time force reactions in Figures 7.9 and 7.10. Notably, all the equations produced significantly higher power loss predictions than the measured values. For comparative purposes, the Buckingham, Merritt, Benedict & Kelley, and Drozdov & Gavrikov frictional coefficient equations were also applied along the contact path.

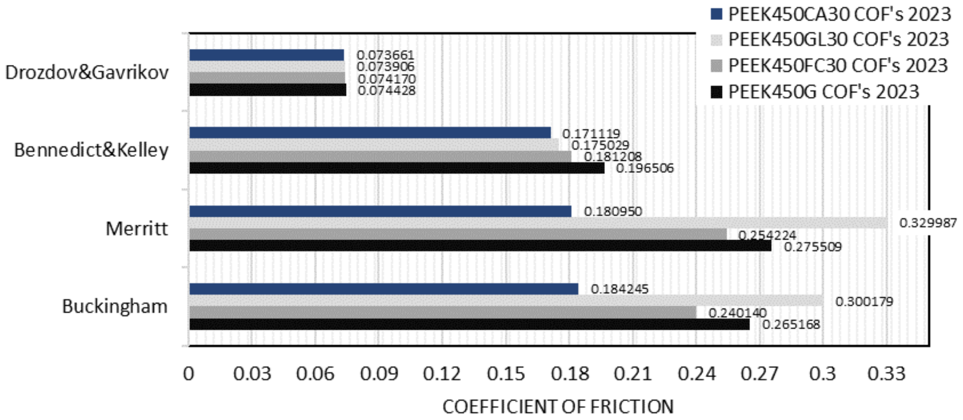

Figure 7. 9 *Frictional Coefficient Results with Four PEEKs*

According to the results depicted in Figure 7.9, the Drozdov and Kelly equation yields the lowest frictional coefficient among the methods used. The Buckingham and Merritt equations produce similar frictional coefficient values, which are influenced by factors related to the contact path, including aspects such as approach and recess lines and angles.

Variations in transmission efficiency and frictional coefficients compared to materials and theoretical expectations, observed before reaching the 10 million cycles mark, are presented in Figures 7.9 and 7.10. Figure 7.10 shows results related to the frictional coefficient derived from the peak frequency of accelerating vibration testing for the four different PEEK materials. These results were obtained in the time interval from 868,029 to 870,640 seconds before the end of the 10 million cycles.

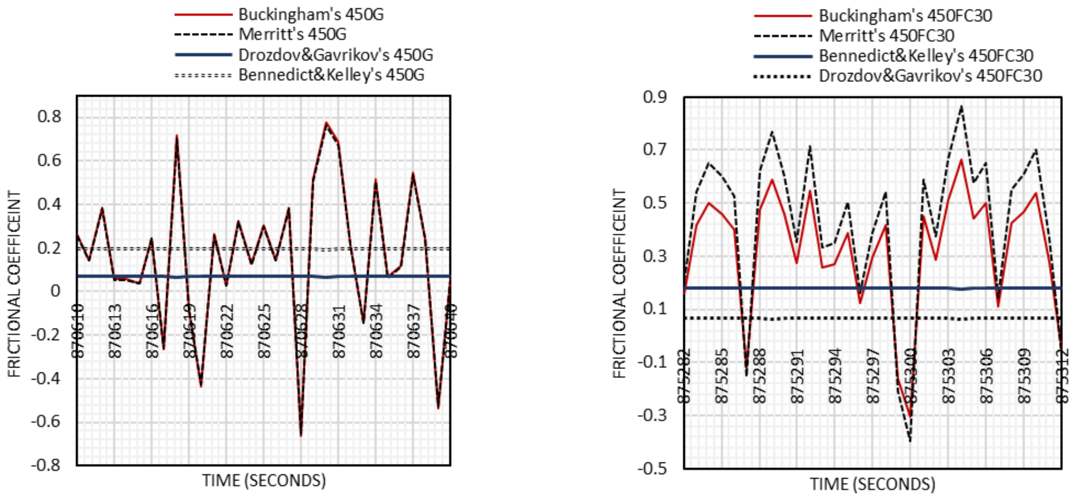

(a) PEEK 450G at the Peak of Frequency

(b) PEEK 450FC30 at the Peak of Frequency

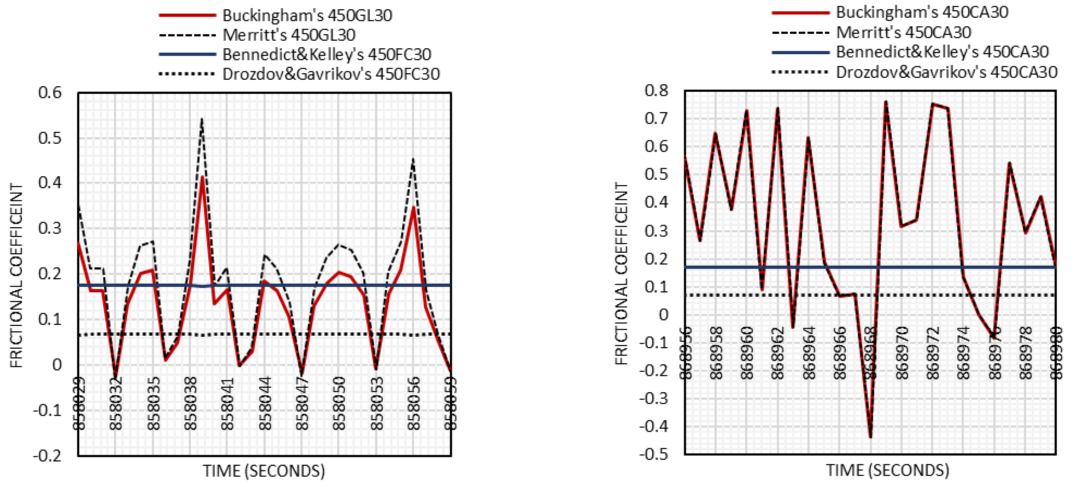

(c) PEEK 450GL30 at the Peak of Frequency

(d) PEEK 450CA30 at the Peak of Frequency

***Figure 7. 10** Four PEEK's Frictional Coefficient Results*

A detailed view from Figure 7.10, representing meshing gears and derived from time and accelerating vibration data converted into peak real-time force reactions, is shown in Figure 7.11. These results, displayed at the peak frequency just before the end of the test period of 10 million cycles, indicate that variations in equations and PEEK materials, particularly regarding gear teeth conditions, significantly impact transmission efficiency and friction within gear systems along the contact path. The findings can be summarised as follows:

1. PEEK 450FC30 exhibited the highest frictional coefficient among the tested materials, particularly at the peak frequency. According to Merritt's predictive equation, this material had the highest frictional coefficient based on vibration frequency and transmission efficiency, indicating the greatest level of friction and the most significant tooth wear compared to the other materials.
2. PEEK 450GL30 displayed a lower frictional coefficient than other PEEK materials across all equations.
3. PEEK 450G and 450CA30 showed similar frictional effects, with values corresponding to the extent of gear tooth damage.

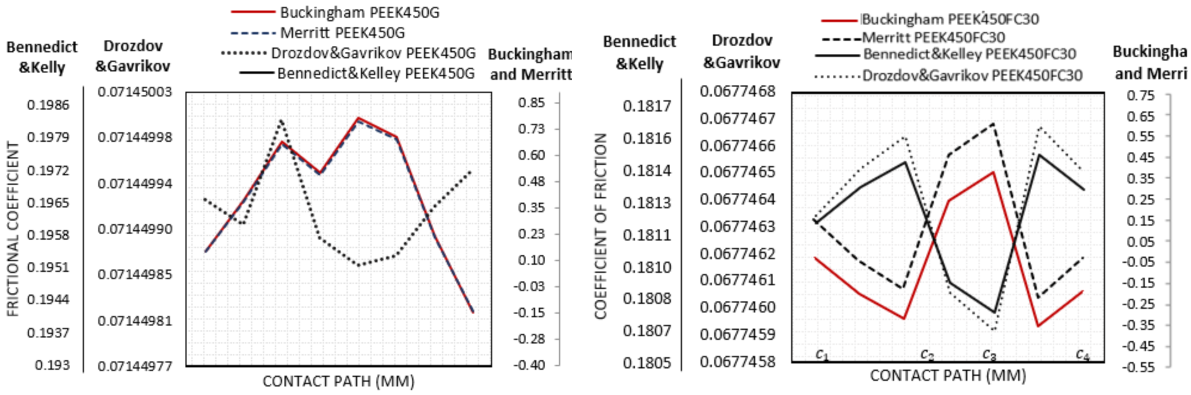

(a) PEEK 450G on the Contact Path

(b) PEEK 450FC30 on the Contact Path

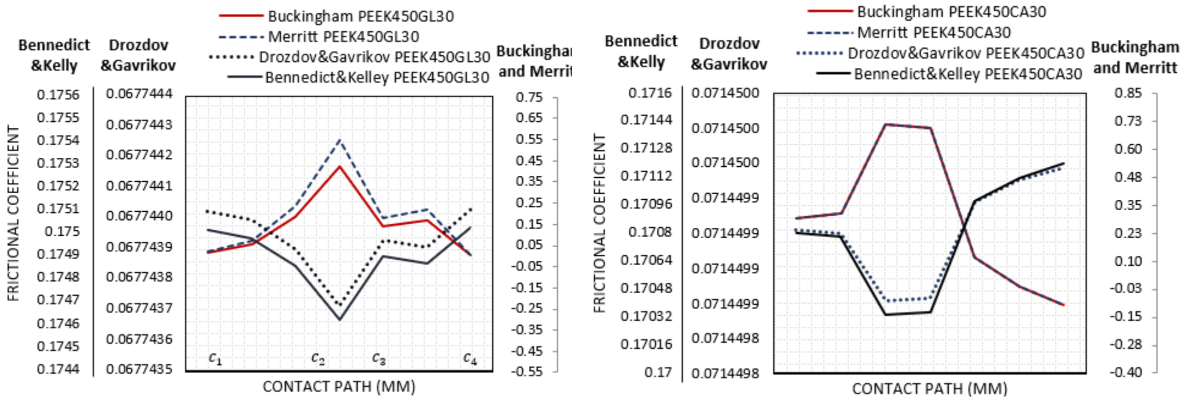

(c) PEEK 450GL30 on the Contact Path

(d) PEEK 450CA30 on the Contact Path

Figure 7. 11 *Peak of Frictional Coefficient Along Contact Path at 10 Million Cycles*

7.5 Power Loss Results

Estimating gear power loss is a pivotal outcome of this research, providing calculated power loss values within the system based on theoretical analysis and empirical findings. These predictions offer critical insights into the efficiency of gear systems under various conditions and geometries.

The four investigations yielded different formulas for calculating sliding power loss and frictional coefficients. These variations largely stem from selecting different coefficients and equations relating to power loss, including using Rao's equation. Each formula considers the specific contribution of the gear's mass moment of inertia, denoted as $I_{p,g}$.

7.5.1 Kono's power loss predictions

In Kono's experimental data, 8.11 and 10.88 Nm torque levels were applied at 1000 rpm to the driving pinion. These data were used to establish a connection with power loss calculations derived from Rao's equation. Figure 7.12 displays the power loss results obtained from Kono's experiments. Additionally, the approximate temperatures for three PEEK materials – 450FC30, 450GL30, and 450CA30 – were observed to fall within the range of 110 to 130 degrees Celsius.

The four investigations proposed different methodologies for estimating power loss due to sliding friction, each employing varied friction coefficients. The power loss predictions depicted in Figure 7.12 indicate the following observations:

- For PEEK 450G and 450FC30, the power loss predictions from the four methods were approximately equal, suggesting that these materials exhibit similar power loss values.

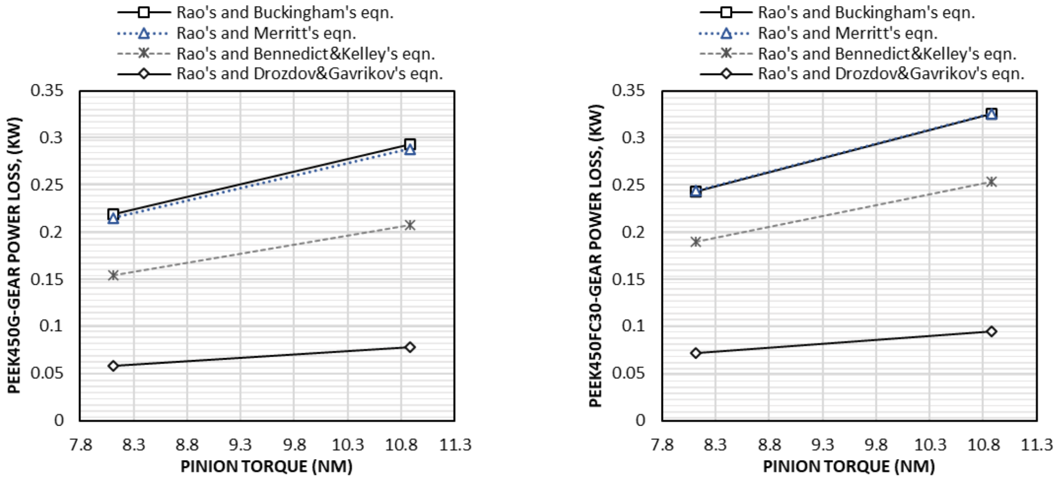

(a) PEEK450G *(b) PEEK450FC30*

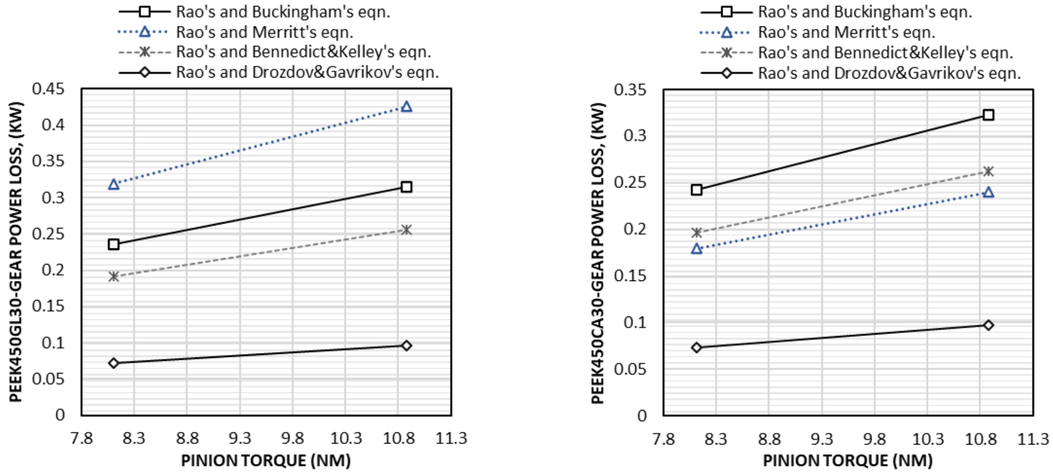

(c) PEEK450GL30 *(d) PEEK450CA30*

Figure 7. 12 *Predicted Kono's Power Loss and Compared the Theories Utilizing Rao's Equation*

When using Merritt's equation, PEEK 450GL30 showed a higher power loss prediction than all four PEEK materials. This indicates that 450GL30 might experience more significant power loss under the conditions tested.

- The lowest power loss results, particularly with Merritt's equation, were noted for PEEK 450CA30. This suggests that 450CA30 may have better efficiency in terms of power loss compared to the other materials.

These findings underscore the importance of selecting appropriate materials and equations for predicting power loss in gear systems. The variations in power loss across different PEEK grades demonstrate how material properties and specific conditions can significantly influence the efficiency and performance of gear mechanisms

7.5.2 Power loss predictions

The power loss predictions in this research are based on the frictional coefficient under force reaction and real-time testing, especially at the same peak frequency, as indicated in Figure 7.11. The analysis focuses on a gearset operating at a pinion speed of 998 rpm, evaluating and contrasting the sliding power loss predictions made by four different methods of calculating friction coefficients under the specified operational conditions. The findings, as shown in Figure 7.13, represent the torque and speeds examined.

Utilising Rao's equation theories, power loss predictions were compared across the four PEEK materials. The results indicated that for PEEK 450G, 450FC30, and 450GL30, the power loss predictions from the four methods, mainly using Merritt's equation, were approximately the same. These materials exhibited similar power loss values according to Merritt's equation. Conversely, when Merritt's equation was applied, PEEK 450CA30 showed the lowest power loss predictions.

The primary results from RAO's sliding and rolling gear power loss equation, as referenced in [133], reveal that power loss in mating wheels is determined by a ratio involving the mass moments of inertia of the gears (I_p and I_g) and the gear ratio of I_p to $\left(\frac{\omega_g}{\omega_p}\right)^2 I_g$. The specific impact of each gear's mass is a moment of inertia on overall energy losses. Additionally, it challenges the common assumption that the frictional coefficient and normal force on gear teeth solely determine the surface forces on both teeth.

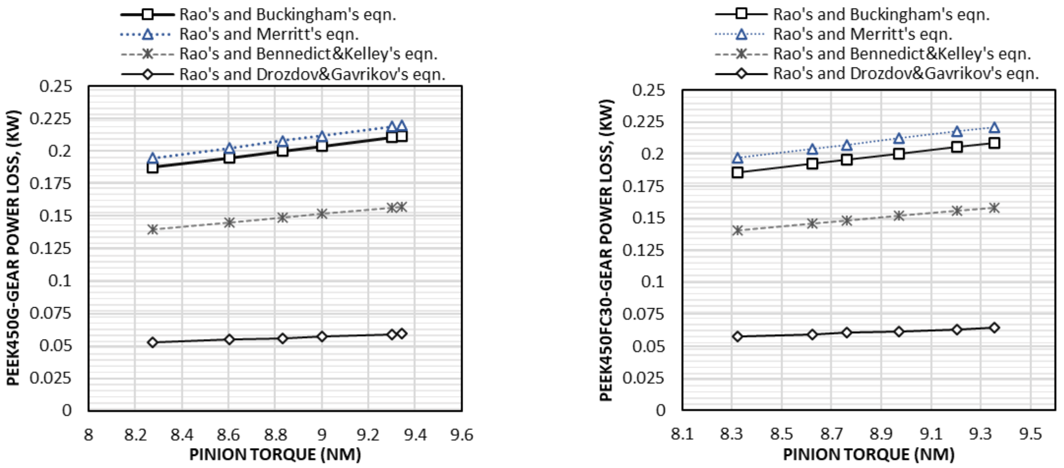

(a) PEEK450G

(b) PEEK450FC30

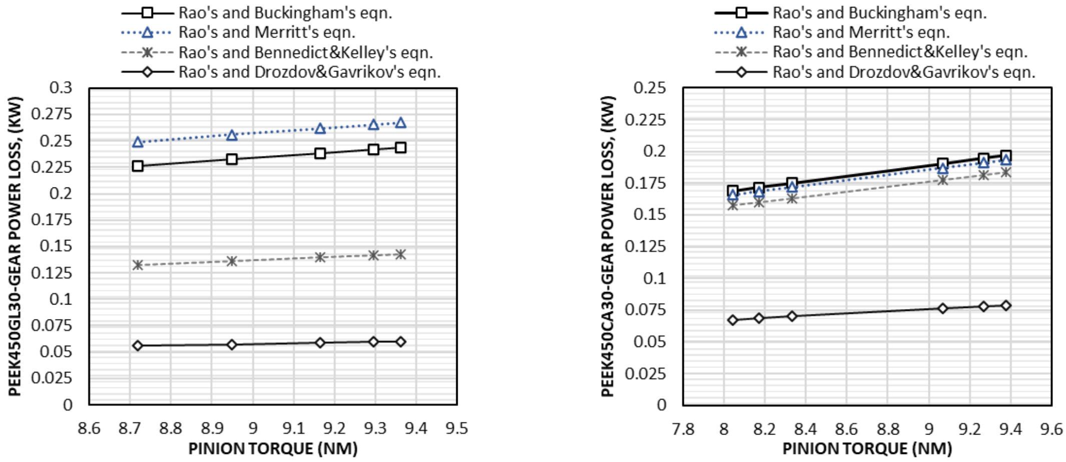

(c) PEEK450GL30

(d) PEEK450CA30

Figure 7. 13 *Predicted Gear Power loss of Four PEEK's 2023, which Comparisons Theories with Rao's Equation*

7.6 Summaries

The investigations led to varying results in sliding power loss and frictional coefficients due to differences in friction coefficient equations. Four different coefficient theories (Buckingham, Merritt, Benedict & Kelley, and Drozdov & Gavrikov) were used to replace specified coefficients in each method, affecting frictional coefficients and power loss predictions in research linked to Rao's sliding power loss equation. The summary of the entire analysis is as follows:

1. The maximum vibration frequency substantially affects tooth wear volume loss and wear size. Higher frequencies lead to more significant wear.
2. Reactive forces and torques, influenced by interactions between gear teeth, also influence tooth wear volume loss and wear size.
3. The friction coefficient varies based on the contact path (line and angle of approach and recess), sliding velocity, vibration frequency, surface temperature on gear teeth and transmission efficiency.
4. The energy loss prediction in the system depends on the relative between vibration frequency, transmission efficiency and gear's mass moment of inertia.

Therefore, the power loss predictions varied among different PEEK materials and methods. Merritt's equation yielded distinctive results, with PEEK 450CA30 having the lowest power loss.

Chapter 8

Analysing Wear and Stress in PEEK Polymer Gears: Tooth Deflection and Friction Dynamics at 30 Degrees Pressure Angle

In Chapter 8, the study focuses on the tooth wear analysis of Victrex's gears. This includes examining tooth deflections, bending stress, wear, and friction-related issues. The primary aim is to evaluate the progression of initial cracks, from pitch and root points to critical cracks within the gear teeth. ANSYS simulation was used to achieve this, building upon the polymer involute gear equations outlined in Chapter 5. In sections discussing tooth gear models, the simulations exposed stress concentration and deformation in the teeth, emphasising how these vary across different frictional coefficients, thereby highlighting discrepancies in wear size.

Victrex's PEEK materials are highly sought after in the engineering of gears, renowned for their exceptional mechanical characteristics and thermal stability. These materials adhere to industry standards, with a 30-degree pressure angle (BS-PA30) and demonstrate outstanding performance under various conditions. Critical mechanical properties include resistance to high temperatures, strength, stiffness, and wear resistance. Additionally, their low coefficient of friction contributes significantly to efficiency.

8.1 Research Background

Victrex's PEEK materials are recognised as high-performance engineering polymers, extensively used in gear design and manufacturing. Their exceptional mechanical properties and thermal stability make them particularly valuable in this field. As detailed in PEEK Table 4.2, these materials can withstand temperatures as high as 250°C (482°F). They offer superior strength, stiffness, and abrasion resistance, extending the lifespan of gears and reducing the need for maintenance. Furthermore, PEEK's low coefficient of friction, ranging from 0.15 to 0.28, enhances its efficiency. [5] [135].

Chapter 8 delves into test design and assessment in engineering using MKII test equipment. This chapter focuses on a gear pair made from Victrex's PEEK 650G. The multifaceted approach combines theoretical analysis, FEA-DS, and real-time experimental testing. The examination pays particular attention to gear transmission dynamics and the complex effects of material expansion/contraction and wear, all influenced by temperature variations.

8.2 Methodology

8.2.1 Material Properties and Gear Geometry

This section offers a detailed overview of the outstanding mechanical properties of PEEK 650G, as depicted in Figure 4.2 of Chapter 4. PEEK 650G exhibits remarkable characteristics, including significant strength and stiffness, exceptional thermal stability, a low friction coefficient, superior wear resistance, chemical resilience, dimensional stability, excellent electrical insulation, and a lightweight nature.

The geometry of the gear, with a 30-degree pressure angle, is utilised to determine the optimal number of teeth and the gear ratio. This determination is crucial for aligning with specific gear applications and achieving desired speed adjustments. The gear teeth profile is meticulously designed, with the 30-degree pressure angle in mind, to ensure optimal gear meshing and minimal friction. Further details of this design are available in Table 4.4 and Figure 4.6 of Chapter 4.

8.2.2 Boundary conditions and method

a. Boundary conditions

The study's test setup involved a torque load of 10.80 Nm and a speed of 1,000 rpm, drawing reference from Kono's research. It focused on PEEK 650G, examining un-lubricated and lubricated testing conditions. The loading conditions are comprehensively outlined in Table 8.1.

Table 8. 1 Parameter Setting

Parameters		*Values*
Weight Apply	lb	*10.10 (~4.58 kg)*
Torque for Shaft Driving	Nm	*9.38 (~180 N)*
Frequency Drive	Hz	*11.30*
Speed Velocity (Output)	rpm	*998 (on Teeth)*
One Cycle (Time per Revolution)		□ *0.05998*
Bending Moment Arm at Tooth Tip for Load Application, y_{bm}	mm	*3.76**
Nominal Load of Contact Line, F_n	N	*332.73**
Tangential Load in Plane of Action, F_t	N	*296.68**
Working Pressure Angle at Tooth Tip, φ_t	Deg	*26.92**

**ISO 6336-1:1996* - [136]

d. Material Properties

The mechanical properties and the fatigue curve of both the pinion and wheel made from PEEK650G material are detailed in Table 4.2 and Figure 8.1. This curve illustrates the relationship between maximum stress and the number of cycles to failure. These data are integral to the material properties used in ANSYS software, offering insights into the material's fatigue behaviour and durability under various stress levels.

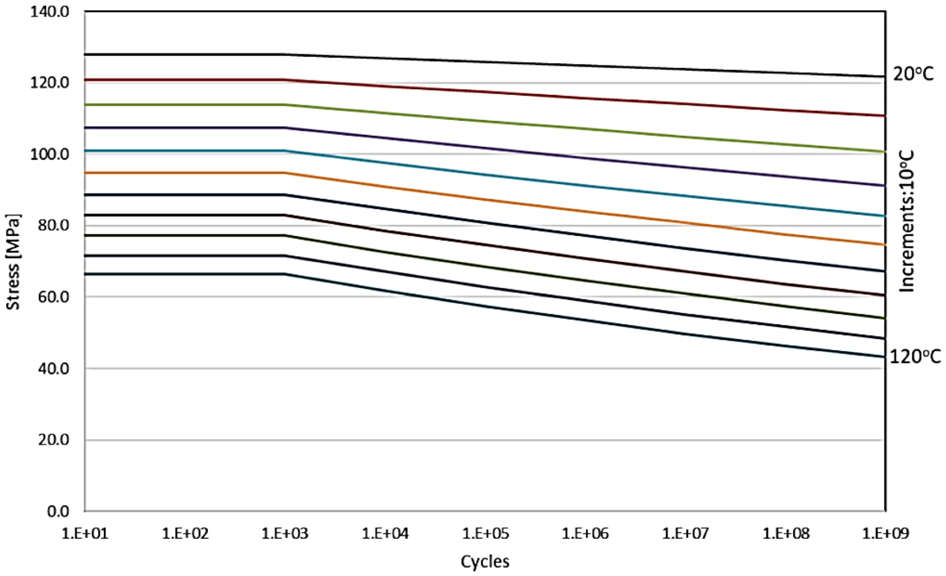

Figure 8. 1 *Fatigue Curve Between the Maximum Stress and Cycles for Pinion and Wheel PEEK650Gs*

c. Method

The experimental methodology is illustrated in Figure 8.2, which presents the schematic diagram of the polymer gear research process and the testing of load conditions. This diagram provides a comprehensive view of the experimental analysis process. The experiments were carried out using the MKII machine, and a detailed description of the load conditions used during testing is also provided in the previous chapter.

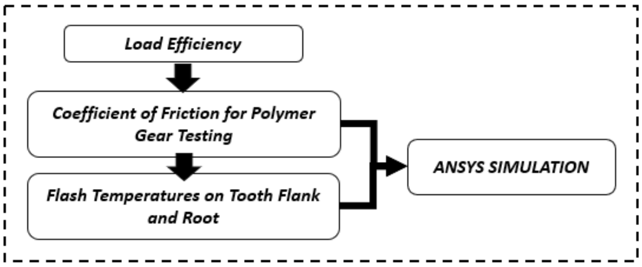

Figure 8. 2 *Schematic Experimental Diagram*

8.3 Revised Equation for Victrex’s Gear

8.3.1 Kinematic Behaviour

A new equation has been developed to characterise the kinematic behaviour of Victrex's gears, specifically considering a BS-PA30 model. This equation addresses the changes in involute tooth geometries resulting from ball contact. It is crucial in predicting wear patterns for both tooth and ball contact geometries in polymer materials. One key aspect of this equation is its ability to measure the diameter of the ball contact circle, which varies across the thickness of the tooth gear. This measurement can be accurately determined at the ball contact circle. The theoretical foundations of this equation, as detailed in Chapter 5 and illustrated in Figures 8.3 and 8.4, indicate a more significant reduction in tooth thickness compared to standard gears. As a result, this work has led to a new equation specifically for calculating the ball contact diameter in these scenarios.

$$d_{ball,w} = d_{ball} + w_{s,T_i}$$

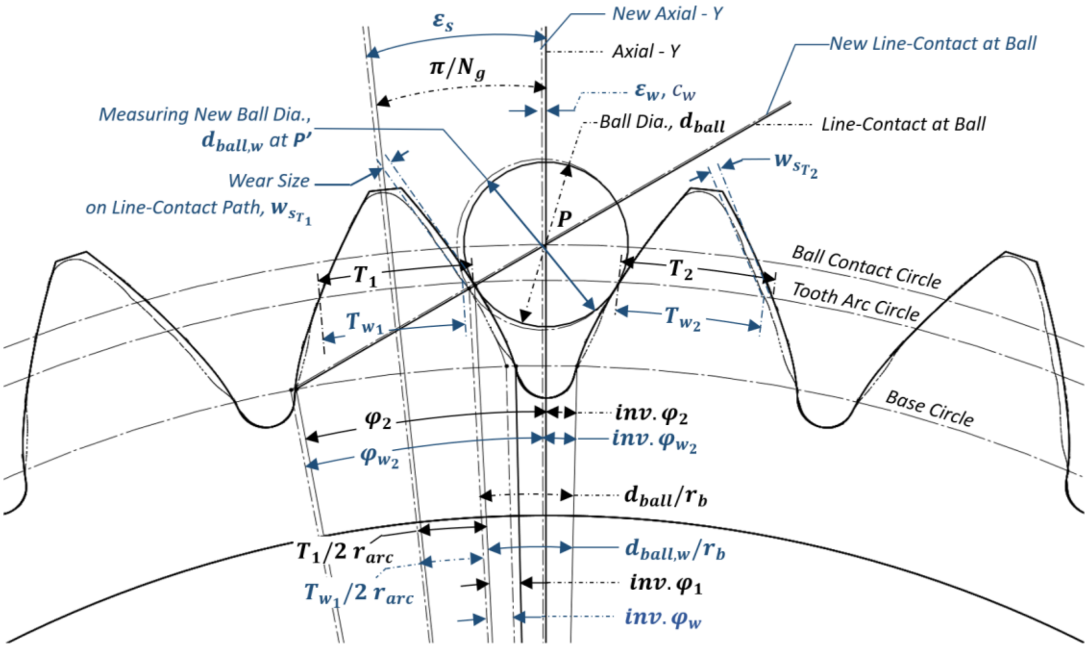

Figure 8. 3 *Involute Tooth Gear Geometry and Ball Contact of BS-PA30 (Un-Worn and Worn Teeth)*

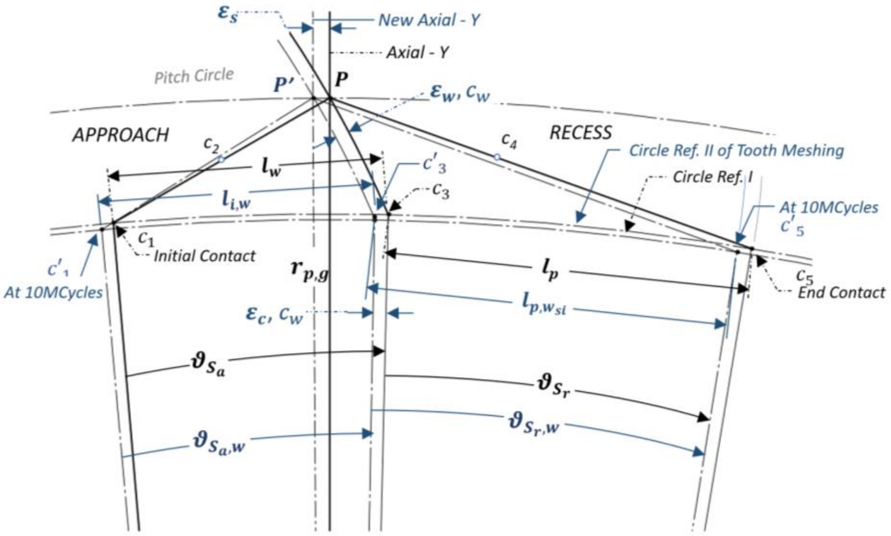

Figure 8. 4 *Revised the Involute Tooth Geometries of BS-PA30 (Un-Worn and Worn Teeth) Due to the Contact Path Line (Sections of Approach and Recess)*

8.3.2 Frictional Behavior and Flash Temperature

Building upon the foundations laid by Buckingham’s and Bulk’s equations, as referenced in Chapters 3 and 5, it's noted that the coefficient of friction is not constant. This variation is due to changes in the involute gear geometry, particularly under tooth wear and failure conditions. The flash temperature, influenced by bending deformation through stress and strain behaviours, viscoelastic hysteresis losses, and changes in the stiffness of polymer materials, is a critical factor to consider. The results indicate that the maximum self-heating occurs on the width-tooth flank, with the flash temperature rise calculated using Bulk’s equation. This finding is significant in understanding and predicting the thermal behaviour of polymer gears under operational stress.

8.4 Experimental Results

8.4.1 Temperature data

The study collected temperature data for PEEK650G BS-PA30, as presented in Figure 8.5. This data encompasses the average initial and bulk temperatures observed on the width-tooth flank during real-time testing. The graph in Figure 8.5 displays temperature measurements taken on the width-tooth flank, recorded at one-second intervals until the completion of the first testing phase, which spanned 10 million cycles.

This data was essential for comparing the temperature increases. A comprehensive presentation of the temperature measurements and the collected temperature data is listed and elaborated upon in Appendix B. This allows for a more detailed analysis of temperature variations over time.

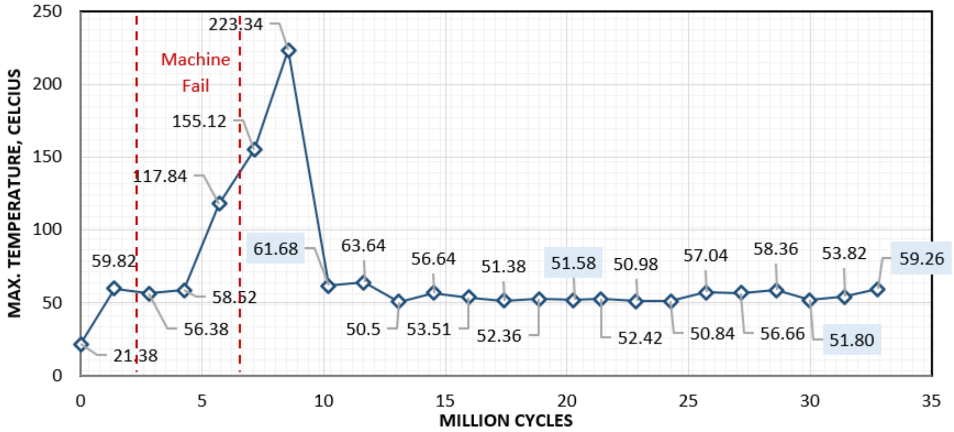

Figure 8. 5 *Collected Surface Temperature on the Width-Tooth Flank in Real Time Testing, PEEK650G-BS-PA30*

8.4.2 Accelerating Vibration Data

The accelerating vibration response was meticulously controlled throughout the testing, ensuring it did not exceed 2.50g. This control was applied across all three axes: x, y, and z. Accelerating vibration measurements were taken to monitor the vibration characteristics thoroughly. These measurements were conducted in three dimensions along the x, y, and z axes, using a sensor on the wheel shaft. The purpose was to monitor and detect vibrations during real-time tooth meshing under specific load conditions. Detailed data regarding the accelerating vibration in all three axes (±x, ±y, and ±z) is provided in Appendix B. This data was recorded continuously at one-second intervals until the completion of the test.

The 3-axis accelerating vibration data and weight and volume loss observations led to further findings, as depicted in Figure 8.6. Notably, frequency data was gathered at 32.80 million cycles. The most significant observation was the highest frequency of accelerating vibration observed in all axial directions (x, y, z). Initially, these vibrations remained within the range of ±0.02g but escalated to values exceeding ±2.5g, starting at 522 hours and persisting until 542 hours, coinciding with a crack. This marked a significant change in the vibration behaviour of the system, likely indicative of the development of a tooth crack.

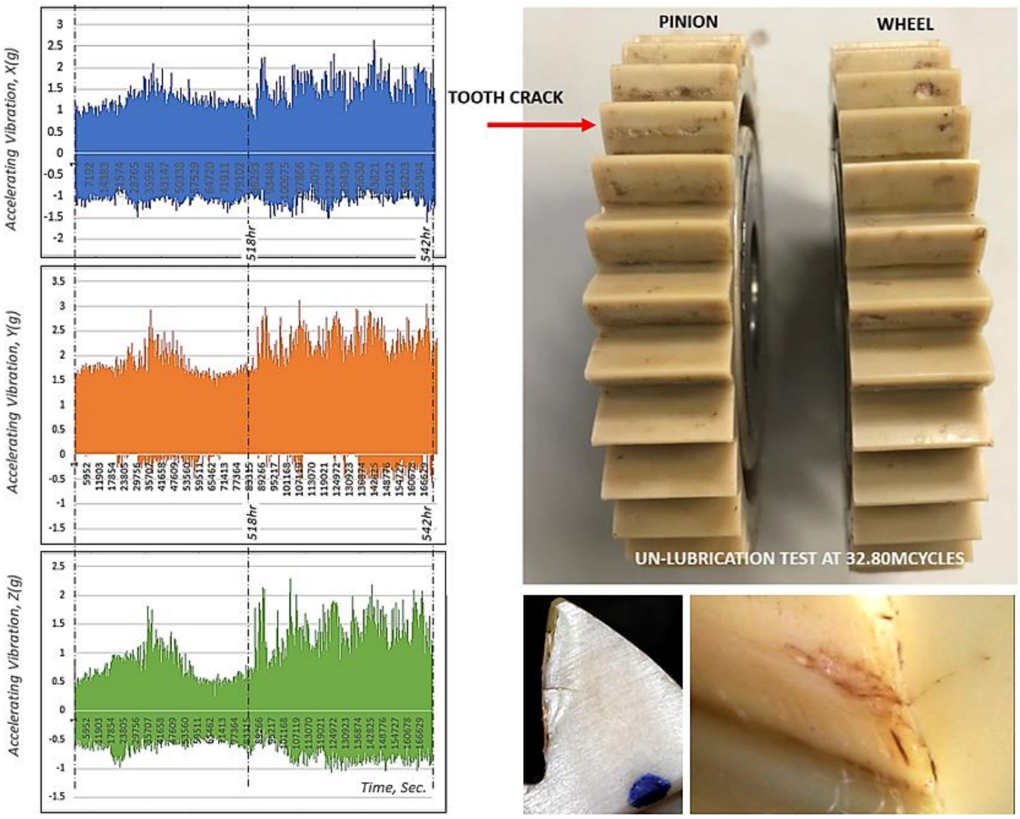

Figure 8. 6 *Accelerating Vibration Data at 32.80 Million Cycles (Crack)*

8.4.3 Tooth Wear and Weight Loss

Micro cameras and PylonC tools were employed to detect changes in the shape of the tooth gears, as depicted in Figure 8.7 and detailed in Table 8.2. When measuring wear in two dimensions, tolerances in the micromillimeter range are to be considered. The data collected by PylonC regarding tooth wear was exported and used to create three-dimensional representations of the worn teeth. This approach provides a comprehensive understanding of the wear patterns experienced by the gear teeth over time.

Key positions, including the "Tip-Circle, Highest-Point of Single-Point Contact (HPSTC), Lowest-Point of Single-Point Contact (LPSTC), and Base Circle," were identified and marked. Tooth wear data from these positions was then extracted and utilised to generate three-dimensional representations of the worn teeth. The wear distance measurement in two dimensions (2D) and three dimensions (3D) was conducted through programmed designs. Consequently, the study offers predictions based on these measurements and representations, shedding light on the volume and weight loss, thereby providing insights into the extent of wear experienced by the gear teeth.

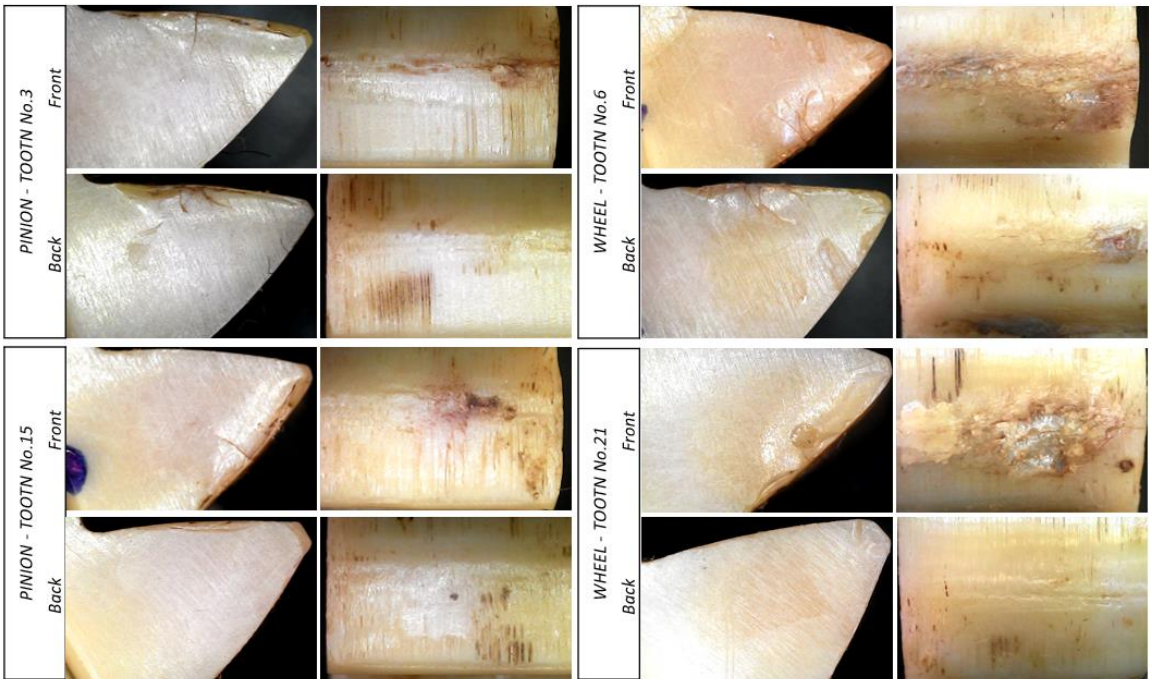

Figure 8. *7 Micro Camera Detected Worn Teeth at Initial Running Until End of Running (Crack at 32.80 Million Cycles)*

Table 8. *2 Detected Wear Size by PylonC*

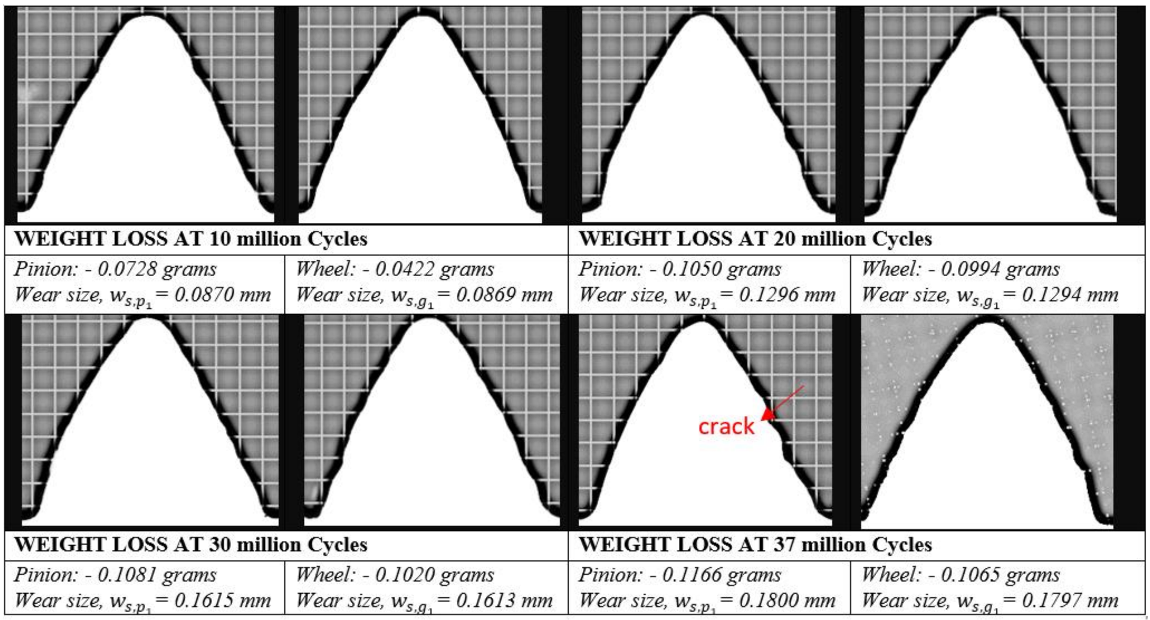

WEIGHT LOSS AT 10 million Cycles		WEIGHT LOSS AT 20 million Cycles	
Pinion: - 0.0728 grams *Wear size,* w_{s,p_1} *= 0.0870 mm*	*Wheel: - 0.0422 grams* *Wear size,* w_{s,g_1} *= 0.0869 mm*	*Pinion: - 0.1050 grams* *Wear size,* w_{s,p_1} *= 0.1296 mm*	*Wheel: - 0.0994 grams* *Wear size,* w_{s,g_1} *= 0.1294 mm*
WEIGHT LOSS AT 30 million Cycles		**WEIGHT LOSS AT 37 million Cycles**	
Pinion: - 0.1081 grams *Wear size,* w_{s,p_1} *= 0.1615 mm*	*Wheel: - 0.1020 grams* *Wear size,* w_{s,g_1} *= 0.1613 mm*	*Pinion: - 0.1166 grams* *Wear size,* w_{s,p_1} *= 0.1800 mm*	*Wheel: - 0.1065 grams* *Wear size,* w_{s,g_1} *= 0.1797 mm*

8.5 Involute Tooth Wear Results

This study examined the tooth shape of four different PEEK grades after 10 million cycles, using Pylon C. Observations of variations in tooth thickness led to a deeper investigation into the kinematics of spur gears and the factors influencing the size of ball contact. These findings, including calculations related to involute tooth gear geometry, ball contact, tooth shape, and thickness changes resulting from wear over 10 million cycles, are detailed in Table 8.3. Additionally, Table 8.4 visually illustrates the changes in involute tooth wear geometries. These illustrations focus on the sections of approach and recess, showing alterations in gear tooth shape and thickness due to the contact path line.

Table 8. 3 *Involute Tooth Geometry and Ball Contact for Wear Teeth*

	$\boldsymbol{r_{arc}(mm)}$	$\boldsymbol{C\ (mm)}$	$\boldsymbol{b_d\ (mm)}$	$\boldsymbol{r_b\ (mm)}$	$\boldsymbol{inv.\varphi_1}$	$\boldsymbol{T_1(mm}$	$\boldsymbol{inv.\varphi_2}$
Initial Run	*30.085*	*60.17*	*3.4300*	*28.1450*	*0.0537*	*2.8080*	*0.11753*
10MCycles	*30.085*	*60.17*	*3.5227*	*28.1450*	*0.0537*	*2.7153*	*0.11928*
20MCycles			*3.5545*			*2.6835*	*0.11988*
30MCycles			*3.5750*			*2.6630*	*0.12063*
CRACK			*3.5943*			*2.6437*	*0.11753*
	$\varepsilon_c(rad)$	$c_w\ (mm)$	$\varepsilon_w\ (deg)$	$\pi/Ng\ (rad)$	$T_1/2r_{arc}\ (rad)$		$b_d/r_b(rad)$
Initial Run	*0*	*0*	*0*	*0.1048*	*0.04667*		*0.1219*
10MCycles	*0.00234*	*0.1338*	*6.1338*	*0.2386*	*0.04513*		*0.1255*
20MCycles	*0.00236*	*0.1384*	*6.1351*	*0.2398*	*0.04460*		*0.1296*
30MCycles	*0.00238*	*0.1468*	*6.1364*	*0.2412*	*0.04426*		*0.1330*
CRACK	*0.00241*	*0.1570*	*6.1379*	*0.2426*	*0.04394*		*0.1219*

The calculations reveal changes in the length of approach and recess along the non-normal contact path, primarily due to increased tooth flank wear. This wear phenomenon was methodically observed at intervals of every 10 million cycles until the occurrence of a crack. Essentially, these calculations offer critical insights into the impact of tooth flank wear on the contact pattern and overall behaviour of the gear system.

Table 8. 4 *Involute Tooth Wear Geometries in the Sections of Approach and Recess*

	Initial Run	10MC	20MC	30MC	CRACK
Approach line of wear, $\boldsymbol{l}_{w_{si}}$ *(mm)*	*-3.7603*	*-3.8648*	*-4.0382*	*-4.1493*	*-4.2546*
Recess line of wear, $\boldsymbol{l}_{p,w_{si}}$ *(mm)*	*3.5000*	*-3.2580*	*3.0372*	*2.8957*	*2.7617*
Angle of wear approach , $\boldsymbol{\delta}_{s_{a,w}}$ *(Deg.)*	*-7.6518*	*-7.3661*	*-7.6965*	*-8.4435*	*-8.6574*
Angle of wear recess, $\boldsymbol{\delta}_{s_{r,w}}$ *(Deg.)*	*7.1221*	*6.6298*	*6.1805*	*5.8926*	*5.6198*
Contact path line of wear, (mm)	*7.2603*	*7.1229*	*7.0755*	*7.0450*	*7.0161*

8.6 Coefficient of Friction Results

The coefficient of friction and flash temperature predictions were calculated and are depicted along the contact path in Figure 8.8. This depiction is based on the rig's horizontal axial reaction force, measured at 180.504 N. The equations were solved to determine the force reaction along the contact path. The Buckingham frictional coefficient equation was also applied along the contact path for comparative analysis. The maximum self-heating on the width-tooth flank was calculated based on the flash temperature rise, as determined by Bulk's equation.

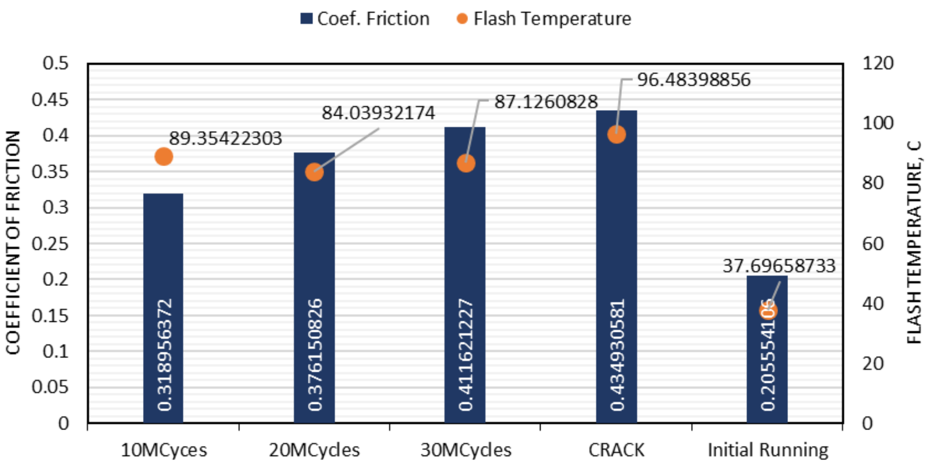

Figure 8. 8 *The Relationship Between the Thermal Contact Coefficient and Flash Temperature in Real-Time Testing*

8.7 Simulation results

The study incorporated finite element analysis, encompassing dynamic structural and transient thermal simulations. These simulations aimed to examine the behaviour of a gear pair, specifically a pair of PEEK650G gears meshing every 10 million cycles until the development of a crack. The simulations were carried out under specific load conditions, which included a 9.38 Nm load, a speed of 1,000 rpm, and a gear rotation of 20 degrees within 0.00333 seconds.

In these simulations, the three-dimensional geometries of the worn gear teeth were integrated into the ANSYS software. Various boundary conditions were then established, including the coefficient of friction, flash temperature, augmented formulation, and interface adjustments to cater to the contact between components. These conditions were applied in both the Dynamic Structural and Thermal Transient analyses. This approach thoroughly understood the gear system's dynamic behaviour and thermal responses under the given conditions.

8.7.1 Rotational Correlation on the Roll Angle Measures Equivalent Stress on Tooth Contact

As shown in Figures 8.9 and 8.10, the ANSYS simulation results analyse the behaviour of maximum equivalent stresses on the contact tooth flanks. These analyses were conducted throughout the initial running phase and at intervals of every 10 million cycles, up to 30 million cycles. The results reveal significant changes in the stress distribution on the involute tooth flanks, which are crucial for predicting tooth failures at each 10-million cycle interval.

The simulated pinion, made of PEEK650G BS-PA30, displayed the lowest maximum equivalent stress values, particularly at the highest point of Single-Point Contact (HPSTC), with stress levels around 137.4 MPa at the end of 30 million cycles. In contrast, the wheel component exhibited maximum equivalent stress levels of approximately 99.71 MPa at the same stage. These findings underscore the differences in stress distribution and the relative durability of these components under specific operating conditions.

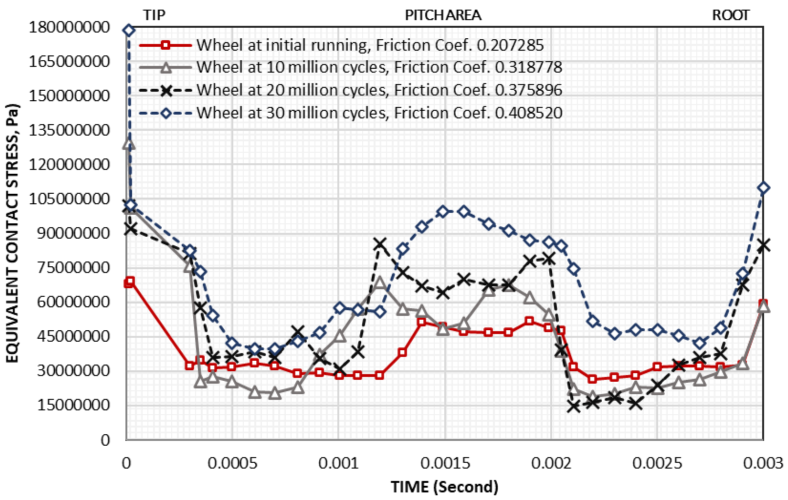

Figure 8. 9 *Contact Sharing Line in the Equivalent Contact Stress on the Pinion*

Moreover, the peak values of maximum equivalent stress were higher for the pinion than for the wheel, especially at the tip of the gear teeth. The pinion reached approximately 200.39 MPa, while the wheel experienced stress levels around 178.39 MPa. Notably, the pinion component encountered higher stress concentrations at the tooth tip, a critical area to consider when assessing the potential for tooth failure in the gear system.

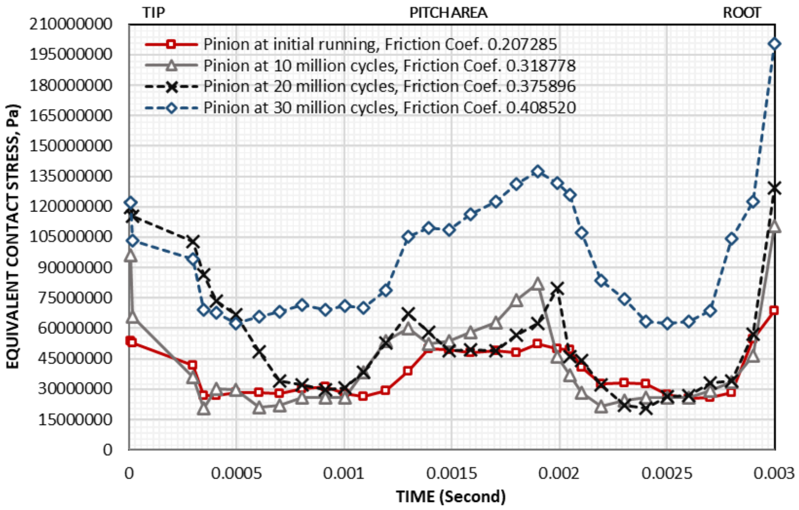

Figure 8. 10 *Contact Sharing Line in the Equivalent Contact Stress on the wheel*

8.7.2 Rotational Correlation on the Roll Angle Measures Tooth Deformation on Tooth Contact

Table 8. 5 *Tooth Deformation Based on Time*

Cycles	***0 million cycles***
Mesh Conditions	*Smaller Contact Sizing and Refinement*
Coefficient of Friction	*0.2056*
Flash Temperature	*37.6956 Celsius*
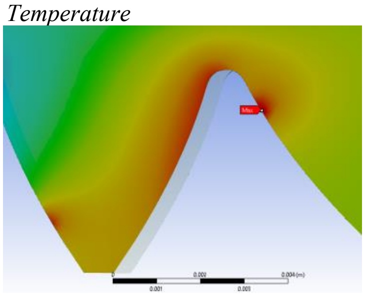	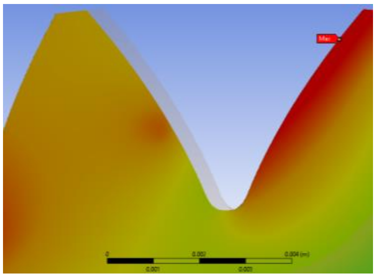
Maximum Deformation: 0.011854 mm of pinion	*Maximum Deformation: 0.006834 mm of wheel*
Cycles	***10 million cycles***
Coefficient of Friction	*0.3188*
Flash Temperature	*89.3387 Celsius*
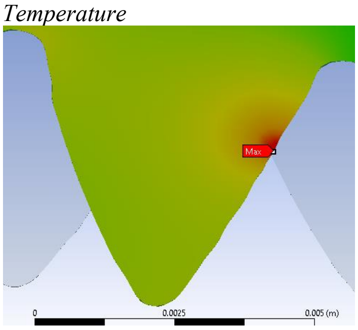	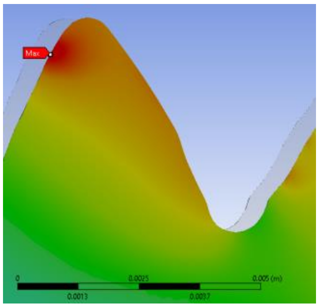
Maximum Deformation: 0.009241 mm of pinion	*Maximum Deformation: 0.008811 mm of wheel*
Cycles	***20 million cycles***
Coefficient of Friction	*0.3759*
Flash Temperature	*84.0173 Celsius*
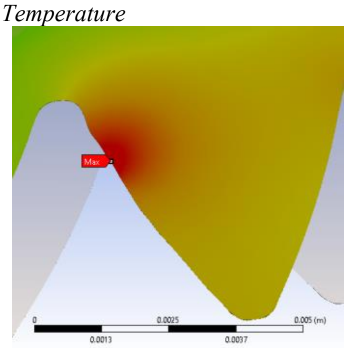	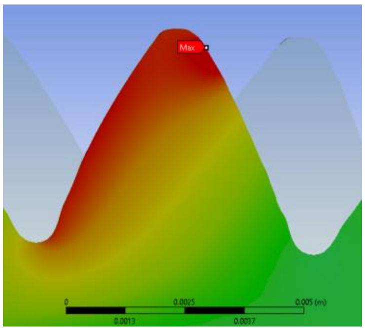
Maximum Deformation: 0.008545 mm of pinion	*Maximum Deformation: 0.009265 mm of wheel*
Cycles	***30 million cycles***
Coefficient of Friction	*0.4085*
Flash Temperature	*86.8599 Celsius*
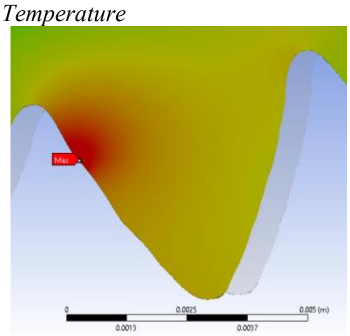	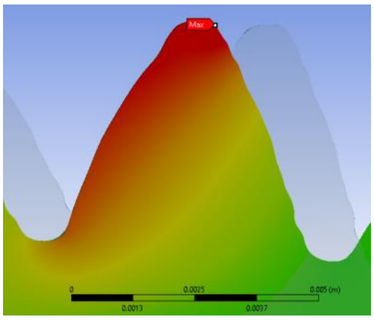
Maximum Deformation: 0.016869 mm of pinion	*Maximum Deformation: 0.023406 mm of wheel*

The results of this study indicate that tooth deformation behaviour changes over time, providing valuable insights into the gear's performance and potential areas of concern, particularly in terms of stress and deformation. As outlined in Table 8.5, the findings on maximum tooth deformation behaviour in the last meshing teeth are as follows:

1. the maximum tooth deformation was observed at the root area during the initial running phase. The measurements were approximately 0.011854 mm for the pinion and around 0.006834 mm for the HPSTC of the wheel

2. During 10 and 20 million cycles, a notable shift in the maximum tooth deformation was observed for the pinion, specifically to the lowest point of Single-Point Contact (LPSTC). The measurements were approximately 0.009241 mm at 10 million cycles and 0.008545 mm at 20 million cycles. Conversely, the wheel exhibited deformation near the tip, measuring around 0.008811 mm and 0.09265 mm at 10 and 20 million cycles, respectively.

3. By the time the study reached 30 million cycles, the highest deformation was recorded at both the root and tip positions for both the pinion and the wheel. As the cycling progressed, the deformation pattern evolved, showing significant deformations on the gear teeth at various locations.

8.8 Chapter Summary

Chapter 8 provided an in-depth exploration of Victrex's PEEK gear tooth wear, explicitly focusing on the 650G grade and considering factors like bending stress, wear, and friction. The study employed ANSYS simulation to assess initial and critical cracks, building upon the polymer gear equations outlined in Chapters 3 and 5, particularly for the BS-PA30 geometry. It analysed tooth stress and deformation in gear models, considering factors such as frictional coefficients, flash temperature, and variations in wear size.

The study highlighted increased surface damage on gear teeth led to higher analytical equivalent stress values. The pinion component showed significant effects, especially in the pitch and tip areas. After 30 million cycles, wear was evident, eventually leading to cracking on the gear tooth surface at the pitch position. At 32.8 million cycles, the coefficient of friction was approximately 0.43493, and the flash temperature reached around 96.48 Celsius, as calculated. The analysis pinpointed the highest analytical equivalent stress values, which continued to rise until cracks developed. These findings underscore the critical importance of equal stress and wear analysis in determining the durability and failure mechanisms of gear components under conditions of involute tooth wear.

Chapter 9

Dynamic Analysis of Crack Propagation in PEEK Polymer Gears: Insights from ANSYS Simulations and Fracture Mechanics

This work focuses on the dynamic behaviours of tooth wear systems and the paths of gear crack propagation that influence the system's performance. Specifically, the study concentrates on a crack that spreads through the pitch area of a gear and affects two key aspects: the stiffness of the gear's meshing teeth over time and vibration responses.

A crack in a polymer gear refers to a fracture in the gear's material. Crack propagation describes the crack extending over time and under the influence of applied loads or stresses. Typically, issues related to the durability, failure analysis, or performance of polymer gears are discussed, especially regarding gear mechanism or materials properties. Researchers may investigate factors contributing to crack initiation and propagation, which affect the overall integrity and reliability of polymer gears in various applications.

9.1 Research Background

The findings in this Chapter 9 establish the time periods associated with gear body positions during the rotation on the crack area and crack propagations of the worn PEEK gear. These findings reveal a significant and noticeable effect on the vibration responses of the gear system regarding reaction force and torque. Notably, as these cracks' wear depth or severity increases, the impact becomes more pronounced. The study focused on analysing the meshing dynamics of a gear pair involving a steel pinion and PEEK wheels. These analyses were conducted to replicate experimental conditions at 10 million cycles, a load of 9.38 Nm, a speed of 1000 rpm, and a gear rotation at 0.0024995 seconds. ANSYS software was employed to simulate the gear's geometries, utilising three-dimensional tooth profiles as the basis for a Crack-Dynamic Structural simulation. This involved a detailed examination of the gear's behaviour and potential issues, mainly related to PEEK materials.

In 2011, Chan proposed that crack depth distribution along the tooth width follows a parabolic function [88], as illustrated in Figure 9.1. When the crack length (b_C) is shorter than the tooth width (b), the solid curve represents the crack curve in Figure 9.1. However, when the crack extends throughout the tooth width, it is depicted as a dashed curve, focusing on the crack depth, $q(x)$. This approach provides a more comprehensive representation of crack behaviour in gears.

$$\begin{cases} q(x) = q_0 \sqrt{\dfrac{x + b_C + b}{b_C}}, & x \in [b - b_C b] \\ q(x) = 0, & x \in [0\ b - b_C] \end{cases}$$

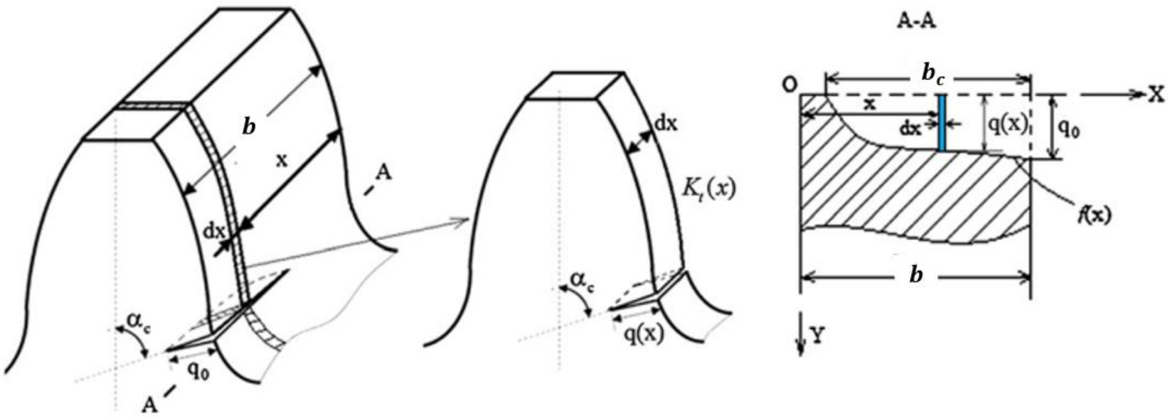

Figure 9. 1 *Crack Depth Distribution Along the Tooth Width (After, [137])*

9.2 Methodology and Boundary Conditions

This chapter delves into the gear wear characteristics of four PEEK grades: 450G, 450FC30, 450GL30, 450CA30, and 650G. This investigation includes both experimental testing and analytical simulation. The primary focus is understanding crack propagation and variations in frictional temperatures between gear pairs, specifically between steel and polymer gears. The simulation employs ANSYS software, emphasising Transient Thermal and Dynamic Structural simulation methods. The objective is to uncover how changes in involute tooth geometries and meshing errors contribute to increased weight loss and the initial development of cracks on tooth flanks.

An experimental study investigated the influence of torque and speed on gear wear. The torque used in the study was set at 9.38 Nm, and the speed was maintained at a constant 1,000 rpm, as outlined in Table 4.5 and Figure 4.7. The study observed an increase in wear on the tooth flank during the real-time operation of the machinery. This wear accumulated as the running cycles progressed, eventually leading to tooth cracks.

9.3 Mode I Fracture of the Critical Stress of Intensity Factor; In-Plane Tensile Opening

The crack propagation state for polymer materials establishes the initial crack-tip size, crack angle, crack length (Cartesian coordinates axis), and radial coordinate of the crack-line relevant to the theory of Modes fracture's stress intensity factor. The critical stress of intensity factor for fracture mode I; in-plane tensile opening. Fracture Mode I is demonstrated by the crack point's opening Mode at the tooth's pitch and root, caused by a force vector or tensile opening [96].

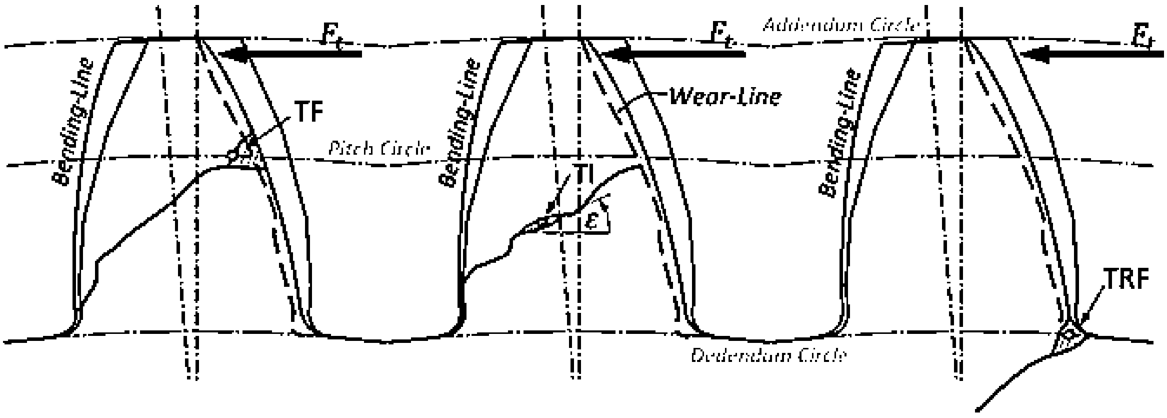

a) Tooth Flank (TF) *b) Tooth Interior (TI)* *c) Tooth Root Flank (TRF)*

***Figure 9. 2** Initial Tooth Fracture Characteristics: Flank, Interior, and Root Flank*

According to Chapter 9.2, the theoretical study of polymer materials' fracture behaviour addressed the crack initiation and crack propagation lives for spur gear models in gears. Multiple approaches were used to estimate the crack tip in TSC and TR for the first crack. Consequently, this study examines changes in the initial crack, crack line and crack direction (Crack angle, crack length of the Cartesian coordinates axis, and radial coordinate) at TSC and TR concerning the theory of Modes fracture.

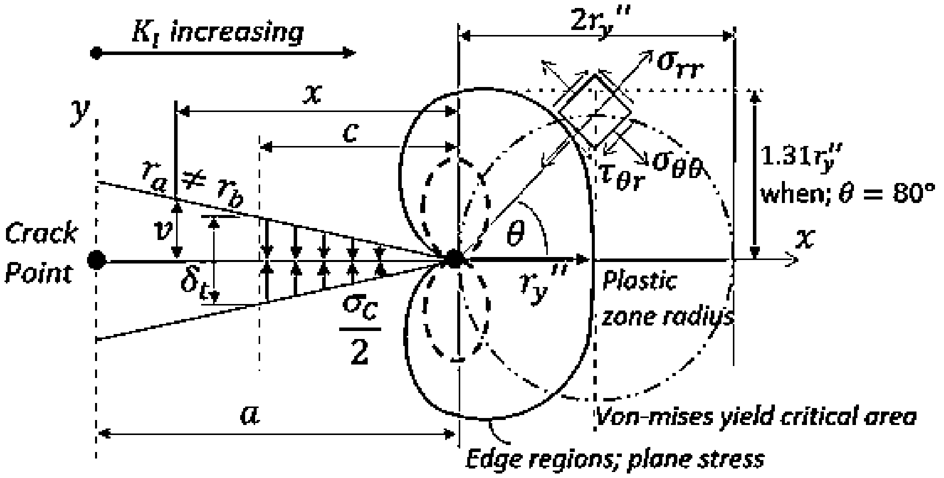

Figure 9. 3 *2D Plane Stress and Plane Strain of Initial Crack-tip to Fracture Mode I*

The crack point's opening mode at the tooth gear's pitch and root demonstrates Fracture Mode I as outlined in Figure 9.3 [18], [138], [95], [139]—the effects from a force vector or tensile opening. The operation of the gears and the workload cause fatigue in the contact surface, gear, and root area. Fatigue of the material leads to a cracking point and crack growth in a direction parallel to the force, eventually resulting in a fracture. Predicting the crack direction relative to Modes of fracture [138], [90], [91], [21], [11], [104], [7] [140] is shown in theory:

Inner-outer contours of plastic zone lines and critical area of radius zone

$$\begin{Bmatrix}\sigma_{xx}\\ \sigma_{yy}\\ \tau_{xy}\end{Bmatrix} = \frac{K_I}{\sqrt{2\pi x}} f_{ij}(\theta) = \frac{K_I}{\sqrt{2\pi x}} \cos\theta \begin{Bmatrix}1 - \sin(\theta/2)\sin(3\theta/2)\\ 1 + \sin(\theta/2)\sin(3\theta/2)\\ \sin(\theta/2)\cos(3\theta/2)\end{Bmatrix}$$

Burger’s vector;

$$\sigma_{rr} = \frac{K_I}{\sqrt{2\pi r_y}} f_{rr}(\theta) = \frac{K_I}{\sqrt{2\pi r_y}}\left[\frac{5}{4}\cos\frac{\theta}{2} - \frac{1}{4}\cos\frac{3\theta}{2}\right]$$

$$\sigma_{\theta\theta} = \frac{K_I}{\sqrt{2\pi r_y}} f_{\theta\theta}(\theta) = \frac{K_I}{\sqrt{2\pi r_y}}\left[\frac{3}{4}\cos\frac{\theta}{2} + \frac{1}{4}\cos\frac{3\theta}{2}\right]$$

$$\tau_{r\theta} = \frac{K_I}{\sqrt{2\pi r_y}} f_{r\theta}(\theta) = \frac{K_I}{\sqrt{2\pi r_y}}\left[\frac{1}{4}\sin\frac{\theta}{2} - \frac{1}{4}\sin\frac{3\theta}{2}\right]$$

In plane stress

$$r_y'' = \frac{1}{2\pi}\left(\frac{K_I}{\sigma_y}\right)^2 cos^2\frac{\theta}{2}\left[4(1 - v + v^2) - 3cos^2(\frac{\theta}{2})\right]$$

In plane strain

$$r_y' \cong \frac{1}{6\pi}\left(\frac{K_I}{\sigma_y}\right)^2$$

Under monotonic loading, $r_y \le \left(\frac{1}{8}\right)a$. When the crack-tip is opening, the corresponding displacement, (δ_t) of crack-opening can be found in both plane stress and plane strain scenarios, given by the following relationships.

$$\delta_{t,p-stress} = \frac{K_I^2}{E\sigma_{y,p-stress}}, \qquad \delta_{t,p-strain} = \frac{K_I^2}{E\sigma_{y,p-strain}}(1 - v^2)$$

$$\sigma_{y,p-strain} \approx \sqrt{3}\,\sigma_{y,p-stress}$$

Thickness effects are observed in the relationship between the significant effect on the actual value of K_{IC} and specimen thickness, b . This is because stress near the crack tip varies from plane strain to plane stress.

$$K_{IC} = \left(\frac{b - 2r_{yc}''}{b}\right)K_{IC}' + \left(\frac{2r_{yc}''}{b}\right)K_{IC}''$$

where for plane stress

$$r''_{yc} = \frac{1}{2\pi}\left(\frac{K_{IC}^2}{\sigma_y}\right)^2$$

9.4 Experimental Data

9.4.1 Peak Frequency of Accelerating Vibration and Temperature data

Regular inspections and maintenance are crucial for identifying tooth cracks early and preventing catastrophic failures. Abnormal vibrations can indicate the presence of cracks. Monitoring vibrations during gear operation can help detect issues. Infrared cameras can detect temperature variations caused by friction in the cracked area.

In the Chapter 4, Figure 4.19, the most significant observation was the occurrence of the highest frequency of accelerating vibration in all axial directions (x, y, z) for PEEK 450G 450GL30. Notably, these vibrations initially fell within the range of ±0.02g but progressively increased to values exceeding ±2.87g, continuing until approximately 190 hours when a crack occurred. Conversely, 450CA30 exhibited un-crack formation compared to the other PEEK materials.

9.4.2 Peak of Force Reactions

Table 9. 1 *Collected Data on the Peak of Accelerating Vibration, Force Reaction, and Temperature*

PEEKs	Crack Time Out	Cycles	Peak Vibration Frequency	Starting Peak Time	Peak Temperature Detected	Force Reaction
450G	236 hrs.+11 min. (850260 sec.)	14.17 million	-2.29g (y-axial)	840260 sec.	71.22 °C Room temp.25.86°C	167.3 N (min.) 194.4 N (max.)
450FC30	292 hrs. (1051200 sec.)	17.52 million	-2.58g (y-axial)	984300 sec.	66.42°C Room temp.23.38°C	164.2 N (min.) 192.5 N (max.)
450GL30	190 hrs. (684000 sec.)	11.40 million	-2.87g (y-axial)	864100 sec.	62.50°C Room temp.23.90°C	144.8 N (min.) 204.2 N (max.)
450CA30	835 hrs. (3006000 sec.)	50.10 million	-2.40g (y-axial)	1184660 sec.	64.60°C Room temp.20.10°C	177.2 N (min.) 188.2 N (max.)

Table 9.1 presents data on force reactions. Specifically, frequency data was recorded at different points in the test duration: 14.17 million cycles for 450G, 17.52 million cycles for 450FC30, 11.40 million cycles for 450GL30, and 50.10 million cycles for 450CA30.

9.4.3 Wear Size

Real-time testing was conducted to collect data on increasing wear size. This involved comparing BS-20PA – PEEKs against Steel G.8, subjected to a torque of 9.38 Nm and a speed of 1,000 rpm using the MARKII testing setup. The analysis focused on the impact of gear surface wear on overall gear performance. Figure 9.4 presents the data collection results, illustrating involute tooth gear failures, as indicated by wear size.

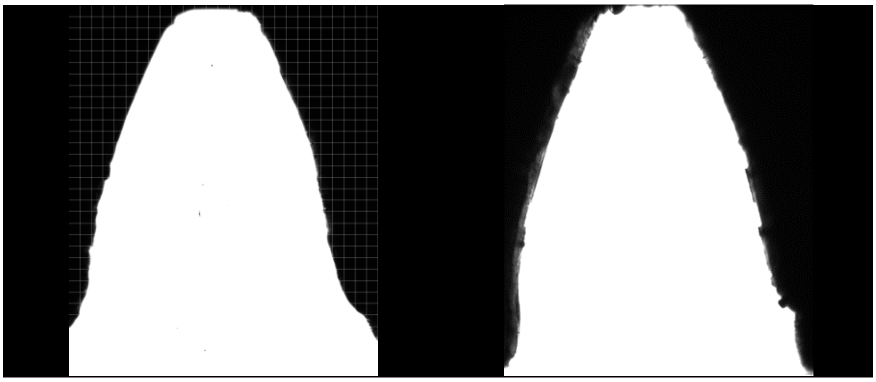

WEIGHT LOSS at 14.17 million cycles *(a) PEEK 450G*

WEIGHT LOSS at 17.52 million cycles *(b) PEEK 450FC30*

WEIGHT LOSS at 11.40 million cycles *(c) PEEK 450GL30*

WEIGHT LOSS at 50.10 million cycles *(d) PEEK 450CA30*

Figure 9. 4 *Photographs of Flank Wear Reduction*

Based on crack data from Table 9.1 and Figure 4.19, PEEK 450GL30 exhibited the most significant wear and developed cracks more rapidly than other PEEK materials among the various grades. In contrast, 450CA30 demonstrated the most minor wear loss and had the smallest initial cracks.

9.5 Numerical Model

9.5.1 3D-Geometries Designing of Tooth Crack

The standard involute gear profile is characterised by the shape of an involute curve and the base circle diameter. This profile ensures uniform pitch, pressure angles, and the positioning of the tooth cracks area. Analysis of this standard profile yields valuable insights into the operation of gear sets, contributing to an enhanced understanding of their performance and noise characteristics.

PEEK 450GL30 and 450G exhibited the most significant wear and developed cracks more rapidly than PEEK others. Therefore, this Chapter focuses on the PEEK 450GL30 and 450G.

Figure 9.5 illustrates two-dimensional geometries generated from worn teeth used in crack simulations. These geometries are shown in front views, displaying 2D line sketches of involute curves on worn gear teeth. The micro-camera, Pylon, was used to capture these images. Among the different PEEK grades, 450GL30 showed the most substantial wear on its teeth. In contrast, 450G, 450FC30, and 450CA30 exhibited similar wear patterns but experienced tooth cracks at different points.

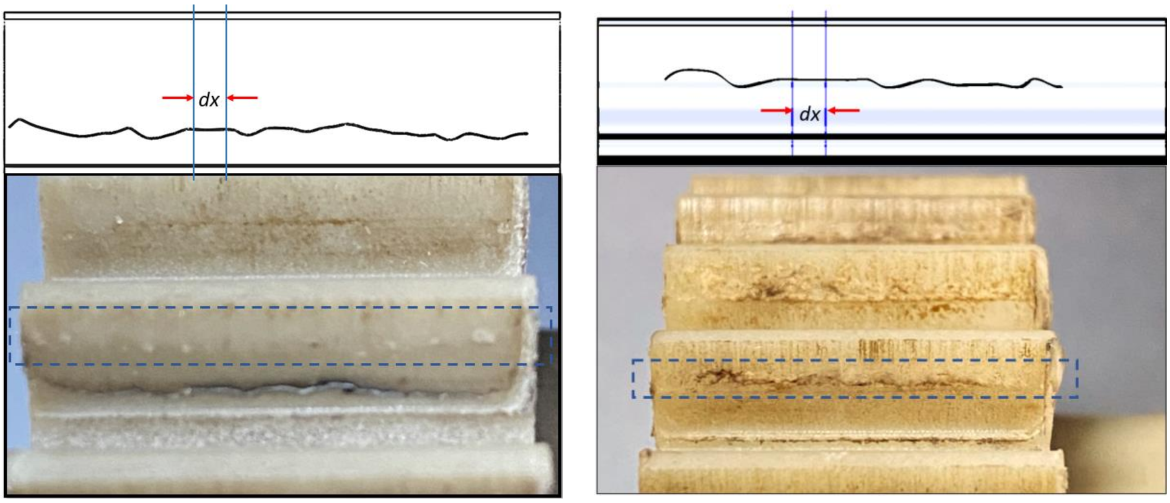

(a) 3D-450G Worn and crack of teeth – Cracked at root

(b) 3D-450GL30 Worn and crack teeth – Cracked at pitch area

Figure 9. 5 *Tooth Geometries of Worn and Cracked Teeth at the end of Cycles, for PEEK 450G and 450GL30, BS-20PA*

9.5.2 Analysing Involute Tooth Gear Geometry and Ball Contact

The study involved analysing the tooth shape of four PEEK grades using a Pylon C camera, specifically at the end of the gear's operational cycles until the development of cracks, as shown in Figure 9.4. The variations in tooth thickness prompted an investigation into the kinematics of spur gears and the factors influencing ball contact size. These findings are detailed in Table 9.2, which presents calculations related to involute tooth gear geometry, ball contact, tooth shape, and thickness due to wear during the crack development period.

Table 9. 2 *Provides Calculations for Involute Tooth Gear Geometry and Ball Contact, Visually Representing Changes in Gear Tooth Shape and Thickness Due to End of Cycle*

Crack	r_{arc} (mm)	C (mm)	$d_{ball,w}$ (mm)	r_b (mm)	$inv.\varphi_1$	T_1 (mm)	$inv.\varphi_2$	ε_s (rad)	c_w (mm)	ε_w (deg)	π/Ng (rad)	$T_1/2r_{arc}$ (rad)	d_{ball}/r_b (rad)
450G	30.135	60.27	3.5313	28.4365	0.0149	2.5786	0.0771	0.0042	0.2391	6.2391	0.3439	0.0428	0.12418
450FC30	30.135	60.27	3.5325			2.6421	0.0782	0.0026	0.1512	6.1512	0.2560	0.0438	0.12422
450GL30	30.135	60.27	3.7488			2.4126	0.0820	0.0067	0.3816	6.3816	0.4864	0.0400	0.13183
450CA30	30.135	60.27	3.4489			2.6532	0.0800	0.0031	0.1793	6.1790	0.2841	0.0467	0.11956

9.5.3 Calculating the Approach and Recess of Contact Path Lines

The tooth profile can alter the contact path and ratio with the contact path calculated. These differences were observed in non-conjugate gears analysed across various test cases. Consequently, the contact ratio was derived from test data, and the results are illustrated in Figure 9.6, showing changes in contact ratio due to worn teeth at the end of running.

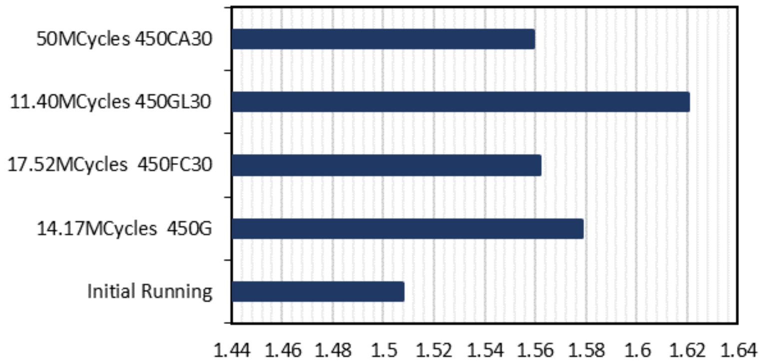

Figure 9. 6 *Contact Ratio Changing Due to Worn Teeth, End of Running*

Table 9. 3 *Illustrates Modified Involute Tooth Geometries for Unworn and Worn Teeth, Considering the Contact Path Line*

	Initial Run	***End of Cycles (Crack)***			
		450G	***450FC30***	***450GL30***	***450CA30***
Wear Size per one tooth, $w_{s,crack}$ (mm)	*0*	*0.2307*	*0.1753*	*0.3704*	*0.1786*
APPROACH, $l_{w_{si}}$ (mm)	*-3.6991*	*-2.8676*	*-2.9201*	*-2.7319*	*-2.9174*
RECESS, $l_{p,w_{si}}$ (mm)	*5.5000*	*6.4546*	*6.3023*	*6.8383*	*6.3114*
ANGLE of APPROACH, $\delta_{S_{a,w}}$ (Deg.)	*-7.4542*	*-5.8258*	*-5.5715*	*-5.5021*	*-5.8757*
ANGLE of RECESS, $\delta_{S_{r,w}}$ (Deg.)	*9.3711*	*13.1132*	*12.6931*	*13.7727*	*12.7114*
CONTACT PATH, (mm)	*9.1691*	*9.3221*	*9.2228*	*9.5702*	*9.2287*

Due to wear, the calculations show changes in the approach and recess lengths along the un-normal contact path due to increased tooth flank wear. Table 9.3 presents modified involute tooth geometries, reflecting the significant impact of tooth flank geometry equations.

9.5.4 Calculating the Frictional Thermal

Flash temperature is influenced by both the rise in temperature caused by mechanical loads and alterations in the stiffness of polymer materials. These changes are driven by factors such as the coefficient of friction, strain responses, tooth wear, and stress-induced bending deformation.

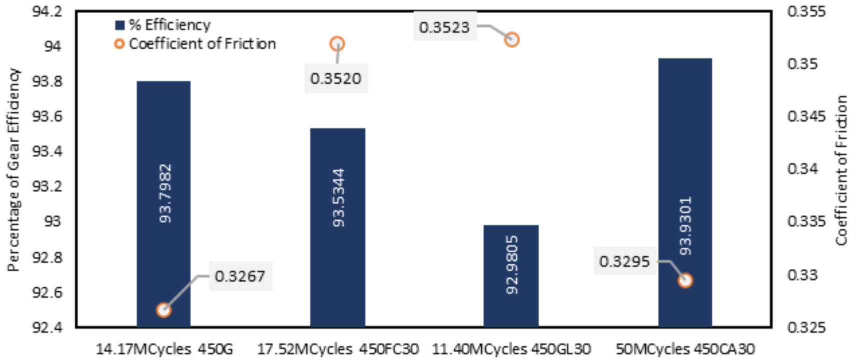

(a) Percentage of Gear Efficiency and Coefficient of Friction

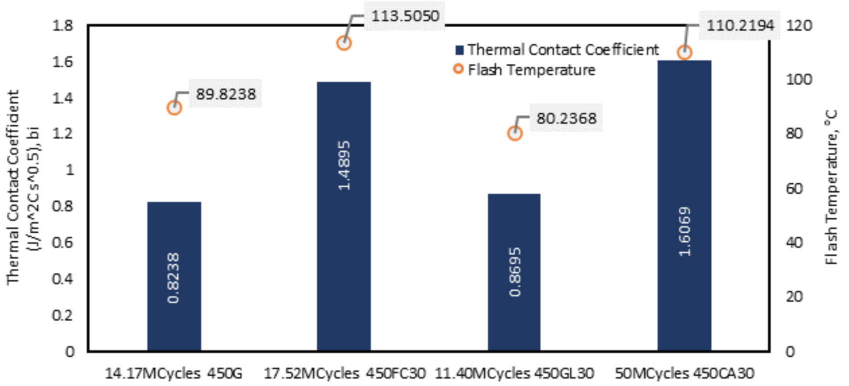

(b) Thermal Contact Efficiency and Flash Temperature

Figure 9. *7 The Coefficient of Friction and Flash Temperature Due to Crack*

In Figure 9.7 (a), the study visually presents the coefficient of friction results, illustrating changes in wear size on tooth flanks at the tooth crack. The research compares variations in transmission efficiency and the coefficient of friction with theoretical expectations and initial running conditions. Measurements were taken from the initial running phase until the tooth cracked. The study evaluates gear transmission efficiency through load tests, specifically comparing four PEEK wheel grades.

In Figure 9.7 (a), the results related to the coefficient of friction and transmission efficiency for different PEEK gear materials are as follows:

- 450GL30: Exhibited the highest wear on its teeth, leading to a significant increase in the coefficient of friction. At around 11.40 million cycles, it experienced gear failure. The gear efficiency dropped to approximately 92.9805%.
- 450G and 450FC30: Showed similar behaviour. They experienced an increase in the coefficient of friction, reaching values of about 0.3267 (93.7982% gear efficiency) for 450G and 0.3523 (93.5344% gear efficiency) for 450FC30. The gear failures occurred at 14.17 million and 17.52 million cycles, respectively.
- 450CA30: Longer lifespan, lasting up to 50.10 million cycles. It exhibited a coefficient of friction of 0.3295, with a gear efficiency of approximately 93.9301%.

These findings suggest that 450GL30 experienced faster gear failure and lower gear efficiency due to higher tooth wear, while 450CA30 demonstrated better durability with a longer lifespan and higher efficiency. The other two materials, 450G and 450FC30 fell between these extremes in terms of wear and performance.

Figure 9.7 (b) depicts the relationship between variations in the thermal contact coefficient and flash temperature calculation. However, 450CA30 and 450FC30 exhibited higher flash temperatures and thermal contact coefficients than 450G and 450GL30. These differences are primarily influenced by material properties, including thermal conductivity, density, and specific heat, which shape flash temperature behaviour significantly.

9.6 Crack Simulation

This research extensively explored the behaviour of polymer gears, focusing mainly on the crack propagation effect through structural-dynamic analysis simulations. These simulations employed a reasonable modulus of elasticity. For more specific details regarding the modulus of elasticity related to wheels made from PEEK material, readers can refer to Chapter 4 for comprehensive information.

Several factors, including the coefficient of friction, strain responses, tooth wear, and stress-induced bending deformation, influenced the observed changes in gear behaviour. The study comprehensively examined polymer gears, explicitly focusing on understanding the viscoelastic effects. For detailed information on Crack-Dynamic Structural analysis simulations, readers are referred to Chapter 5 of the study.

9.6.1 Boundary Conditions

a. Create a 3D model of the gear and the crack, define the gear's geometry, mesh it into finite elements, and introduce the crack into the model.

b. Material properties include the modulus of elasticity, Poisson's ratio, and fracture toughness.

c. Define how the gear is constrained or loaded. The setup specified how the gear connects to other system parts and external forces or torques. An experimental study was conducted to analyse the effects of torque and speed on gear wear. The torque was set at 9.38 Nm, and the speed was maintained at 1,000 rpm, with 15 degrees of gear rotation in 0.0024995 seconds, as outlined in Table 4.5 and Figure 4.21.

d. Define initial crack and crack growth: Set up the mesh for the initial crack and monitor crack growth over time using ANSYS software. Increased wear and the appearance of cracks on the tooth flank were observed during real-time machine operation, with the wear accumulating up to the end of cycles. The significance of these factors in simulating gear crack and crack propagations is illustrated in Figure 9.8, based on Figure 9.5.

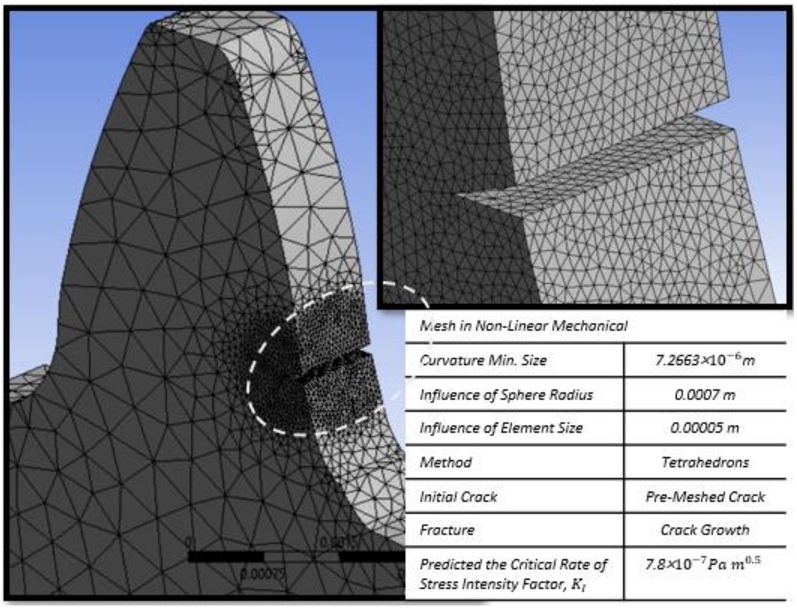

Mesh in Non-Linear Mechanical	
Curvature Min. Size	$7.2663\times10^{-6} m$
Influence of Sphere Radius	0.0007 m
Influence of Element Size	0.00005 m
Method	Tetrahedrons
Initial Crack	Pre-Meshed Crack
Fracture	Crack Growth
Predicted the Critical Rate of Stress Intensity Factor, K_I	$7.8\times10^{-7} Pa\ m^{0.5}$

(a) PEEK 450G-initial crack at root area

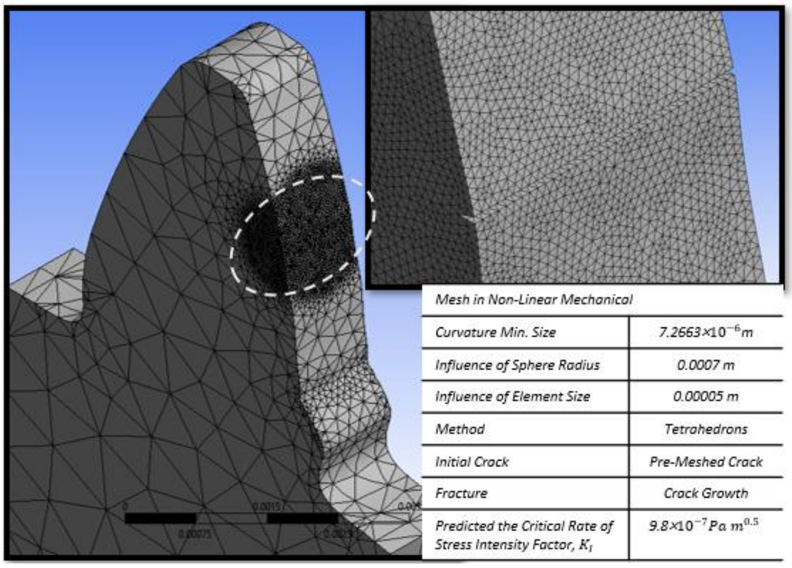

Mesh in Non-Linear Mechanical	
Curvature Min. Size	$7.2663\times10^{-6} m$
Influence of Sphere Radius	0.0007 m
Influence of Element Size	0.00005 m
Method	Tetrahedrons
Initial Crack	Pre-Meshed Crack
Fracture	Crack Growth
Predicted the Critical Rate of Stress Intensity Factor, K_I	$9.8\times10^{-7} Pa\ m^{0.5}$

(b) PEEK 450GL30-initial crack at pitch area

Figure 9. 8 *Example of Setting Up the Mesh of an Initial Crack of PEEK 450G and 450GL30*

In non-linear mechanical simulations, as shown in Figure 9.8, achieving an optimal mesh is crucial. This involves setting a minimum size for curvature accuracy around $7.2663 \times 10^{-6}\ m$ and assessing the impact of a sphere radius of $0.0007\ m$. Additionally, the choice of element size $0.00005\,m$ and the use of tetrahedron-based meshing methods significantly affect the accuracy and efficiency of simulations. Furthermore, incorporating pre-meshed cracks, both initial and those expected to propagate during fracture analysis, is essential for accurately predicting crack growth behaviour in complex structural systems.

9.6.2 Simulation Results

To perform a static analysis to simulate the cyclic loading and its effects on the material, ANSYS calculates stress and strain distributions within the component over the specified number of cycles.

9.6.2.1 Stress Intensity Factors (SIFs) Based on Frequency

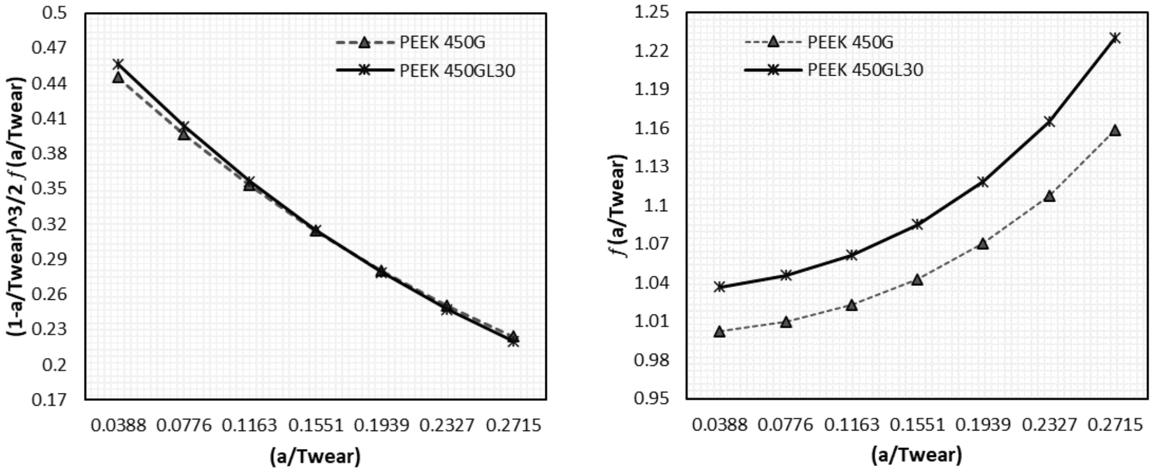

(a) Tada et al.'s Equation *(b) Irwin's Equation*

Figure 9. 9 *Tooth Wear-Dimensionless of the SIFs*

The load frequency refers to analysing these factors, considering the applied load varies with time and frequency. SIFs are crucial for understanding crack propagation and assessing the potential for material failure. The consideration for load frequency, which can change over time and at different frequencies, is included in the calculations or analyses. Thus, SIFs are calculated based on load frequency-dependent data in units of $MPa\, m^{-5}$, as illustrated in Figures 9.9 and 9.10.

SIFs are determined based on the numerical values of $f(\frac{a}{T_{wear}})$ and the crack opening displacement at the surface (a/T_{wear}), using Tada et al. and Irwin's equations, depicted by the curves in Figure 9.9 (a) and (b). Based on worn teeth and crack area, the results predicted more than 0.5% accuracy of four-point bending for PEEK 450G and 450GL30.

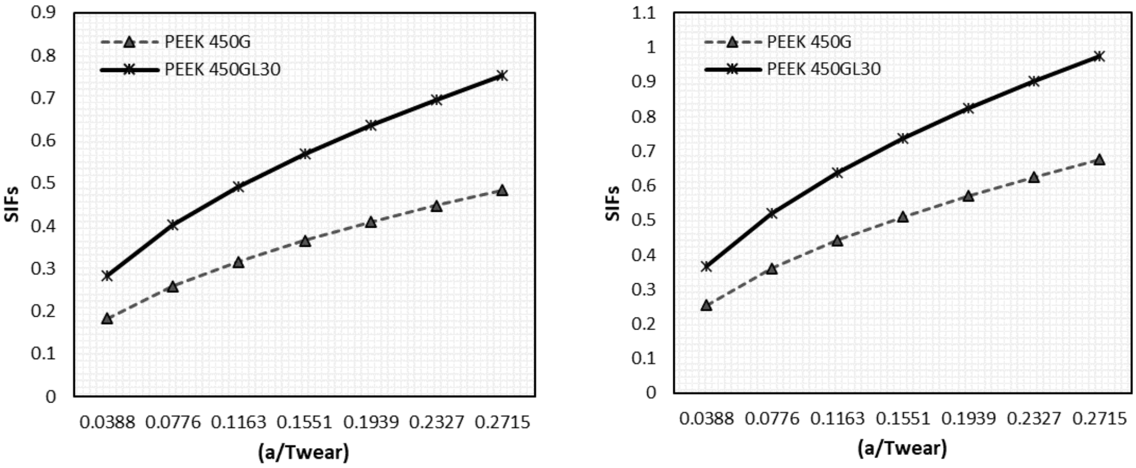

(a) Tooth Wear-SIFs-Lowest Frequency *(b) Tooth Wear-SIFs-Highest Frequency*

Figure 9. 10 *SIFs Based on the Lowest and Highest Frequencies*

In Figure 9.11, these results include information on the SIFs (representing a Mode I problem), the crack opening displacement at the surface (a/T_{wear}), and the additional rotation induced by the presence of the crack. Based on worn teeth, the lowest and highest frequencies were found from the force reactions and maximum equivalent stresses for PEEK 450G and 450GL30.

In literature, in Linear Elastic Fracture Mechanics (LEFM) analysis, SIFs describe displacements and stresses around the crack front, which are crucial for analysing fatigue crack growth. As the crack extends, the SIFs reach a critical state, leading to fracture initiation due to deformation. The studies from fatigue crack growth using approaches for simple and complex geometries in two and three dimensions [125].

9.6.2.2. Crack Initiation

The location and size of potential crack initiation sites are based on factors such as stress concentrations, material properties, and geometry have been determined. According to Figure 9.8, the results of the stress and elastic strain distributions are based on the lowest and highest frequencies, as found in Figures 9.11 and 9.12.

PEEK 450GL30 – Highest Frequencies

In Figure 9.11, an initial crack in a 450G and 450GL30 were found at the gear's root and pitch area, respectively. The prediction of stress concentration within the polymer gear's material can be made. Thess prediction may indicate that stress concentrations are significant enough to initiate a small crack at the root and pitch area of the gear tooth, characterized by a specific length or displacement denoted as (dx).

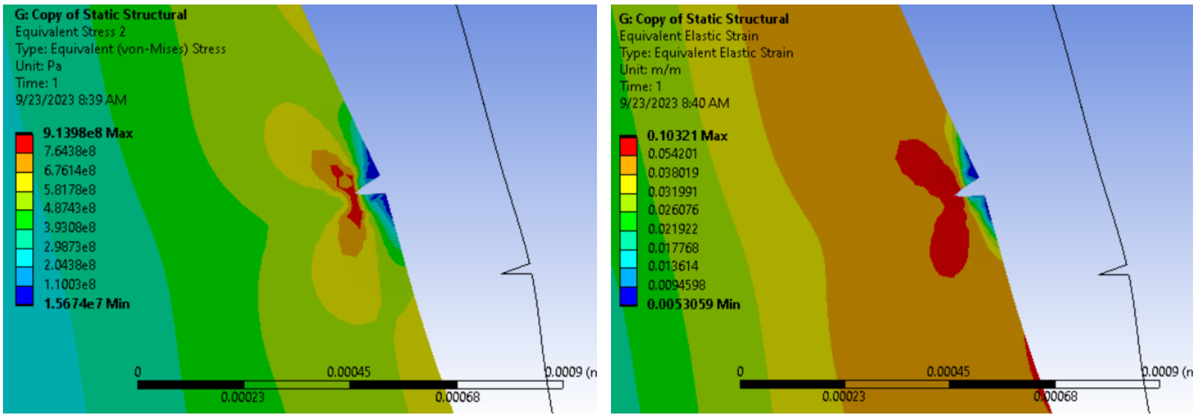

(a) Equivalent Stress - Highest Frequency *(b) Equivalent Elastic Strain - Highest Frequency*

Figure 9. 11 *Initial Crack - Stress and Elastic Strain Distributions – 450GL30*

This initial crack formation is critical in understanding the gear's structural integrity and potential Mode I failure of polymer material. In Figures 9.11 and 9.12, Finite Element Analysis (FEA) calculates the stress distribution within the gear, focusing on the region around the initial crack. Due to critical stress and elastic strain levels, stress concentrations are determined based on the lowest and highest frequencies of two PEEK grades. Figure 9.12 (a) shows that the stress distribution increased to 913 MPa and 0.10321 m/m of strain distribution, as shown in Figure 9.11 (b).

9.6.2.3 Crack propagations

The analysis continues until the cracks reach a critical size. The required size is often defined based on failure criteria, as shown in Figures 9.13 and 9.14, which presents the results of the cracks that have propagated within the component along the line of the crack. ANSYS displays the crack paths and visualizes stress and strain distributions.

Figure 9.12, 450G30 starting crack propagation at root, the stress and elastic strain distributions results show a maximum around 0.53667 m/m and 3129.9 MPa, respectively. In Figure 9.13, the simulation demonstrates the progressive extension of the crack over time; stress intensity factors are computed at the root and pitch area to assess its growth tendency. The SIFs and fatigue properties of 450GL30 are considered to predict crack growth rates. The results found the SIFs increased around 18.343 $MPa\,m^{-5}$, with the stress distribution increasing to 4234.2 MPa and 0.53667 m/m of strain distribution, as shown in Figure 9.13 (b).

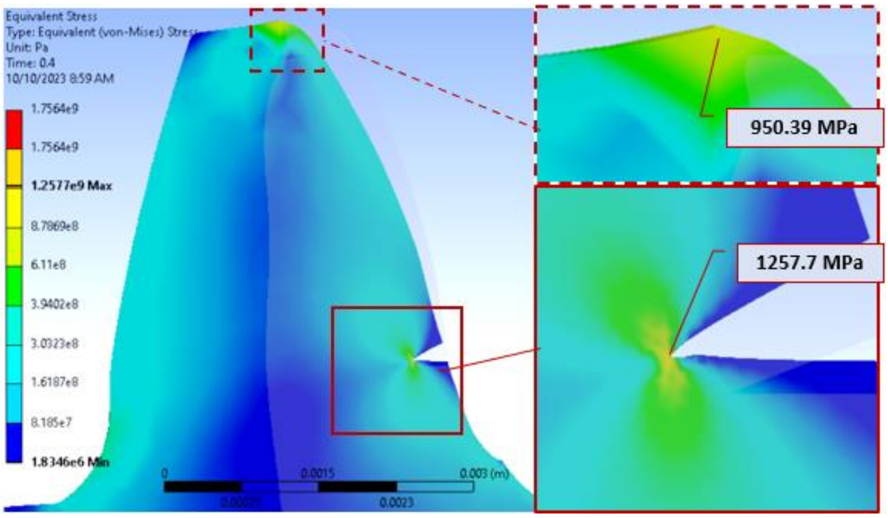

(a) Equivalent Stress - Highest Frequency

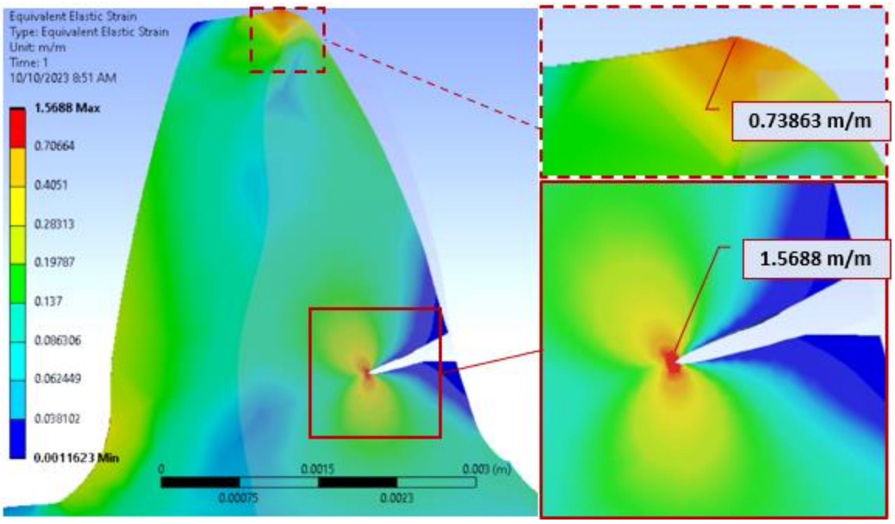

(b) Equivalent Elastic Strain - Highest Frequency

Figure 9. 12 *Starting Crack Propagation - Stress and Elastic Strain Distributions – 450G*

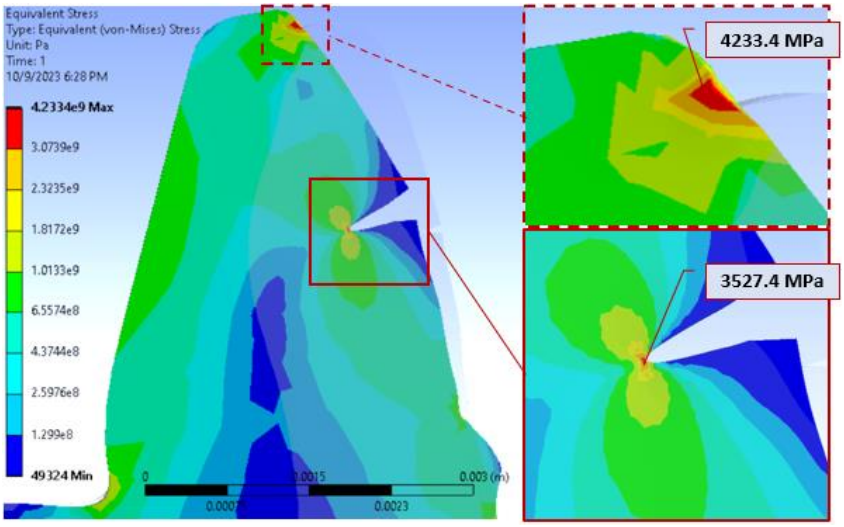

(a) Equivalent Stress - Highest Frequency

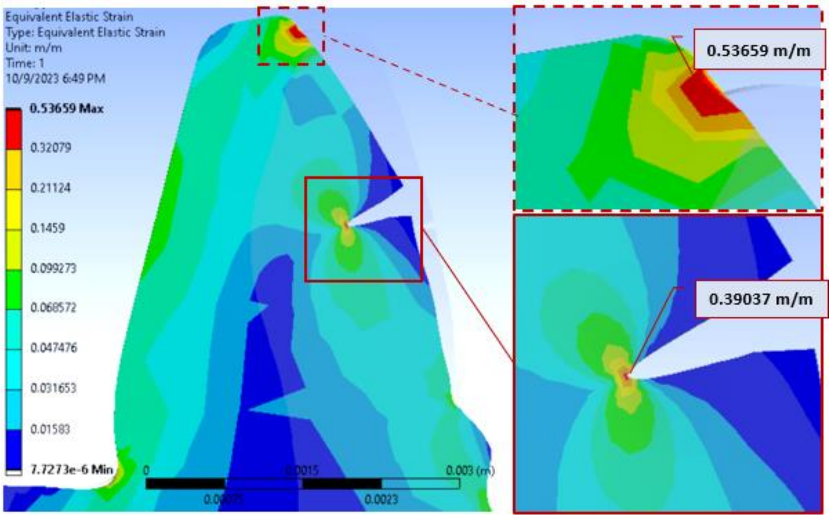

(b) Equivalent Elastic Strain - Highest Frequency

Figure 9. 13 *Starting Crack propagation - Stress and Elastic Strain Distributions – 450GL30*

9.6.2.4 SIFs – Fatigue Fracture

The behaviour of Stress-Intensity Factors SIFs, represented by K_I, is significantly influenced by the particular material properties, loading conditions, and the geometry of the crack under consideration. The Paris law, previously mentioned, is frequently employed to K_I describe evolve as the crack grows under fatigue conditions. It is crucial to consider all pertinent factors and conduct comprehensive analyses to ascertain whether K_I is rising, decreasing, or staying constant as the crack propagates.

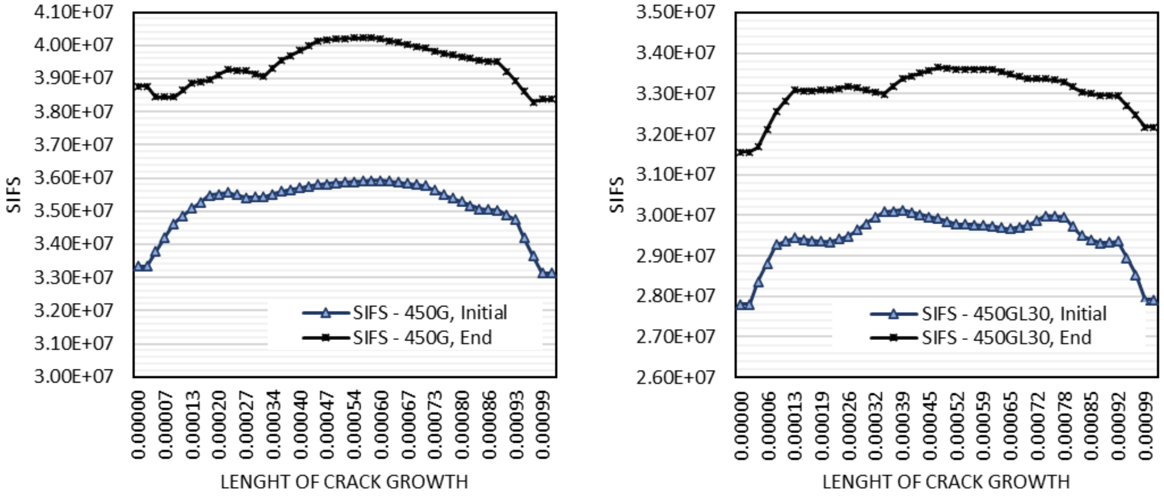

(a) SIFs – PEEK 450G *(b) SIFs – PEEK 450GL30*

Figure 9.14 *SIFs Based on Crack Growth*

In Figure 9.14 (a), concerning the behaviour of Stress SIFs, specifically for 450G, an initial increase in SIFs is observed during applied load tests. This is particularly prominent in Mode I crack propagation (the opening mode), where higher tensile stress drives crack growth. As the crack's length extends to 1.00 mm, the SIFs also increase to 40.2 $MPa\, m^{-5}$ due to the longer crack experiencing elevated stress concentrations. This trend is depicted in the maximum alternating equivalent stress, reaching 4104.4 MPa in Figure 9.15 (a), signifying significant stress concentrations around the crack's tip (TR).

Over time, K_I stabilize and remains consistent within a distance range of approximately 0.40 to 0.60 mm under conditions of stable crack growth. However, K_I eventually decreases to 38.3 $MPa\, m^{-5}$is decrease can be attributed to the influence of compressive stresses ahead of the crack tip, which reduces the effective stress driving crack growth, resulting in a decline in K_I

In the case of 450GL30-SIFs, stress-driven crack growth in the opening mode is evident. As illustrated in Figure 9.14 (b), the crack length extends to 1.01 mm, and the SIFs increase to 3.37 $MPa\, m^{-5}$. as the longer crack experiences higher stress concentrations. This results in the maximum alternating equivalent stress reaching 4233.4 MPa in Figure 9.15 (b), indicating significant stress concentrations around the TSC. Over time, K_I remains relatively stable within a distance range of 0.0004 to 0.0006 during stable crack growth conditions. However, in the same range, K_I decreases to 38.3 $MPa\, m^{-5}$.

To determine the specific fatigue life of gear tooth cracks, experimental testing and computer simulations must be conducted. This process entails using a combination of both experimental testing and computer simulations.

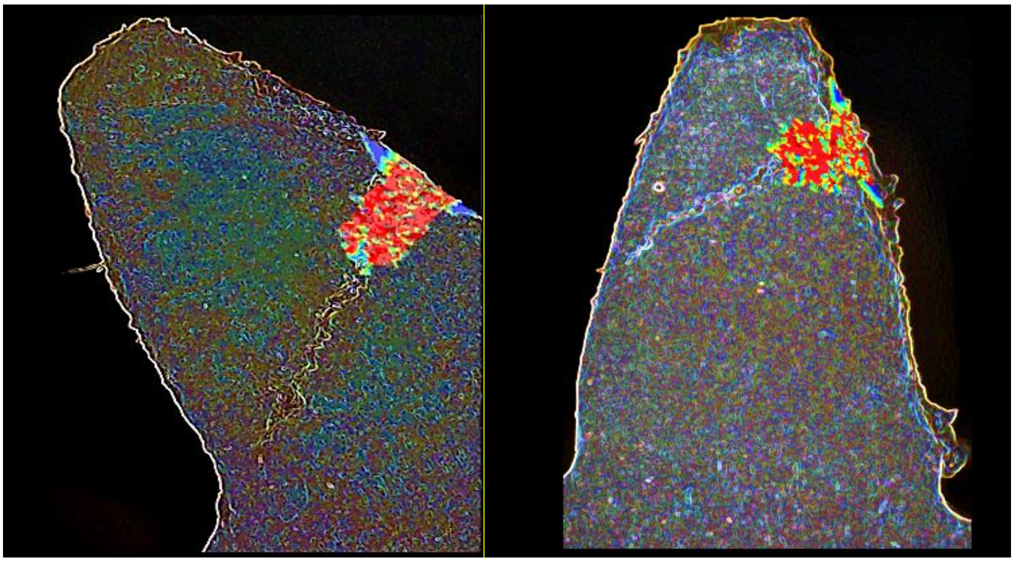

(a) PEEK 450G-TR *(b) PEEK 450GL30-TSC*

Figure 9.15 *Alternating Equivalent Stress Prediction on the Tooth Crack Area*

In Figure 9.15 (a), for 450G-SIFs, the maximum alternating equivalent stress remains stable, and the fatigue life values range from approximately 0 to 2508 cycles within the red-coloured area, indicating a higher likelihood of possible failure in this range. In contrast, the blue area suggests a longer potential fatigue life, extending to approximately 9.77 million cycles.

In Figure 9.15 (b), 450GL30's remaining stress and fatigue life values are limited to approximately 0 to 0.09236 cycles within the red zone. This signifies a significantly shorter fatigue life compared to 450G at TR. The red zone indicates a faster path to failure for the component under consideration.

Therefore, the various factors were including material properties, loading conditions, and crack geometry, influence the behaviour of SIFs. In the case of 450G, SIFs initially increase due to tensile stress promoting crack growth. However, they decrease as compressive stresses ahead of the crack tip reduce SIFs—the fatigue life values for 450G range from 0 to approximately 2508 cycles. For 450GL30, stress-driven crack growth in the opening mode increases SIFs as the crack lengthens. SIFs remain relatively stable over time within a specific range before decreasing. These findings highlight the complex interactions of factors affecting SIF behaviour during crack growth. The remaining stress and fatigue life values for 450GL30 are limited to approximately 0 to 0.09236 cycles.

Finally, considering the material properties, it can be inferred that PEEK 450GL30 has a higher yield strength than PEEK 450G, as it could withstand a longer crack length before propagation occurred.

9.7 Chapter Summary

In summary, Chapter 9 presents a comprehensive investigation into the dynamics of crack propagation in various PEEK gears. This chapter combined experimental approaches with analytical methodologies to offer an in-depth understanding of gear wear characteristics, fracture mechanics principles, and the influence of various loads and temperature conditions on gear functionality.

1. Crack Propagation in PEEK Gears: The study reveals that crack propagation in polymer gears, particularly those made of PEEK material, is significantly influenced by operational conditions such as load and temperature. This underscores the material's behaviour under stress and its impact on gear longevity.

2. Use of ANSYS Software: The employment of ANSYS for Crack-Dynamic Structural simulation is pivotal, providing detailed insights into how cracks initiate and evolve in the gear's structure.

3. Fracture Mechanics and Wear Characteristics: The research emphasises the importance of understanding fracture mechanics concerning the gear's wear characteristics. This knowledge is critical for predicting gear failure and developing strategies to mitigate wear and tear, enhancing gear performance and lifespan.

Chapter 10

Summary

This extensive research focuses on polymer composite materials, explicitly exploring four grades of PEEK (450 and 650G), in line with industrial gear geometry standards such as BS/ISO 6336, and using Victrex^{TM} materials. Conducted at the Mason Institute of Tribology laboratory, this study employs the MARK II testing machine and covers six critical areas of investigation.

Firstly, the research introduces an innovative equation tailored for polymer or plastic materials. This equation is pivotal in understanding changes in involute tooth geometries, mainly influenced by meshing kinematic behaviour. It incorporates a range of factors such as ball contact, the contact path line (including approach and recess sections), base pitch, and contact angles, all within the framework of recognised frictional temperatures. Additionally, the study examines tooth wear characteristics by measuring weight and distance and investigates frictional behaviours on the tooth flank, drawing upon the equations of Buckingham and Merritt.

Secondly, the research applies four distinct coefficient theories - Buckingham, Merritt, Benedict & Kelley, and Drozdov & Gavrikov - to substitute specified coefficients in each methodology. These theories are crucial in determining frictional coefficients and forecasting power loss, mainly through Rao's sliding power loss equation. The Drozdov & Kelly equation, notably, predicts the lowest friction values, consistently under 0.1, while the other theories suggest higher friction values above 0.1.

Thirdly, Structural and thermal-dynamic geometries are analysed using FEA. This aspect of the research identifies changes in the contact pressure stress interface and the extended stress distribution across tooth flanks, highlighting significant shifts in load sharing, tooth deformation, and equivalent stress behaviours.

Fourthly, the study delves into crack propagation, examining worn teeth and cracks. This analysis reveals alterations in the approach lengths and recess along the un-normal contact path, leading to increased wear on tooth flanks and the onset of initial cracks.

Fifthly, the research underscores the importance of LEFM analysis, focusing on Stress Intensity Factors (SIFs) critical for evaluating fatigue crack growth. As cracks progress, SIFs reach a critical threshold, culminating in fracture initiation due to deformation. Various factors, including the coefficient of friction, strain responses, tooth wear, and stress-induced bending deformation, influence the changes in gear behaviour observed in this study.

The results presented in this thesis provide a platform for further research to enhance the understanding of polymer gear performance; further could include:

1. Extended Material Analysis: While the study extensively covers PEEK materials, additional polymer composites could be examined to broaden the understanding of gear performance across a broader range of materials. Investigations into how different polymer

blends and additives influence gear performance, such as wear resistance, thermal properties, and strength, would be valuable.

2. Long-Term Durability Studies: Conducting long-term durability and endurance tests under various operational conditions would provide deeper insights into the life span of polymer gears. This would include extended cyclic loading tests and environmental conditioning (e.g., exposure to various temperatures, humidity levels, and corrosive environments) to simulate real-world applications more accurately.

3. Advanced Simulation Models: More complex and dynamic simulations could offer more detailed insights into the stresses, strains, and heat distribution within polymer gears during operation. This could also include simulating more complex gear systems and load scenarios.

4. Microstructure Analysis: A more in-depth study of the microstructural changes in polymer gears under load could reveal insights into how micro-level changes impact macro-level performance.

5. Innovations in Gear Design: Exploring new gear designs, such as non-standard tooth profiles or innovative gear geometries, could improve performance, noise reduction, and efficiency. This might involve experimenting with different tooth shapes, helix angles, and pitch configurations.

6. Lubrication and Surface Treatment Studies: Researching the impact of various lubrication methods and surface treatments on the performance of PEEK gears would provide insights into reducing wear and increasing efficiency.

7. Thermal Management Strategies: Given the importance of temperature in gear performance, developing and testing new thermal management strategies, i.e. cooling designs, active cooling systems, or materials with improved thermal conductivity through design.

8. Impact of Manufacturing Techniques: Investigating how different manufacturing methods (like injection moulding, 3D printing, or machining) affect the properties and performance of polymer gears will yield essential findings as manufacturing technologies evolve.

9. Real-World Application Testing: Field testing in actual application scenarios, such as automotive, aerospace, or industrial machinery, could provide practical insights into performance under real working conditions.

10. Fatigue and Failure Analysis: A deeper exploration into the fatigue behaviour and failure mechanisms of polymer gears, including pitch-line fractures, will determine limitations and guide design improvements.

From the basis of the research presented in this thesis, each of these areas offers the potential to significantly expand the current understanding of polymer gear systems, leading to improvements in their design, manufacturing, and application across various industries.

In conclusion, this comprehensive thesis encompasses various investigations and analyses about polymer composite materials, mainly the PEEK grades, within gear performance. It provides an in-depth examination of tooth wear, frictional coefficients, stress distribution, crack propagation, and the effects of multiple factors on gear functionality. The findings of this research offer significant contributions to the understanding of polymer gear materials and mechanisms, enhancing our knowledge of their behaviour under diverse conditions.

References

[1] D. Walton and A. J. Goodwin, The wear of unlubricated metallic spur gears, Birmingham, UK: School of Manufacturing and Mechanical Engineering, The University of Birmingham, 1998.

[2] S. Kono, “Increase in power density of plastic gears for automotive applications.,” University of Birmingham, Birmingham, United Kingdom, 2003.

[3] S. Kono, Increase in power density of plastic gears for automotive applications, Birmingham, United Kingdom, 2003.

[4] K. D. Dearn, Tribological and Performance Aspects of Polymer Gears [Ph.D. thesis], Birmingham, United Kingdom, 2009.

[5] Victrex, “Victrex PEEK: Advantages for automotive applications,” Victrex PEEK, 2018.

[6] M. Irfan, “Meta Modeling of Transmission Error for Spur, Helical and Planetary Gears for Wind Turbine Application,” Department of Applied Mechanics, Chalmers University of Technology, Goteborg, Sweden, 2013.

[7] R. M. Lias, M. Awang, M. N. Talib, M. R. Senawi and M. A. Samad, “Investigation of Axial Misalignment Effects to the Gear Tooth Strength Properties Using FEM Model,” *Journal of Mechanical Engineering and Sciences,* pp. Volume 12, Issue 2, pp. 3581-3592, 2018.

[8] M. Ely and K. Vietsch, “The Important of Shaft Alignment: Strategies for Ensuring the Uptime of Rotating Equipment,” 30 November 2011. [Online].

[9] M. Irfan, Meta Modeling of Transmission Error for Spur, Helical and Planetary Gears for Wind Turbine Application, Goteborg, Sweden: Department of Applied Mechanics, Chalmers University of Technology, 2013.

[10] F. Curà, A. Mura and M. Gravina, “Load distribution in Spline Coupling Teeth with Parallel Offset Misalignment,” *Proceedings of the Institution of Mechanical Engineers, Part C: Journal of Mechanical Engineering Science,* 2013.

[11] S. Prabhakaran, D. S. Balaji and C. Joel, “Stress Analysis and Effect of Misalignment in Spur Gear,” *International Journal of Applied Engineering Research,* pp. Volume 9, pp. 13061-13071, 2014.

[12] M. Akerblom, “Gear Noise and Vibration: A Literature Survey,” Volvo Construction Equipment Components, Eskilstuna, Sweden.

[13] L. Shuting, “Effects of Misalignment Error, Tooth Modifications and Transmitted,” *Mechanism and Machine Theory, ,* pp. 125-136, 2014.

[14] M. D. Vlittie, “Misalignment No Beauty in Gear sets. Gear Technology,” *Gear Technology, USA: Randall Publications LLC 1996-2015,* p. 11, 2015.

[15] W. M. Ghazali, D. N. Idris, A. H. Sofian, J. P. Siregar and M. S. Edrus, “A Review on Failure Characteristics of Polymer Gear,” in *The 2nd International Conference on Automotive Innovation and Green Vehicle (AiGEV 2016)*, 2017.

[16] C. H. Kim, “Durability improvement method for plastic spur gears,” *Tribology International 39,* p. 1454–1461, 2006.

[17] S. Selvaraj and R. Gnanamoorthy, “Damage Mechanisms in Injection Molded Unreinforced, Glass and Carbon Reinforced Nylon 66 Spur Gears,” *Applied Composite Materials 11,* pp. 337-397, 2004.

[18] A. J. Kinloch and R. J. Young, Fracture Behavior of Polymers, London and New York, United Kingdom and United State: Applied Science Publishers, 1983.

[19] H.-J. Dennig, S. Monn and A. Vodermayer, “Thermoplastic high performance composite gears,” in *International Conference on Gears 2019*, 2019.

[20] BS 6336, “BS 6336 - Calculation of load capacity of spur and helical gears,” he British Standards Institution, 2023.

[21] BS 6168, “Specification for Non-Metallic Spur Gears,” The British Standards Industry, 1987.

[22] ANSI/AGMA 1010-F14, “Appearance of GearTeeth - Terminology of Wear and Failure,” American National Standard/American Gear Manufacturers Association, 2014.

[23] “Victrex PEEK: the foundation of victrex innovations,” Victrex PEEK.

[24] “Victrex PEEK: Advantages for automotive applications,” Victrex PEEK.

[25] P. K. Meuleman, D. Walton, K. D. Dearn, D. J. Weale and I. Driessen, “Minimization of transmission errors in highly loaded plastic gear trains,” *JMES439 © IMechE,* p. Mechanical Engineering Science, 2007.

[26] R. Tharmakulasingham, G. Alfano and M. Alfano, “Reduction of gear pair transmission error with tooth profile modification,” p. www.semanticscholar.org, 2008.

[27] K. S. S. Satyendra, “Behaviour of Iron and Steel Materials during Tensile Testing,” 2016. [Online].

[28] B. R. Hoehn and K. Michaelis, “Influence of oil temperature on gear failures,” *Tribology International 37(2),* pp. 103-109, 2004.

[29] B. R. Hohn, K. Michaelis and H. P. Otto, “Pitting load carrying capacity under increased thermal conditions,” in *3rd International Conferance on Integrity, Reliability and Failure*, Portugal, 2009.

[30] G. Knauer, “Zur Grübchentragfähigkeit einsatzgehärteter Zahnräder – Einfluß von Werkstoff,” *Schmierstoff und Betriebstemperatur,* 1988.

[31] R. Tharmakulasingam, Transmission Error in Spur Gears: Static and Dynamic [PhD], United Kingdom: Brunel University, 2009.

[32] A. Fernández, M. Iglesias, A. d. Juan, A. Diez, P. García and F. Viadero, “Gear transmission dynamics: Effects of index and run out errors,” *Applied Acoustics ,* 2015.

[33] Ely, M; Vietsch, K, "The Important of Shaft Alignment: Strategies for Ensuring the Uptime of Rotating Equipment," 30 November 2011. [Online]. Available: https://www.flowcontrolnetwork.com/the-importance-of-shaft-alignment/.

[34] K. D. Dearn, T. Hoskins, D. G. Petrov, S. Dearn and R. Banks, "Applications of Dry Film Lubricants for Polymer Gears, Wear," *SciVerse ScienceDirect,* pp. 99-108, 2013.

[35] R. D. Houser and D. Wesley, "Methods for Measuring Gear Transmission Error under Load and at Operating Speeds," *SAE Technical,* p. 891869, 1989.

[36] I. Atanasovska and V. N. Stanojevic, "3D Spur Gear FEM Model for the Numerical Calculation of Face Load Factor,," *Automatic Control and Robotics Vol. 6,* pp. 131-143, 2007.

[37] "Plastic Gears – Lightweight and Rust-proof," https://khkgears.net/new/plastic_gears.html.

[38] A. B. Copper, The efficiency and friction of plastic cylindrical gears [PhD Thesis], Birmingham, United Kingdom, 2003.

[39] Dearn, K D; Kukureka, S N; Walton, D;, "Chapter 14: Engineering Polymers and Composites for Machine Elements," in *Polymer Tribology*, World Scientific Publishing Co Pte Ltd., 2009.

[40] K. Singh, Siddhartha and P. K. Singh, "Polymer spur gears behaviors under different loading conditions: A review," in *Proceedings of the Institution of Mechanical Engineers, Part J: Journal of Engineering Tribology*, 2019.

[41] M. J. Jenkins, "Relaxation behaviour in blends of PEEK and PEI," *Polymer Volume 41, Issue 18,* pp. 6803-6812, 2000.

[42] C. Herzog, M. Wolf, D. Schubert and D. D. Drummer, "In situ investigation of the influence of varying load conditions on," *Forsch Ingenieurwes 86,* p. 545–555, 2022.

[43] Z. Lu, H. Liu, C. Zhu, H. Song and G. Yu, "Identification of failure modes of a PEEK-steel gear pair under lubrication," *International Journal of Fatigue ,* 2019.

[44] J. Cathelin, J. P. d. Vaujany, M. Guingand and L. Chazeau, "Loaded Behavior of Gears Made of Fiber-Reinforced PA6," *Gear Technology,* 2014.

[45] Y. H. Huh, P. Park, D. J. Kim and J. H. Park, "Effect of Biaxial Static Loads on Fatigue Crack Propagation Behavior under Cyclic Tensile and Torsional Loading," *Trans Tech Publications, Engineering Materials Online,* pp. 720-723, 2006.

[46] D. P. Rocha and D. M. Miguel, BULK TEMPERATURE IN POLYMER-METAL, University of Pordo, 2017.

[47] Park, Chan IL;, "The sliding friction under quasi-static conditions causes the principle of the transmission error (TE) of spur gears.," *Journal of Mechanical Science and Technology 33,* pp. 1311-1319, 2019.

[48] BS 6336-2, "BS 6336-2: 2006 Calculation of load capacity of spur and helical gears — Part 2 : Calculation of surface durability (pitting)," Britsh Standards, 2008.

[49] BS 6336-5, "BS 6336-5 Calculation of load capacity of spur and helical gears: Part 5 Strength and quality of materials," Britsh Standards, 2003.

[50] BS 6336-3, “BS 6336-3 Calculation of load capacity of spur and helical gears —Part 3: Calculation of tooth bending strength,” BRITISH STANDARD, 2006.

[51] B. 6336-6, “BS 6336-6 Calculation of load capacity of spur and helical gears - Part 6: Calculation of service life under variable load,” BRITISH STANDARD, 2006.

[52] A. Kumar, A. Parey and P. K. Kankar, “Vibration based fault detection of polymer gear,” 2021.

[53] BS 6336-1, “Calculation of load capacity of spur and helical gears,” 2020. [Online]. Available: https://doi.org/10.3403/BSISO6336.

[54] M. Karimpour, K. D. Dearn and D. Walton, “A kinematic analysis of meshing polymer gear teeth,” in *Proceedings of the Institution of Mechanical Engineers Part L Journal of Materials Design and Applications*, 2010.

[55] A. Pogacnik and J. Tavcar, “An accelerated multilevel test and design procedure for polymer gears,” *Materials and Design 65,* p. 961–973, 2015.

[56] T. Itagaki, H. Takahashi, H. Iizuka, M. Takahashi and R. Nemoto, “Evaluating Fatigue Life of Injection-Molded-Plastic-Gear added with Carbon Particle made from Rice Hull,” in *The 3rd International Conference on Design Engineering and Science, ICDES*, 2014.

[57] H. Nigus, “Review: Failure Detection Method of Polymer Composite Gears,” *Mechanics, Materials Science & Engineering Journal,* 2017.

[58] H. Blok, “The flash temperature concept,” *Wear,* pp. 483-494, 1963.

[59] X. Tian and J. Francis E. Kennedy, “Contact Surface Temperature Models for Finite Bodies in Dry and Boundary Lubricated Sliding,” *Journal of Tribology, The American Society of Mechanical Engineers,* pp. 411-418, 1993.

[60] X. Ling, X. Jing, C. Zhang and S. Chen, “Polyether Ether Ketone (PEEK) Properties and Its Application Status,” vol. 453(1):012080, 2020.

[61] H. E. Merritt, Gears, 3rd Edition, London, United Kingdom: SIR ISAAC PITMAN & SONS, Ltd., 1954.

[62] N. P. Doll, A. Verdesca, E. Bastos, T. A. Osswald and R. Kleiss, “METHODOLOGY FOR QUASI-VISCOELASTIC SIMULATION OF POLYMER,” in *Proceedings of the Technical Conference & Exhibition*, Orlando, Florida, USA, 2015.

[63] Nuruzzaman, Dewan Muhammad; Rahaman, Mohammad Lutfar; Chowdhury, Mohammad Asaduzzaman, “Friction coefficient and wear rate of polymer and composite materials at different sliding speeds,” Vols. 6(3):231 - 245, 2012.

[64] M. A. Chowdhury , D. M. Nuruzzaman , B. K. Roy , S. Samad , R. Sarker and A. M. Rezwan, “Experimental Investigation of Friction Coefficient and Wear Rate of Composite Materials Sliding Against Smooth and Rough Mild Steel Counterfaces,” vol. 35 No.4, no. 286-296, 2013.

[65] N. El-Tayeb and I. Mostafa, “The effect of laminate orientations on friction and wear mechanisms of glass reinforced polyester composite,” *Wear, Vol.195,* pp. 186-91, 1996.

[66] N. El-Tayeb and R. Gadelrab, “Friction and wear properties of e-glass fiber reinforced epoxy compositesunder different sliding contact conditions,” *Wear, Vol.192,* pp. 112-17, 1996.

[67] S. Bahadur and Y. Zheng, “Mechanical and tribological behavior of polyester reinforced with short glass fibers,” *Wear, Vol.137,* pp. 251-66, 1990.

[68] Bahadur, S; Polineni, V.K., “Tribologicalstudies of glass fabric-reinforced polyamide compositesfilled with CuO and PTFE,” *Wear, Vol. 200,* pp. 95-104, 1996.

[69] M. Watanabe, “The friction and wear properties of nylon,” *Wear, Vol. 110,* pp. 379-88, 1968.

[70] Bahadur, S; Tabor, D, “Role of fillers in the friction and wear behavior of high-density polyethylene,” *Polymer Wear and Its Control-Chapter 17,* pp. 253-268, 1985.

[71] E. Buckingham, Analytical Mechanics of Gears, United Kingdom: McGraw-Hill Publishinh Company, 1949.

[72] C. M. Fernandes, R. C. Martins and J. H. Seabra, “Coefficient of friction equation for gears based on a modified Hersey parameter,” *Tribology International, Vol.101,* pp. 204-217, 2016.

[73] G. H. Benedict and B. W. Kelley , “Instantaneous coefficients of gear tooth friction.,” *A S L E Transactions, Vol. 4,* pp. 59-70, 1961.

[74] Y. Drozdov and Y. Gavrikov, *Wear, Vol. 11,* pp. 291-302, 1968.

[75] S. Takanashi and A. Shoji, “Measurement of the Coefficient of Kinetic Friction of Plastic Materials used for Gears,” *Journal of the Japan Society of Precision Engineering, Volume 47,* pp. 944-948, 1981.

[76] L. Schlenk, Unterscuchungen zur fresstragfähigkeit von grozahnrädern [Ph.D Thesis], TU München, 1994.

[77] Hai, Xu, Development of a general mechanical efficiency prediction methodology [PhD Thesis], The Ohio State University, 2005.

[78] M. Irfan., “Meta Modeling of Transmission Error for Spur, Helical and Planetary Gears for Wind Turbine Application,” Chalmers University of Technology, Goteborg, Sweden, 2013.

[79] B. Cerne, J. Duhovinik and J. Tavcar, “Semi-analytical flash temperature model for thermoplastic polymer spur gears with consideration of linear thermo-mechanical material characteristicst: https://www.researchgate.net/publication/338234148,” *Journal of Computational Design and Engineering,* 2019.

[80] D. Zorko, “Investigation on the high-cycle tooth bending fatigue and thermo-mechanical behavior of polymer gears with a progressive curved path of contact,” *International Journal of Fatigue 151,* 2021.

[81] R. Errichello, “Encyclopedia of Tribology: Gear Sliding,” *Springer reference,* pp. 1520-1523.

[82] “AGMA 913-A98, Method for Specifying the Geometry of Spur and Helical Gears,” American Gear Manufacturers Association, 1998.

[83] “ISO 21771:2007(E), Gears – Cylindrical Involute Gears and Gear Pairs – Concepts and Geometry,” International Standards Organization, 2007.

[84] S. M. Bae, K. J. Seo and D. E. Kin, “Effect of friction on the contact stress of a coated polymer gear,” *Friction,* pp. ISSN 2223-7690, 2020.

[85] K. Witold, W. Szymanski, D. Batory and P. Niedzielski, “Tribological Properties and Characterization of Diamond Like Carbon Coatings Deposited by MW/RF and RF Plasma-Enhanced CVD Method on Poly(ether-ether-ketone),” *Plasma Processes and Polymers 11(9),* 2014.

[86] Kinloch, A J; Young, R J, Fracture Behaviour of polymers, Springer-Science+Business Media, B.V., 1983.

[87] P. J. G. Schreurs, Fracture Mechanics, Netherlands: Technology Materials Technology, University of Eindhoven, 2012.

[88] Z. Chen and Y. Shao, “Dynamic Simulation of Spur Gear with Tooth Root Crack Propagating Along Tooth Width and Crack Depth,” *Engineering Failure Analysis,* pp. 2149-2164, 2011.

[89] K. Gopinath, “Machine Design II Module 2 - GEARS Lecture 1 - INTRODUCTION Contents,” p. https://www.academia.edu..

[90] Q. L. Zeng, K. Wang, L. R. Wan and X. Zhang, “Accurate Modelling and Transient Meshing Analysis of Involute Spur Gear Based on the Principle of Gear Shaping,” *International Journal of Simulation Modelling,* pp. 322-333, 2017.

[91] AGMA 908, “Geometry Factors for Determining the Pitting Resistance and Bending Strength of Spur, Helical and Herringbone Gear Teeth,” American Gear Manufacturers Association standard, 1989.

[92] AGMA 2001-B88, “AGMA 2001-B88 - Geometry Factors for Determining the Pitting Resistance and Bending Strength of AGMA 2001-B88 Spur, Helical and Herringbone Gear Teeth,” American Gear Manufacturers Association standard, 2001.

[93] “Gear Meshing,” 2005. [Online].

[94] “Gear Nomenclature - For Mechanical Engineers,” Kohara Gear Industry Co.,Ltd, Japan, p. https://khkgears.net.

[95] M. Parvin and J. G. Williams, “The effect of temperature on the fracture of polycarbonate,” *Journal of Materials Science volume,* 1975.

[96] S. S. Lee, J. H. Lee, I. K. Park, S. J. Song and M. Y. Choi, “Effect of Biaxial Static Loads on Fatigue Crack Propagation Behavior under Cyclic Tensile and Torsional Loading,” *Key Engineering Materials,* pp. 321-323, 2006.

[97] BS 2782-306A, BS 2782-306A - Methods of testing plastics, The British Standards Institution, 2006.

[98] Larson, E R;, “Material Selection Based on Performance: in Thermoplastic Material Selection,” *ScienceDirect,* 2015.

[99] Saba , N; Sultan,, M T H, “An Overview of Mechanical and Physical Testing of Composite Materials: in Mechanical and Physical Testing of Biocomposites, Fibre-Reinforced Composites and Hybrid Composites,” *ScienceDirect,* 2019.

[100] ASTM D 5045, “ASTM D 5045 Standard Test Methods for Plane - Strain Fracture Toughness and Strain Energy Release Rate of Plastic Materials,” American Society for Testing and Materials, 1999.

[101] M. Zappalorto, M.Salviato and M.Quaresimin, “Mixed mode (I + II) Fracture Toughness of Polymer Nanoclay Nanocomposites,” *Engineering Fracture Mechanics,* pp. 50-64, 2013.

[102] BS 7910, “BS 7910 Guide to methods for assessing the acceptability of flaws in metallic structures,” BRITISH STANDARD, 2015.

[103] Kinloch, A J; Young, R J, Fracture Behavior of Polymers, London and New York, United Kingdom and United State: Applied Science Publishers, 1983.

[104] P. J. G. Schreurs, “Fracture Mechanics,” *Technology Materials Technology,* 2012.

[105] G. C. Sih, “Strain-energy-density factor applied to mixed mode crack problems,” *International Journal of Fracture,* pp. 305-321, 1974.

[106] H. Ma, X. Pang, J. Zeng, Q. Wang and B. Wen, “Effects of gear crack propagation paths on vibration responses of the perforated gear system,” *Mechanical Systems and Signal Processing 62-63,* pp. 113-218, 2015.

[107] BS ISO 6336, “Calculation of load capacity of spur and helical gears,” 2020. [Online]. Available: https://doi.org/10.3403/BSISO6336.

[108] QTC gears, “QTC gears: ELEMENTS OF METRIC GEAR TECHNOLOGY,” 2022. [Online].

[109] Q. Sun, Y. Sun and L. Li, “Strength analysis and tooth shape optimization for involute gear with a few teeth,” *Advances in Mechanical Engineering, SAGE Journals,* 2018.

[110] J. R. Colbourne, “Contact Ratio, Interference and Backlash,” *The Geometry of Involute Gears,* pp. 83-109, 1987.

[111] H. Long, A. A. Lord, D. T. Gethin and B. J. Roylance, “Operating temperatures of oil-lubricated medium-speed gears: numerical models and experimental results,” in *Proceedings of the Institution of Mechanical Engineers Part G Journal of Aerospace Engineering*, 2003.

[112] C. K. Reece, H. V. Gerpen, V. G. Reece and C. F. Iowa, “Selection of a Proper Ball Size to Check an Involute Spur or Helical Gear Tooth,” *Gear Technology,* pp. 434-436, 1987.

[113] K. G. Budinski, Guide to friction, wear, and erosion testing, American Society for Testing and Materials (ASTM) International, 2021.

[114] A. C. Rao, “Gear frction coefficients and forces,” *Wear 53,* pp. 87-93, 1978.

[115] M. Beghini, F. Presicce and C. Santus, “A Method to Define Profile Modification of Spur Gear and Minimize the Transmission Error,” *American Gear Manufacturers Association (AGMA),* 2004.

[116] M. Takahashi, T. Itakagi, H. Takahashi, T. Koide and Y. Kobori, “Lifetime and meshing-teeth temperature of a crossed helical gear consisting of a plastic gear and a metal gear: In case of no-lubrication,” *Journal of Advanced Mechanical Design, Systems, and Manufacturing,* 2017.

[117] N. E. Anderson and S. H. Loewenthal, “Part and Full Load Spur Gear Efficiency,” *NASA TP-1622,* pp. 79-46, 1979.

[118] Y. P. Chiu, “Approximate Calculation of Power Loss in Involute Gears,” *ASME,* pp. 75-GTP-2, 1975.

[119] E. E. Shipley, “Loaded Gears in Action. Gear Handbook,” *D. W. Dudley, ed., McGraw Hill Book Co., Inc.,,* pp. 14-60, 1962.

[120] Z. Wan, H. Cao, Y. Zi, W. He and Y. Chen, “Mesh stiffness calculation using an accumulated integral potential energy method and dynamic analysis of helical gears,” *Mechanism and Machine Theory, Volume 92,* pp. 447-463, 2015.

[121] T. Jabbour, G. Asmar, M. Abdulwahab and J. Nasr, “Real contact ratio and tooth bending stress calculation for plastic/plastic and plastic/steel spur gears,” *Mechanics & Industry 22, Published by EDP Sciences,* p. 30, 2021.

[122] Y. Yang, N. Hu, Z. Cheng, J. Hu and L. Zhang, “Improved Mesh Stiffness Method and Vibration Analysis of a Planetary Gear System with a Spatial Tooth Crack,” *Machines, MDPI,* 2022.

[123] C. T. Sun and Z. H. Jin, “Chapter 6 Crack Tip Plasticity,” in *Fracture Mechanics*, https://doi.org/10.1016/C2009-0-63512-1, 2012, pp. 123-169.

[124] H. Tada, P. C. Paris and G. R. Irwin, “The Stress Analysis of Cracks Handbook,” *ASME Press,* 2000.

[125] A. M. Abdulnaser and A. F. Yahya , “3D modelling of fatigue crack growth and life predictions using ANSYS,” *Ain Shams Engineering Journal,* vol. 101636, no. 13, 2021.

[126] H. Ma, X. Pang, J. Zeng, Q. Wang and B. Wen, “Effects of gear crack propagation paths on vibration responses,” *Mechanical Systems and Signal Processing 62-63,* pp. 113-128, 2015.

[127] S. Wu, M. J. Zuo and A. Parey, “Simulation of spur gear dynamics and estimate of fault growth,” *Journal of Sound and Vibration 317,* pp. 608-624, 2008.

[128] “BS/ISO 6336-1 Calculation of load capacity of spur and helical gears — Part 1: Basic principles, introduction and general influence factors,” Retrieved from The British Standards Institution: https://doi.org/10.3403/BSISO6336., 1996.

[129] M. SEPE, “MATERIALS: The Problems with Single-Point Data: Part 10,” *Plastic Technology,* 2016.

[130] C. H. Kim, “Durability improvement method for plastic spur gears,” *Tribology International 39(11),* pp. 1454-1461, 2006.

[131] T. Costopoulos, “Calculation of transmission errors, actual path of contact and actual contact ratio of non-conjugate gears,” 2002.

[132] C. M. Fernandes, P. M. Marques, R. C. Martins and J. H. Seabra, “Influence of Gear Loss Factor on the Power Loss Prediction,” *Mechanical Sciences,* vol. Volume 6, no. 2, pp. 81-88, 2015.

[133] A. C. Rao, “Gear Friction Coefficient and Forces,” *Wear 53,* Vols. Elsevier Sequaoia S.A., Lausanne, pp. 87-93, 1979.

[134] N. Y. Drozdov and A. Y. Gavrikov, “Friction and scoring under the conditions of Simultaneous rolling and sliding of bodies,” *Wear 11 (4),* no. Elsevier Sequoia S.A. Lausanne, pp. 291-302, 1967.

[135] Victrex, “Victrex PEEK: the foundation of victrex innovations,” Victrex PEEK, 2019.

[136] BS/ISO 6336-1 Calculation of load capacity of spur and helical gears — Part 1: Basic principles, introduction and general influence factors, Retrieved from The British Standards Institution: https://doi.org/10.3403/BSISO6336, 1996.

[137] Z. Chen and Y. Shao, “Dynamic simulation of spur gear with tooth root crack propagating along tooth width and crack depth,” *Engineering Failure Analysis,* vol. 18, pp. 2149-2164, 2011.

[138] J. G. Williams, “Fracture mechanics of polymers,” *Polymer Engineering & Science, Volume 17, Issue 3,* 1977.

[139] G. R. Irwin, “Linear fracture mechanics, fracture transition, and fracture control,” *Engineering Fracture Mechanics, Volume 1, Issue 2,* pp. 241-257, 1968.

[140] Z. Chen and Y. Shao, “Dynamic Simulation of Spur Gear with Tooth Root Crack Propagating Along Tooth Width and Crack Depth,” *Engineering Failure Analysis,* pp. 2149-2164, 2011.

[141] BS ISO 6336-1, “Calculation of load capacity of spur and helical gears,” 2020. [Online]. Available: https://doi.org/10.3403/BSISO6336.

[142] E. Trenton, Behavior of Viscoelastic Materials, Gears.

[143] BS2782-306A, BS2782-306A - Methods of testing plastics, The British Standards Institution, 2006.

[144] A. J. Kinloch and R. J. Young, Fracture Behavior of Polymers. Edited by A J Kinloch and R J Young, London and New York: Applied Science Publishers, 1983.

Appendixes

Appendix A: Collected the surface temperature, accelerating vibrations and weight losses data

A-I Temperature Collected

Chapter 4 was presented the Surface Temperature (°C) data for wheel PEEK 450CA30 collected at intervals of 1 to 7. Appendix A will show the temperature data for wheel PEEKs after 10 million cycles, providing insights until the occurrence of a crack.

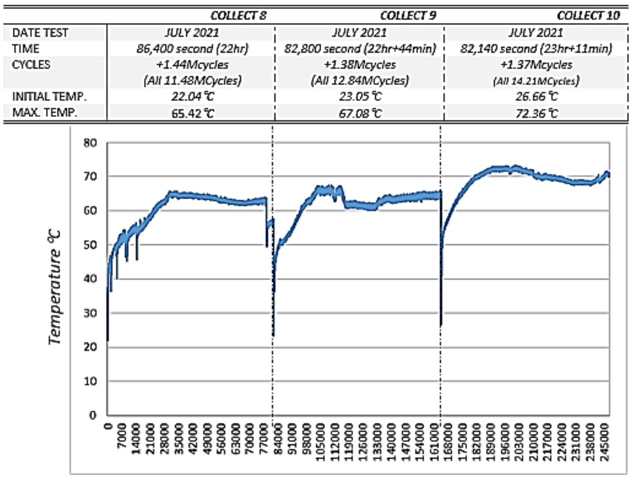

	COLLECT 8	COLLECT 9	COLLECT 10
DATE TEST	JULY 2021	JULY 2021	JULY 2021
TIME	86,400 second (22hr)	82,800 second (22hr+44min)	82,140 second (23hr+11min)
CYCLES	+1.44Mcycles (All 11.48MCycles)	+1.38Mcycles (All 12.84MCycles)	+1.37Mcycles (All 14.21MCycles)
INITIAL TEMP.	22.04 ℃	23.05 ℃	26.66 ℃
MAX. TEMP.	65.42 ℃	67.08 ℃	72.36 ℃

Figure A-1 *Surface Temperature (℃) for Wheel PEEK 450G, Collected at 8-10 (Crack)*

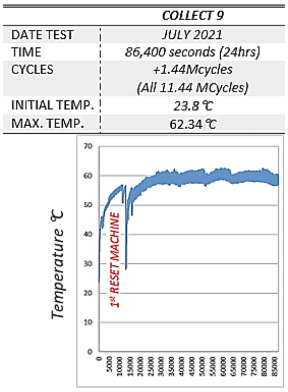

	COLLECT 9
DATE TEST	JULY 2021
TIME	86,400 seconds (24hrs)
CYCLES	+1.44Mcycles (All 11.44 MCycles)
INITIAL TEMP.	23.8 ℃
MAX. TEMP.	62.34 ℃

Figure A-2 *Surface Temperature (℃) for Wheel PEEK 450GL30, Collected at 9 (Crack)*

	COLLECT 8	COLLECT 9	COLLECT 10	COLLECT 11	COLLECT 12	COLLECT 13	COLLECT 14	COLLECT 15	COLLECT 16
DATE TEST	*JULY 2021*	*JULY 2021*	*JULY 2021*	*JULY 2021*	*JULY 2021*	*AUGUST 2021*	*AUGUST 2021*	*AUGUST 2021*	*AUGUST 2021*
TIME	*79,200 second (22hr)*	*81,840 second (22hr+44min)*	*59,400 second (16hr+50min)*	*80,280 second (22hr+18min)*	*72,900 second (22hr)*	*89,520 second (24hr+52min)*	*86,400 second (24hr)*	*66,500 second (18hr+45min)*	*86,400 second (24hr)*
CYCLES	*+1.32Mcycles (All 11.36MCycles)*	*+1.44Mcycles (All 12.724MCycles)*	*+1.44Mcycles (All 13.71MCycles)*	*+1.34Mcycles (All 15.05MCycles)*	*+1.32Mcycles (All 16.37MCycles)*	*+1.49Mcycles (All 17.86MCycles)*	*+1.44Mcycles (All 19.30MCycles)*	*+1.11Mcycles (All 20.41MCycles)*	*+1.44Mcycles (All 21.85MCycles)*
INITIAL TEMP.	*28.58℃*	*28.06C*	*31.76℃*	*23.56℃*	*24.56℃*	*19.92℃*	*23.98℃*	*23.96℃*	*24.86℃*
MAX. TEMP.	*62.28℃*	*65.10℃*	*54.08℃*	*60.18℃*	*67.04℃*	*64.86℃*	*65.34℃*	*67.52℃*	*62.42℃*

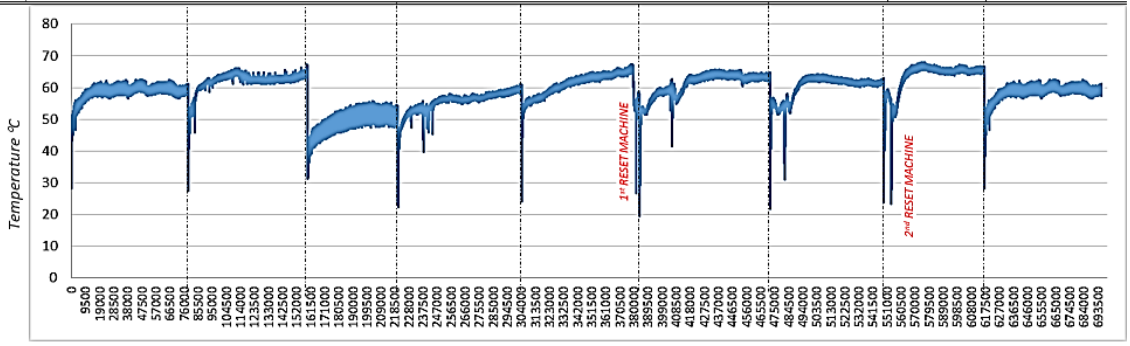

Figure A-3 *Surface Temperature (℃) for Wheel PEEK 450FC30, Collected at 8-16 (Crack)*

	COLLECT 8	COLLECT 9	COLLECT 10	COLLECT 11	COLLECT 12	COLLECT 13	COLLECT 14
DATE TEST	*JULY 2021*	*AUGUST 2021*	*AUGUST 2021*	*AUGUST 2021*	*AUGUST 2021*	*AUGUST 2021*	*AUGUST 2021*
TIME	*94,800 second (26hr+20min)*	*84,300 second (23hr+25min)*	*86,400 second (24hr)*	*80,580 second (22hr+38min)*	*89,520 second (24hr+52min)*	*73,585 second (20hr+44min)*	*75,600 second (21hr)*
CYCLES	*+1.58Mcycles (All 11.58MCycles)*	*+1.41Mcycles (All 12.99MCycles)*	*+1.44Mcycles (All 14.43MCycles)*	*+1.34Mcycles (All 16.37MCycles)*	*+1.49Mcycles (All 17.86MCycles)*	*+1.23Mcycles (All 19.30MCycles)*	*+1.26Mcycles (All 21.14MCycles)*
INITIAL TEMP.	*22.70℃*	*18.40℃*	*22.96℃*	*23.36℃*	*19.92℃*	*19.88℃*	*23.76℃*
MAX. TEMP.	*61.87℃*	*67.43℃*	*69.50℃*	*68.78℃*	*65.86℃*	*68.98℃*	*62.31℃*

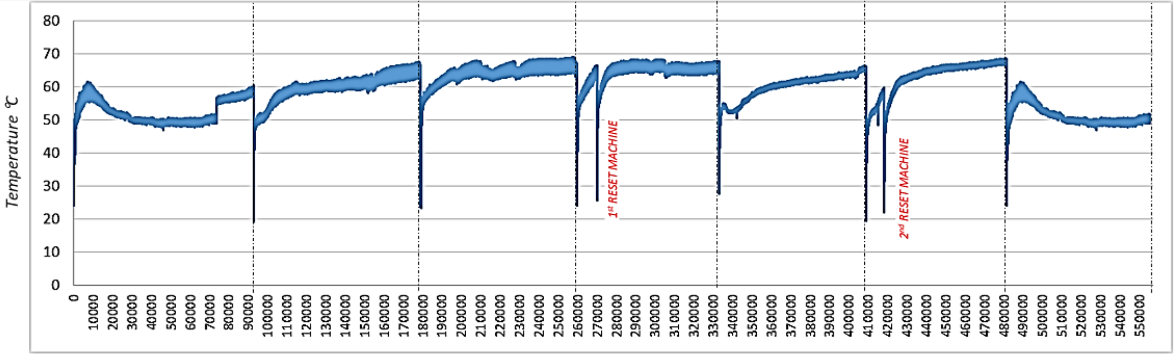

	COLLECT 17	COLLECT 18	COLLECT 19	COLLECT 20	COLLECT 21	COLLECT 22	COLLECT 23	COLLECT 24
DATE TEST	*SEPTEMBER 2021*	*SEPTEMBER 2021*	*SEPTEMBER 2021*	*MARCH 2022*	*MARCH 2022*	*MARCH 2022*	*MARCH 2022*	*MARCH 2022*
TIME	*72,540 second (20hr+15min)*	*72,000 second (20hr)*	*64,000 second (17hr+47min)*	*80,580 second (22hr+38min)*	*66,000 second (18hr+30min)*	*75,600 second (21hr+15min)*	*62,700 second (17hr+25min)*	*67,500 second (18hr+45min)*
CYCLES	*+1.21Mcycles (All 12.79MCycles)*	*+1.20Mcycles (All 13.99MCycles)*	*+1.07Mcycles (All 15.06MCycles)*	*+1.34Mcycles (All 16.40MCycles)*	*+1.10Mcycles (All 17.50MCycles)*	*+1.23Mcycles (All 18.78MCycles)*	*+1.05Mcycles (All 19.82MCycles)*	*+1.13Mcycles (All 20.95MCycles)*
INITIAL TEMP.	*23.16℃*	*24.04℃*	*23.34℃*	*19.98℃*	*22.46℃*	*17.20℃*	*18.90℃*	*19.50℃*
MAX. TEMP.	*57.70℃*	*60.36℃*	*56.64℃*	*50.20℃*	*52.52℃*	*52.96℃*	*52.18℃*	*54.74℃*

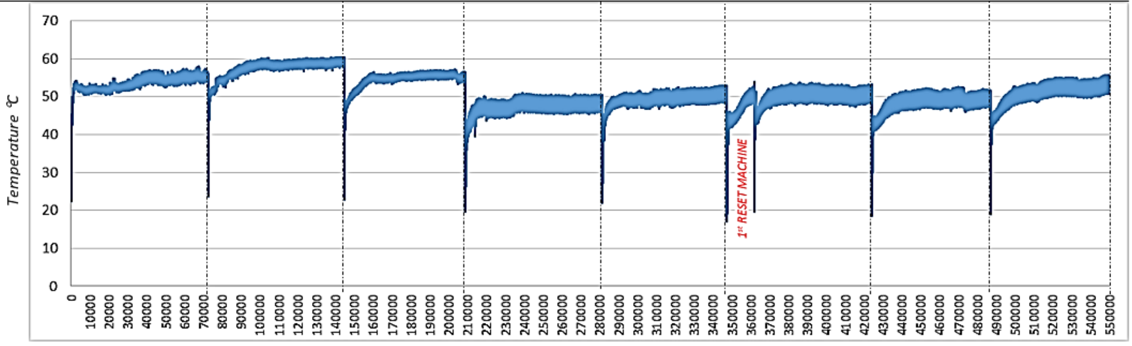

Figure A-4 *Surface Temperature (℃) for Wheel PEEK 450CA30, Collected at 8-24*

	COLLECT 25	COLLECT 26	COLLECT 27	COLLECT 28	COLLECT 29	COLLECT 30	COLLECT 31
DATE TEST	MARCH 2022	MARCH 2022	MARCH 2022	MARCH 2022	MARCH 2022	MARCH 2022	MARCH 2022
TIME	64,800 second (18hr)	68,400 second (19hr)	69,300 second (19hr+15min)	69,900 second (19hr+25min)	84,600 second (23hr+30min)	76,800 second (21hr+20min)	85,500 second (23hr+45min)
CYCLES	+1.08Mcycles (All 22.03MCycles)	+1.14Mcycles (All 23.71MCycles)	+1.16Mcycles (All 24.87MCycles)	+1.17Mcycles (All 26.03MCycles)	+1.41Mcycles (All 27.44MCycles)	+1.28Mcycles (All 28.72MCycles)	+1.43Mcycles (All 30.15MCycles)
INITIAL TEMP.	19.56℃	19.94℃	21.22℃	20.86℃	25.16℃	25.34℃	17.98℃
MAX. TEMP.	56.42℃	56.80℃	59.12℃	58.86℃	54.52℃	56.72℃	61.16℃

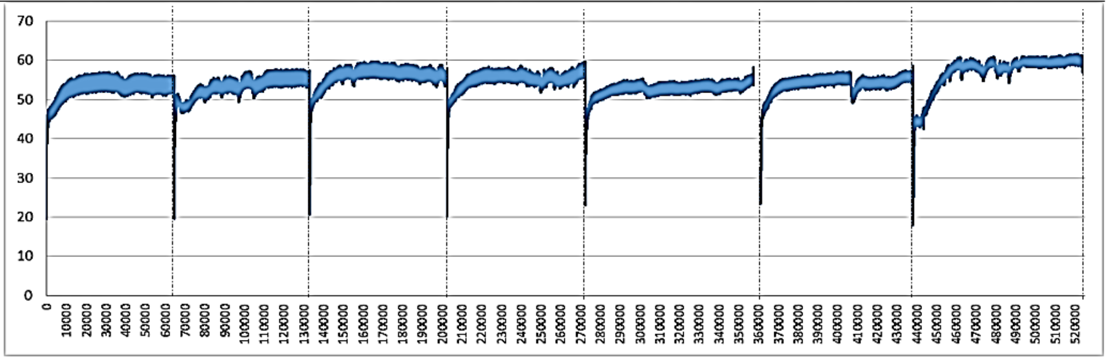

	COLLECT 32	COLLECT 33	COLLECT 34	COLLECT 35	COLLECT 36	COLLECT 37	COLLECT 38
DATE TEST	MARCH 2022	APRIL 2022	APRIL 2022	APRIL 2022	APRIL 2022	APRIL 2022	APRIL 2022
TIME	69,900 second (19hr+25min)	67,800 second (18hr+50min)	69,300 second (18hr+50min)	66,600 second (18hr+30min)	69,300 second (18hr+50min)	64,800 second (18hr)	66,600 second (18hr+30min)
CYCLES	+1.17Mcycles (All 31.32MCycles)	+1.13Mcycles (All 32.45MCycles)	+1.13Mcycles (All 33.58MCycles)	+1.11Mcycles (All 34.69MCycles)	+1.13Mcycles (All 35.82MCycles)	+1.08Mcycles (All 36.90MCycles)	+1.11Mcycles (All 38.01MCycles)
INITIAL TEMP.	22.46℃	23.16℃	21.38℃	21.56℃	23.22℃	N/A	21.56℃
MAX. TEMP.	63.46℃	63.64℃	63.54℃	68.10℃	63.02℃	N/A	67.68℃

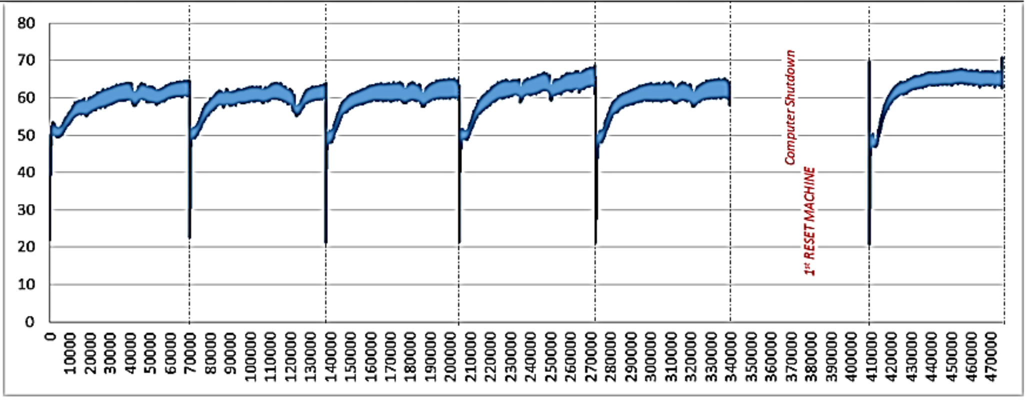

Figure A-5 *Surface Temperature (℃) for Wheel PEEK 450CA30, Collected at 25-40 (Crack)*

A-II Accelerating Vibration Collected

The accelerating vibration data for wheel PEEKs during the initial running period provides insights leading up to the occurrence of a crack.

450G	COLLECT 1	COLLECT 2	COLLECT 3	COLLECT 4	COLLECT 5	COLLECT 6	COLLECT 7
ACCEL. VIBRA. (MAX. AVG)	N/A	N/A	N/A	3.54X, 3.52Y, 3.48Z -1.83 X, -0.44Y, -1.32Z	1.51X, 2.21Y, 1.37Z -1.78 X, -1.46Y, -0.83Z	1.41X, 2.01Y, 1.01Z -1.52X, -0.04Y, -0.81Z	1.55X, 2.18Y, 0.91Z -1.98X, -0.34Y, -0.82Z
LOAD TEST (LOW & HIGH)				Avg. 183.20N	Avg. 184.35N	Avg. 182.31N	Avg. 182.68N

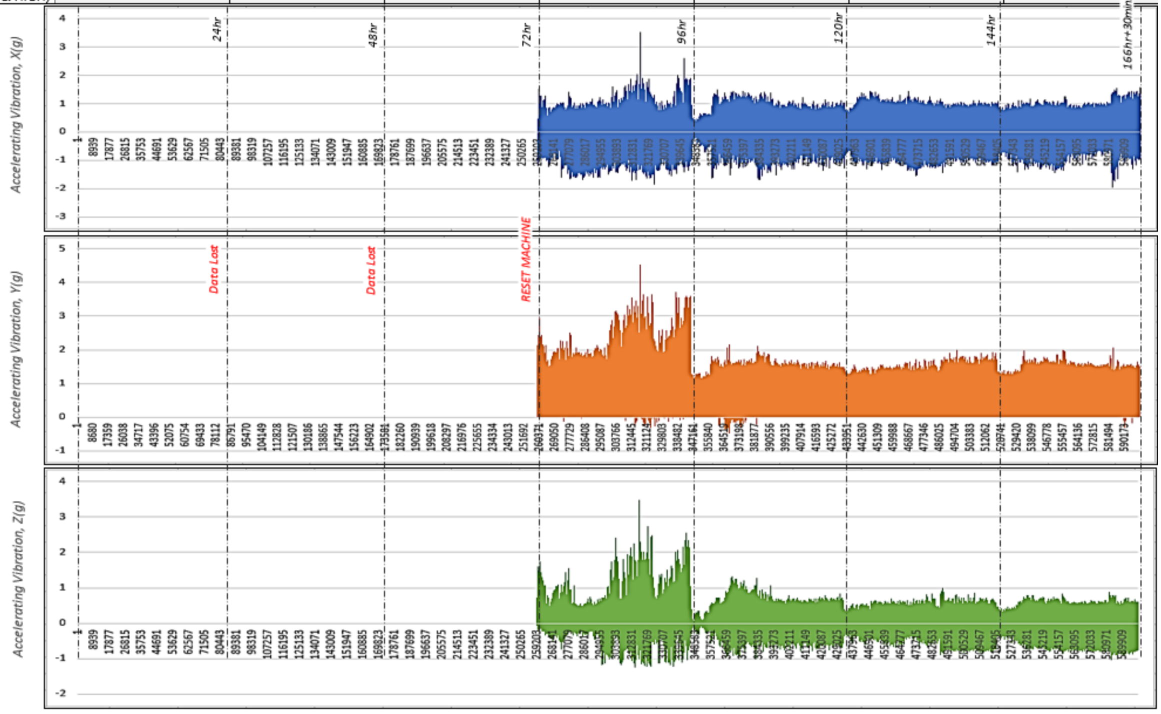

	COLLECT 8	COLLECT 9	COLLECT 10
ACCEL. VIBRA. (MAX. AVG)	2.38X, 2.20Y, 2.48Z -1.52X, -1.74Y, -1.31Z	1.99X, 1.99Y, 2.03Z -1.78X, -1.27Y, -0.51Z	2.43X, 2.20Y, 2.24Z -1.23X, -1.14Y, -0.72Z
LOAD TEST (LOW & HIGH)	Avg. 183.90N 174.5-193.3N	Avg. 183.9N 164.9-202.9N	Avg. 180.85N 167.3 – 194.4N

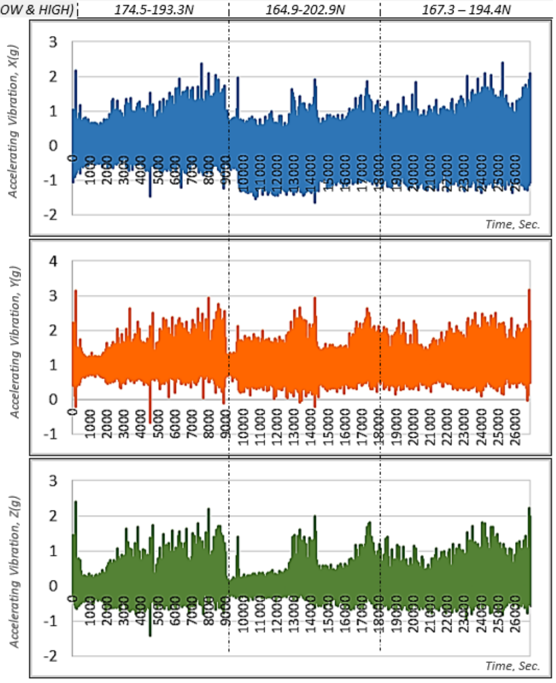

Figure A-5 *Accelerating Vibration (g) for Wheel PEEK 450G, Collected at 1-10 (Crack)*

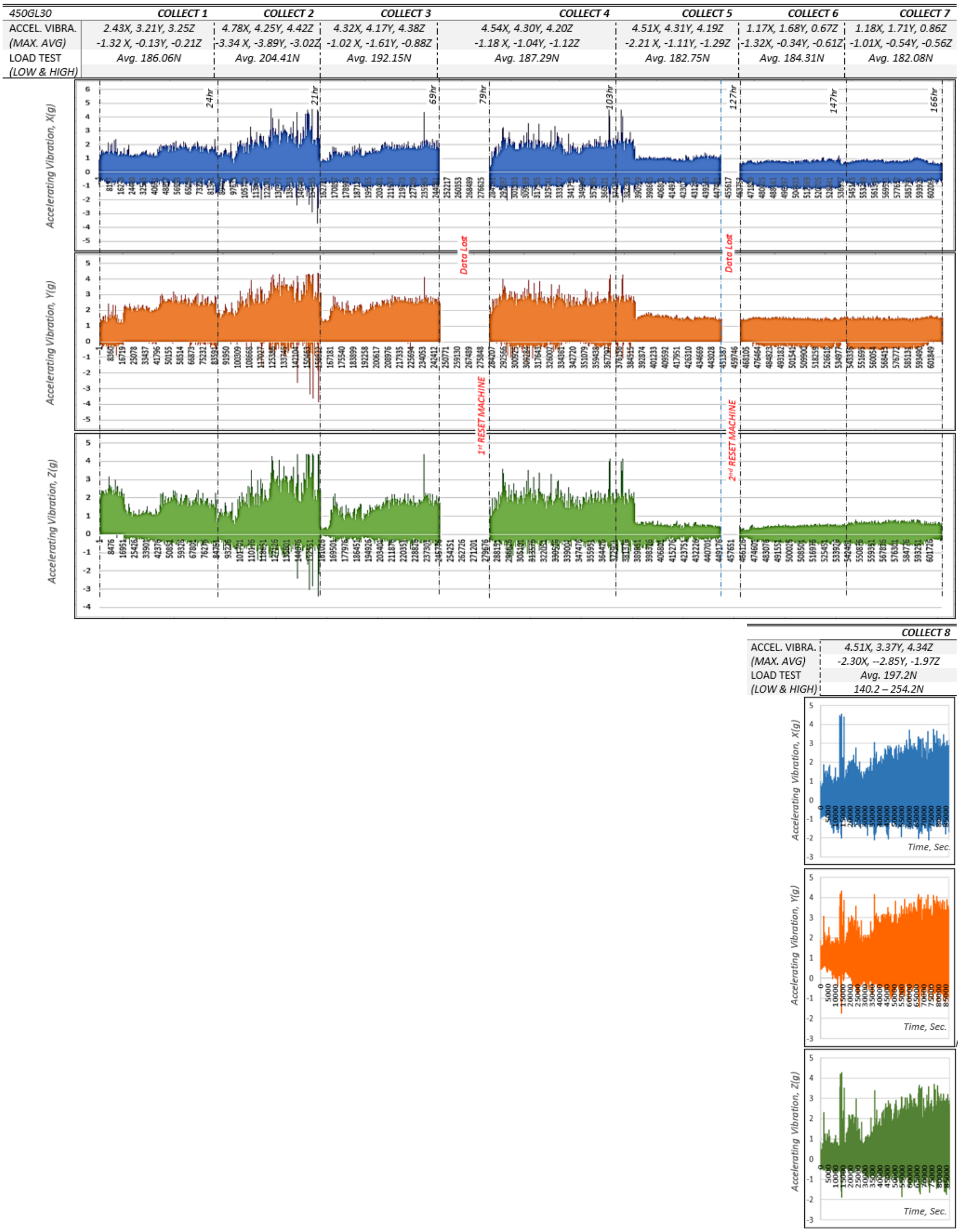

450GL30	COLLECT 1	COLLECT 2	COLLECT 3	COLLECT 4	COLLECT 5	COLLECT 6	COLLECT 7
ACCEL. VIBRA.	2.43X, 3.21Y, 3.25Z	4.78X, 4.25Y, 4.42Z	4.32X, 4.17Y, 4.38Z	4.54X, 4.30Y, 4.20Z	4.51X, 4.31Y, 4.19Z	1.17X, 1.68Y, 0.67Z	1.18X, 1.71Y, 0.86Z
(MAX. AVG)	-1.32 X, -0.13Y, -0.21Z	-3.34 X, -3.89Y, -3.02Z	-1.02 X, -1.61Y, -0.88Z	-1.18 X, -1.04Y, -1.12Z	-2.21 X, -1.11Y, -1.29Z	-1.32X, -0.34Y, -0.61Z	-1.01X, -0.54Y, -0.56Z
LOAD TEST	Avg. 186.06N	Avg. 204.41N	Avg. 192.15N	Avg. 187.29N	Avg. 182.75N	Avg. 184.31N	Avg. 182.08N
(LOW & HIGH)							

	COLLECT 8
ACCEL. VIBRA.	4.51X, 3.37Y, 4.34Z
(MAX. AVG)	-2.30X, --2.85Y, -1.97Z
LOAD TEST	Avg. 197.2N
(LOW & HIGH)	140.2 – 254.2N

__Figure A-6__ Accelerating Vibration (g) for Wheel PEEK 450GL30, Collected at 1-8 (Crack)

450FC30	COLLECT 1	COLLECT 2	COLLECT 3	COLLECT 4	COLLECT 5	COLLECT 6	COLLECT 7
ACCEL. VIBRA. (MAX. AVG)	1.01X, 0.46Y, 0.64Z -1.32 X, -0.13Y, -0.21Z	1.31X, 1.85Y, 1.03Z -1.15 X, -0.73Y, -0.69Z	1.42X, 1.87Y, 1.18Z -1.21 X, -1.01Y, -0.87Z	1.52X, 1.91Y, 0.89Z -1.51 X, -0.64Y, -0.64Z	0.97X, 1.63Y, 0.59Z -1.22 X, -0.39Y, -0.29Z	4.47X, 4.28Y, 4.48Z -1.81X, -1.82Y, -0.68Z	2.02X, 2.63Y, 2.89Z -1.12X, -0.80Y, -1.23Z
LOAD TEST (LOW & HIGH)	Avg. 180.46N	Avg. 181.45N	Avg. 182.05N	Avg. 183.29N	Avg. 183.15N	Avg. 204.31N	Avg. 198.81N

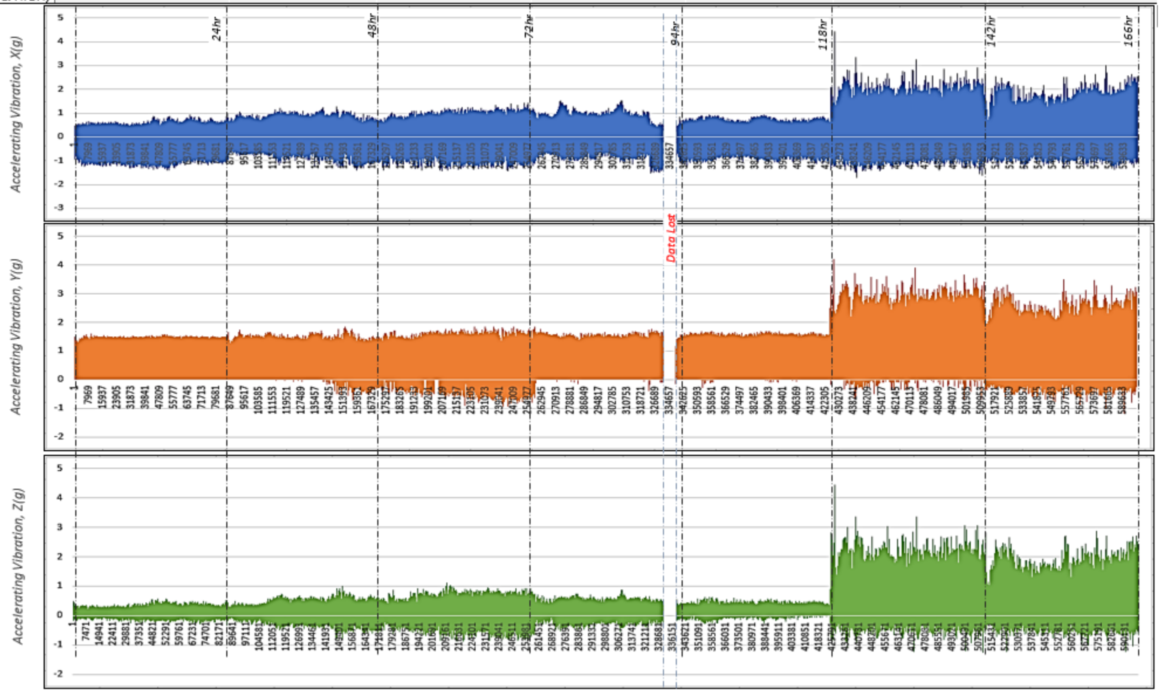

	COLLECT 8	COLLECT 9	COLLECT 10	COLLECT 11	COLLECT 12	COLLECT 13	COLLECT 14	COLLECT 15	COLLECT 16
ACCEL. VIBRA. (MAX. AVG)	4.31X, 3.57Y, 4.23Z	4.35X, 3.08Y, -4.28Z	4.38X, 3.10Y, 3.98Z	4.37X, 3.89Y, 3.81Z	1.98X, 1.91Y, 1.99Z	4.38X, 3.35Y, 4.21Z	3.22X, 2.71Y, 3.11Z	4.38X, 3.35Y, 4.21Z	3.22X, 2.71Y, 3.11Z
	-3.25X, -4.87Y, -3.42Z	-3.01X, -5.12Y, -3.88Z	-2.01X, -2.11Y, -1.78Z	-1.67X, -2.21Y, -0.78Z	-1.88X, -2.12Y, -0.32Z	-3.20X, -4.00Y, -2.87Z	-1.74X, -2.21Y, -1.41Z	-3.20X, -4.00Y, -2.87Z	-1.74X, -2.21Y, -1.41Z
LOAD TEST (LOW & HIGH)	Avg. 193.95N	Avg. 196.9N	Avg. 201.82N	Avg. 177.35N	Avg. 179.2N	Avg. 179.2N	Avg. 183.90N	Avg. 193.95N	Avg. 183.90N
	177.4-210.5N	172.9-220.9N	179.55-224.1N	164.9-190.8N	163.5-194.9N	163.5-194.9	154.9 - 212.9N	177.4-210.5N	154.9 - 212.9N

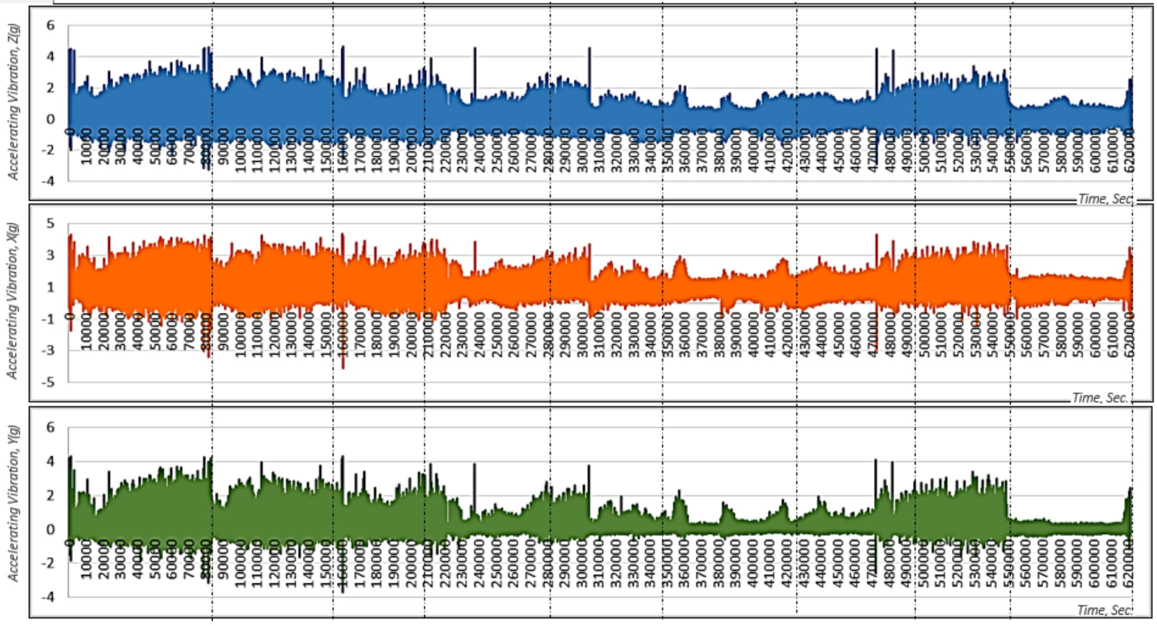

Figure A-7 Accelerating Vibration (g) for Wheel PEEK 450FC30, Collected at 1-16 (Crack)

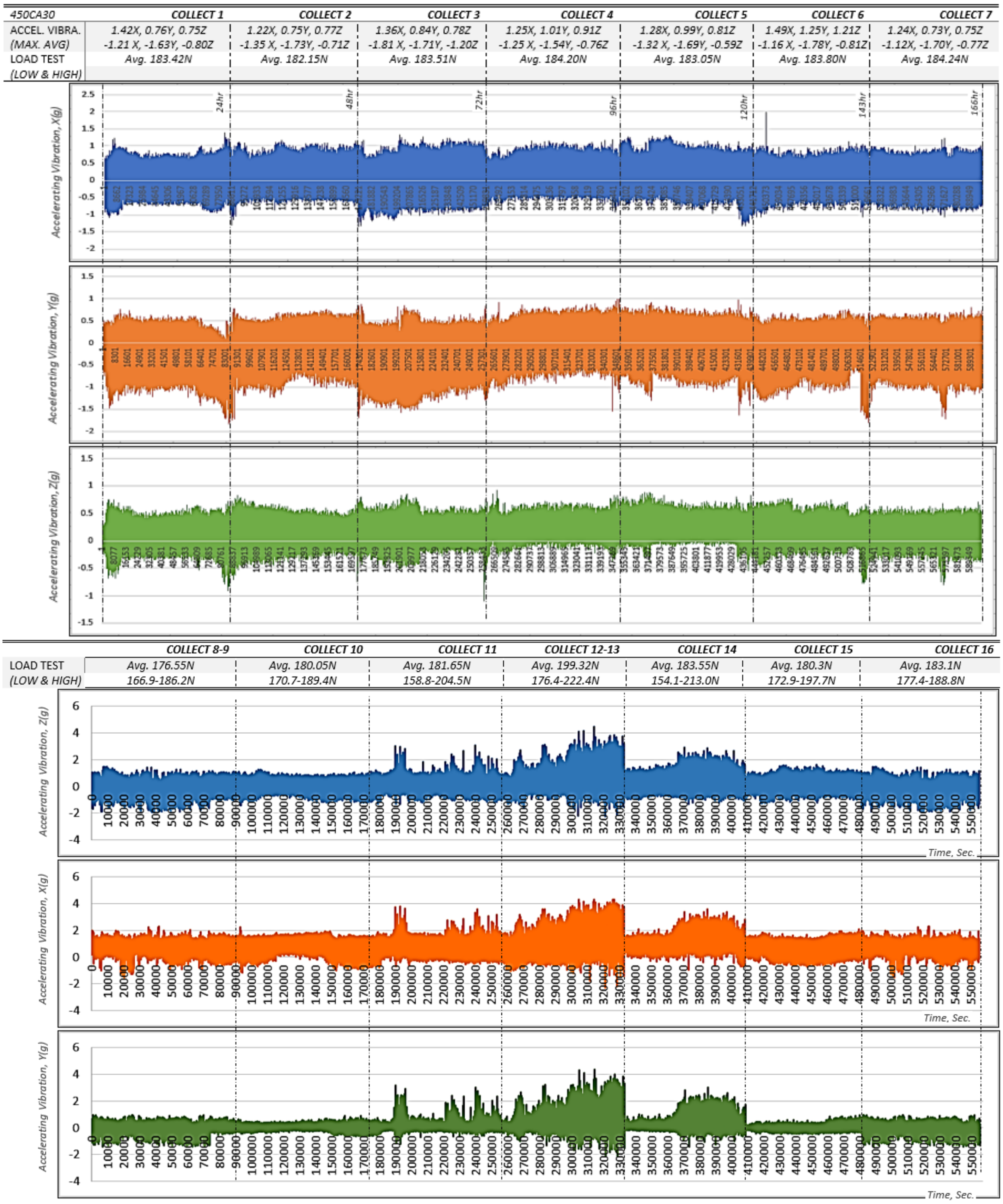

450CA30	COLLECT 1	COLLECT 2	COLLECT 3	COLLECT 4	COLLECT 5	COLLECT 6	COLLECT 7
ACCEL. VIBRA. (MAX. AVG)	1.42X, 0.76Y, 0.75Z -1.21 X, -1.63Y, -0.80Z	1.22X, 0.75Y, 0.77Z -1.35 X, -1.73Y, -0.71Z	1.36X, 0.84Y, 0.78Z -1.81 X, -1.71Y, -1.20Z	1.25X, 1.01Y, 0.91Z -1.25 X, -1.54Y, -0.76Z	1.28X, 0.99Y, 0.81Z -1.32 X, -1.69Y, -0.59Z	1.49X, 1.25Y, 1.21Z -1.16 X, -1.78Y, -0.81Z	1.24X, 0.73Y, 0.75Z -1.12X, -1.70Y, -0.77Z
LOAD TEST (LOW & HIGH)	Avg. 183.42N	Avg. 182.15N	Avg. 183.51N	Avg. 184.20N	Avg. 183.05N	Avg. 183.80N	Avg. 184.24N

	COLLECT 8-9	COLLECT 10	COLLECT 11	COLLECT 12-13	COLLECT 14	COLLECT 15	COLLECT 16
LOAD TEST (LOW & HIGH)	Avg. 176.55N 166.9-186.2N	Avg. 180.05N 170.7-189.4N	Avg. 181.65N 158.8-204.5N	Avg. 199.32N 176.4-222.4N	Avg. 183.55N 154.1-213.0N	Avg. 180.3N 172.9-197.7N	Avg. 183.1N 177.4-188.8N

Figure A-8 *Accelerating Vibration (g) for Wheel PEEK 450CA30, Collected at 1-16 (Crack)*

	COLLECT 17	COLLECT 18	COLLECT 19	COLLECT 20	COLLECT 21	COLLECT 22	COLLECT 23	COLLECT 24
LOAD TEST	*Avg. 180.6N*	*Avg. 177.15N*	*Avg. 177.95N*	*Avg. 173.7N*	*Avg. 183.30N*	*Avg. 181.1.0N*	*Avg. 183.5N*	*Avg. 180.65N*
(LOW & HIGH)	*166.5-194.7N*	*164.8-189.5N*	*156.0-199.9N*	*149.5 - 197.9N*	*169.1 - 197.5N*	*164.8 – 197.4N*	*168.6-198.4N*	*164.1-197.2N*

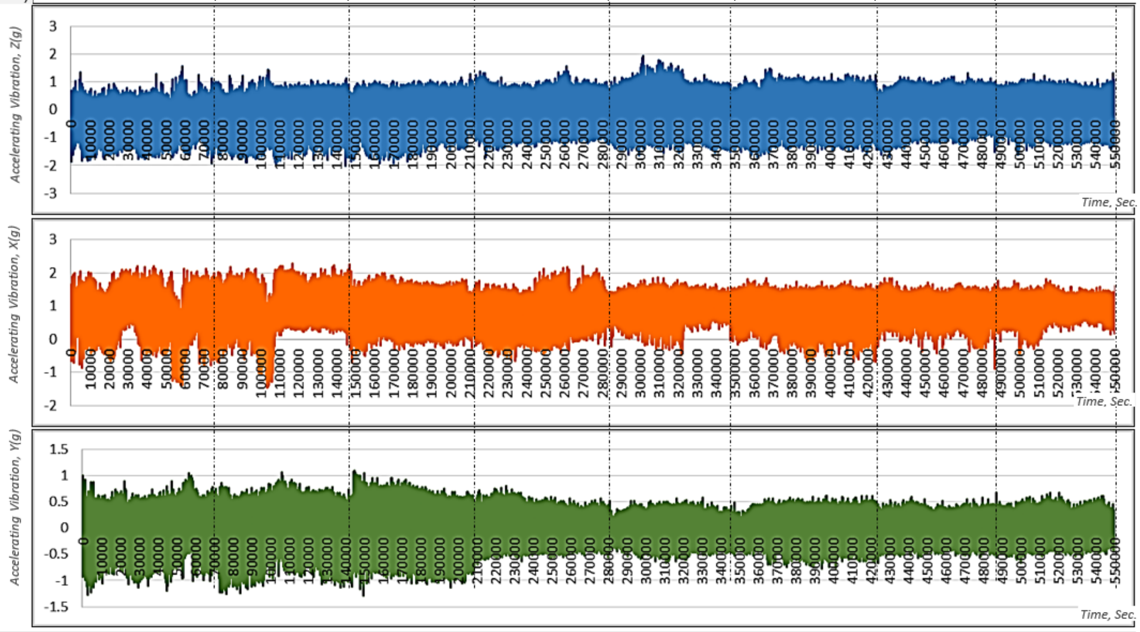

	COLLECT 25	COLLECT 26	COLLECT 27	COLLECT 28	COLLECT 29	COLLECT 30	COLLECT 31
LOAD TEST	*Avg. 181.25N*	*Avg. 181.15N*	*Avg. 182.90N*	*Avg. 178.25N*	*Avg. 183.30N*	*Avg. 179.0N*	*Avg. 181.85N*
(LOW & HIGH)	*160.5 - 202.0N*	*162.2 - 200.1N*	*170.3 – 195.5N*	*159.1 - 197.4N*	*169.1 - 197.5N*	*168.3 - 189.7N*	*158.4 - 205.3N*

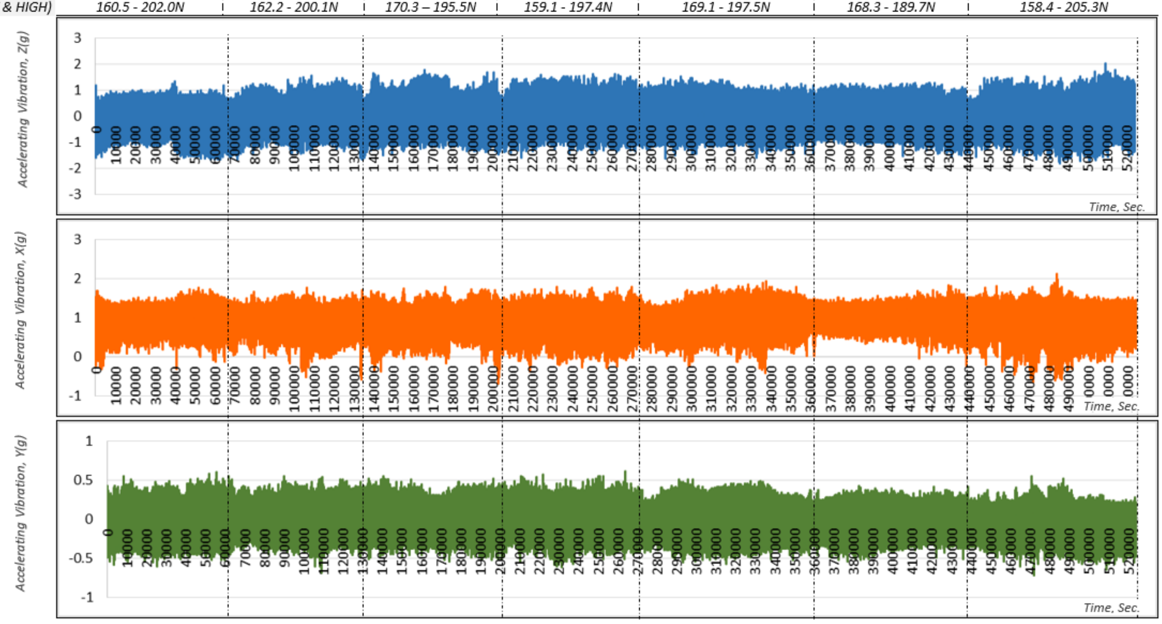

***Figure A-9** Accelerating Vibration (g) for Wheel PEEK 450CA30, Collected at 17-31 (Crack)*

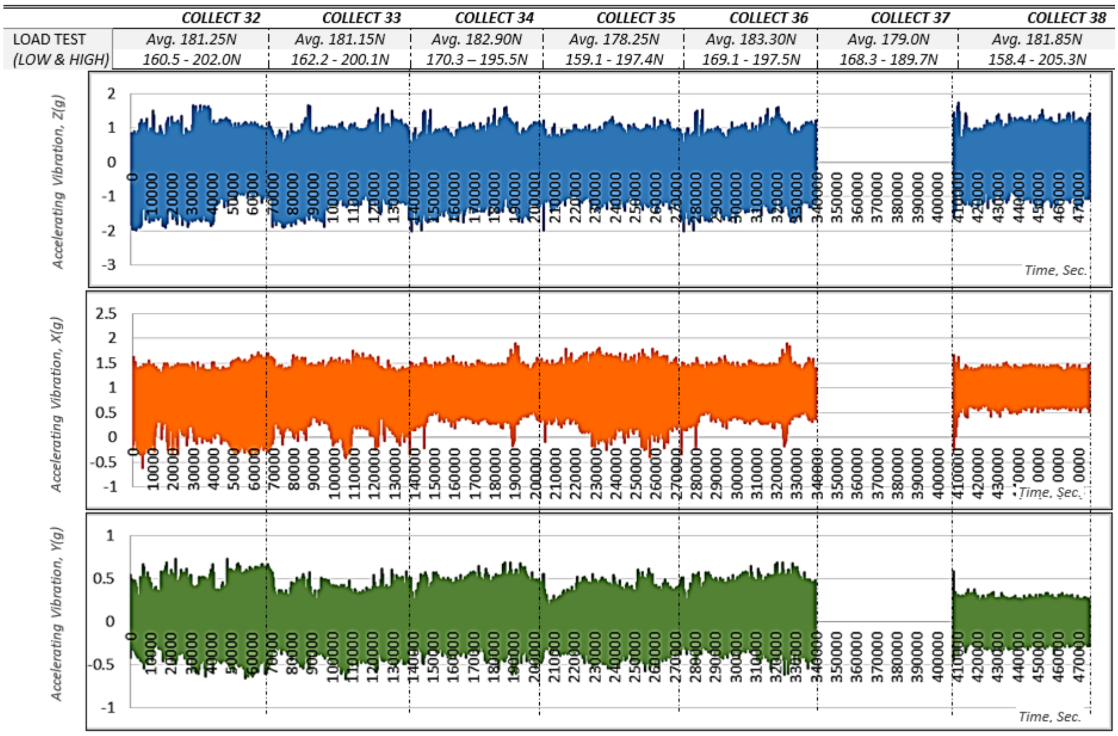

Figure A-10 Accelerating Vibration (g) for wheel PEEK 450CA30, Collected at 32-38 (Crack)

A-III Weight Losses Data

The experimental results in Table A-1 and A-2 were collected for the weight reduction of all four types of PEEKs. The graphs showed that a significant decrease in the weight of pinion and wheel.

Table A-1 Crack Time Over

PEEKs	Crack Time Over	Cycles
450G	236 hrs.+11 min. (850260 sec.)	14.17 million
450FC30	292 hrs. (1051200 sec.)	17.52 million
450GL30	190 hrs. (684000 sec.)	11.40 million
450CA30	835 hrs. (3006000 sec.)	50.10 million

Table A-2 *Data Collection for Weight Loss in Real time Testing, for BS-20PA*

Collected Data	**450G**	**450FC30**	**450GL30**	**450CA30**
	(Grams)	*(Grams)*	*(Grams)*	*(Grams)*
START	122.7626	115.163	118.7242	116.0189
1	122.6724 (-0.0902)	114.9799 (-0.1831)	-	115.9690 (-0.0499)
2	122.6179 (-0.1447)	-	118.3552 (-0.3690)	115.9421 (-0.0768)
3	122.5849 (-0.1777)	114.8839 (-0.2791)	118.1144 (-0.6098)	115.9135 (-0.1054)
4	122.4435 (-0.3191)	114.7899 (-0.3731)	117.9550 (-0.7692)	115.8859 (-0.1130)
5	122.1916 (-0.5710)	114.7091 (-0.4539)	117.7439 (-0.9803)	115.8629 (-0.1360)
6	121.9798 (-0.7828)	114.6334 (-0.5296)	117.5385 (-1.1857)	115.8476 (-0.1513)
8	121.8558 (-0.9068)	114.5665 (-0.5965)	117.3849 (-1.3393)	115.8197 (-0.1792)
9	121.7120 (-1.0506)	114.5141 (-0.6489)	117.2700 (-1.4542)	115.7908 (-0.2281)
10	121.6801 (-1.0825)	114.4672 (-0.6958)	--------Crack--------	115.7714 (-0.2475)
11	121.6478 (-1.1148)	114.3998 (-0.7632)		115.7488 (-0.2401)
12	--------Crack--------	114.3406 (-0.8224)		115.7216 (-0.2973)
13		114.2907 (-0.8723)		115.6998 (-0.3191)
14		114.2400 (-0.9230)		115.6761 (-0.3428)
15		114.1918 (-0.9712)		115.6430 (-0.3759)
16		--------Crack--------		115.6132 (-0.4057)
17				115.5871 (-0.4318)
18				115.5610 (-0.4057)
19				115.5211 (-0.4978)
20				115.5019 (-0.5170)
21				115.4803 (-0.5386)
22				115.4711 (-0.5478)
23				115.4419 (-0.5770)
24				115.4178 (-0.6011)
25				115.3881 (-0.6308)
26				115.3732 (-0.6457)
27				115.3589 (-0.6600)
28				115.3330 (-0.6730)
29				115.3199 (-0.6990)
30				-
31				115.2974 (-0.7215)
32				115.2736 (-0.7453)
33				115.2608 (-0.7581)
34				115.2487 (-0.7702)
35				115.2169 (-0.8020)
36				115.2018 (-0.8171)
37				115.1940 (-0.8249)
38				115.1730 (-0.8450)
39				115.1231 (-0.8958)
				--------Crack--------

Appendix B: Collected the surface temperature, accelerating vibrations and weight losses data

B-I Temperature Collected

Surface Temperature (℃) data for PEEK 650G vs 650G

	COLLECT 1	COLLECT 2	COLLECT 3	COLLECT 4	COLLECT 5	COLLECT 6	COLLECT 7
DATE TEST	29-30 APRIL 2021	3-4 MAY 2021	4-5 MAY 2021	6-7 MAY 2021	10-11 MAY 2021	11-12 MAY 2021	13-14,17 MAY 2021
TIME	82,800 sec. (23hr)	86,400 second (24hr)	86,400 second (24hr)	86,400 second (24hr)	86,400 second (24hr)	86,400 second (23hr+43min.)	86,400 second (8hr×3days)
CYCLES	1.38Mcycles	+1.44Mcycles (All 2.82MCycles)	+1.44Mcycles (All 4.26MCycles)	+1.44Mcycles (All 5.70MCycles)	+1.44Mcycles (All 7.14MCycles)	+1.44Mcycles (All 8.55MCycles)	+1.44Mcycles (All 10.20MCycles)
INITIAL TEMP.	21.38 ℃	18.10 ℃	21.65 ℃	21.88 ℃	19.44 ℃	22.56 ℃	19.44|19.34 |19.22 ℃
MAX. TEMP.	59.82 ℃	56.38 ℃	58.52 ℃	117.84 ℃	155.12 ℃	223.34 ℃	56.94|64.20|61.68 ℃
WEIGHT LOSS	-0.0033 gram Of pinion	-0.0017 gram (All -0.0050 gram) ^{P}	-0.0364 gram (All -0.0314 gram) ^{P}	-0.0020 gram (All -0.0334 gram) ^{P}	-0.0123 gram (All -0.0457 gram) ^{P}	-0.0205 gram (All -0.0539 gram) ^{P}	-0.0189 gram (All -0.0728 gram) ^{P}
	-0.0098 gram Of wheel	-0.0005 gram (All -0.0103 gram) ^{W}	-0.0004 gram (All -0.0107 gram) ^{W}	-0.0003 gram (All -0.0110 gram) ^{W}	-0.0090 gram (All -0.0200 gram) ^{W}	-0.0114 gram (All -0.0314 gram) ^{W}	-0.0108gram (All -0.0422 gram) ^{W}

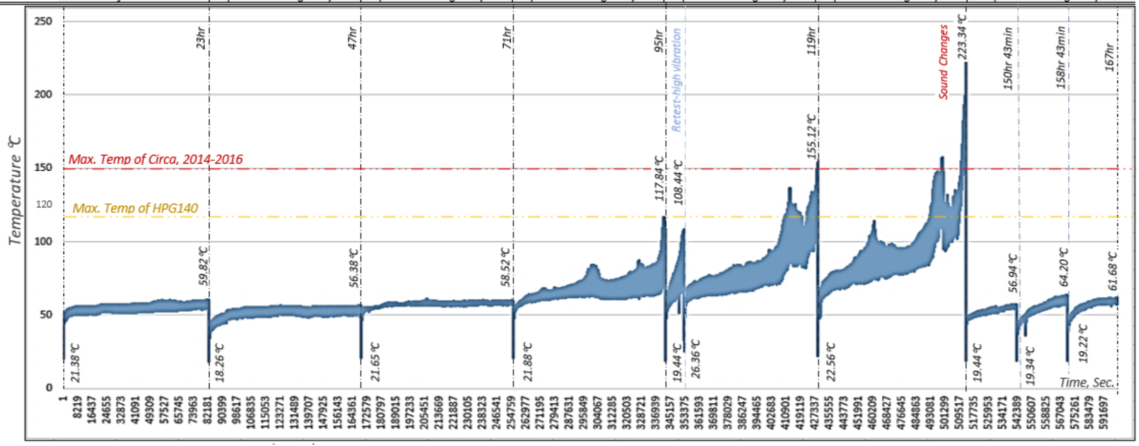

	COLLECT 8	COLLECT 9	COLLECT 10	COLLECT 11	COLLECT 12	COLLECT 13	COLLECT 14
DATE TEST	JUNE 2021	JUNE 2021	JUNE 2021	JUNE 2021	JUNE 2021	JUNE 2021	JUNE 2021
TIME	86,400 second (8hr×3days)	86,400 second (24hr)	86,400 second (24hr)	86,400 second (24hr)	86,400 second (24hr)	86,400 second (24hr)	72,000 second (20hr)
CYCLES	+1.44Mcycles (All 11.64MCycles)	+1.44Mcycles (All 13.08MCycles)	+1.44Mcycles (All 14.52MCycles)	+1.44Mcycles (All 15.96MCycles)	+1.44Mcycles (All 17.40MCycles)	+1.44Mcycles (All 18.84MCycles)	+1.44Mcycles (All 20.28MCycles)
INITIAL TEMP.	27.24|N/A|22.16 ℃	18.26 ℃	24.34 ℃	21.88 ℃	24.94 ℃	29.22 ℃	21.04 ℃
MAX. TEMP.	85.12|N/A|63.64 ℃	50.50 ℃	56.64 ℃	53.51 ℃	51.38 ℃	52.36 ℃	51.58 ℃
WEIGHT LOSS (DATA FOR 8-14)							-0.0322 gram (All -0.1050 gram) ^{P}
							-0.0147 gram (All -0.0572 gram) ^{W}

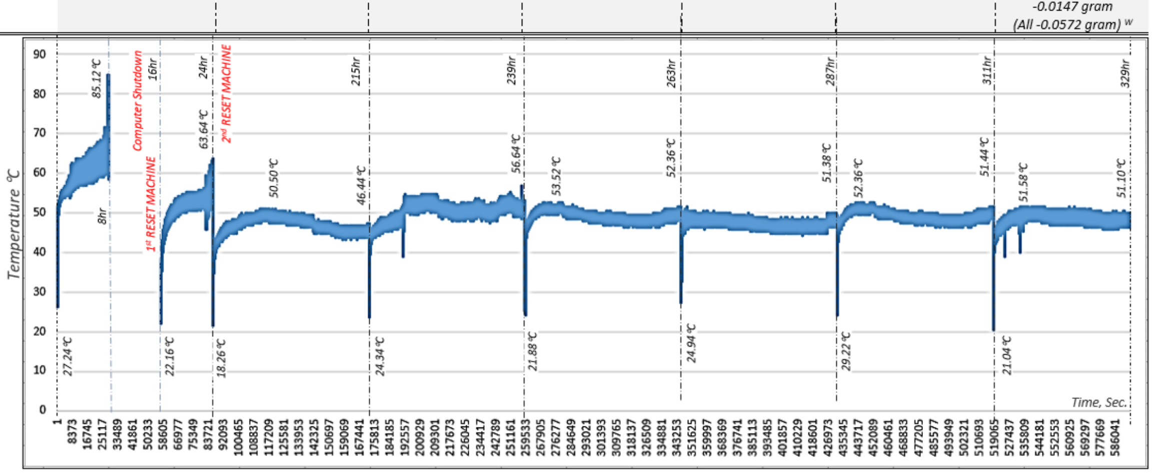

Figure B-1 *Surface Temperature (℃) Data for PEEK 650G vs 650G Until Crack*

	COLLECT 15	COLLECT 16	COLLECT 17	COLLECT 18	COLLECT 19	COLLECT 20	COLLECT 21
DATE TEST	JUNE 2021	JUNE 2021	JULY 2021	JULY 2021	JULY 2021	JULY 2021	JULY 2021
TIME	82,800 second (23hr)	86,400 second (24hr)	86,400 second (24hr)	86,400 second (24hr)	86,400 second (24hr)	86,400 second (24hr)	72,000 second (20hr)
CYCLES	+1.38Mcycles (All 21.40MCycles)	+1.44Mcycles (All 22.84MCycles)	+1.44Mcycles (All 24.28MCycles)	+1.44Mcycles (All 25.72MCycles)	+1.44Mcycles (All 27.16MCycles)	+1.44Mcycles (All 28.60MCycles)	+1.44Mcycles (All 29.98MCycles)
INITIAL TEMP.	25.40℃	18.20℃	22.00℃	22.92℃	22.40℃	19.54℃	22.64℃
MAX. TEMP.	52.42℃	50.98℃	50.84℃	57.04℃	56.66℃	58.36℃	51.80℃
WEIGHT LOSS *(DATA FOR 8-14)*							-0.0031 gram (All -0.1081 gram) ^{P}
							-0.0026 gram (All -0.0598 gram) ^{W}

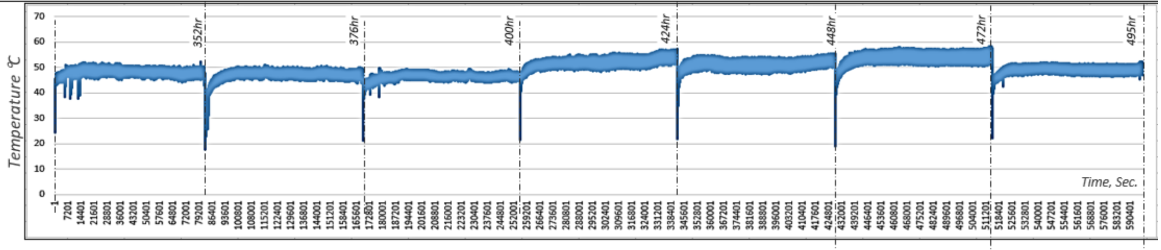

	COLLECT 22	COLLECT 23
DATE TEST	JULY 2021	JULY 2021
TIME	82,800 second (24hr)	86,400 second (Total 542hrs)
CYCLES	+1.38Mcycles (All 31.42MCycles)	+1.44Mcycles (All 32.80MCycles)
INITIAL TEMP.	19.86℃	24.88℃
MAX. TEMP.	53.82℃	59.26℃
WEIGHT LOSS *(DATA FOR 22-23)*		-0.0085 gram (All -0.1166 gram) ^{P}
		-0.0045 gram (All -0.0643 gram) ^{W}

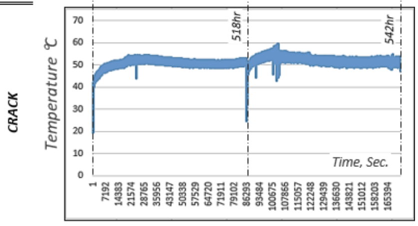

Figure B-1 *Surface Temperature (℃) data for PEEK 650G vs 650G Until Crack (Cont.)*

B-II Accelerating Vibration Collected

Accelerating Vibration (g) data for PEEK 650G vs 650G

	COLLECT 1	COLLECT 2	COLLECT 3	COLLECT 4	COLLECT 5	COLLECT 6	COLLECT 7
ACCEL. VIBRA.	3.52x, 3.29y, 3.64z	3.50x, 3.25y, 3.66z	2.98x, 2.81Y, 2.83Z	3.49x, 2.88Y, 2.93Z	2.28x, 2.07Y, 1.90z	2.88x, 2.06Y, 3.08Z	3.16x, 2.78Y, 3.04Z
(MAX. AVG)	-2.25X, -2.43Y, -2.32Z	-1.78X, -2.20Y, -1.67Z	-1.81X, -1.73Y, -1.4Z	-1.49X, -1.51Y, -1.88Z	-2.02X, -1.99Y, -1.29Z	-1.90X, -2.28Y, -1.13Z	-1.66X, -1.37Y, -0.93Z
LOAD TEST	Avg. 181.25N	Avg. 181.15N	Avg. 182.90N	Avg. 178.25N	Avg. 183.30N	Avg. 179.0N	Avg. 181.85N
(LOW & HIGH)	160.5 - 202.0N	162.2 - 200.1N	170.3 – 195.5N	159.1 - 197.4N	169.1 - 197.5N	168.3 - 189.7N	158.4 - 205.3N

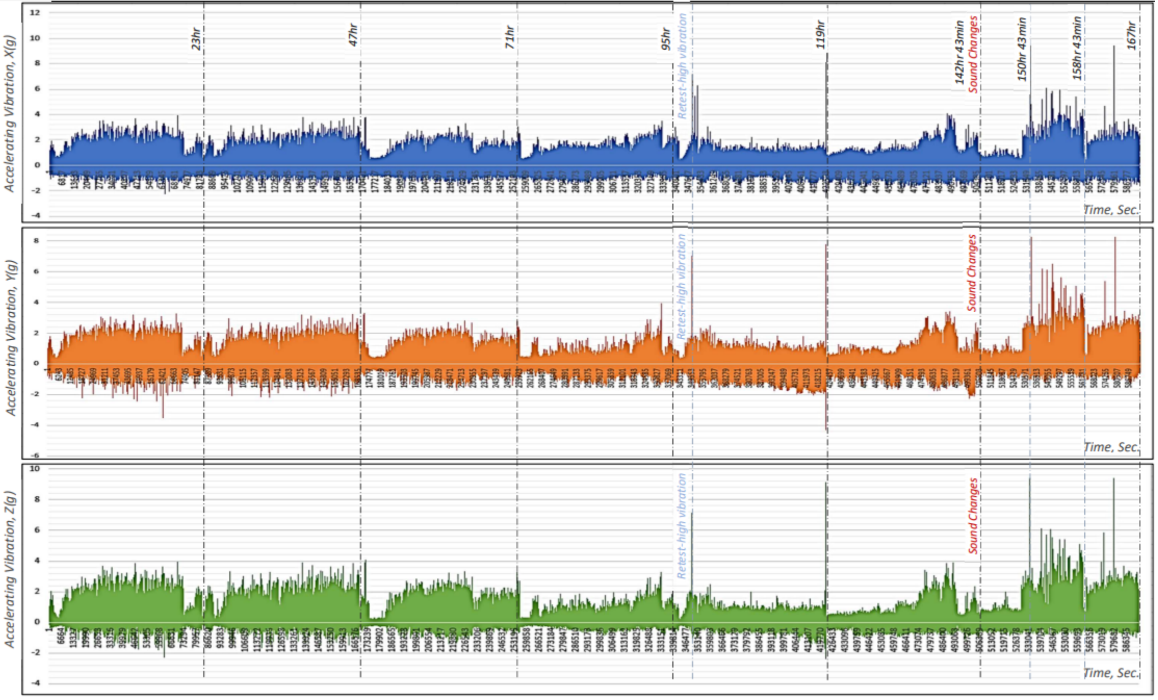

Figure B-2 *Accelerating Vibration (g) Data for PEEK 650G vs 650G Until crack*

	COLLECT 8	COLLECT 9	COLLECT 10	COLLECT 11	COLLECT 12	COLLECT 13	COLLECT 14
ACCEL. VIBRA.	5.09X, 5.32Yy, 5.83z	1.37X, 1.08Y, 1.20Z	1.52X, 1.17Y, 1.29Z	0.98X, 0.60Y, 0.43Z	1.6X, 1.08Y, 1.05z	4.53X, 3.20Y, 4.43Z	3.26X, 2.53Y, 3.0Z
(MAX. AVG)	-1.94X, -1.66Y, -1.04Z	-1.41X, -1.26Y, -1.01Z	-1.49X, -1.26Y, -1.04Z	-0.99X, -1.46Y, -0.40Z	-1.26X, -1.16Y, -1.08Z	-1.53X, -2.26Y, -1.73Z	-1.47X, -2.08Y, -1.08Z
LOAD TEST	Avg. 204.175N	Avg. 188.90N	Avg. 193.45N	Avg. 184.2N	Avg. 185.05N	Avg. 185.80N	Avg. 180.95N
(LOW & HIGH)	163.80 – 244.55N	176.30 – 201.50 N	178.70 – 208.20N	171.80 – 196.60 N	171.60 - 198.50N	168.3 – 203.30N	162.30 – 199.60N

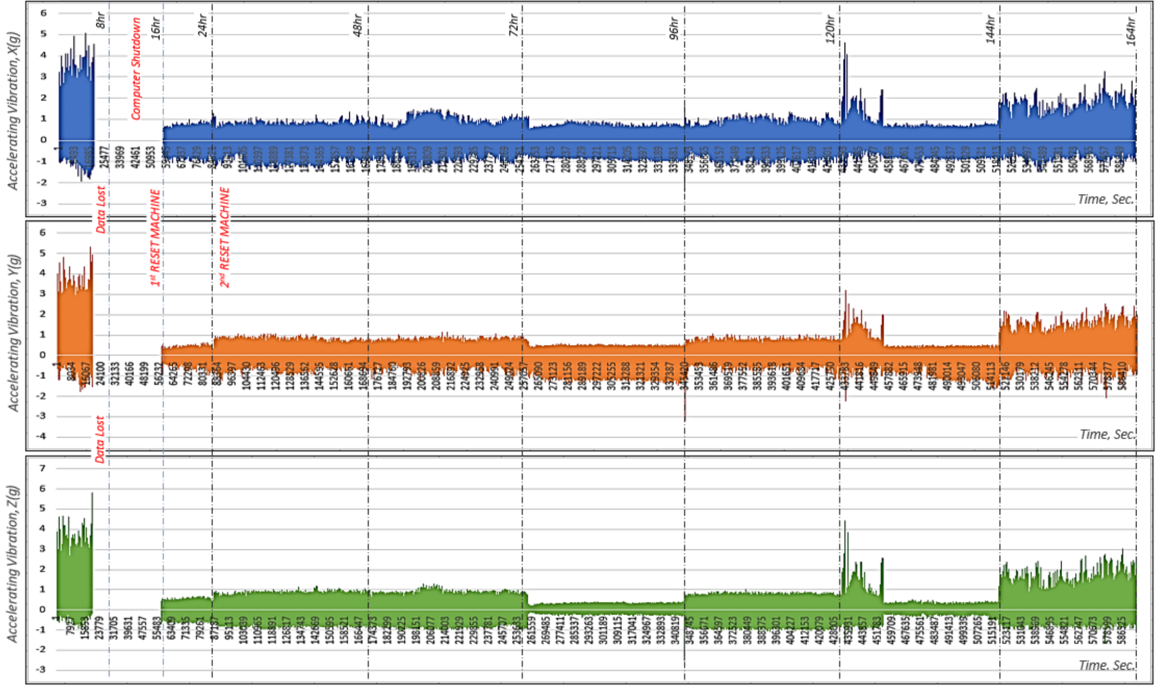

	COLLECT 15	COLLECT 16	COLLECT 17	COLLECT 18	COLLECT 19	COLLECT 20	COLLECT 21
ACCEL. VIBRA.	4.40X, 3.51Y, 4.28Z	4.36X, 3.34Y, 4.34Z	N/A	1.78X, 1.67Y, 1.68Z	1.89X, 1.28Y, 1.65z	2.67X, 2.10Y, 2.18Z	3.06X, 2.253Y, 2.81Z
(MAX. AVG)		-3.50X, -4.86Y, -3.87Z			-1.56X, -2.01Y, 1.17Y		
LOAD TEST	Avg. 198.057N	Avg. 204.55N	N/A	Avg. 184.2N	Avg. 185.05N	Avg. 185.80N	Avg. 204.2N
(LOW & HIGH)	163.80 – 244.55N	163.50 – 245.60N		171.80 – 196.60 N	171.60 - 198.50N	168.3 – 203.30N	163.80 – 244.60N

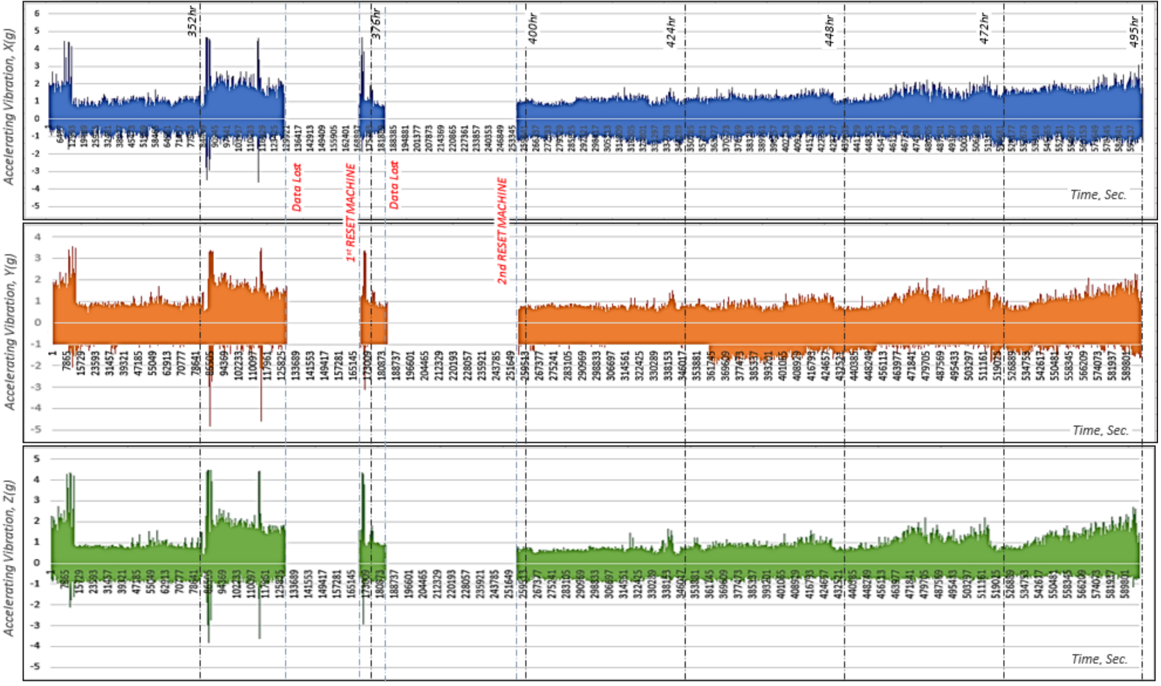

Figure B-2 *Accelerating Vibration (g) Data for PEEK 650G vs 650G Until Crack*

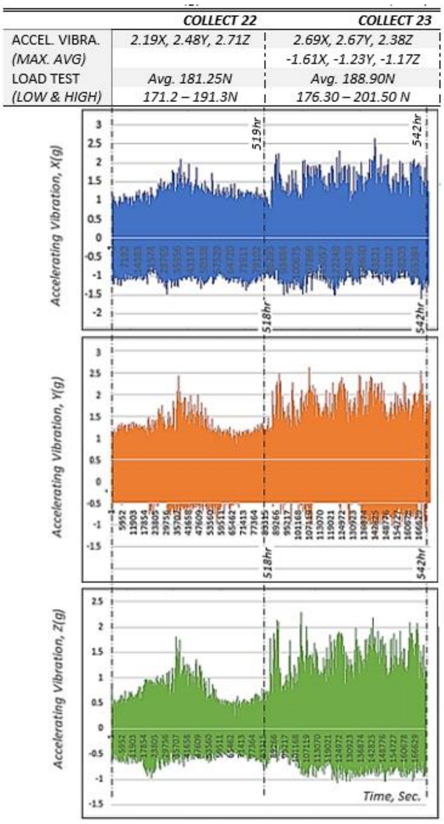

	COLLECT 22	COLLECT 23
ACCEL. VIBRA. (MAX. AVG)	2.19X, 2.48Y, 2.71Z	2.69X, 2.67Y, 2.38Z -1.61X, -1.23Y, -1.17Z
LOAD TEST (LOW & HIGH)	Avg. 181.25N 171.2 – 191.3N	Avg. 188.90N 176.30 – 201.50 N

__Figure B-2__ Accelerating Vibration (g) Data for PEEK 650G vs 650G Until Crack

B-III Weight Losses Data

The experimental results in Figure B-1 were collected for the weight reduction of all four types of PEEK 650G gearboxes every 20-24 hours. The graphs showed a significant decrease in the weight of the pinion and wheel.

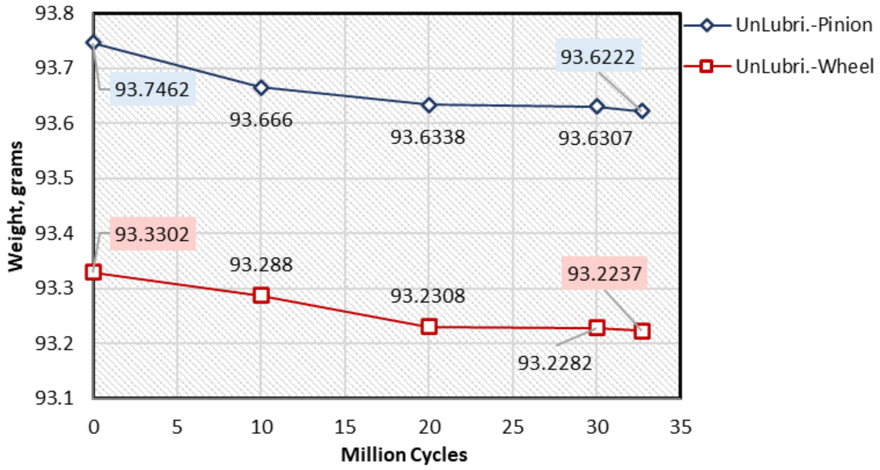

__Figure B-3__ Data Collection for Weight Loss in the Real Time Testing, for BS-30PA